| | |
|---|---|
| **Titre:** Title: | 3-D Time-Domain Finite Element Modeling of Nonlinear Conductive and Ferromagnetic Thin Films |
| **Auteur:** Author: | Bruno De Sousa Alves |
| **Date:** | 2021 |
| **Type:** | Mémoire ou thèse / Dissertation or Thesis |
| **Référence:** Citation: | De Sousa Alves, B. (2021). 3-D Time-Domain Finite Element Modeling of Nonlinear Conductive and Ferromagnetic Thin Films [Ph.D. thesis, Polytechnique Montréal]. PolyPublie. https://publications.polymtl.ca/9923/ |

**POLYTECHNIQUE MONTRÉAL**
affiliée à l'Université de Montréal

# 3-D time-domain finite element modeling of nonlinear conductive and ferromagnetic thin films

**BRUNO DE SOUSA ALVES**
Département de génie électrique

Thèse présentée en vue de l'obtention du diplôme de *Philosophiæ Doctor*
Génie électrique

Décembre 2021

**POLYTECHNIQUE MONTRÉAL**
affiliée à l'Université de Montréal

Cette thèse intitulée :

**3-D time-domain finite element modeling of nonlinear conductive and ferromagnetic thin films**

présentée par **Bruno DE SOUSA ALVES**
en vue de l'obtention du diplôme de *Philosophiæ Doctor*
a été dûment acceptée par le jury d'examen constitué de :

**Serge PRUDHOMME**, président
**Frédéric SIROIS**, membre et directeur de recherche
**Marc LAFOREST**, membre et codirecteur de recherche
**Frédéric TRILLAUD**, membre
**Christophe GEUZAINE**, membre externe

# ACKNOWLEDGEMENTS

First and foremost, I want to express my genuine appreciation and gratitude to my supervisors, Dr. Frédéric Sirois and Dr. Marc Laforest, for their valuable support, guidance and intensive contribution through all the stages of my project. Their excellent advice, constructive feedback, and careful editing contributed enormously to the writing of this thesis and the publications we completed together.

I also would like to express my appreciation to my thesis committee members, Dr. Christophe Geuzaine, Dr. Frédéric Trillaud and Dr. Serge Prudhomme, for taking their time to read this thesis carefully, for participating in my defence, and for providing valuable comments on my research. Moreover, I want to thank CAPES (Coordenação de Aperfeiçoamento de Pessoal de Nível Superior) and the Fonds de recherche du Québec for their financial support, and Mitacs for supporting my research internship at Katholieke Universiteit Leuven.

I thank Dr. Ruth V. Sabariego for hosting me at Katholieke Universiteit Leuven during my research internship in 2019 and for her collaboration on the work developed in the fifth chapter of this thesis. I also thank Dr. Valtteri Lahtinen for all the discussion we had about my project, especially during its early stages, and for his collaboration in the paper presented as the sixth chapter of this thesis.

I gratefully acknowledge my colleagues at Polytechnique Montreal for the constant exchange of ideas and support. In particular, Simon Richard, Jonathan Bellemare, Jean-Hughes Fournier Lupien, Christian Lacroix, Lucile Moret, Amanda Hébert, Yan Chevalier-St-Jean, Mathieu Masse, Maxime Tousignant, Marina Gasparini, Iben Brahim Yahya and Gregory Giard. I want to thank Alexandre Arsenault, especially for all our discussions about using thin and thick cuts in the $H$-$\phi$-formulation and his collaboration in the two papers we developed together during this time. I extend my acknowledgment to all Polytechnique Montreal staff members, especially to Mrs. Suzanne Le Bel, Mrs. Nathalie Lévesque and Mrs. Brigitte Gal, the Electrical Engineering Department staff, and the librarians.

Last but not least, I'd like to thank all my friends and family who contributed with their emotional support. In particular, my parents, Sandra de Sousa Alves and Jucelito Alves, my brother, Pedro de Sousa Alves, and my partner, Guilherme Martigango Zilli, for their encouragement and support throughout my studies.

# RÉSUMÉ

L'application directe de la méthode des éléments finis (FEM) pour modéliser des régions minces est entravée par (i) le rapport largeur/épaisseur très élevé de ces régions qui empêche l'utilisation des mailleurs automatisés, (ii) les caractéristiques non linéaires des matériaux qui empêchent certaines simplifications, et (iii) la nature tridimensionnelle de ces applications qui exige une complète représentation de la géométrie des dispositifs comportant des régions minces. La manière classique de surmonter les difficultés du maillage lors de la modélisation de régions minces est d'appliquer l'approche des coques minces (*thin-shell* - TS). Cependant, les approches TS avec la FEM actuellement disponibles sont principalement limitées à l'analyse en régime harmonique des régions minces avec des propriétés linéaires en 2-D. Cette thèse de doctorat propose un modèle éléments finis pour les domaines de calcul composés de régions minces pour l'analyse en régime transitoire des dispositifs électromagnétiques tout en prenant en compte les propriétes non-linéaires des matériaux conducteurs et ferromagnétiques en 3-D.

Deux approches ont été proposées, mises en œuvre, validées et appliquées pour simuler des problèmes de référence et réalistes en 2-D et en 3-D. Dans une première étape, nous avons défini des fonctions de base hyperboliques dérivées d'un ensemble de solutions harmoniques pour un problème linéaire de la diffusion de flux 1-D à travers l'épaisseur de la région mince. L'application de ces fonctions de base dans une approche TS nous a permis d'estimer le comportement transitoire des champs magnétique et électrique à l'intérieur de la région mince qui était représentée comme une géométrie de dimension réduite dans le domaine du calcul (une surface en 3-D ou une ligne en 2-D). Le modèle proposé a été appliqué pour estimer le comportement électromagnétique des boucliers planaires dans les régimes harmoniques et transitoires. Avec l'ajout de quelques solutions à haute fréquence aux fonctions de base hyperboliques, l'approche a fourni des résultats en bon accord avec ceux obtenus avec des modèles éléments finis classiques sous une complète et appropriée discrétisation des régions minces (avec différence relative inférieure à 3%), tout en réduisant le nombre total de degrés de liberté d'environ 80% et le temps de calcul d'environ dix fois. L'ensemble des fonctions de base hyperboliques a également été utilisé pour estimer le comportement non linéaire d'un blindage ferromagnétique soumis à une excitation externe.

Dans une deuxième étape, nous avons proposé une discrétisation virtuelle à travers l'épaisseur des régions minces pour traiter la caractéristique hautement non linéaire entre le champ électrique et la densité de courant dans les rubans supraconducteurs à haute

température (HTS) critique. Ces rubans comprennent généralement un empilement de films minces faits des matériaux conducteurs et ferromagnétiques. Compte tenu de leur capacité de courant élevée avec de faibles pertes en courant alternatif, les rubans HTS ont attiré une attention considérable de l'académie et de l'industrie pendant les dernières années. Ainsi, la définition d'un modèle efficace et précis pour estimer leur comportement peut aider à faire mûrir cette technologie et la viabilité économique des dispositifs électromagnétiques composés par ces rubans. Pourtant, les approches TS par éléments finis actuellement disponibles dans la littérature considèrent des approximations qui empêchent leur application pour estimer les distributions de courant et de champs dans les rubans HTS avec n'importe quelle configuration. Dans la deuxième approche TS proposée, une géométrie de dimension réduite a remplacé le volume de la région mince dans le domaine de calcul. La physique à l'intérieur des rubans HTS a été prise en compte par les conditions d'interface développées à partir de la discrétisation virtuelle sur leur épaisseur. De plus, les bases de cohomologie des régions non-conductrices ont été utilisées pour imposer le courant de transport dans les rubans. Il est montré dans cette thèse que l'approche TS proposée avec une discrétization vituelle de l'épaisseur surmonte les principales limitations des autres modèles (par exemple, l'approche TS classique et la formulation $T$-$A$ qui est largement utilisée pour modéliser des dispositifs HTS de nos jours). Les conditions d'interface ont été développées ici pour les cas 2-D et 3-D. Les résultats ont été validés dans une série de problèmes de référence de complexité croissante, et avec des solutions analytiques bien établies. Enfin, nous avons également appliqué le modèle TS pour simuler le comportement électromagnétique d'un câble Roebel 3-D comprenant 14 rubans HTS entièrement transposés. Par rapport à un modèle FEM standard, l'approche TS a permis d'accélérer la simulation jusqu'à dix fois tout en maintenant la précision de la solution. La réduction de la charge de calcul sans compromettre la précision de la solution rend les approches proposées prometteuses pour la simulation de la prochaine génération de dispositifs électromagnétiques comprenant des régions minces conductrices et ferromagnétiques non linéaires tels que les réacteurs à fusion nucléaire ou des systèmes de transport à haute vitesse.

# ABSTRACT

The direct application of the finite element method (FEM) to model thin regions is hampered by (i) the high aspect ratio of such regions that impedes the use of automated mesh generators, (ii) the nonlinear material properties that impedes some simplifications, and (iii) the three-dimensional nature of its applications that requires a complete geometrical representation of devices comprising the thin regions. The classical way to overcome the mesh difficulties when modeling thin regions is to apply the so-called thin-shell (TS) model. However, currently available finite-element TS models are mainly limited to the time-harmonic analysis of thin regions with linear properties in 2-D. This Ph.D. thesis aimed to propose a rigorous 3-D TS model to the time-transient analysis of EM devices while considering the nonlinearities of both the conductive and ferromagnetic materials.

Two new TS models were proposed, implemented, validated, and applied to simulate 2-D and 3-D benchmark and realistic problems. As a first approach, we defined hyperbolic basis functions derived from a set of harmonic solutions for a 1-D linear flux diffusion problem across the thickness of the thin region. Applying these basis functions in a TS model allowed estimating the time-transient behavior of the electric and magnetic fields inside the thin region that was represented as a reduced dimension geometry in the calculus domain (a surface in 3-D or a line in 2-D). The proposed model was applied to estimate the electromagnetic behavior of planar shields in the time-harmonic and the time-transient regimes. With the addition of a few high-frequency solutions to the hyperbolic basis functions, the approach provided results in good agreement with those obtained with standard finite-element models under a complete and suitable discretization of the thin regions (relative difference of less than 3%), while reducing the total number of degrees of freedom in more 80% and computation time by about ten times. The set of hyperbolic basis functions was also used to estimate the nonlinear behavior of a ferromagnetic shield under external excitation.

As a second model, we proposed a virtual discretization across the thickness of the thin regions to deal with the highly nonlinear relationship between the electric field and the current density in high-temperature superconducting (HTS) tapes. These tapes generally comprise a stack of thin films made of conductive and ferromagnetic materials. Given their high current capacity and low AC losses, HTS tapes have gained considerable attention from academia and industry in recent years, and defining an efficient and accurate model to estimate their behavior can help mature this technology and the economical operation of devices involving such tapes. Still, the currently finite-element TS models available in

the literature consider too many approximations that impede their application to estimate current and fields distributions in HTS tapes in any configuration. In the proposed TS model, a reduced-dimension geometry replaced the volume of the thin region in the computational domain. The physics inside the HTS tapes were taken into account by interface conditions obtained from the virtual discretization across their thickness. Moreover, the edge-based cohomology basis functions were used to impose the transport current in the tapes. It is shown in this thesis that the proposed TS overcomes the main limitations of the other models (e.g. the classical TS approach and the $T$-$A$-formulation). The equations were here developed for 2-D and 3-D cases. The results were validated in a series of benchmark problems of increasing complexity and well-established analytical solutions. Finally, we also applied the TS model for simulating the electromagnetic behavior of a fully transposed 3-D Roebel cable comprising 14 HTS tapes. Compared to a standard FEM model, the proposed TS model was able to speed up simulations up to ten times while maintaining the solution accuracy. The reduction in computational burden without compromising accuracy makes the proposed approaches promising for the simulation of the next generation of electromagnetic devices comprising both nonlinear conductive and ferromagnetic thin regions such as nuclear fusion reactors, high-speed transportation systems and many others.

# TABLE OF CONTENTS

# LIST OF TABLES

# LIST OF FIGURES

# LIST OF SYMBOLS AND ABBREVIATIONS

## Alphanumeric symbols

| | |
|---|---|
| $\mathbb{R}^3$ | : Three-dimensional oriented Euclidean space |
| $\mathbb{R}^2$ | : Two-dimensional oriented Euclidean space |
| $\boldsymbol{x} = (x, y, z)$ | : Point $\in \mathbb{R}^3$ |
| $\boldsymbol{x} = (x, y)$ | : Point $\in \mathbb{R}^2$ |
| $u$, $\boldsymbol{u}$ | : Any scalar and vector field in $\mathbb{R}^3$ |
| $\jmath$ | : Imaginary unit |
| $\boldsymbol{h}$ | : Magnetic field (A/m) |
| $\boldsymbol{b}$ | : Magnetic flux density (T) |
| $\boldsymbol{e}$ | : Electric field (V/m) |
| $\boldsymbol{d}$ | : Electric flux density (C/m$^2$) |
| $\boldsymbol{j}$ | : Electric current density (A/m$^2$) |
| $q$ | : Electric charge density (C/m$^3$) |
| $L^2(\Omega)$, $\boldsymbol{L}^2(\Omega)$ | : Spaces of square integrable scalar and vector fields over $\Omega$ |
| $H^1(\Omega)$, $\boldsymbol{H}^1(\Omega)$ | : First order Sobolev spaces of scalar and vector fields over $\Omega$ |
| $\boldsymbol{H}(\mathbf{curl}; \Omega)$ | : Stream function space $\{\boldsymbol{u} \in \boldsymbol{L}^2(\Omega) : \nabla \times \boldsymbol{u} \in \boldsymbol{L}^2(\Omega)\}$ |
| $\boldsymbol{H}(\mathrm{div}; \Omega)$ | : Flux space $\{\boldsymbol{u} \in \boldsymbol{L}^2(\Omega) : \nabla \cdot \boldsymbol{u} \in L^2(\Omega)\}$ |
| $\boldsymbol{H}^1_{\mathrm{dR}}(\Omega)$ | : Subspace of $\boldsymbol{L}^2$ having zero curl, but not defined as gradients |
| $\boldsymbol{H}^2_{\mathrm{dR}}(\Omega)$ | : Subspace of $\boldsymbol{L}^2$ having zero divergence, but not defined as curls |
| $\mathcal{W}^k(C^k(\hat{\Omega}))$ | : Whitney $k$-forms on the triangulation $\hat{\Omega}$, for $0 \leq k \leq 3$ |
| $v$ | : Electric scalar potential (V) |
| $\boldsymbol{a}$ | : Magnetic vector potential (Vs/m) |
| $\boldsymbol{t}$ | : Current vector potential (A/m) |
| $t$ | : Time (s) |
| $f$ | : Frequency (Hz) |
| $m_0$ | : Saturation magnetic field (A/m) |
| $e_c$ | : Electric field criterion (V/m) |
| $j_c$ | : Critical current density (A/m$^2$) |
| $T_c$ | : Critical temperature (K) |
| $n_{\mathrm{s}}$ | : Power-law index |
| $\boldsymbol{n}$ | : Outward normal unit |
| $\mathcal{K}$ | : Abstract simplicial complex |
| $\mathcal{C}_i$ | : $i^{\mathrm{th}}$ cutting surface making $\Omega$ simply connected |
| $c_k$, $c^k$ | : Any $k$-chain and $k$-cochain in $\mathcal{K}$ |

| | |
|---|---|
| $C_k$, $C^k$ | : Groups of all $k$-chains and $k$-cochains in $\mathcal{K}$ |
| $z_k$, $z^k$ | : $k$-cycle and $k$-cocycle in $\mathcal{K}$ |
| $Z_k$, $Z^k$ | : Groups of all $k$-cycles and $k$-cocycles in $\mathcal{K}$ |
| $b_k$, $b^k$ | : $k$-boundary and $k$-coboundary in $\mathcal{K}$ |
| $B_k$, $B^k$ | : Groups of all $k$-boundaries and $k$-coboundaroes in $\mathcal{K}$ |
| $\mathcal{M}_k$ | : Incidence matrix mapping $(k-1)$-chain to a $k$-chain |
| $\mathcal{H}_k$, $\mathcal{H}^k$ | : $k$-homology and $k$-cohomoogy groups of $\mathcal{K}$ |
| $\mathrm{H}_1$, $\mathrm{H}^1$ | : Matrices including the basis representatives of $\mathcal{H}_k$, $\mathcal{H}^k$ |

**Greek symbols**

| | |
|---|---|
| $\Omega$ | : Bounded open set of $\mathbb{R}^3$ |
| $\Omega_c$ | : Conducting subdomain of $\Omega$ |
| $\Omega_s$ | : Thin region in $\Omega$ |
| $\widehat{\Omega}$ | : Triangulation of $\Omega$ |
| $\Gamma$ | : Boundary of $\Omega$ $(= \partial\Omega)$ |
| $\Gamma_s$ | : Interface in $\Omega$ |
| $\Gamma_h$, $\Gamma_e$, $\Gamma_b$ | : Portions of $\Gamma$ where boundary conditions for the fields are applied |
| $\phi$ | : Magnetic scalar potential (A) |
| $\sigma$ | : Electric conductivity (S/m) |
| $\rho$ | : Electric resistivity ($\Omega$/m) |
| $\mu$ | : Magnetic permeability (H/m) |
| $\mu_0$ | : Magnetic permeability of vacuum $(= 4\pi 10^{-7}\,\mathrm{H/m})$ |
| $\mu_r$ | : Relative magnetic permeability $(= \mu/mu_0)$ |
| $\mu_{r0}$ | : Relative magnetic permeability at origin of the $B$-$H$ curve |
| $\nu$ | : Magnetic reluctivity $\nu = 1/\mu$ |
| $\omega$ | : Angular frequency $\omega = 2\pi f$ (rad/s) |
| $\sigma_i^k$ | : $i^{\text{th}}$ $k$-dimensional chain in $\mathcal{K}$ |
| $\tau_i^k$ | : $i^{\text{th}}$ $k$-dimensional cochain in $\mathcal{K}$ |
| $\delta$ | : Penetration depth (m) |
| $\eta_h$, $\eta_e$ | : Coefficients of the two ICs in the classical TS approach |
| $\vec{\psi}$ | : Hyperbolic basis functions |

**Abbreviations**

| | |
|---|---|
| EM | : Electromagnetic |
| FEM | : Finite element method |
| AC | : Alternating current |
| HTS | : High-temperature supercondutor |

| | |
|---|---|
| PDE | : Partial differential equations |
| CSM | : Critical state model |
| $k$-D | : $k$-dimensional |
| BVP | : Boundary value problem |
| BC | : Boundary condition |
| IC | : Interface condition |
| IBC | : Impedance-type boundary condition |
| NR | : Newton Raphson |
| DDG | : Discrete differential geometry |
| TS | : Thin shell |
| TSTC | : Twisted stack tape conductor |
| CORC | : Conductor on round core |
| ACSR | : Aluminium conductor steel-reinforced |
| NR | : Newton-Raphson |
| PBC | : Periodic boundary condition |
| DoFs | : Degrees of freedom |
| NoIs | : Number of iterations |
| LPS | : Linear problems solved |

**Operators**

| | |
|---|---|
| $^C$ | : Complement |
| $\partial_t$ | : Time derivative |
| $\partial_x$, $\partial_y$, $\partial_z$ | : Space derivatives |
| $\partial_k$, $\partial^k$ | : $k$-boundary and $k$-coboundary operators |
| **grad** | : Gradient ($= \nabla$) |
| **rot** | : Curl, rotational or rotor ($= \nabla\times$) |
| div | : Divergence ($= \nabla\cdot$) |
| $\mathcal{NS}$ | : Null space |
| $\mathcal{R}$ | : Range |
| $\times$ | : Vector product |
| $\cdot$ | : Scalar product |
| $\Re$, $\Im$ | : Real and imaginary parts |
| im, ker | : Image and kernel |
| **d** | : Exterior derivative |
| $\circ$ | : Composition of functions |
| $(.,.)_\Omega$, $\langle .,. \rangle_\Gamma$ | : Volume and surface integrals of the scalar product of their two arguments |
| $\otimes$ | : Kronecker product |

# LIST OF APPENDICES

# CHAPTER 1 INTRODUCTION

Large shifts in science and engineering drive the evolution of numerical models to faithfully represent the electromagnetic (EM) behavior of electric and electronic devices. Among the existing numerical methods, the Finite Element Method (FEM) is considered as one of the most powerful tool for investigating in detail the current and field distributions inside these devices. This method is widely recognized for its numerical efficiency and ability to treat nonlinearities and complex geometries [1]. However, despite FEM analysis of EM devices including nonlinearities being recurrent in literature [2–4], modeling such devices with nonlinear material features in complex geometries remains a challenge [5].

A particular case is the modeling of thin-film structures. Their high aspect ratio by itself makes the discretization computationally expensive in FEM applications [6, 7]. With the added complexity of the nonlinear material responses, modeling thin films using standard FEM quickly becomes unsustainable with the currently available computational resources. Nevertheless, these thin structures are indispensable components in many devices, and being able to estimate their behavior by simulation is the key to optimize their design and to achieve economical production and operation.

Electromagnetic shields are a typical example of thin-film application [8–11]. They are often employed to mitigate stray fields in the surroundings of EM devices. Maintaining these fields at an acceptable value is a constraint in the devices design process and must comply with the exposure limits for humans, and for EM compatibility and interference reasons. Hence, shields are essential parts of rotating machines, large power transformers, induction heating equipment, and welding and forming machines.

The problem of modeling ferromagnetic and conductive shields using FEM has been extensively treated in the literature, but currently available models are still mostly restricted to linear shielding problems and time-harmonic analysis. Existing models for nonlinear time-transient analysis consider many simplifications that hinder their effectiveness in complex geometries and stray field configurations, or sometimes require complicated analytical calculations to be performed at the pre-processing stage of the simulations [12]. Other examples of thin-films structures in electrical engineering include laminated iron cores in electrical machines, resistive barriers, air gaps in power transformers, conductive coatings in power cables, and many others.

In recent years, a new challenge to the numerical modeling of thin films has emerged. The discovery of superconducting materials operating above 77 K [13] combined with

industrial-scale thin-film deposition techniques [14–16] has brought high-temperature superconducting (HTS) applications to reality. Second-generation (2G) HTS tapes gained considerable attention in both industry and academia due to their relatively high operating temperatures, high current capacity, and low AC losses [17–20]. However, modeling the EM behavior of HTS tapes is limited by (i) the high aspect ratio of the superconducting layer in these tapes ($\approx$ 10,000), (ii) the highly nonlinear macroscopic relationship between the electric field and the current density [21], and (iii) the three-dimensional nature of many HTS applications [22].

Superconductor applications often require cables with higher current capacity than a single tape and lower AC losses than a single-piece coated conductor. Therefore, in order to maximize current capacity, minimize AC losses, optimize cooling needs and provide structural support, superconducting cables typically combine many HTS tapes. Each tape itself comprises a stack of thin films made of different materials. Their superconducting layer is 4-12 mm wide and 1 $\mu$m thick [18]. So far, three main HTS cables architectures have been proposed: (i) twisted stack tape conductor (TSTC) [23], (ii) conductor on round core (CORC) [24], (iii) transposed Roebel cable [25–28]. All of them transpose or twist the HTS tapes along the cables' length, creating a truly three-dimensional (3-D) geometry that helps reduce total AC losses and retain enough flexibility and mechanical stability in these cables. This complete transposition reduces induced currents and current loops in the strands in a way that the current is evenly distributed between them, but the economical operation of HTS cables can only be achieved by optimizing their overall design in such a way.

Accurately and efficiently estimating the 3-D behavior of HTS cables is key to maturing this technology. Large-scale HTS applications are still costly, and their optimization can only be achieved through numerical simulation if a relevant model can capture their behavior. Establishing a nonlinear finite-element model for HTS tapes and cables can help the development of world-changing technologies such as clean energy from fusion [29] or high-speed transportation [30].

In this thesis, we focus on developing new approaches to simulate nonlinear thin-film structures, thus aiming to contribute to the development of cutting-edge technologies, from nonlinear shields to large-scale HTS devices. This document was elaborated from original journal articles that were written on the present subject. They are inserted in the body of the document, which is organized as follows.

Chapter 2 introduces fundamental concepts of computational electromagnetics, useful for the deep understanding of the available models for thin films and the proposed approaches based on the FEM. The concepts of algebraic topology are presented in parallel to the classical

differential representation of Maxwell's equations. The ideas in this abstract formulation of Maxwell's equations are used to find the suitable spaces for the scalar and vector fields quantities and to reduce computational cost in 3-D simulations. Two dual FEM formulations are presented and discussed.

Chapter 3 presents a critical review of the numerical approaches currently available for modeling thin structures with the FEM. The concept of surface current density is introduced and the models are compared in terms of the equations used to define the physics of the thin regions. The advantages and disadvantages of these approaches are highlighted. The general presentation given in this chapter is more detailed than in the papers and helps to understand our contribution to modeling thin regions.

In Chapter 4, we present our research objectives and the working assumptions we selected to achieve these objectives. Two FEM approaches are proposed in this thesis. The first one considers hyperbolic basis functions derived from a set of time-harmonic solutions of the linear flux diffusion problem inside the thin film. The approach is shown to provide sufficiently accurate results when compared with a standard FEM and a complete discretization of the thin films. The example of a two-dimensional planar shield is studied in time-harmonic and time-transient regimes, considering linear conducting and ferromagnetic shields. The method is also extended to the nonlinear analysis of a ferromagnetic shield. Full details about the proposed approach are given in Chapter 5, including the definition of the approach, the FEM implementation, validation, application and discussions.

In Chapter 6, the second proposed approach is introduced, discussed, and tested in 2-D simulations. We propose a virtual discretization across the thickness of the HTS tapes. This approach, when used with a single virtual finite element, is demonstrated to be equivalent or dual to many popular models currently available in the literature, e.g. the classical thin-shell approach [31–34] and the so-called $T$-$A$-formulation [35]. With the virtual mesh refinement, our approach is shown to be efficient and accurate in evaluating the EM behavior of HTS tapes in any configuration. It is then extended to the 3-D cases in Chapter 7. This chapter presents the model definition, its validation on benchmark problems, and its application for modeling a fully transposed HTS Roebel cable with 14 strands.

In Chapter 8, the objectives of this thesis are evaluated in light of the proposed techniques and of the results obtained. Finally, in Chapter 9, the results of this work are summarized and avenues for future research work on the subject are suggested.

# CHAPTER 2 FUNDAMENTALS OF COMPUTATIONAL ELECTROMAGNETICS

## 2.1 Introduction

This chapter starts with the general electromagnetic problem definition and its approximation in the magnetodynamic form, which is suitable to estimate the EM response of devices at low frequency of operation. Next, we present the mathematical background necessary to solve the problem using the finite element method. Then, two dual formulations based on the magnetic and electric fields are introduced. From the integral form of the governing equations, we review some useful concepts of algebraic topology, a mathematical discipline that applies to computational electromagnetism. The definition of the cohomology of the function spaces for scalar and vector fields, and its equivalence with the cohomology theory in algebraic topology are especially put in evidence. The concepts and ideas presented in this chapter form the basis for the development of the more novel FE techniques in this thesis and can be found in many classical references [36–38].

## 2.2 Problem definition

### 2.2.1 Fundamental equations

All physical laws in electromagnetism are governed by Maxwell's equations, which form a system of *partial differential equations* (PDEs) connecting the magnetic and electric phenomena through six physical quantities [36]. The classical representation of these equations are

$$\nabla \times \boldsymbol{h} = \boldsymbol{j} + \partial_t \boldsymbol{d}, \qquad \Rightarrow \qquad \textit{Ampère's law} \tag{2.1}$$

$$\nabla \times \boldsymbol{e} = -\partial_t \boldsymbol{b}, \qquad \Rightarrow \qquad \textit{Faraday's law} \tag{2.2}$$

$$\nabla \cdot \boldsymbol{b} = 0, \qquad \Rightarrow \qquad \textit{Gauss's law for magnetism} \tag{2.3}$$

$$\nabla \cdot \boldsymbol{d} = q, \qquad \Rightarrow \qquad \textit{Gauss's law for electrostatics} \tag{2.4}$$

where $\boldsymbol{h}$ is the *magnetic field*, $\boldsymbol{b}$ is the *magnetic flux density*, $\boldsymbol{e}$ is the *electric field*, $\boldsymbol{d}$ is the *electric flux density*, $\boldsymbol{j}$ is the *current density* and $q$ is the *electric charge density*. In practice, given the materials constitutive relations (presented in Section 2.2.3) and appropriate boundary conditions, these equations can be solved.

### 2.2.2 Frequency and time-dependent regimes

The set of equations (2.1)-(2.4) has a wide range of applications, from the theory of electromagnetic waves (*high frequency*) to the calculation of the fields behavior inside EM devices (*low frequency*). Under some physical and geometrical conditions, these equations can be greatly simplified.

In this thesis, we are solely interested in estimating the EM response of devices at low frequencies. The electric charge $q$ and the displacement current $\partial_t \boldsymbol{d}$ are neglected. So, the relevant governing equations become

$$\nabla \times \boldsymbol{h} = \boldsymbol{j}, \tag{2.5}$$

$$\nabla \times \boldsymbol{e} = -\partial_t \boldsymbol{b}, \tag{2.6}$$

$$\nabla \cdot \boldsymbol{b} = 0. \tag{2.7}$$

The EM problem described by these equations is often called a *magnetodynamic* or an *eddy-current* problem [39] since it allows estimating the time-dependent response of the fields and the induced currents in conductive parts of the modeled device.

Two time-integration regimes can be considered when solving equations (2.5)-(2.7): the *time-transient* and *time-harmonic* regimes [40]. In the time-transient regime, given the initial state of the system, a numerical method such as implicit Euler can be applied to update the fields at each time instant $t_i \in \mathbb{R}$, $i = 0, 1, \ldots, N$ [41]. The time derivative of a quantity $\boldsymbol{u}$ at time $t_i$ can be approximated by

$$\partial_t \boldsymbol{u}(\boldsymbol{x}, t)\Big|_{t_i} \approx \frac{\boldsymbol{u}(\boldsymbol{x}, t_i) - \boldsymbol{u}(\boldsymbol{x}, t_{i-1})}{t_i - t_{i-1}}, \tag{2.8}$$

where $\boldsymbol{x}$ denotes the coordinates of a position in $\mathbb{R}^3$, and $\boldsymbol{u}(\boldsymbol{x}, t_0)$ the initial state.

When a sinusoidal excitation is considered, the problem is simpler to solve in the frequency domain (time-harmonic regime). A quantity $\boldsymbol{u}$ having a sinusoidal variation can be expressed as

$$\boldsymbol{u}(\boldsymbol{x}, t) = \hat{\boldsymbol{u}}(\boldsymbol{x}) \sin(\omega t + \theta_{\boldsymbol{u}}(\boldsymbol{x})), \tag{2.9}$$

where $\omega = 2\pi f$ is the angular frequency, $\hat{\boldsymbol{u}}(\boldsymbol{x})$ is the field magnitude, and $\theta_{\boldsymbol{u}}(\boldsymbol{x})$ is a related phase shift at position $\boldsymbol{x}$. The time-harmonic representation of this field consists in defining it as the real part of a complex representation (*phasor*) denoted $\bar{\boldsymbol{u}}(\boldsymbol{x}) = \hat{\boldsymbol{u}}(\boldsymbol{x}) \exp(\jmath\theta_{\boldsymbol{u}})$, where

$\jmath = \sqrt{-1}$ is the imaginary unit, i.e.

$$\boldsymbol{u}(\boldsymbol{x}, t) = \Re\{\bar{\boldsymbol{u}}(\boldsymbol{x})\}, \tag{2.10}$$

where $\Re\{.\}$ returns the real part of a complex number.

Faraday's law (2.6) can then be written as

$$\nabla \times \boldsymbol{e} = -\jmath\omega\boldsymbol{b}, \tag{2.11}$$

where the constant $\jmath\omega$ replaces the time derivative from (2.6), further simplifying the calculations.

On the one hand, the magnetodynamic problem can be solved in time-harmonic regime (without any numerical method for the time discretization) as long as the problem remains linear and the different frequencies remain uncoupled. On the other hand, the time-transient regime is necessary to determine the time-evolution of the field quantities for time variations that are non sinusoidal and to deal with nonlinearities such as with ferromagnetic and superconducting materials, whose nonlinear constitutive relations are given in the next section. Still, the time-harmonic regime will be considered in this thesis to obtain analytical reference solutions and to describe old and new models of EM fields in thin regions, particularly in Chapter 3.

### 2.2.3 Constitutive relations

In addition to (2.5)-(2.7), *constitutive relations* are required to express the materials' properties and determine how the six physical quantities interact. The two basic constitutive relations for a magnetodynamic problem are

$$\boldsymbol{b} = \mu\boldsymbol{h}, \qquad \text{or} \qquad \boldsymbol{h} = \nu\boldsymbol{b}, \tag{2.12}$$

$$\boldsymbol{j} = \sigma\boldsymbol{e}, \qquad \text{or} \qquad \boldsymbol{e} = \rho\boldsymbol{j}, \tag{2.13}$$

where $\mu$ is the *magnetic permeability*, $\nu = 1/\mu$ is the *magnetic reluctivity*, $\sigma$ is the *electrical conductivity* and $\rho = 1/\sigma$ is the *electrical resistivity*. These constitutive operations can be either linear or nonlinear, and the medium is likewise referred to as either *linear* and *nonlinear*, respectively, in terms of its electromagnetic behavior [42]. In nonlinear cases, the magnetic permeability and/or the electrical resistivity depend on the fields quantities, and the nonlinear system of equations, in either the time or frequency regime, is solved using an iterative scheme such as the *Picard* or the *Newton–Raphson* methods [41].

### Nonlinear permeability

A high permeability generally characterizes ferromagnetic materials when compared to the free space (vacuum). Therefore, a *relative permeability* $\mu_r = \mu/\mu_0$, where $\mu_0 = 4\pi \times 10^{-7}$ is the permeability of the vacuum, is often used to describe the magnetic response of these materials to an applied field.

Although the permeability is constant in the free space, this is not the case for ferromagnetic materials. Their permeability can vary with the position in the medium (*non uniformity*), the field orientation (*anisotropy*), the temperature, and many other parameters. In a nonlinear medium, we often consider that $\mu$ depends on the intensity of the magnetic field. The $B$-$H$ characteristic (2.12) can then be expressed as

$$\boldsymbol{b} = \mu(\boldsymbol{h})\boldsymbol{h}. \tag{2.14}$$

Generally speaking, the magnetic permeability depends on the magnetic field history and not only of the field at each time instant. This phenomenon arises because of the hysteretic behavior of the $B$-$H$ characteristic in ferromagnetic materials. Therefore, nonlinear simulations are usually performed in a time-transient regime rather than in a time-harmonic regime since the latter cannot account for the hysteretic behavior.

All ferromagnetic materials are characterized by nonlinearity and hysteresis. These effects are more or less pronounced depending on the material, and models that take these effects into account are still under development [40]. In this thesis, we restricted ourselves to the study of cases where the coercive force is meager, the hysteresis was neglected, and the ferromagnetic materials can be modeled by their first magnetization curve approximated by

$$\mu(\boldsymbol{h}) = \mu_0 \left(1 + \left(\frac{1}{\mu_{r0} - 1} + \frac{|\boldsymbol{h}|}{m_0}\right)^{-1}\right), \tag{2.15}$$

where $\mu_{r0}$ is the relative permeability at origin and $m_0$ the saturation magnetic field in A/m [43]. This means that, for simplicity, only the saturation effects of ferromagnetic materials were taken into account in our simulations. Note that this is not a limitation of the methods developed in this thesis.

### Nonlinear resistivity

The resistivity of conventional (ohmic) conductors is often assumed constant and defines the slope of their $E$-$J$ characteristic (2.13). In the case of superconductors, the resistivity

is highly non-linear and can be modeled as a function of the current density (and/or the magnetic field), i.e.

$$\boldsymbol{e} = \rho(\boldsymbol{j})\boldsymbol{j}. \tag{2.16}$$

The simplest model of the $E$-$J$ characteristic of type-II superconductors[1] assumes that the current density is either zero or equal to a *critical current density* ($j_c$). In this so-called *critical state model* (CSM or *Bean model*) [45], $j_c$ is independent of the local magnetic field.

In general, $\rho$ also depends on the temperature. Below a *critical temperature* denoted by $T_c$, the resistivity of a superconductor is zero, but when its temperature passes beyond $T_c$, a transition to the so-called *normal state* occurs (i.e. an ohmic state, without superconducting properties). The CSM can be sufficiently accurate to represent the resistivity of superconductors with sharp transition to normal state, which is normally the case of superconductors with low $T_c$. However, superconductors with high $T_c$ exhibit a smoother transition than that represented by the CSM.

Based on experimental results [21], the $E$-$J$ characteristic of type-II superconductors around a critical current density $j_c$ can be fitted in a power-law, which is often expressed as

$$\boldsymbol{e} = \frac{e_c}{j_c}\left|\frac{\boldsymbol{j}}{j_c}\right|^{n_\mathrm{s}-1}\boldsymbol{j}, \tag{2.17}$$

where $e_c$ is the electric field criterion used to define $j_c$ (generally, $e_c = 1\,\mu\mathrm{V/m}$), and the power index $n_\mathrm{s}$ determines the steepness of the $E$-$J$ curve. The electrical resistivity is then modeled by

$$\rho(\boldsymbol{j}) = \frac{e_c}{j_c}\left(\frac{|\boldsymbol{j}|}{j_c}\right)^{n_\mathrm{s}-1}. \tag{2.18}$$

Note that the power law (2.18) is a very general form and, depending on the value of $n_\mathrm{s}$, it can express the resistivity of ohmic conductors ($n_\mathrm{s} = 1$), the resistivity of high-temperature superconductors ($30 < n_\mathrm{s} < 50$), and the resistivity of low-temperature superconductors ($n_\mathrm{s} \to \infty$, equivalent to the CSM).

In all the simulations with superconductors in this thesis, we assumed that $j_c$ was constant and independent of the field and temperature. This means that only the superconducting state was considered in our simulations, and not its transition to the normal state. Moreover, we considered $j_c = 5 \times 10^8\,\mathrm{A/m^2}$, and the exponent $n_s$ was fixed between 21 and 101 for the

[1]Superconductors of type-I exhibit perfect diamagnetism and zero resistivity. Type-II superconductors may exhibit zero resistivity but the magnetic flux is partially allowed to penetrate inside them (partial diamagnetism). The effect of expelling out the magnetic flux associated to superconductors with perfect diamagnetism is called the *Meissner effect* since it was first observed by Meissner in 1933 [44].

examples presented in Chapters 6 and 7.

### 2.2.4 Definition of the computational domain

We seek to solve (2.5)-(2.7) with constitutive relations (2.12) and (2.13) in an open set of the Euclidean space $\mathbb{R}^3$ denoted by $\Omega$ (*domain*) with a piecewise smooth boundary $\partial\Omega$ denoted by $\Gamma$. The domain $\Omega$ may contain $c$ holes (or *cavities*), which means that the boundary $\Gamma$ will consist of $c+1$ closed connected surfaces $\Gamma_i$, $i = 0 \ldots, c$. If the domain contains at least one cavity, it is called *non-simply connected* (or *multiply connected*). Otherwise, it is denoted as a *simply connected* domain. Moreover, it may contain $\ell$ loops if there exists $\ell$ cutting surfaces $C_i$, $i = 1, \ldots, \ell$, that makes $\Omega \setminus (\bigcup_{i=1} C_i)$ simply connected. This general description of $\Omega$ can be extended to each of its individual connected subdomains [46].

In order to illustrate this, Fig. 2.1 shows a typical representation of a 2-D computational domain. The conducting and non-conducting subdomains of $\Omega$ are denoted by $\Omega_c$ and $\Omega_c^C$, respectively (i.e. $\Omega = \Omega_c \cup \Omega_c^C$). A cavity with boundary $\Gamma_1$ and a cutting surface $C_1$ are also depicted. The domain boundary is $\Gamma = \Gamma_0 \cup \Gamma_1$, and the outward normal unit vector on $\Gamma$ is denoted by $\boldsymbol{n}$. Moreover, the interface $\Gamma_s$ divides $\Omega$ into $\Omega^+$ and $\Omega^-$, which can include both conducting and nonconducting subdomains. It is important to note that the outward normal unit vectors on the boundaries of $\Omega^+$ and $\Omega^-$ are pointing outside each subdomain. At the interface $\Gamma_s$, we therefore have $\boldsymbol{n}^+ = -\boldsymbol{n}^-$. Also note that, in our current description, the domain does not include any subdomain with high aspect ratio (thin region). The problem of modeling thin regions will be considered in Chapter 3.

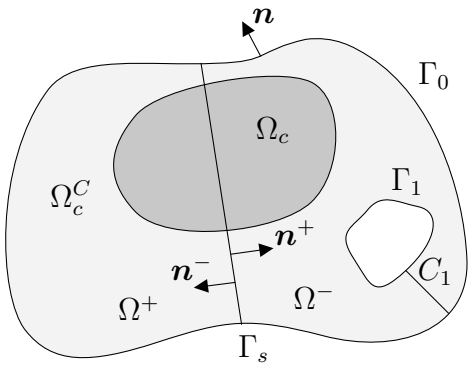


Figure 2.1 Computational domain $\Omega = \Omega_c \cup \Omega_c^C$, its boundary $\Gamma = \partial\Omega$ and the interface $\Gamma_s$ between two subdomains of $\Omega$, i.e. $\Omega^+$ and $\Omega^-$.

### 2.2.5 Boundary conditions

In order to ensure the uniqueness of the solutions to Maxwell's equations, the EM problems are treated as *boundary values problems* (BVPs). Besides the equations (2.5)-(2.13), it is also necessary to specify *boundary conditions* (BCs). We can define BCs for magnetic and electric quantities on $\Gamma$. These conditions are chosen to represent particular physical behavior, to enforce symmetries in the fields, or to confine the fields within the domain [40]. Thus, for the magnetic field on boundaries portions $\Gamma_h \subset \Gamma$, for the electric field on $\Gamma_e \subset \Gamma$, and the magnetic flux density on $\Gamma_b \subset \Gamma$, the *homogeneous* BCs are obtained from (2.5)-(2.7), i.e.

$$\boldsymbol{n} \times \boldsymbol{h} = 0, \quad \text{on } \Gamma_h, \tag{2.19}$$

$$\boldsymbol{n} \times \boldsymbol{e} = 0, \quad \text{on } \Gamma_e, \tag{2.20}$$

$$\boldsymbol{n} \cdot \boldsymbol{b} = 0, \quad \text{on } \Gamma_b. \tag{2.21}$$

Moreover, (2.19)-(2.20) may have a nonzero value on the right side called *non-homogeneous* BCs, mainly depending on the initial conditions and/or external field excitation.

### 2.2.6 Interface conditions

Considering the interface between two subdomains of $\Omega$ (e.g. $\Omega^-$ and $\Omega^+$ in Fig. 2.1), the field components may be discontinuous and consequently not differentiable [40]. In these cases, the integration of Maxwell's equations using the divergence theorem includes integral terms on the interface ($\Gamma_s$) between these two subdomains, i.e. $\Gamma_s = \partial\Omega^- \cap \partial\Omega^+$. The continuity of the fields is ensured by three *interface conditions* (ICs) in a magnetodynamic problem, which can be expressed as

$$\boldsymbol{n} \times \left(\boldsymbol{h}^+ - \boldsymbol{h}^-\right) = 0, \quad \text{on } \Gamma_s, \tag{2.22}$$

$$\boldsymbol{n} \times \left(\boldsymbol{e}^+ - \boldsymbol{e}^-\right) = 0, \quad \text{on } \Gamma_s, \tag{2.23}$$

$$\boldsymbol{n} \cdot \left(\boldsymbol{b}^+ - \boldsymbol{b}^-\right) = 0, \quad \text{on } \Gamma_s. \tag{2.24}$$

Equations (2.22) and (2.23) ensure the continuity of the tangential components of the magnetic and electric fields, respectively, while (2.24) ensures the continuity of the normal component of the magnetic flux density on $\Gamma_s$. As for the BCs, the ICs (2.22)-(2.24) may have a nonzero value on the right side, mainly depending on the physical behavior of the fields and their respective discontinuities at the interface $\Gamma_s$. We will see later in this thesis that properly defining ICs is essential to model the EM phenomena of thin regions when they are approximated by an interface in the computational domain.

### 2.3 Function spaces of field quantities

In computational electromagnetism, Maxwell's equations are numerically solved in a subdomain $\Omega$ of the three-dimensional Euclidean space $\mathbb{R}^3$. Therefore, for a magnetodynamic problem, scalar and vector fields are defined at any point $\boldsymbol{x} = (x, y, z) \in \Omega \subset \mathbb{R}^3$ and at any instant of time $t \in \mathbb{R}$ [46]. The components of the solution for (2.5)-(2.7) live in the spaces of square integrable scalar and vector fields defined as

$$L^2(\Omega) = \left\{ u : \Omega \to \mathbb{R} \,\middle|\, \int_\Omega u^2 \,\mathrm{d}\Omega < \infty \right\}, \tag{2.25}$$

$$\boldsymbol{L}^2(\Omega) = \left\{ \boldsymbol{u} : \Omega \to \mathbb{R}^3 \middle|\, \int_\Omega \|\boldsymbol{u}\|^2 \,\mathrm{d}\Omega < \infty \right\}, \tag{2.26}$$

respectively, where $u$ and $\boldsymbol{u}$ are any scalar and vector fields, $\|\boldsymbol{u}\|$ is the Euclidean norm of $\boldsymbol{u}$, and $\mathrm{d}\Omega$ a volume element. The components of the vector field $\boldsymbol{u}$ are denoted $(u_x, u_y, u_z)$, with $u_x, u_y, u_z$ of type $\Omega \to \mathbb{R}$. Note that, for convenience, the space and time dependence of $u$ and $\boldsymbol{u}$ are omitted.

The spaces $L^2$ and $\boldsymbol{L}^2$ are *Hilbert spaces* and can accommodate the field quantities characterized by a finite energy [47]. However, Maxwell's equations involve linear differential operators, and functions spaces of partial derivatives must be introduced. Subspaces of $L^2$ and $\boldsymbol{L}^2$ for which the first-order partial derivatives are square-integrable are called *Sobolev spaces* and are defined as

$$H^1(\Omega) = \left\{ u \in L^2(\Omega) : \partial_x u, \partial_y u, \partial_z u \in L^2(\Omega) \right\}, \tag{2.27}$$

$$\boldsymbol{H}^1(\Omega) = \left\{ \boldsymbol{u} \in \boldsymbol{L}^2(\Omega) : \partial_x \boldsymbol{u}, \partial_y \boldsymbol{u}, \partial_z \boldsymbol{u} \in \boldsymbol{L}^2(\Omega) \right\}, \tag{2.28}$$

respectively for scalar and vector fields, where $\partial_x$, $\partial_y$ and $\partial_z$ represent the partial derivatives with respect to $x$, $y$ and $z$, respectively, and must be interpreted as *weak derivatives* (i.e. in the sense of distributions) [48].

Defining the gradient of a scalar field as

$$\mathbf{grad} u = \nabla u = (\partial_x u, \partial_y u, \partial_z u), \tag{2.29}$$

we can define the following Hilbert subspace

$$H(\mathbf{grad}; \Omega) = \left\{ u \in L^2(\Omega) : \nabla u \in \boldsymbol{L}^2(\Omega) \right\}, \tag{2.30}$$

which implies that $H(\mathbf{grad}; \Omega) = H^1(\Omega)$. Moreover, with the **curl** and div operators of a

vector field defined respectively as

$$\mathbf{curl}\boldsymbol{u} = \nabla \times \boldsymbol{u} = (\partial_y u_z - \partial_z u_y, \partial_z u_x - \partial_x u_z, \partial_x u_y - \partial_y u_x), \tag{2.31}$$

$$\mathrm{div}\boldsymbol{u} = \nabla \cdot \boldsymbol{u} = \partial_x u_x + \partial_y u_y + \partial_z u_z, \tag{2.32}$$

we can define the following Hilbert subspaces corresponding to the **curl** and div operators as

$$\boldsymbol{H}(\mathbf{curl}; \Omega) = \left\{ \boldsymbol{u} \in \boldsymbol{L}^2(\Omega) : \nabla \times \boldsymbol{u} \in \boldsymbol{L}^2(\Omega) \right\}, \tag{2.33}$$

$$\boldsymbol{H}(\mathrm{div}; \Omega) = \left\{ \boldsymbol{u} \in \boldsymbol{L}^2(\Omega) : \nabla \cdot \boldsymbol{u} \in L^2(\Omega) \right\}, \tag{2.34}$$

which are also subspaces of $L^2(\Omega)$ and $\boldsymbol{L}^2(\Omega)$.

In addition to using differential operators in the definition of the spaces, the fields may still be restricted to subspaces where appropriate BCs to the underlying problem are required. Considering the domain boundary comprising two complementary surfaces $\Gamma_h$ and $\Gamma_e$ of $\Gamma$ such that

$$\Gamma = \Gamma_h \cup \Gamma_e \quad \text{and} \quad \Gamma_h \cap \Gamma_e = \varnothing, \tag{2.35}$$

where the scalar fields $u_h$ and $u_e$, or the *traces* (or tangential components) of vector fields $\boldsymbol{n} \times \boldsymbol{u}_h$ and $\boldsymbol{n} \times \boldsymbol{u}_e$, are imposed, respectively, the function spaces with homogeneous BCs corresponding to the $\mathbf{grad}_h$, $\mathbf{curl}_h$ and $\mathrm{div}_h$ operators are

$$H^1_{h,0}(\Omega) = \left\{ u \in L^2(\Omega) : \nabla u \in \boldsymbol{L}^2(\Omega), u|_{\Gamma_h} = 0 \right\}, \tag{2.36}$$

$$\boldsymbol{H}_{h,0}(\mathbf{curl}; \Omega) = \left\{ \boldsymbol{u} \in \boldsymbol{L}^2(\Omega) : \nabla \times \boldsymbol{u} \in \boldsymbol{L}^2(\Omega), \boldsymbol{n} \times \boldsymbol{u}|_{\Gamma_h} = 0 \right\}, \tag{2.37}$$

$$\boldsymbol{H}_{h,0}(\mathrm{div}; \Omega) = \left\{ \boldsymbol{u} \in \boldsymbol{L}^2(\Omega) : \nabla \cdot \boldsymbol{u} \in L^2(\Omega), \boldsymbol{n} \cdot \boldsymbol{u}|_{\Gamma_h} = 0 \right\}. \tag{2.38}$$

The function spaces with homogeneous BCs corresponding to the $\mathbf{grad}_e$, $\mathbf{curl}_e$ and $\mathrm{div}_e$ operators are defined similarly by substituting the subscript $h$ by $e$ in (2.36)-(2.38), respectively.

Generalizing the above definition for subspaces where non-homogeneous BCs may be required on $\Gamma_h$ and $\Gamma_e$, denoted simply as $H^1_h(\Omega)$, $\boldsymbol{H}_h(\mathbf{curl}; \Omega)$, $\boldsymbol{H}_h(\mathrm{div}; \Omega)$ and $L^2_h(\Omega)$ for the magnetic field, and $H^1_e(\Omega)$, $\boldsymbol{H}_e(\mathbf{curl}; \Omega)$, $\boldsymbol{H}_e(\mathrm{div}; \Omega)$ and $L^2_e(\Omega)$ for the electric field, respectively, the general continuous structure for Maxwell's equations is given by the following Tonti

diagram [40]:

$$\begin{array}{ccccccc} H_h^1(\Omega) & \xrightarrow{\nabla} & \boldsymbol{H}_h(\mathbf{curl};\Omega) & \xrightarrow{\nabla\times} & \boldsymbol{H}_h(\mathrm{div};\Omega) & \xrightarrow{\nabla\cdot} & L_h^2(\Omega) \\ \updownarrow & & \updownarrow & & \updownarrow & & \updownarrow \\ L_e^2(\Omega) & \xleftarrow{\nabla\cdot} & \boldsymbol{H}_e(\mathrm{div};\Omega) & \xleftarrow{\nabla\times} & \boldsymbol{H}_e(\mathbf{curl};\Omega) & \xleftarrow{\nabla} & H_e^1(\Omega) \end{array} \tag{2.39}$$

where the horizontal arrows represent the fundamental laws and vertical arrows represent constitutive relations which connect the vector fields placed in these spaces.

Finally, the fields quantities in the magnetodynamic form of Maxwell's equations can be placed in their affine spaces, i.e.

$$\boldsymbol{h} \in \boldsymbol{H}_h(\mathbf{curl};\Omega), \tag{2.40}$$

$$\boldsymbol{j} \in \boldsymbol{H}_h(\mathrm{div};\Omega), \tag{2.41}$$

$$\boldsymbol{e} \in \boldsymbol{H}_e(\mathbf{curl};\Omega), \tag{2.42}$$

$$\boldsymbol{b} \in \boldsymbol{H}_e(\mathrm{div};\Omega). \tag{2.43}$$

## 2.4 Magnetic field weak formulation

The set of differential equations (2.5)-(2.7) along with the boundary conditions is called the *strong form* of the EM problem. The development of a finite element formulation requires that strong form be replaced by a more general *weak* or *variational form*. If the strong form of Maxwell's equations is satisfied, then so will the weak form, but the opposite is not necessarily true. The weak solution will also be a strong solution only if it is sufficiently smooth, i.e. continuous with all involved derivatives continuous in every point of the calculus domain up to its boundaries.

To develop the weak form of the magnetodynamic problem, we recall Green's identities. Let $u \in H^1(\Omega)$ and $\boldsymbol{u}, \boldsymbol{v} \in \boldsymbol{H}^1(\Omega)$ be any scalar and vector fields in $\Omega$, the *Green First Identity* is obtained by integrating the vector calculus identity

$$\boldsymbol{v} \cdot \nabla u + u \nabla \cdot \boldsymbol{v} = \nabla \cdot (u\boldsymbol{v}), \tag{2.44}$$

in $\Omega$ and applying the divergence theorem, i.e.

$$(\boldsymbol{v}, \nabla u)_\Omega + (\nabla \cdot \boldsymbol{v}, u)_\Omega = \langle u, \boldsymbol{n} \cdot \boldsymbol{v} \rangle_\Gamma \tag{2.45}$$

where $(\cdot,\cdot)_\Omega$ and $\langle \cdot,\cdot \rangle_\Gamma$ denote respectively the volume integral over $\Omega$ and the surface integral

over $\Gamma$ of the scalar product of their two arguments.

*Green's Second Identity* is obtained by integrating the vector calculus identity

$$\boldsymbol{u} \cdot (\nabla \times \boldsymbol{v}) - (\nabla \times \boldsymbol{u}) \cdot \boldsymbol{v} = \nabla \cdot (\boldsymbol{v} \times \boldsymbol{u}), \tag{2.46}$$

in $\Omega$ and applying Stokes' theorem, i.e.

$$(\boldsymbol{u}, \nabla \times \boldsymbol{v})_\Omega - (\nabla \times \boldsymbol{u}, \boldsymbol{v})_\Omega = \langle \boldsymbol{u} \times \boldsymbol{n}, \boldsymbol{v} \rangle_\Gamma \tag{2.47}$$

The key take-away from these identities is that they continue to hold even for weakly differentiable functions and that the boundary terms $\langle u, \boldsymbol{n} \cdot \boldsymbol{v} \rangle_\Gamma$ in (2.45) and $\langle \boldsymbol{u} \times \boldsymbol{n}, \boldsymbol{v} \rangle_\Gamma$ in (2.47) are well-defined in a weak sense (under integration) [48].

The strong form of the magnetodynamic problem defined in terms of the magnetic field (*H-formulation*), is obtained by applying (2.5) in (2.6) and using (2.12) and (2.13), i.e.

$$\nabla \times (\rho \nabla \times \boldsymbol{h}) + \partial_t \mu \boldsymbol{h} = 0 \tag{2.48}$$

together with the BCs. Then, by multiplying (2.48) by a test function $\boldsymbol{g}$, integrating over $\Omega$, and using (2.47), the weak form of this formulation reads:

Find $\boldsymbol{h} \in \boldsymbol{H}_h(\mathbf{curl}; \Omega)$ such that

$$\Big(\rho \nabla \times \boldsymbol{h}, \nabla \times \boldsymbol{g}\Big)_\Omega + \partial_t \Big(\mu \boldsymbol{h}, \boldsymbol{g}\Big)_\Omega + \Big\langle \boldsymbol{n} \times \boldsymbol{e}, \boldsymbol{g} \Big\rangle_{\Gamma_e} = 0 \tag{2.49}$$

$\forall\ \boldsymbol{g} \in \boldsymbol{H}_{h,0}(\mathbf{curl}; \Omega)$.

The domain $\Omega$ includes the conducting and non-conducting subdomains and boundary regions, as presented in the problem definition (Section 2.2). The last term of (2.49) arises from the application of Green's identity (2.47) and can be used to impose a non-homogeneous BC in the weak sense. It depends essentially on the trace of the electric field on $\Gamma_e$, i.e. it is a Neumann BC in the $H$-formulation. If the BCs are completely Dirichlet or homogeneous, this term vanishes [40]. Note also that $\boldsymbol{h} \in \boldsymbol{H}_h(\mathbf{curl}; \Omega)$ already includes the non-homogeneous Dirichlet BCs on $\Gamma_h$.

## 2.5 Scalar and vector potentials

The definition of scalar and vector potentials allows us to satisfy the equations associated with the nullspace of an operator in the strong sense. For example, defining the electric

or the magnetic field as the gradient of a scalar potential gives the nullspace for the **curl** operator, and describing them as a vector potential gives the nullspace for the div operator. Or equivalently, when a scalar potential defines the magnetic field, the curl-free (or current-free) condition (2.5) is automatically satisfied in $\Omega_c^C$, and when the magnetic flux density is defined as the curl of another vector field, the divergence-free condition (2.7) is automatically satisfied in $\Omega$. In this section, we will show that not every curl or divergence-free field is given by a potential, but thanks to more sophisticated mathematics theory, we will show that this is correct up to a connection that depends on the underlying topology of the domain.

### 2.5.1 Magnetic scalar potential

Given that the current density $\boldsymbol{j}$ vanishes in the non-conducting subdomain $\Omega_c^C$, we can define the *magnetic scalar potential* ($\phi$) as

$$\boldsymbol{h} = -\nabla\phi, \tag{2.50}$$

at least locally within $\Omega_c^C$. For smooth fields $\boldsymbol{h}$ in a convex or star-shaped domain this definition is easy verified. It implies that the integration of $\boldsymbol{h}$ over any loop in $\Omega_c^C$ is equal to zero, since $\nabla \times (-\nabla\phi) = 0 \ \forall\phi$, satisfying Ampère's law (2.5) locally in $\Omega_c^C$. The magnetic scalar potential can be thus placed in its own affine space

$$\phi \in H_h^1(\Omega), \tag{2.51}$$

where non-homogeneous BCs are included in the definition of the function space.

### 2.5.2 Magnetic vector potential

From (2.7), we can further define the magnetic flux density $\boldsymbol{b}$ as the curl of the *magnetic vector potential* $\boldsymbol{a}$, i.e.

$$\boldsymbol{b} = \nabla \times \boldsymbol{a}. \tag{2.52}$$

The natural affine function space for $\boldsymbol{a}$ is

$$\boldsymbol{a} \in \boldsymbol{H}_e(\mathbf{curl}; \Omega). \tag{2.53}$$

This definition allows us to obey the divergence-free condition of the magnetic flux density in the strong sense, i.e. directly through the PDEs and BCs governing the problem. Note that, from definition (2.52) and Faraday's law (2.6), $\boldsymbol{a}$ is the primitive in time of the electric field, i.e. $\boldsymbol{e} = -\partial_t \boldsymbol{a}$.

### 2.5.3 Electric scalar potential

The introduction of the magnetic vector potential (2.52) implies $\nabla \times (\boldsymbol{e} + \partial_t \boldsymbol{a}) = 0$, which gives rise to the definition of the *electric scalar potential* $v$ as

$$\boldsymbol{e} + \partial_t \boldsymbol{a} = -\nabla v. \tag{2.54}$$

This potential can be placed in its own natural affine function space

$$v \in H^1_e(\Omega), \tag{2.55}$$

which accounts for non-homogeneous BCs.

### 2.5.4 Obstruction to the existence of potentials

The spaces $H^1(\Omega)$, $\boldsymbol{H}(\mathbf{curl};\Omega)$, $\boldsymbol{H}(\mathrm{div};\Omega)$ and $L^2(\Omega)$ form the following de Rham complex

$$0 \xrightarrow{i} H^1(\Omega) \xrightarrow{\nabla} \boldsymbol{H}(\mathbf{curl};\Omega) \xrightarrow{\nabla\times} \boldsymbol{H}(\mathrm{div};\Omega) \xrightarrow{\nabla\cdot} L^2(\Omega) \xrightarrow{j} 0. \tag{2.56}$$

This is called a *complex* if any two successive compositions vanish, or equivalently if

$$\begin{aligned} \mathcal{R}(\mathbf{grad}) \subset \mathcal{NS}(\mathbf{curl}) \subset \boldsymbol{H}(\mathbf{curl},\Omega), \\ \mathcal{R}(\mathbf{curl}) \subset \mathcal{NS}(\mathrm{div}) \subset \boldsymbol{H}(\mathrm{div},\Omega), \end{aligned} \tag{2.57}$$

where $\mathcal{NS}$ and $\mathcal{R}$ are respectively the nullspace and the range of the operators.

The question of finding $\phi$ such that $\boldsymbol{h} = -\nabla\phi$ in (2.50) is expressed in the de Rham complex as: given $\boldsymbol{h} \in \mathcal{NS}(\mathbf{curl}) \subset \boldsymbol{H}(\mathbf{curl},\Omega)$, is $\boldsymbol{h} \in \mathcal{R}(\mathrm{div})$? Similarly, the question of finding $\boldsymbol{a}$ such that $\boldsymbol{b} = \nabla \times \boldsymbol{a}$ is expressed in the de Rham complex as: given $\boldsymbol{b} \in \mathcal{NS}(\mathrm{div})$, is $\boldsymbol{b} \in \mathcal{R}(\mathbf{curl})$? Unfortunately, if $\boldsymbol{h} \in \mathcal{R}(\mathbf{grad})$ then its integral over a loop around a cavity, such as a wire, will vanish while we expect it to provide the current through this loop. In fact, this calculation shows that while the magnetic field $\boldsymbol{h}$ will determine the current, $\boldsymbol{h} - \nabla\phi$ for any $\phi \in H^1(\Omega)$ will predict the same current. This leads us to conclude that the magnetic field is defined up to the addition of $-\nabla\phi$, what is usually referred to as a gauge, and the current determined by the loops around the conductors in $\Omega$ will select $\boldsymbol{h}$. Mathematically, the magnetic field will correspond to a class in the quotient space

$$\boldsymbol{H}^1_{\mathrm{dR}}(\Omega^C_c) \coloneqq \mathcal{NS}(\mathbf{curl})/\mathcal{R}(\mathbf{grad}), \tag{2.58}$$

where the class is defined up to the addition of an arbitrary gradient $-\nabla\phi$. This is called

the first de Rham *cohomology* space. There also exists a second cohomology space

$$\boldsymbol{H}^2_{\mathrm{dR}}(\Omega_c^C) \coloneqq \mathcal{NS}(\mathrm{div})/\mathcal{R}(\mathbf{curl}), \tag{2.59}$$

but we will not be using it in this work. In general, for any complex, we can define a cohomology and we will later introduce homology and cohomology in a purely geometrical setting that will also provide a method to compute the appropriate element $\boldsymbol{h}$ in $\boldsymbol{H}^1_{\mathrm{dR}}(\Omega_c^C)$.

For the moment, we want to further explore the connection between a vector field $-\nabla\phi$ and its values along cuts. If we define a vector field as $\boldsymbol{u} = \nabla u$ in $\Omega$ multiply connected, where $u$ is a scalar field, from (2.58), we have

$$\nabla \times \nabla u = 0 \quad \text{and} \quad \nabla \cdot \nabla u = 0. \tag{2.60}$$

The condition $\boldsymbol{n} \cdot \boldsymbol{u}|_\Gamma = 0$ in (2.58) becomes $\partial_{\boldsymbol{n}} u|_\Gamma = 0$, where $\partial_{\boldsymbol{n}}$ is the derivative with respect to the normal, i.e. $u$ is constant along that connected component of the boundary. Given that $\boldsymbol{u}$ is continuous in $\Omega$, i.e. $\boldsymbol{u}|_{C_i^+} = \boldsymbol{u}|_{C_i^-}$, for $i = 1, \ldots, \ell$, we have

$$u|_{C_i^+} - u|_{C_i^-} = c_i, \qquad i = 1, \ldots, \ell, \tag{2.61}$$

where $c_i$ are constants associated to each cut $C_i$ in $\Omega$, and $C_i^\pm$ correspond to the sides of $C_i$ [46]. Consequently, there exists a basis of the space $\boldsymbol{H}^1_{\mathrm{dR}}(\Omega)$ identified as functions defined in $\Omega$ with a unit discontinuity across each cut $C_i$ that makes $\Omega$ simply connected [49,50]. Moreover, the definition of the vector field $\boldsymbol{u}$ through the gradient of the scalar field $u$ cannot represent the circulation of $\boldsymbol{u}$ over loops in $\Omega$ if it is multiply connected since $u|_{C_i^+} = u|_{C_i^-}$. We will see later that the *edge-based cohomology basis representatives* (or *thick cuts* [51]) of discretized domains form a suitable basis for the subspace $\boldsymbol{H}^1_{\mathrm{dR}}(\Omega)$.

Moreover, thanks to the introduced BCs, for $u \in H^1_{h,0}(\Omega)$ and $\boldsymbol{u} \in \boldsymbol{H}_{h,0}(\mathbf{curl}; \Omega)$, we have that

$$u|_{\Gamma_h} = 0 \Rightarrow \boldsymbol{n} \times \nabla u|_{\Gamma_h} = 0, \tag{2.62}$$

$$\nabla \times \boldsymbol{u}|_{\Gamma_h} = 0 \Rightarrow \boldsymbol{n} \cdot \nabla \times \boldsymbol{u}|_{\Gamma_h} = 0, \tag{2.63}$$

meaning that by imposing homogeneous BCs for a scalar field automatically satisfies the homogeneous BCs for a vector field, if it is defined as the gradient of the scalar field. In addition, the homogeneous BCs for a divergence-free field can be equivalently satisfied if this field is written as the curl of another vector field for which homogeneous BCs are imposed. However, these conditions are not satisfied in $\boldsymbol{H}^1_{\mathrm{dR}}(\Omega)$, as exemplified above.

## 2.6 Magnetic vector potential weak formulation

The continuous structure of the Maxwell equations represented by the Tonti diagram (2.39) involves two de Rham complexes expressing the function spaces of magnetic and electric variables. They are often classified as *primal* and *dual*, respectively [46]. This classification gives rise to an equivalent classification of the EM problems defined in terms of the magnetic or electric field quantities also as primal and dual, respectively.

The strong form of the magnetodynamic problem defined in terms of the magnetic vector potential (*A-formulation*) is obtained by applying (2.6) in (2.5) and using (2.12) and (2.13), and the definition (2.52), i.e.

$$\nabla \times (\nu \nabla \times \boldsymbol{a}) + \sigma \partial_t \boldsymbol{a} = 0, \tag{2.64}$$

together with suitable BCs.

By multiplying (2.64) by a test function $\boldsymbol{g}$, integrating over $\Omega$, and using (2.47), the weak form of this formulation reads:

Find $\boldsymbol{a} \in \boldsymbol{H}_e(\mathbf{curl}; \Omega)$ such that

$$\Big(\nu \nabla \times \boldsymbol{a}, \nabla \times \boldsymbol{g}\Big)_\Omega + \Big(\sigma \partial_t \boldsymbol{a}, \boldsymbol{g}\Big)_\Omega + \Big\langle \boldsymbol{n} \times \boldsymbol{h}, \boldsymbol{g} \Big\rangle_{\Gamma_h} = 0, \tag{2.65}$$

$\forall\ \boldsymbol{g} \in \boldsymbol{H}_{e,0}(\mathbf{curl}; \Omega)$.

The last term in (2.65) can be used to impose a non-homogeneous BC on $\Gamma_h$. This is a Neumann BC for the $A$-formulation since it depends essentially on the trace of the magnetic field. If the BCs are completely Dirichlet or homogeneous, this term vanishes [40]. Note that $\boldsymbol{a} \in \boldsymbol{H}_e(\mathbf{curl}; \Omega)$ already includes non-homogeneous Dirichlet BCs on $\Gamma_e$.

The vector potential $\boldsymbol{a}$ is not unique in the $A$-formulation. If $\boldsymbol{a}$ is the solution to (2.65), any vector field $\boldsymbol{a} + \nabla u$, where $u$ is any scalar field, is also a solution to (2.65). Uniqueness can be resolved, for example, by using the Coulomb gauge ($\nabla \cdot \boldsymbol{a} = 0$).

Generally, the expression for the electric field also involves the electric scalar potential as defined in (2.54). The strong form of the so-called $A$-$V$-formation reads

$$\nabla \times (\nu \nabla \times \boldsymbol{a}) + \sigma \partial_t \boldsymbol{a} + \sigma \nabla v = 0, \tag{2.66}$$

and its weak form reads:

Find $\boldsymbol{a} \in \boldsymbol{H}_e(\mathbf{curl};\Omega)$ and $v \in H^1_e(\Omega)$ such that

$$\Big(\nu\nabla\times\boldsymbol{a},\nabla\times\boldsymbol{g}\Big)_{\Omega}+\Big(\sigma\partial_t\boldsymbol{a},\boldsymbol{g}\Big)_{\Omega_c}+\Big(\sigma\nabla v,\boldsymbol{g}\Big)_{\Omega_c}+\Big\langle\boldsymbol{n}\times\boldsymbol{h},\boldsymbol{g}\Big\rangle_{\Gamma_h}=0, \tag{2.67}$$

$\forall\ \boldsymbol{g}\in\boldsymbol{H}_{e,0}(\mathbf{curl};\Omega)$, and

$$\Big(\sigma\partial_t\boldsymbol{a},\nabla g\Big)_{\Omega_c}+\Big(\sigma\nabla v,\nabla g\Big)_{\Omega_c}=0, \tag{2.68}$$

$\forall\ g\in H^1_{e0}(\Omega)$. In the $A$-$V$-formulation the potential $\boldsymbol{a}$ is unique in $\Omega_c$, but not in $\Omega_c^C$ where $\boldsymbol{e}$ is not evaluated. As for the pure $A$-formulation, the $A$-$V$-formulation also requires a gauge [52]. In 2-D cases, however, $\boldsymbol{a}$ is perpendicular to the plane and the Coulomb gauge is implicit.

## 2.7 Integral and differential forms

To develop the discrete spaces equivalent to the functions spaces for scalar and vector fields, we introduce here the concept of integral and differential forms. The more natural form of Ampère's and Faraday's laws for magnetodynamic problems is their integral forms that can be written respectively as

$$\int_{\partial\Sigma}\boldsymbol{h}\cdot\mathrm{d}\boldsymbol{\ell}=\int_{\Sigma}\boldsymbol{j}\cdot\boldsymbol{n}\,\mathrm{d}S, \tag{2.69}$$

$$\int_{\partial\Sigma}\boldsymbol{e}\cdot\mathrm{d}\boldsymbol{\ell}=-\int_{\Sigma}\partial_t\boldsymbol{b}\cdot\boldsymbol{n}\,\mathrm{d}S. \tag{2.70}$$

where $\boldsymbol{n}$ is the outward normal of any surface $\Sigma$ in $\Omega$ with oriented boundary $\partial\Sigma$, and $\mathrm{d}\boldsymbol{\ell}$ and $\mathrm{d}S$ are line and surface elements. Note that Stokes' theorem can be used to deduce the differential forms (2.5) and (2.6) from (2.69) and (2.70), respectively. These equations connect the circulations of $\boldsymbol{h}$ and $\boldsymbol{e}$ along a closed curve (a *loop* or a *cycle*) to $\boldsymbol{j}$ and $-\partial_t\boldsymbol{b}$ through any surface encompassed by this cycle. The flux of $\boldsymbol{j}$ through the surface is the total current that passes through it, and the flux of $\boldsymbol{b}$ through $\Sigma$ is called the *magnetic flux*. The rate of change of the magnetic flux over time is the *electromotive force* or the voltage between the terminals of $\Omega_c$. Moreover, the application of the divergence theorem to (2.7) over $\Omega$ gives the associated integral form

$$\int_{\partial\Omega}\boldsymbol{b}\cdot\boldsymbol{n}\,\mathrm{d}S=0, \tag{2.71}$$

which indicates that the magnetic flux through any closed surface $\partial\Omega$, boundary of a volumetric element, is null.

Expressing Maxwell's equations in their integral forms shows that the vector fields have two different natures: one in which a field is defined with reference to a line, and the other one in which it is defined with reference to a surface [37]. Writing it formally, if $\mathcal{S}_1(\Omega)$ is the set of all smooth 1-D curves (with boundary) and $\mathcal{S}_2(\Omega)$ is the set of all smooth 2-D surfaces (with boundary), then we have two parings

$$\begin{aligned} \langle , \rangle : \mathcal{S}_1(\Omega) \times \boldsymbol{H}(\mathbf{curl}; \Omega) &\to \mathbb{R} \\ (\ell, \boldsymbol{u}) &\mapsto \int_\ell \boldsymbol{u} \cdot \mathrm{d}\boldsymbol{\ell}, \end{aligned} \tag{2.72}$$

$$\begin{aligned} \langle , \rangle : \mathcal{S}_2(\Omega) \times \boldsymbol{H}(\mathrm{div}; \Omega) &\to \mathbb{R} \\ (\Sigma, \boldsymbol{u}) &\mapsto \int_\Sigma \boldsymbol{u} \cdot \boldsymbol{n} \mathrm{d}S. \end{aligned} \tag{2.73}$$

Above, each $\boldsymbol{u} \in \boldsymbol{H}(\mathbf{curl}; \Omega)$ defines something integrable over a curve, that is what mathematicians call a 1-differential form. Similarly, each $\boldsymbol{u} \in \boldsymbol{H}(\mathrm{div}; \Omega)$ defines a 2-differential form, i.e. something integrable over a surface.

In this sense, we can identify from (2.69) and (2.70) $\boldsymbol{h}$ and $\boldsymbol{e}$ as *integral 1-forms* and $\boldsymbol{b}$ and $\boldsymbol{j}$ as *integral 2-forms*. Similarly, from (2.5) and (2.6), the field equations can be interpreted in terms of *differential forms*. The vector fields $\boldsymbol{h}$ and $\boldsymbol{e}$ are identified as forms of degree 1 (*differential 1-forms*) and $\boldsymbol{b}$ and $\boldsymbol{j}$ as forms of degree 2 (*differential 2-forms*). Note that we maintained the boldface notation for the differential $k$-forms, but these quantities are not vector fields. They are independent of coordinates, i.e. their components have 3 parameters but they do not transform under change of coordinates as vectors [53]. We will see in Section 2.8.8 that we can define maps (called *Whitney maps*) from $k$-forms to vector fields in $\Omega \in \mathbb{R}^3$.

The definition of integral and differential forms motivates the introduction of the *exterior derivative*, which is a linear operator denoted by $\mathbf{d}$ that maps a differential $k$-form to a differential $(k+1)$-form that satisfies Stokes' theorem

$$\int_\Sigma \mathbf{d}\boldsymbol{u} = \int_{\partial\Sigma} \boldsymbol{u}, \tag{2.74}$$

where $\Sigma$ is a $(k+1)$-dimensional subdomain with boundary of $\Omega$. In practice, $\Sigma$ can be any surface within $\Omega$.

The orientation of the contour $\partial\Sigma$ defines the sign of the value assigned for integrals on the right side of (2.69) and (2.70). That is, depending on the orientation of the loop over which the magnetic (or the electric) field is integrated, the total current (or magnetic flux) that passes through the surface $\Sigma$ changes its sign. We say that a form $\boldsymbol{u}$ is closed if $\mathbf{d}\boldsymbol{u} = 0$

but it is possible to show that $\mathbf{d}(\mathbf{du}) = \mathbf{0}$ for all $\boldsymbol{u}$, hence $\mathbf{du}$ is always closed, which is dual to the usual geometrical identity $\partial(\partial\Sigma) = \varnothing$. This fundamental relation of exterior derivatives is also a rewriting of the standard vector calculus identities $\nabla \times (\nabla u) = 0 \ \forall u$ and $\nabla \cdot (\nabla \times \boldsymbol{u}) = 0 \ \forall \boldsymbol{u}$.

Assuming the presented differential forms, the introduction of the exterior derivative $\mathbf{d}$ allows us to rewrite Ampere's and Faraday's laws respectively as

$$\mathbf{d}\boldsymbol{h} = \boldsymbol{j}, \qquad \mathbf{d}\boldsymbol{e} = -\partial_t \boldsymbol{b}, \tag{2.75}$$

which are denoted as *topological laws* [37] since they only rely on the topological concepts of orientation and boundaries of *manifolds*[2]. Moreover, the **grad**, **curl** and div operators are particular realizations of $\mathbf{d}$ (depending on the index $k$ of the $k$-form). Since $\mathbf{d} \circ \mathbf{d} = 0$, the conservation law

$$\mathbf{d}\boldsymbol{b} = 0, \tag{2.76}$$

is satisfied locally.

The magnetic and electric scalar potentials, $\phi$ and $v$, respectively, can be trivially identified as 0-forms. The circulation of the magnetic vector potential $\boldsymbol{a}$ is a 1-form since it is the primitive in time of the electric field. The relationships between the field quantities and the potentials are rewritten using the exterior derivative definition as

$$\boldsymbol{h} = \mathbf{d}\phi, \qquad \boldsymbol{b} = \mathbf{d}\boldsymbol{a}, \qquad \boldsymbol{e} = -\partial_t \boldsymbol{a} - \mathbf{d}v. \tag{2.77}$$

From the point of view of the de Rham complex, and considering the presented topological aspects, we can intuitively compare the topological laws (2.75) and differential form of Maxwell's equations (2.5)-(2.6). Maxwell's house, illustrated in Fig. 2.2, summarizes the relationships between the different variables in a manner that emphasizes the duality ($\boldsymbol{h}$ or $\boldsymbol{b}$, $\boldsymbol{e}$ or $\boldsymbol{j}$), the role of the constitutive relations ($\sigma$, $\epsilon$ and $\rho$) and how these are expressed in the hierarchy of $k$-forms and differential operators. The elegance of these representations is further deepened when the Hodge star ($\star$), an invariant operator of differential geometry, is used to express the constitutive relations, but we refer to [55] for those details.

We will see next that the discrete form of the fundamental laws in electromagnetism has a direct link with differential geometry and cohomology theory in algebraic topology. The ideas of such a mathematical discipline, briefly described in Section 2.8, will help us find the basis

[2] A manifold is a topological space which locally resembles the real $k$-dimensional Euclidean space. For a precise definition see [54].

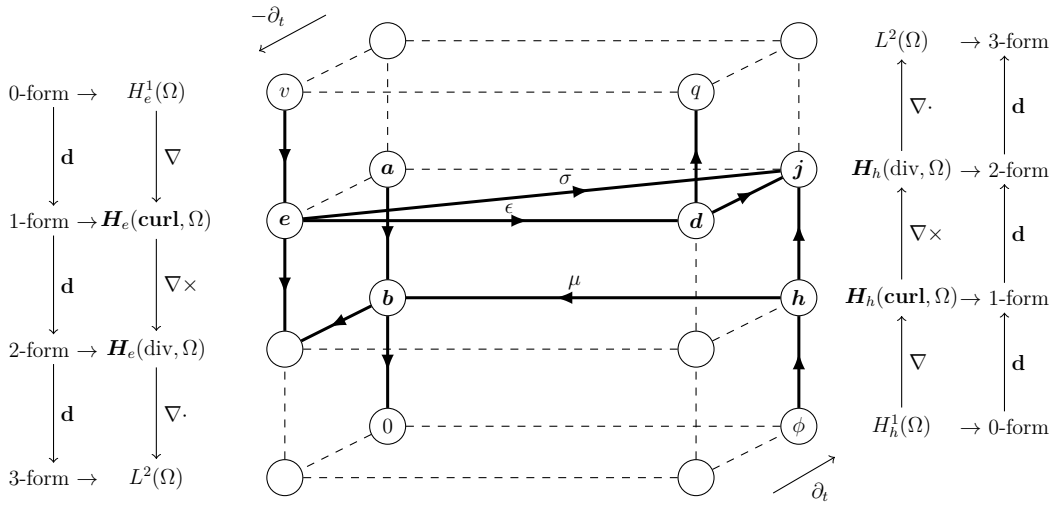


Figure 2.2 Maxwell's house for vector fields, their function spaces, and related differential space of $k$-forms (adapted from [53]).

representatives for the subspace $\boldsymbol{H}^1_{\mathrm{dR}}$, introduced in Section 2.3. These representatives are not restricted to the simulations of thin regions as aimed in this thesis. Still, the introduction of such concepts will be necessary to thoroughly understand the novel models proposed, especially in Chapters 6 and 7.

## 2.8 Discrete differential forms

The development of discrete equivalents of geometric notions and methods on classical differential geometry is the aim of the discrete differential geometry (DDG) discipline [56]. Indeed, the tools and ideas of disciplines such as algebraic topology [57] can be relevant to the numerical solution of Maxwell's equations when using the finite element method, for which the computational domain is normally discretized into a mesh. It will be seen here that an analogue to the de Rham complex exists at the discrete level and that the cohomology groups of Section 2.5.4 are equivalent to cohomology groups appearing in discrete representatives of the geometry. In fact, the numerical discretization of the funtion spaces in the de Rham complex, namely Nédélec elements, include the Whitney forms of the discretized cohomology. The key is to appreciate the structural coherence between the continous de Rham complex and the discrete simplicial complex and this compatibility, as expressed in [37, 49, 55], which is the reason why the differential definitions of cohomology are equivalent.

This section recalls some fundamental concepts of discrete cohomology theory on simplicial complexes. Our objective here is to find continuous discrete representatives for the spaces

where the scalar and vector fields involved in Maxwell's equations live. For convenience, all the definitions are presented for *simplicial meshes*, which are defined next.

### 2.8.1 Simplicial meshes

The simplest geometrical figure determined by $k+1$ points in the Euclidean space $\mathbb{R}^k$ is called a *k-simplex*. Thus, a triangular mesh in 2-D is only composed of geometrical simplices satisfying specific connectivity conditions. Each triangle in such a mesh corresponds to a 2-simplex, each edge to a 1-simplex, and each node to a 0-simplex. Tetrahedral elements in 3-D meshes are 3-simplices. Examples of some simplices are given in Fig. 2.3.

If the intersection of two $k$-simplicies is empty, or if it is a $i$-simplex, for $i < k$, they are said to be *properly situated*. If all the pairs of $k$-simplices in a mesh are properly situated, then the mesh is said to be conformal [51]. Examples of two properly and non-properly situated simplices are depicted in Fig. 2.4a and 2.4b, respectively.

A *triangulation* or *simplicial mesh* of $\Omega$, denoted by $\hat{\Omega}$, can be thus identified as a collection of simplices. Moreover, the set of all $k$-simplices, $0 \leq k \leq 3$, properly situated is called *simplicial complex* [58].

### 2.8.2 Abstract simplicial complex

The concept of an *abstract simplicial complex* is useful to separate the topological information from the geometrical shape [58]. Only incidence information (*connectivity*) is considered [51]. The abstract simplicial complex is a finite set of *vertices* with certain subsets. The maximum dimension of this complex is the maximum dimension of its simplices. For example, the abstract simplicial complex $\mathcal{K}$ representing the 2-simplex shown in Fig. 2.5 is

$$\mathcal{K} = \{\{\sigma_1^0\}, \{\sigma_2^0\}, \{\sigma_3^0\}, \{\sigma_1^0, \sigma_2^0\}, \{\sigma_1^0, \sigma_3^0\}, \{\sigma_2^0, \sigma_3^0\}, \{\sigma_1^0, \sigma_2^0, \sigma_3^0\}\}, \tag{2.78}$$

where its elements are called *k-facets*. This representation includes all nodes, edges and faces in the 2-D mesh, which is given by the single triangle in this example. The 2-facet $\{\sigma_1^0, \sigma_2^0, \sigma_3^0\}$

(a) 0-simplex (b) 1-simplex (c) 2-simplex (d) 3-simplex

Figure 2.3 Some $k$-simplices for $0 \leq k \leq 3$ (adapted from [58]).

(a) Properly situated 2-simplices (b) non-properly situated 2-simplices

Figure 2.4 Properly situated and non-properly situated simplices.

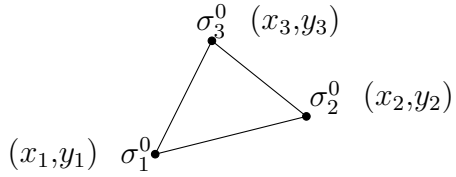


Figure 2.5 2-simplex example.

correspond to the topological information related to the face of the triangle (a 2-simplex) formed by the vertices $\sigma_1^0, \sigma_2^0$ and $\sigma_3^0$. For 3-D simplicial meshes, the region determined by each tetrahedral element given by its four vertices is also added to $\mathcal{K}$.

In order to have an equivalence between the incidence information and the geometry, we can assign to the abstract complex a *geometrical realization* denoted by $\Omega_k$ [58]. For example, in Fig. 2.5, assigning $\sigma_1^0, \sigma_2^0, \sigma_3^0$ to different points in the space $(x_1, y_1)$, $(x_2, y_2)$ and $(x_3, y_3)$ in $\mathbb{R}^2$, one achieves different geometrical realizations of $\mathcal{K}$ (triangles of any shape, for example). Therefore, the mesh of a discretized domain $(\hat{\Omega})$ defines a simpicial complex, but this mesh is only one of the multiple realizations of this complex. That is, the geometry in Fig. 2.5 is one geometrical realizations of $\mathcal{K}$. All these realizations of $\mathcal{K}$ are said to be *homeomorphic*, which intuitively means they are topological identical [57].

Finite element meshes enlarged by an orientation qualify as a valid complex. The orientation of each simplex in these meshes can be defined simply by selecting some particular ordering of its vertices. Therefore, any simplex has only two possible orientations. If those orderings differ by an odd permutation they are designated as *reversed*. For example, in Fig. 2.5, if for the 2-simplex is given the orientation $\{\sigma_1^0, \sigma_2^0, \sigma_3^0\}$, the orientation of its 1-facets (equivalent to its boundaries) is $\sigma_1^1 = \{\sigma_1^0, \sigma_2^0\}$, $\sigma_2^1 = \{\sigma_2^0, \sigma_3^0\}$ and $\sigma_3^1 = \{\sigma_3^0, \sigma_1^0\}$.

### 2.8.3 Chains and cochains

A *k-chain* ($c_k$) is a formal combination of $k$-simplices oriented with integer coefficients [51]. The group of all $k$-chains in a given complex $\mathcal{K}$ is denoted by $C_k$. In Fig. 2.6, the example of a 1-chain iso-oriented by a path from $\sigma_4^0$ to $\sigma_1^0$ (in blue) is $c_1 = -\sigma_1^1 - \sigma_4^1 - \sigma_5^1 + \sigma_8^1 + \sigma_9^1$. This 1-chain can be represented by the vector $(-1, 0, 0, -1, -1, 0, 0, 1, 1, 0)^T$ associated to the coefficients assigned to the ordered list of 1-simplices in the complex and according to the path orientation.

The group of the elementary *k-cochains* (denoted by $C^k$ with each $k$-cochain denoted by $c^k$) is equal to the group of all linear maps going from $C_k$ to integers. More generally, we can define $C_k(\mathbb{R})$ as real multiples of $k$-simplices, and $C^k(\mathbb{R})$ as linear maps from $C_k(\mathbb{R})$ to $\mathbb{R}$ [55]. The value assigned by a *k-cochain* to a collection of $k$-chains is the sum of the values assigned to the individual $k$-chains, i.e., there exists a natural pairing

$$\begin{aligned} \langle , \rangle_C : C_k(\mathbb{Z}) \times C^k(\mathbb{Z}) &\to \mathbb{Z} \\ \left(\sum a_i c_i, \sum b^j c^j\right) &\mapsto \sum_{i,j} a_i b^j c^j(c_i) \end{aligned} \tag{2.79}$$

obtained simply evaluating a $k$-cochain $c^j$ on a $k$-chain $c_j$, where $a_i$ and $b^j$ are the chains and cochains coefficients, respectively, and $c^j(c_i) = \delta_{ij}$. Clearly, it suffices to define each map in $C^k$ by defining its effect in each individual $k$-chain. This is therefore a discrete version of integrating a $k$-form over a $k$-dimensional submanifold (see Section 2.7 for the definition of $k$-forms). For illustration, the value assigned by a 1-cochain to $c_1$ in our example is the sum of the values assigned to each 1-simplex in this 1-chain weighed by their respective orientations (i.e. a line integral of a differential 1-form over the path defined by $c_1$).

### 2.8.4 Boundary and coboundary operators

For any oriented $k$-simplex $\sigma^k$, its boundary is defined as a $(k-1)$-chain of $\mathcal{K}$ over $\mathbb{Z}$. Therefore, for $k \geq 1$ we can define the *boundary operator* $\partial_k : C_k(\mathcal{K}) \to C_{k-1}(\mathcal{K})$. If $k = 0$, we define $\partial_0(\sigma^0) = 0$. The boundary operator is formally a *homomorphism* [57]. In other words, the boundary of each 3-simplex is a union of closed 2-simplices, the boundary of each 2-simplex the union of closed 1-simplices, and the boundary of a 1-simplex consists of two vertices. Consequently, each $k$-simplex is contained in the boundary of a $(k+1)$-simplex, for $0 \leq k \leq 2$.

Given that $\partial_k$ is a linear map and $C_k$ is a sum of $k$-simplices oppositely oriented, the fundamental condition $\partial_{k-1}(\partial_k(C_k)) = 0$ can be easily verified. Let us consider again the

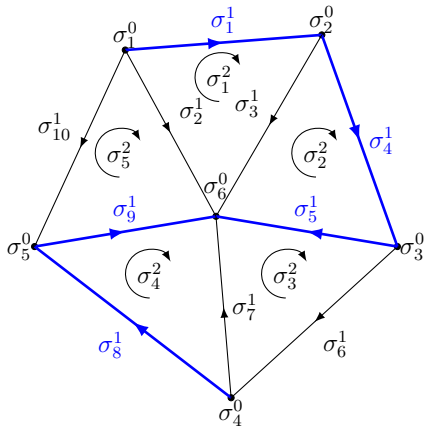


Figure 2.6 Simplices and a 1-chain example depicted in blue (adapted from [51]).

oriented abstract simplicial complex $\mathcal{K}$ corresponding to the simplices in Fig. 2.6. The boundary of the 2-chain $c_2 = \sigma_4^2 + \sigma_5^2$ (depicted in Fig. 2.7a) is

$$\begin{aligned}\partial_2 c_2 &= \partial_2\sigma_4^2 + \partial_2\sigma_5^2 = \partial_2\{\sigma_4^0, \sigma_5^0, \sigma_6^0\} + \partial_2\{\sigma_5^0, \sigma_1^0, \sigma_6^0\} \\ &= \{\sigma_4^0, \sigma_5^0\} + \{\sigma_5^0, \sigma_6^0\} - \{\sigma_4^0, \sigma_6^0\} - \{\sigma_1^0, \sigma_5^0\} + \{\sigma_1^0, \sigma_6^0\} - \{\sigma_5^0, \sigma_6^0\} \\ &= \{\sigma_4^0, \sigma_5^0\} - \{\sigma_1^0, \sigma_5^0\} + \{\sigma_1^0, \sigma_6^0\} - \{\sigma_4^0, \sigma_6^0\} = \sigma_8^1 - \sigma_{10}^1 + \sigma_2^1 - \sigma_7^1.\end{aligned}$$

That can be represented by the 1-chain $c_1 = \partial_2 c_2$ or in the basis of our chains $(0, 1, 0, 0, 0, 0, -1, 1, 0, -1)^T$ depicted in Fig 2.7b. Applying again the boundary operator to $c_1$, we have

$$\begin{aligned}\partial_1 c_1 &= \partial_1\sigma_8^1 - \partial_1\sigma_{10}^1 + \partial_1\sigma_2^1 - \partial_1\sigma_7^1 \\ &= \sigma_5^0 - \sigma_4^0 - \sigma_5^0 + \sigma_1^0 + \sigma_6^0 - \sigma_1^0 - \sigma_6^0 + \sigma_4^0 = 0,\end{aligned}$$

thereby illustrating $\partial_{k-1}(\partial_k(C_k)) = 0$.

If the boundary of a $k$-chain is zero, this chain is also called a *cycle* [58]. The set of all $k$-cycles of $\mathcal{K}$ is denoted by $Z_k$, which is a subgroup of $C_k$ because it can be written as the kernel of $\partial_k$ (i.e. $Z_k = \ker(\partial_k)$). In addiction, since $\partial_{k-1}(\partial_k(C_k)) = 0$, we conclude that every boundary is a cycle homologous to zero, but not every cycle is a boundary in the case of multiple connected discretized domains. The subgroup of boundaries of $Z_k$ is denoted by $B_k$, which can be written as the image of $\partial_{k+1}$ (i.e. $B_k = \mathrm{im}(\partial_{k+1})$).

Given that the boundary operator is a linear map, it can be expressed as an *incidence matrix* $\mathcal{M}_k$. Each column of $\mathcal{M}_k$ represents a $(k-1)$-chain that is the boundary of the

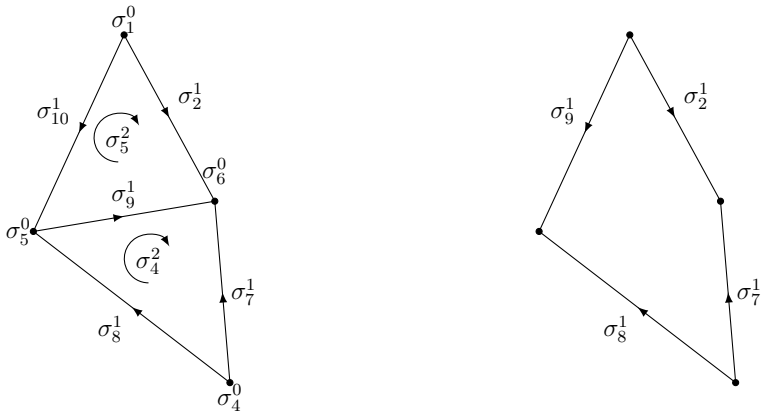


Figure 2.7 (a) 2-chain example taken from $\mathcal{K}$ depicted in Fig. 2.6 and its boundary (a 1-chain that is also denoted as a 1-cycle).

$k$-chain in $\mathcal{K}$ represented by the rows of this matrix. For example, for the complete simplicial complex with geometrical realization represented in Fig. 2.6, we have

$$\mathcal{M}_1 = \begin{bmatrix} -1 & -1 & 0 & 0 & 0 & 0 & 0 & 0 & 0 & -1 \\ 1 & 0 & -1 & -1 & 0 & 0 & 0 & 0 & 0 & 0 \\ 0 & 0 & 0 & 1 & -1 & -1 & 0 & 0 & 0 & 0 \\ 0 & 0 & 0 & 0 & 0 & 1 & -1 & -1 & 0 & 0 \\ 0 & 0 & 0 & 0 & 0 & 0 & 0 & 1 & -1 & 1 \\ 0 & 1 & 1 & 0 & 1 & 0 & 1 & 0 & 1 & 0 \end{bmatrix},$$

and

$$\mathcal{M}_2 = \begin{bmatrix} 1 & 0 & 0 & 0 & 0 \\ -1 & 0 & 0 & 0 & 1 \\ 1 & -1 & 0 & 0 & 0 \\ 0 & 1 & 0 & 0 & 0 \\ 0 & 1 & -1 & 0 & 0 \\ 0 & 0 & 1 & 0 & 0 \\ 0 & 0 & 1 & -1 & 0 \\ 0 & 0 & 0 & 1 & 0 \\ 0 & 0 & 0 & 1 & -1 \\ 0 & 0 & 0 & 0 & -1 \end{bmatrix}.$$

Note that $\mathcal{M}_1\mathcal{M}_2 = [0]$. Moreover, the vector representing the boundary of the 2-chain

$c_2 = \sigma_4^2 + \sigma_5^2$ in Fig. 2.7a in the basis of our 1-chains ($c_1$) can be obtained directly by adding the forth and fifth columns of $\mathcal{M}_2$, for example.

We can now define a *coboundary operator* as $\partial^{k-1} : C^{k-1}(\mathcal{K}) \to C^k(\mathcal{K})$ by the duality principle, i.e. $\forall\, c_k \in C_k(\mathcal{K})$, $\forall\, c^k \in C^k(\mathcal{K})$, $(\partial^{k-1} c^{k-1})(c_k) = c^{k-1}(\partial_k c_k)$. Therefore, since $\mathcal{M}_k$ is a matrix of boundary operator $\partial_k$, the incidence matrix of coboundary operators $\partial^{k-1}$ is $\mathcal{M}_k^T$. Also,

$$\partial_{k-1} \circ \partial_k = 0 \to (\mathcal{M}_{k-1}\mathcal{M}_k) = 0 \to (\mathcal{M}_{k-1}\mathcal{M}_k)^T = \mathcal{M}_k^T \mathcal{M}_{k-1}^T = 0.$$

It is easy to identify that the boundary and coboundary operators are closely related to the exterior derivatives introduced in Section 2.7. The exterior derivative of a $k$-cochain assigns to each $(k+1)$-facet in $\mathcal{K}$ the sum of integers values associated to the $k$-cycle corresponding to the boundary of this facet weighted with respective orientation [37]. Therefore, the incidence information contained in the matrices $\mathcal{M}_k^T$ is useful to define the differential operators purely from the topology of the problem. For example, the topological (here discrete) gradient, curl and divergence are given by matrices $\mathcal{M}_1^T$, $\mathcal{M}_2^T$ and $\mathcal{M}_3^T$, respectively, and can be represented as in Fig. 2.8.

Recalling the definition of the integral forms in Section 2.7, the discrete integral of a $k$-form is determined by fixing the number it assigns to every $k$-cycle in $\Omega_k$. For example, the total current that passes through a 2-facet is the value assigned to the integration of the magnetic field over the 1-cycle equivalent to the boundary of this facet. This definition is equivalent to the 1-cochains (in this case, also a 1-cocyle) given in Section 2.8.3.

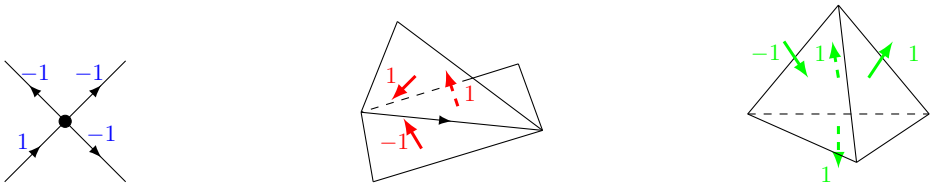


(a) Discrete gradient (b) Discrete curl (c) Discrete divergence

Figure 2.8 Representation of exterior derivatives on cochains (adapted from [37]).

### 2.8.5 Chain and cochain classification

In general, we define a *(co)chain complex* as a sequence of *abelian groups*[3] connected by homomorphisms (the (co)boundary operators) for which the composition of any two consecutive maps is zero (fundamental condition). In our case, the boundary operators define the (co)chain complex to be studied.

The group $C_k$ of all $k$-chain in a complex $\mathcal{K}$ form a chain complex with boundary operator $\partial_k$. This chain complex is represented in Fig. 2.9. Equivalently, the group $C^k$ of all $k$-cochain in a complex $\mathcal{K}$ form a *cochain complex* with coboundary operator $\partial^k$. This cochain complex is represented in Fig. 2.10.

From $\partial_{k-1} \circ \partial_k = 0$, it is possible to verify that the image of $\partial_k$ is a subgroup of the kernel of $\partial_{k-1}$, or, the image of $\partial_{k+1}$ is a subgroup of the kernel of $\partial_k$. We can thus classify the chains as:

- $B_k(\mathcal{K}) = \text{im}(\partial_{k+1})$ is the *$k$-boundary group* of $\mathcal{K}$. The elements of $B_k(\mathcal{K})$ are called *boundaries*.
- $Z_k(\mathcal{K}) = \ker(\partial_k)$ is the *$k$-cycle group* of $\mathcal{K}$. The elements of $Z_k(\mathcal{K})$ are called *cycles*.

The same classification can be given for the cochains:

- $B^k(\mathcal{K}) = \text{im}(\partial^{k-1})$ is the *$k$-coboundary group* of $\mathcal{K}$. The elements of $B^k(\mathcal{K})$ are called *coboundaries*.
- $Z^k(\mathcal{K}) = \ker(\partial^k)$ is the *$k$-cocycles group* of $\mathcal{K}$. The elements of $Z^k(\mathcal{K})$ are called *cocycles*.

### 2.8.6 Homology and cohomology groups

The *homology group* $\mathcal{H}_k$ is the quotient group of the subgroup of cycles $Z_k$ and the subgroup of boundaries $B_k$ in $C_k$ [59]. The subgroup $Z_k$ is exactly the kernel of $\partial_k$ and $B_k$ is the image of $\partial_{k+1}$. The homology group is thus defined as

$$\mathcal{H}_k(\mathcal{K}) = Z_k(\mathcal{K})/B_k(\mathcal{K}) = \ker(\partial_k)/\text{im}(\partial_{k+1}) \text{ for } k \in \mathbb{N}.$$

For a simply-connected domain, every cycle in $\Omega_k$ is homologous to its boundary. Or equivalently, every $k$-cycle in $C_k$ is the boundary of a $(k+1)$-chain in $C_{k+1}$, and $Z_k(\mathcal{K}) = B_k(\mathcal{K})$. However, when $\Omega_k$ is multiply connected, its boundary consists of $c+1$ closed surfaces.

[3] An abelian group is a group in which the result of applying the boundary operator (in this case) does not depend on the order in which they are written, i.e., the boundary operator is commutative.

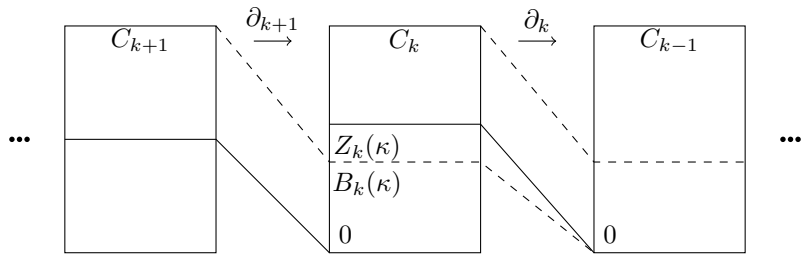


Figure 2.9 Chain complex.

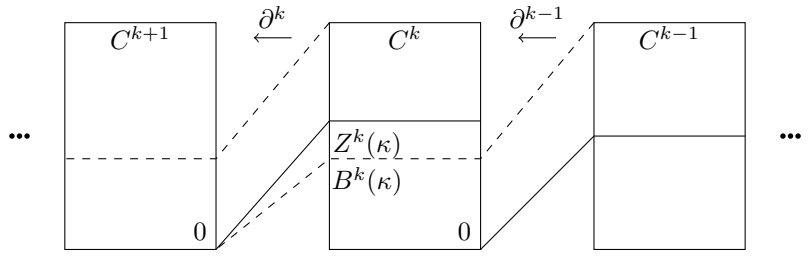


Figure 2.10 Cochain complex.

There exists thus a homology basis comprising $c$ cycles homologous to the boundary of each cavity in $\Omega_k$. These cycles are dual to $c$ cutting surfaces called *cohomology representatives* that make the domain simply connected.

The *cohomology group* $\mathcal{H}^k$ has a definition dual to the homology group $\mathcal{H}_k$. It represents the quotient group of the subgroups of $k$-cocycles and $k$-coboundaries, i.e.

$$\mathcal{H}^k(\mathcal{K}) = Z^k(\mathcal{K})/B^k(\mathcal{K}) = \ker(\partial^k)/\mathrm{im}(\partial^{k-1}) \text{ for } k \in \mathbb{N}. \tag{2.80}$$

Informally, the cohomology group assigns a value to the cycles in the homology group. Therefore, it is possible to show that the pairing (2.79) also passes to the quotient

$$\begin{aligned} \langle , \rangle_{\mathcal{H}} &: \mathcal{H}_k(\mathcal{K}) \times \mathcal{H}^k(\mathcal{K}) \to \mathbb{Z} \\ (c, \ell) = \left( \left[ \sum a_i c_i \right], \left[ \sum b^j c^j \right] \right) &\mapsto \left\langle \sum a_i c_i, \sum b^j c^j \right\rangle. \end{aligned} \tag{2.81}$$

The cohomology basis representative of $\mathcal{K}$ is the discrete equivalent of the subspace $\boldsymbol{H}^1_{\mathrm{dR}}(\Omega)$, i.e. with $\Omega$ discretized as $\hat{\Omega}$. A homology and cohomology solver for finite element meshes was implemented in the open source code Gmsh [60] and is an integrated part of the meshing process [55]. The algorithm uses only the connectivity information of the mesh to create the abstract simplicial complex. The *cells* ($k$-facets, $0 \leq k \leq 3$, for 3-D domains) in this complex

are combined and reduced to scale down the problem size, which is then solved in the Smith normal form.

Appendix A discusses how to select the cohomology basis representatives for imposing current constraints in problems involving multiple conductors in 2-D and 3-D domains. We also present results obtained with periodic boundary conditions after proposing changes in the Gmsh algorithm to take into account the periodicity while computing the discrete cohomology basis representatives. These modifications allowed us to reduce the computational domain (and number of state variables) in cases of periodic geometries.

Among its benefits, the cohomology basis representatives has a small support on $\hat{\Omega}$ that represents a significant reduction in the number of variables compared to a model based purely on a vector field formulation [61]. Moreover, it allows obeying Ampère's law in $\Omega_c^C$ when using $\phi$ as the state variable, for example, and directly coupling the finite element problem with circuit models [62, 63]. No additional integration constraint is required to impose current or voltage constraints in $\Omega_c$ (the cavities in $\Omega_c^C$). This definition will be important later in this thesis when we impose current constraints in thin conducting regions such as those in HTS tapes.

### 2.8.7 Illustrative example of homology and cohomology computation

In this section, we present in detail a pedagogical example of the homology and cohomology calculation in a multiply connected domain in order to understand how this theory is used in practice. Let us consider the example of an abstract simplicial complex $\mathcal{K}$ with geometrical realization depicted in Fig. 2.11 and defined as

$$\mathcal{K} = \{\{\sigma_1^0\}, \{\sigma_2^0\}, \{\sigma_3^0\}, \{\sigma_4^0\}, \{\sigma_1^0, \sigma_2^0\}, \{\sigma_1^0, \sigma_3^0\}, \{\sigma_2^0, \sigma_3^0\}, \{\sigma_2^0, \sigma_4^0\}, \{\sigma_3^0, \sigma_4^0\}, \{\sigma_2^0, \sigma_3^0, \sigma_4^0\}\},$$

which is similar to the example presented in [59]. We seek to compute the homology and cohomology basis representatives for this complex. This calculation will occupy us for the remainder of this section. Although it is long, it helps to make much of our earlier abstract discussion more concrete and more generally to appreciate automated homology/cohomology solvers such as that in Gmsh [60].

The complex $\mathcal{K}$ comprises a single 2-facet $\sigma_1^2 = \{\sigma_2^0, \sigma_3^0, \sigma_4^0\}$. The triangle $\{\sigma_0^1, \sigma_0^2, \sigma_0^3\} \notin \mathcal{K}$, but its boundaries $\{\sigma_0^1, \sigma_0^2\}$, $\{\sigma_0^1, \sigma_0^3\}$ and $\{\sigma_0^2, \sigma_0^3\} \in \mathcal{K}$ (see Fig. 2.11), which means that the discretized domain represented by $\mathcal{K}$ is multiply connected (the triangle $\{\sigma_0^1, \sigma_0^2, \sigma_0^3\}$ represents a cavity). Therefore, the following homology groups can be identified:

- $\mathcal{H}_k(\mathcal{K}) = 0$ for $k < 0$ or $k > 2$ since there are no simplices in these dimensions;

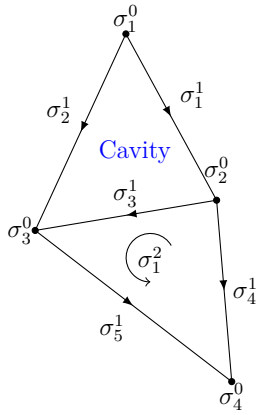


Figure 2.11 Geometrical realization of $\mathcal{K}$ used as example for the homology computation.

- $\mathcal{H}_0(\mathcal{K}) \cong \mathbb{Z}$ since the vertices in $\mathcal{K}$ are all connected by a sequence of 1-chains. In general, the dimension of $\mathcal{H}_0(\mathcal{K})$ is the number of connected components [59];
- $\mathcal{H}_1(\mathcal{K}) = Z_1(\mathcal{K})/B_1(\mathcal{K}) \cong \mathbb{Z}$ (discussed next);
- $\mathcal{H}_2(\mathcal{K}) = Z_2(\mathcal{K})/B_2(\mathcal{K})$, and, since $\partial_2(\sigma_1^2) \neq 0$, $Z_2(\mathcal{K}) = 0$, we have $\mathcal{H}_2(\mathcal{K}) = 0$.

To find $\mathcal{H}_1(\mathcal{K})$, we start by computing $Z_1(\mathcal{K})$ (see definition in Section 2.8.5). To this end, it suffices to solve

$$\begin{aligned}
&\partial_1(\lambda_1\sigma_1^1 + \lambda_2\sigma_2^1 + \lambda_3\sigma_3^1 + \lambda_4\sigma_4^1 + \lambda_5\sigma_5^1) \\
&\quad = \partial_1(\lambda_1\{\sigma_1^0, \sigma_2^0\} + \lambda_2\{\sigma_1^0, \sigma_3^0\} + \lambda_3\{\sigma_2^0, \sigma_3^0\} + \lambda_4\{\sigma_2^0, \sigma_4^0\} + \lambda_5\{\sigma_3^0, \sigma_4^0\}) \\
&\quad = \lambda_1(\sigma_2^0 - \sigma_1^0) + \lambda_2(\sigma_3^0 - \sigma_1^0) + \lambda_3(\sigma_3^0 - \sigma_2^0) + \lambda_4(\sigma_4^0 - \sigma_2^0) + \lambda_5(\sigma_4^0 - \sigma_3^0) \\
&\quad = \sigma_1^0(-\lambda_1 - \lambda_2) + \sigma_2^0(\lambda_1 - \lambda_3 - \lambda_4) + \sigma_3^0(\lambda_2 + \lambda_3 - \lambda_5) + \sigma_4^0(\lambda_4 + \lambda_5) = 0,
\end{aligned}$$

or, equivalently,

$$\begin{cases} -\lambda_1 - \lambda_2 = 0 \\ \lambda_1 - \lambda_3 - \lambda_4 = 0 \\ \lambda_2 + \lambda_3 - \lambda_5 = 0 \\ \lambda_4 + \lambda_5 = 0 \end{cases}, \tag{2.82}$$

which can be reduced to the row echelon form using only integer operations between the equations in this system (the so-called *Smith Normal Form* [38]) as

$$\begin{cases} \lambda_1 + \lambda_2 = 0 \\ \lambda_2 + \lambda_3 + \lambda_4 = 0 \\ \lambda_4 + \lambda_5 = 0 \end{cases}. \tag{2.83}$$

By keeping $\lambda_3$ and $\lambda_5$ free, the solution for (2.83) is spanned by $(-1,1,-1,0,0)^T$ and $(-1,1,0,-1,1)^T$. So, $Z_1(\mathcal{K}) \cong \mathbb{Z}^2$ and is generated by

$$z_1 = -\sigma_1^1 + \sigma_2^1 - \sigma_3^1, \tag{2.84}$$

$$z_2 = -\sigma_1^1 + \sigma_2^1 - \sigma_4^1 + \sigma_5^1. \tag{2.85}$$

which means that every cycle in $\mathcal{K}$ can be constructed as a formal combination of the cycles $z_1$ and $z_2$. We recommend that reader draw them over the geometrical realization depicted in Fig. 2.11.

Next, we compute the subgroup of 1-boundaries $B_1(\mathcal{K}) = \text{im}(\partial_2)$, i.e.

$$\partial_2(\sigma_1^2) = \partial_2(\{\sigma_2^0, \sigma_3^0, \sigma_4^0\}) = \{\sigma_3^0, \sigma_4^0\} - \{\sigma_2^0, \sigma_4^0\} + \{\sigma_2^0, \sigma_3^0\} = \sigma_5^1 - \sigma_4^1 + \sigma_3^1. \tag{2.86}$$

It is clear that $B_1(\mathcal{K}) \cong \mathbb{Z}$ and is generated by $b_1 = z_1 + z_2$. Hence, $\mathcal{H}_1(\mathcal{K}) \cong \mathbb{Z}$ and is generated by either $z_1$ or $z_2$. The cycle $z_1$ is not the boundary of any $(k+1)$-cycle, and $z_2 = z_1 + \partial_2(\sigma_1^2)$. Moreover, the triangle $\{\sigma_0^1, \sigma_0^2, \sigma_0^3\}$ in Fig. 2.11 represents a cavity in $\Omega_k$, and both the cycles $z_1$ and $z_2$ encompass this cavity. For these reasons, the cycles $z_1$ and $z_2$ are said to be *homologous*.

The ranks of the $k$-cohomology groups are equivalent to the ranks of the $k$-homology groups according to the so-called *Universal Coefficients Theorem* [38]. We have $\mathcal{H}^k(\mathcal{K}) = 0$ for $k < 0$ or $k > 1$. For $k = 0$, $\mathcal{H}^0(\mathcal{K}) \cong \mathbb{Z}$ since for any 0-cocycle, we know that its application to the boundary of a 1-chain will vanish. In particular, we can verify that the value assigned by a 0-cocylcle on any pair of 0-chains formed of isolated nodes must be opposite in value, hence there is only a single degree of freedom, i.e. its value to be assigned to a single 0-chain in $\mathcal{K}$. Finally, it remains us to find a 1-cohomology group defined as $\mathcal{H}^1(\mathcal{K}) = Z^1(\mathcal{K})/B^1(\mathcal{K}) = \ker(\partial^1)/\text{im}(\partial^0)$.

Let us assume that the value assigned to each 1-chain $\sigma_i^1$ by a 1-cochain in $\mathcal{K}$ is $\tau_i^1$, for $i = 1$ to the number 1-facets in $\mathcal{K}$ (5 in our example). To find $Z^1(\mathcal{K})$, we proceed exactly as we did to find $Z_1(\mathcal{K})$, i.e. we solve

$$\partial^1 \left(\lambda^1\tau_1^1 + \lambda^2\tau_2^1 + \lambda^3\tau_3^1 + \lambda^4\tau_4^1 + \lambda^5\tau_5^1\right) = 0. \tag{2.87}$$

Given that $\partial^1\tau_1^1 = 0$ and $\partial^1\tau_2^1 = 0$, $\lambda^1$ and $\lambda^2$ are free. Also, since $\partial^1\tau_3^1 = -\partial^1\tau_4^1 = \partial^1\tau_5^1 = \tau_1^2$, we have $\lambda^3 - \lambda^4 + \lambda^5 = 0$. Then, keeping $\lambda^4$ and $\lambda^5$ free, the solution to (2.87), is spanned by $z^1 = (1,0,0,0,0)^T$, $z^2 = (0,1,0,0,0)^T$, $z^3 = (0,0,1,1,0)^T$ and $z^4 = (0,0,-1,0,1)^T$. So, $Z^1 \cong \mathbb{Z}^4$.

The subgroup of 1-coboundaries is $B^1(\mathcal{K}) = \text{im}(\partial^0)$ and includes

$$\partial^0 \tau_1^0 = -\tau_2^1 - \tau_1^1, \tag{2.88}$$
$$\partial^0 \tau_2^0 = \tau_1^1 - \tau_3^1 - \tau_4^1, \tag{2.89}$$
$$\partial^0 \tau_3^0 = \tau_2^1 + \tau_3^1 - \tau_5^1 \tag{2.90}$$
$$\partial^0 \tau_4^0 = \tau_4^1 + \tau_5^1. \tag{2.91}$$

Note however that $\partial^0 \tau_1^0 = -(\partial^0 \tau_2^0 + \partial^0 \tau_3^0 + \tau_4^0)$, i.e. the first 0-cobounday (2.88) can be written as a formal combination of the three others 0-coboundaries. Therefore, the group $B^1(\mathcal{K})$ is spanned by $b^1 = (1, 0, -1, -1, 0)^T$, $b^2 = (0, 1, 1, 0, -1)^T$ and $b^3 = (0, 0, 0, 1, 1)^T$, i.e. $B^1(\mathcal{K}) \cong \mathbb{Z}^3$.

Finally, $\mathcal{H}^1(\mathcal{K}) \cong \mathbb{Z}$ generated by any of the 1-cocycles $z^i$, $1 \leq i \leq 4$, since the coboundaries $b^i$, $1 \leq 0 \leq 3$, cannot define any of these 1-cocycles. These 1-cocycles are said *cohomologous*, i.e. they can be obtained from another 1-cocycle with the addition of a coboundary. For example, $z^1 = -z^4 + b^1 + b^3$, $z^2 = z^4 + b^2$ and $z^3 = -z^4 + b^3$. The cohomology basis representative starts with an outer boundary edge ($\tau_1^1$, $\tau_2^1$, $\tau_5^1$ or $\tau_4^1$) and ends with a inner boundary edge ($\tau_1^1$, $\tau_2^1$ or $\tau_3^1$). Moreover, the value assigned by, for example, $z^4$ to the 1-cycles in $\mathcal{K}$ is the same value assigned to every 1-cycle constructed by any combination of $z_1$ and 1-boundaries. The cohomology basis represented by $z^4$ is said to be dual to the homology basis represented by, for example, $z_1$. These homology and cohomology basis representatives are illustrated in Fig. 2.12.

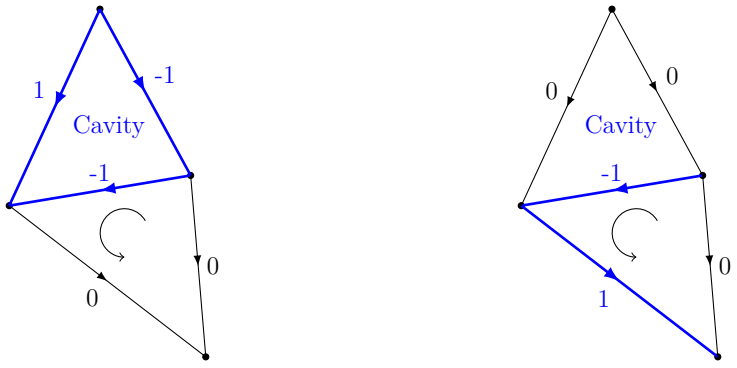


(a) Homology basis representative $z_1$ (b) Cohomology basis representative $z^4$

Figure 2.12 Homology and cohomology basis representatives for the exemplified $\mathcal{K}$. The 1-chain and the 1-cochain representing this basis are spanned by $z_1 = (-1, 1, -1, 0, 0)^T$ and $z^4 = (0, 0, -1, 0, 1)^T$, corresponding the 1-simplices (edges depicted in blue with respective orientation) in the $\mathcal{K}$ that is geometrically represented in Fig. 2.11.

The cohomology basis representative of $\mathcal{K}$ is also a basis for the subspace $\boldsymbol{H}^1_{\mathrm{dR}}(\Omega)$ with $\Omega$ discretized as $\hat{\Omega}$. For example, with $\boldsymbol{h} = -\nabla\phi$, the integral form of Ampère's law (2.69) yields zero. Defining $\boldsymbol{h} = -\nabla\phi + \boldsymbol{h}'$, where $\boldsymbol{h}'$ represent the circulation of the magnetic field over $z^4$, satisfies (2.69) for any cycle in $\hat{\Omega}$. Actually, $\boldsymbol{h}'$ can be seen as a discontinuity of $\phi$ distributed along the edges representing $z^4$ (e.g. in a transition layer according to [62, 64]). The integration of $\boldsymbol{h}'$ over these edges is equivalent to the net current that flows in the cavity $\{\sigma^1_0, \sigma^2_0, \sigma^3_0\}$ in Fig. 2.11.

### 2.8.8 Whitney forms

Now that we have introduced the differential and integral forms of the quantities of interest, and the useful concepts of algebraic topology, we need to define the discrete geometrical objects that approximate smooth differential forms, just like the traditional finite-element interpolating functions. To construct the differential $k$-forms and the integral forms to make sense over the discretized domain $\widehat{\Omega}$, i.e. a mesh, we consider the so-called *Whitney maps* [65], which form the spaces denoted as $\mathcal{W}^k(C^k(\hat{\Omega}))$, $0 \leq k \leq 3$, of Whitney $k$-forms on the triangulation $\hat{\Omega}$. For convenience, we restrict ourselves to the study of mapping $\mathcal{W}^k$ in simplicial meshes.

Let us consider a single tetrahedron $T$ with vertices $\sigma^0_0$, $\sigma^0_1$, $\sigma^0_2$ and $\sigma^0_3$. We start with the case of differential 0-forms, for example those associated with a scalar field $u$. The value of $u$ at any point $\boldsymbol{x}$ of $T$ can be determined by the interpolation of the values $u(\sigma^0_i)$ in each vertex $\sigma^0_i$, $0 \leq i \leq 3$, and based on barycentric coordinate functions $w_i(\boldsymbol{x})$, i.e.

$$u(\boldsymbol{x}) = \sum_{i=0}^{3} u(\sigma^0_i) w_i(\boldsymbol{x}). \tag{2.92}$$

For this reason, the functions $w_i$ are often denoted as *nodal basis functions*. They are 0-forms associated to the vertices of $T$. The *degrees of freedom* (DoFs), or the variables of the discrete problem, are then the values of $u$ at the vertices of $T$, i.e. $u(\sigma^0_i)$.

For 1-forms, such as those related to a vector field $\boldsymbol{u}$, we define that any oriented line in $T$ can be represented by the weighted sum of the edges of $T$. If $\sigma^0_i$ and $\sigma^0_j$, $0 \leq i, j \leq 3$, are the vertices of these edges, the differential 1-form related to each edge $\sigma^1_{ij} = \{\sigma^0_i, \sigma^0_j\}$ (1-simplex) is

$$\boldsymbol{w}_{ij} = w_i \nabla w_j - w_j \nabla w_i, \tag{2.93}$$

where $w_i$ and $w_j$ are the nodal basis functions associated to the vertices $\sigma^0_i$ and $\sigma^0_j$, respectively. It is important to note that the circulation of $\boldsymbol{w}_{ij}$ is 1 along the corresponding

oriented edge $\sigma^1_{ij}$, and 0 along the other edges. The vector field in $T$ can then be defined as a linear combination of Whitney 1-forms, i.e.

$$\boldsymbol{u} = \sum_{\sigma^1_{i,j} \in \mathcal{E}} u(\sigma^1_{i,j}) \boldsymbol{w}_{ij}. \tag{2.94}$$

where $\mathcal{E}$ represents the set of edges of the 3-simplex. In this case, the DoFs are the circulations of $\boldsymbol{u}$ along the edges $\sigma^1_{i,j}$, i.e. $u(\sigma^1_{i,j})$. For this reason, Whitney elements of degree 1 are often called *edge elements* [66].

The procedure of finding the Whitney $k$-forms associated to the $k$-simplex can be generalized as [65]

$$\boldsymbol{w}_{i_0,\ldots,i_k} = k! \sum_{j=0}^{k} (-1)^j w_{i_j} \nabla w_{i_0} \times \ldots \times \nabla w_{i_{j-1}} \times \nabla w_{i_{j+1}} \times \ldots \times \nabla w_{i_k} \tag{2.95}$$

where $w_{i_j}$ are the nodal basis functions associated to the vertices $\sigma_{i_j}$, $j \leq 0 \leq k$, of the $k$-simplex. These Whitney $k$-forms are order-one Nédelec elements [37] and appear later in this thesis for the representation of the scalar and vector fields ($k = 0$ and 1, respectively). When the Whitney forms are constructed as above, we obtain discrete spaces of the functions spaces in the de Rham complex that are preserved under the $\mathbf{d}$ operator. These spaces have many additional properties, particularly a special discrete form of the Helmholtz Decomposition [36].

### 2.8.9 Magnetic field discrete form

The magnetic field $\boldsymbol{h}$ is discretized with Whitney elements as follows:

$$\boldsymbol{h} = \sum_{e \in \Omega_c} h_e \boldsymbol{w}_e - \sum_{n \in \Omega_c^C} \phi_n \nabla w_n + \sum_{i \in C} I_i \boldsymbol{\psi}_i \tag{2.96}$$

where $\boldsymbol{w}_e$ is the edge basis function of edge $e$ (Whitney 1-form), $w_n$ the nodal basis function of node $n$ (Whitney 0-form), and $\boldsymbol{\psi}_i$ is the edge-based cohomology basis functions (thick cuts) associated to each conducting subdomain $\Omega_{c,i}$ in $\Omega$. These thick cuts are equivalent to the sum Whitney 1-forms defined along the cohomology basis representatives introduced in Section 2.8.6. The coefficients $h_e$ and $\phi$ are the DoFs, i.e. the circulation of $\boldsymbol{h}$ along the edges and the magnitude of $\phi$ at the nodes of the discretized domain. The coefficients $I_i$ gives the intensity of the magnetic filed circulations along the thick cuts (equivalent to the current that flows in each disjoint conducting subdomain $\Omega_{c,i}$). They can be either constrained to impose the total current in $\Omega_{c,i}$, or be part of the unknowns of the problem for cases of induced current analysis. Moreover, they allow coupling the finite element model to an external

circuit, as presented in [62].

Finally, by using (2.96) in (2.49) and applying the *Galerkin weighted residuals method*, we obtain the system of equations of the $H$-formulation to be solved at each instant of time $t$, and at each iteration of the numerical scheme used to treat the nonlinear problem (the *Picard* or the *Newton–Raphson* methods [41], for example).

### 2.8.10 Potentials discrete forms

The potentials $\boldsymbol{a}$ and $v$ are discretized as Whitney 1-form and 0-form, respectively, as

$$\boldsymbol{a} = \sum_{e \in \Omega} a_e \boldsymbol{w}_e, \tag{2.97}$$

and

$$v = \sum_{i \in C} v_i w_i, \tag{2.98}$$

where $a_e$ are the circulations of $\boldsymbol{a}$ along the edge $e$, $v_i$ is the electric scalar potential at each conducting region $\Omega_{c,i}$, and $w_i$ are basis functions associated with the cross section of a conducting region $\Omega_{c,i}$ in a 2-D case. In 3-D, the basis functions $w_i$ have a support limited to the thick cut (a transition layer [43]) related to the cohomology of the $\Omega_{c,i}$ (instead of $\Omega_c^C$ as in the $H$ formulation) when its terminals are connected. The strength of $v_i$ in the transition layer is equivalent to the voltage in $\Omega_{c,i}$.

The scalar potential defined only in the thick cut in $\Omega_{c,i}$ is called the generalized source potential [63], but $v$ can be defined everywhere in $\Omega_c$ [67]. This definition does not affect the solution, i.e. the field distributions obtained with either the generalized source potential or the standard electrical potential are identical [43]. However, the use of the generalized source potential reduces the total number of DoFs and allows coupling the $A$-$V$-formulation with an exterior circuit, as proposed in [63].

Finally, by using (2.97) and (2.98) in (2.67) and applying the Galerkin weighted residuals method, we obtain the system of equations of the $A$-$V$-formulation to be solved at each instant of time $t$ and at each iteration of the numerical scheme used to treat the nonlinear problem (the *Picard* or the *Newton–Raphson* methods [41], for example).

## 2.9 Chapter summary and remarks

In this chapter, the fundamentals of computational electromagnetics were presented in a very general way. They are required for the understanding of the existing approaches for

modeling thin structures presented in the next chapter and are the basis of the methods proposed in Chapters 5-7. The concepts of algebraic topology were presented in parallel to the differential representation of Maxwell's equations, demonstrating that there is a direct link with differential geometry and the cohomology theory in algebraic topology.

Two finite element formulations were presented: the $H$- and the $A$- formulations. These formulations are dual in multiple senses. First, the working variables are the magnetic field and the magnetic vector potential (the primitive of the electric field in time), respectively. Second, while in the $H$-formulation the vector field representing $\boldsymbol{h}$ is defined in conducting parts of the domain, in the $A$-formulation, a vector field representing $\boldsymbol{a}$ is defined in non-conducting parts of this domain (but also in the conducting subdomain in addition to $v$). Third, the coefficients of the cohomology basis representatives of the non-conducting domain are related to the total currents that flow in the cavities in the $H$-formulation. In contrast, the coefficients of the cohomology basis representatives of the conducting subdomains are related to the voltage between the terminals of these subdomains.

Each formulation has its own advantages and disadvantages. While the $H$-formulation requires cuts to obey Ampère's law in non-conducting regions when the scalar potential expresses the magnetic field, the $A$-formulation requires a gauge and the definition of the electric scalar potential. Moreover, in [43], the authors showed that the $A$-formulation would be preferable for treating problems involving nonlinear ferromagnetic materials, while the $H$-formulation was advantageous for modeling superconductors since they involves the nonlinear constitutive laws in inverse ways. Indeed, $H$-formulation has been widely used to model HTS devices [68–70]. Ideally, a *mixed* (or *coupled*) $H$-$A$-formulation would perfectly suit problems involving both nonlinear ferromagnetic and conductive materials, although this may lead to numerical stabilization problems [71–73].

There also exist derivations of the two dual formulations considering other scalar and vector potentials as working variables, such as formulations based on the *current vector potential* ($T$) [74], for example. Still, most of these formulations rely on the computational electromagnetics fundamentals presented in this chapter.

# CHAPTER 3 MODELING THIN REGIONS WITH THE FINITE-ELEMENT METHOD

## 3.1 Introduction

This chapter presents a critical literature review on modeling thin regions using the finite element method. It starts with the definition of the computational domain in problems involving such thin regions and their representation as reduced-dimension geometries (interfaces) in the computational domain. Next, the concept of surface current density is introduced. Two surface current densities are used to define interface conditions (ICs) which express the physics of the thin regions on the interfaces. Then, currently available finite element models in the literature are introduced. We conclude the chapter by discussing the equivalence of these models in terms of the ICs.

## 3.2 Domain specification

A region is denoted thin when it has a very small thickness ($d$) compared to its longitudinal and transversal dimensions, i.e. when it has a high aspect ratio (also sometimes called a *shell*). Establishing a conformal simplicial mesh for such thin regions using automatic mesh generators may lead to discrete systems of equations that are computationally expensive. It may include too many finite elements which increases the total number of DoFs and the computational burden, or finite elements with high aspect ratio that compromise the solution accuracy and the model convergence.

The classical way to overcome the problem of meshing thin regions is to represent them as reduced-dimension geometries in the computational domain. In this approximation, the thin volumes in 3-D (or surfaces in 2-D) are replaced by surfaces (or lines) situated halfway between their original wide faces (a zero-thickness or a reduced-dimension geometry $d \to 0$), and the physics of the thin region is taken into account by interface conditions (see definition in Section 2.2.6) on the geometry representing the shell.

An example of a 2-D standard domain and its equivalent with a line representing the thin region is shown in Fig. 3.1. Both domain representations include complementary subdomains $\Omega_c$ and $\Omega_c^C$, corresponding to those introduced in Section 2.2.4. In the standard 2-D domain (Fig. 3.1a), the shell volume is denoted as $\Omega_s$, with boundaries $\Gamma_s^{\pm}$, is part of the subdomain $\Omega_c$, which may also include other conductive thick structures. For coupling $\Omega_s$ and $\Omega_c^C$, the outward normal vectors seen from within these domains are of opposite signs.

We denote outward normal vectors in $\Gamma_s^{\pm}$ seen from $\Omega_c^C$ as $\boldsymbol{n}_\Gamma^{\pm}$, and those from $\Omega_s$ as $\boldsymbol{n}_s^{\pm}$, and we have $\boldsymbol{n}_s^{\pm} = \boldsymbol{n}_\Gamma^{\mp}$. In the reduced-dimension representation of the thin volume (Fig. 3.1b), an interface $\Gamma_s$ replaces $\Omega_s$. For convenience, the outward normal vector on $\Gamma_s$ is defined $\boldsymbol{n}_s = \boldsymbol{n}_s^+ = -\boldsymbol{n}_s^-$. The surface $\Gamma_s$ may have its geometrical entities (nodes, edges and faces) duplicated creating a crack in the computational domain ($\Gamma_s = \Gamma_s^+ \cup \Gamma_s^-$) or not ($\Gamma_s = \Gamma_s^+ = \Gamma_s^-$) depending on the model used to represent the physics inside the thin region and the chosen FE formulation (as we will see in Sections 3.6.2 and 3.6.3).

In this chapter, we will assume that the shell geometry can be defined in its own local coordinate system $xyz$ (Fig. 3.2). Its thickness $d$ (thinnest dimension) is in the $y$-direction, and its width and length are in the $xz$ plane. The surface $\Gamma_s$ is consequently in the plane $xz$ and the outward normal vector $\boldsymbol{n}_s$ points along the $y$-direction.

### 3.3 Surface current densities

To include the EM behavior of the thin region in FE simulations using the zero-thickness geometry, Ampère's and Faraday's laws, (2.5) and (2.6), respectively, are generally rewritten in their *symmetric form* [31] as

$$\nabla \times \boldsymbol{h} = \boldsymbol{j}_e, \tag{3.1}$$

$$\nabla \times \boldsymbol{e} = \boldsymbol{j}_h, \tag{3.2}$$

where $\boldsymbol{j}_e = \sigma \boldsymbol{e}$ is the *electric current density* and $\boldsymbol{j}_h = -\partial_t \mu \boldsymbol{h}$ is the *magnetic current density* (or *surface magnetic flux*). When $\Gamma_s$ replaces $\Omega_s$, a model needs to be introduced

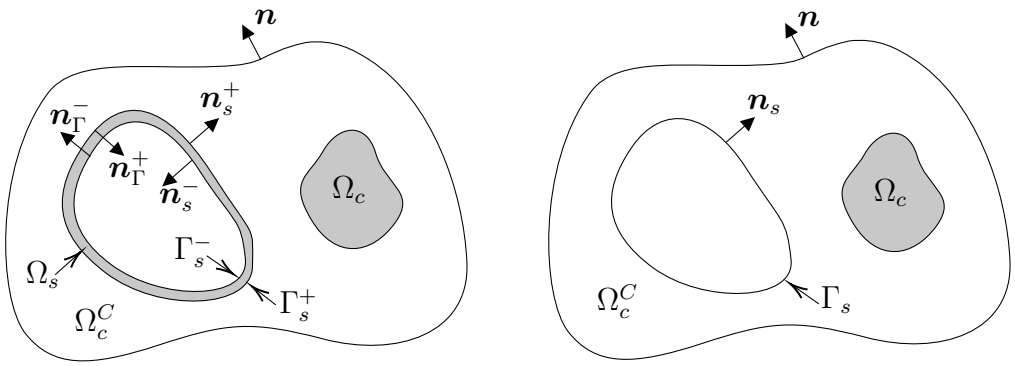


(a) Standard domain (b) Reduced-dimension representation

Figure 3.1 Standard 2-D domain and its equivalent with the thin region represented as a reduced-dimension geometry ($\Omega_s \to \Gamma_s$).

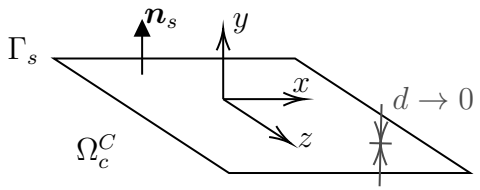


Figure 3.2 Local coordinate system $xyz$ for a single shell.

to approximate the current densities $\boldsymbol{j}_e$ and $\boldsymbol{j}_h$ inside $\Omega_s$ as *surface current densities* $\boldsymbol{k}_e$ and $\boldsymbol{k}_h$, respectively, defined only on $\Gamma_s$. The current densities $\boldsymbol{j}_e$ and $\boldsymbol{j}_h$ determine the surface current densities according to

$$\boldsymbol{k}_e = \int_{-d/2}^{d/2} \boldsymbol{j}_e \mathrm{d}y, \tag{3.3}$$

$$\boldsymbol{k}_h = \int_{-d/2}^{d/2} \boldsymbol{j}_h \mathrm{d}y, \tag{3.4}$$

where the integrals are computed analytically over the thickness of the thin region, i.e. $-d/2 \leq y \leq d/2$.

By applying the divergence theorem in (3.1) and (3.2), the discontinuities of the tangential components of the magnetic and the electric fields are associated with the surface current densities and can be expressed as follows

$$\boldsymbol{n}_s \times \left(\boldsymbol{h}^+ - \boldsymbol{h}^-\right) = \boldsymbol{n}_s \times (\boldsymbol{n}_s \times \boldsymbol{k}_e)\,, \tag{3.5}$$

$$\boldsymbol{n}_s \times \left(\boldsymbol{e}^+ - \boldsymbol{e}^-\right) = \boldsymbol{n}_s \times (\boldsymbol{n}_s \times \boldsymbol{k}_h)\,, \tag{3.6}$$

where $\boldsymbol{h}^\pm$ and $\boldsymbol{e}^\pm$ are the magnetic and electric fields on $\Gamma_s^\pm$, respectively. Expressions (3.5) and (3.6) represent two ICs, as defined in Section 2.2.6. Equation (3.5) relates $\boldsymbol{k}_e$ to a discontinuity of the tangential components of the magnetic field, and (3.6) relates $\boldsymbol{k}_h$ to a discontinuity of the tangential components of the electric field. These expressions are the basis of several approaches used to avoid meshing thin regions. These approaches are critically reviewed next.

### 3.4 Strip approximation

If the current densities $\boldsymbol{j}_e$ and $\boldsymbol{j}_h$ are assumed constant across the thickness of the thin structure, (3.3) and (3.4) become simply $\boldsymbol{k}_e = \boldsymbol{j}_e d$ and $\boldsymbol{k}_h = \boldsymbol{j}_h d$. Therefore, for prescribed values of $\boldsymbol{j}_e$ and $\boldsymbol{j}_h$, the ICs (3.5) and (3.6) can easily be established. In the so-called *strip* approximation [75–77], analytical solutions generally based on the Biot-Savart law define the

current density profiles along the wide dimensions of the thin region (i.e. in the $xz$ plane) and the field distribution in the surroundings.

In [78], the authors proposed a strip approximation based on FEM. They assumed that the properties of the conductors do not vary significantly along the thickness of superconducting tapes. The integral expressions for the current density inside the strip proposed in [76] were jointly solved with FEM system of equations. Basically, these expressions were used to define the surface current density $\boldsymbol{k}_e$ in a 2-D infinitely long representation of superconducting tapes. The current density $\boldsymbol{k}_h$ was implicitly assumed to be zero, which is a valid approximation for superconductors where $\mu \approx \mu_0$. Moreover, the total current flowing in the tape was obtained by integrating $\boldsymbol{k}_e$ over the tape width. The model showed good agreement with reference solutions obtained with standard FEM while avoiding meshing the thin tapes, leading to a reduction of the computational burden. However, only a single thin tape in 2-D was studied in this paper.

In [79], the problem of multiple interacting superconducting tapes was tackled. It was shown that at low transport current and small inter-tape separation, the strip approximation previously introduced in [78] underestimated the AC losses in tapes carrying anti-parallel currents. Indeed, since the surface current $\boldsymbol{k}_e$ is assumed constant across the thickness of the tapes, the tangential component of the magnetic field ($\boldsymbol{h}_t = \boldsymbol{n}_s \times \boldsymbol{h}$) is linear in $y$, in accordance with (3.5). Consequently, the strip approximation cannot completely represent the EM behavior of the superconducting tapes in such cases. Similar conclusions were presented in [80]. In that paper, the authors applied the strip approximation to model a conductor on round core cable (CORC), and observed that the AC losses are underestimated for short spiral pitches, which is in accordance with the conclusions of [79], since the effects of the inter-tape separation become more important in this configuration. The approximation was then extended to simulations involving both EM and thermal effects in HTS tapes in [81], but it is still limited for problems involving only a few HTS tapes.

More recently, a model based on the mixed $T$-$A$-formulation [35] was proposed to solve the current challenges in modeling superconducting tapes. We present this formulation in detail in Section 3.8. Before this, we introduce the concept of *shell elements* and the *Thin-Shell* (TS) approach in the time-harmonic regime (denoted here as the *classical* TS approach). We demonstrate that the strip approximation in FEM is, in fact, a particular realization of the TS approach.

### 3.5 Shell finite elements

Special finite elements were introduced in the early 90s to model narrow gaps [82], thin iron plates in electrical machines [83], and the perturbation of iron ships in the Earth's magnetic field [84]. They were denoted as shell elements in [33] and applied in time-invariant (*magnetostatic*) simulations using the magnetic scalar potential as the state variable. These elements were also classified as shell elements with and without potential jump, depending on the physics of the shell. In [85], the special finite elements were applied to simulate conducting sheets using the $A$-formulation in order to avoid defining discontinuities of the magnetic scalar potential in multiply connected domains, as discussed in Section 2.5.4.

In [86], the shell elements (called *degenerate finite elements*) were introduced for both scalar and vector fields. In [87], the authors applied more than one degenerate finite element to model the EM and thermal behavior of multilayered conductive composite materials in the time-harmonic regime. In [88], a degenerate prismatic element was applied in a mixed formulation in the time-transient regime in 3-D. Only one element was considered across the thickness of the conductor. The concept of degenerate finite elements was also used in many high-frequency analyses of thin sheets in [89, 90].

The basic idea behind the shell element approach is that volumic elements can be reduced to surface elements that allow discontinuities of the tangential components of the fields on $\Gamma_s$. For example, a prismatic finite element can be reduced to triangular surfaces representing its original wide faces. The volume integrals representing the physics inside the shell are transformed to surface integrals and the field penetration from the lateral faces of the elements (its edges in the $y$-direction) are neglected ($d \to 0$ in Fig. 3.2). In general, nodal and edge degenerate finite elements are derived considering *Lagrange first-order polynomials* to interpolate the scalar and vector field quantities across the thickness of the element. With these polynomials, the field profiles across the thickness of the thin region are linear, which is a good approximation in cases where the thickness of the sheet is sufficiently small with respect to penetration depth of the tangential fields in the shell.

Let us consider an example with the $H$-formulation applied to a 2-D infinitely long representation of the thin region, i.e. we assume that the fields are independent of $z$ (e.g. the length direction in Fig. 3.2). In the degenerate finite element approach, rectangular elements (in 2-D) can be represented as lines. The tangential component of $\boldsymbol{h}$ is thus assumed to be only in the $x$-direction ($\boldsymbol{h}_t = h_x \hat{\boldsymbol{\imath}}$). Therefore, the magnetic field strength inside a shell element is written

$$h_x(x, y, t) = h_x^+(x, t)\theta^+(y) + h_x^-(x, t)\theta^-(y) \tag{3.7}$$

where $h_x^{\pm}$ is the magnitude of its tangential component on $\Gamma_s^{\pm}$, respectively. The variation of the tangential field across the $y$-direction is taken into account by the functions $\theta^{\pm}(y)$ that are often defined as first-order Lagrange polynomials, i.e.

$$\theta^{+}(y) = \frac{d/2 - y}{d}, \qquad \theta^{-}(y) = \frac{y - d/2}{d}, \tag{3.8}$$

The strong form of the $H$-formulation for the problems in terms of $h_x$ is given by (2.48). Multiplying this form by a test functions $g$, and integrating it over the thickness of the thin region, we obtain

$$\int_{-d/2}^{d/2} \rho \frac{\partial h_x}{\partial y} \frac{\partial g}{\partial y} \mathrm{d}\Omega + \int_{-d/2}^{d/2} \mu \partial_t h_x g \mathrm{d}\Omega + e_z^{+} - e_z^{-} = 0, \tag{3.9}$$

where $e_z$ is the strength of the tangential component of $\boldsymbol{e}$, i.e. $\boldsymbol{e}_t = e_z \hat{\boldsymbol{k}}$.

Finally, for a single degenerate FE across $d$, from (3.9) and choosing (3.8) for $g$, we obtain a system of equations that can be expressed in the matrix form as

$$\begin{bmatrix} e_z^{+} \\ -e_z^{-} \end{bmatrix} = \frac{\partial_t \mu d}{6} \begin{bmatrix} 2 & 1 \\ 1 & 2 \end{bmatrix} \cdot \begin{bmatrix} h_x^{+} \\ h_x^{-} \end{bmatrix} + \frac{\rho}{d} \begin{bmatrix} 1 & -1 \\ -1 & 1 \end{bmatrix} \cdot \begin{bmatrix} h_x^{+} \\ h_x^{-} \end{bmatrix}, \tag{3.10}$$

which represents the relationship between the tangential components of the electric and the magnetic fields that can be used to define the ICs (3.5) and (3.6).

The shell element approach can easily be extended to the $A$-formulation. Since a single degenerate element is considered across the thickness of the thin region, these type of shell elements have the same limitations as the strip approximation. The fields $\boldsymbol{h}_t$ and $\boldsymbol{e}_t$ have a linear profile across $d$, defined by (3.8), and the surface current densities $\boldsymbol{k}_e$ and $\boldsymbol{k}_h$ are constant in each degenerate element. The main advantage is that the degenerate element approach allows discontinuities of $\boldsymbol{h}_t$ and $\boldsymbol{e}_t$, and both the electric and magnetic effects inside the shell can then be taken into account simultaneously.

### 3.6 The classical thin-shell approach

In [32], the shell elements were generalized as ICs for the static, high frequency and induced-currents problems. An analytical solution involving hyperbolic trigonometric functions to a 1-D problem across $d$ was used to define these ICs. The shell elements were then extended to magnetodynamic problems in harmonic regime and used to compute induced currents in thin conducting shells with strong skin effect in [91]. In [31], the ICs where treated as

impedance-type BCs (or IBCs) for 3-D magnetodynamic problems involving both conducting and magnetic shells, with the magnetic scalar potential as state variable. In that paper, the general form of the ICs were obtained from the solution of a planar wave problem, equivalent to the development of *surface impedance boundary conditions* (SIBCs) proposed in [92]. These impedance-type BCs are the core of the classical TS aproach.

The impedance-type BCs were further used in the $A$-formulation to solve problems involving thin magnetic shields in [93, 94], while similar work was done in [34] using a mixed $A$-$\phi$-formulation. In [95], the general form of the ICs in the classical TS approach were extended to the dual formulations that we presented in Section 2.6. The problem of multilayered screens in time-harmonic regime was tackled in [8]. Nowadays, the TS approach with impedance-type BCs is still widely applied in time-harmonic simulations [96].

In order to better understand the fundamentals of the classical TS approach and explore its limitations, we briefly introduce its main equations in this section. Time-dependent extensions of this approach will be discussed in Section 3.7. As opposed to the strip approximation, in the classical TS approach, the time-harmonic response of the fields quantities across the thickness of the thin structure are used to defined the ICs (3.5) and (3.6). The surface current densities $\boldsymbol{k}_e$ and $\boldsymbol{k}_h$ are locally defined from the analytical solution to a 1-D linear flux diffusion problem defined across the $y$-direction (the shell thickness). This approach permits the tangential components of the fields to completely penetrate the reduced-dimension geometry and is accuracy also in cases where this penetration is smaller than $d$.

### 3.6.1 Interface conditions in the thin-shell approach

In order to include the physics across the thickness of the thin region using the classical TS approach, we shall express $\boldsymbol{k}_e$ and $\boldsymbol{k}_h$ in terms of the behavior of the electric and magnetic fields across the $y$-direction. For this purpose, we solve auxiliary 1-D local problems purely in terms of these field quantities. We will use the geometry described in Section 3.2 with local coordinate system defined as in Fig. 3.2. The tangential components of the magnetic and electric field, denoted $\boldsymbol{h}_t^{\pm}$ and $\boldsymbol{e}_t^{\pm}$, respectively, on $\Gamma_s^{\pm}$, are in the plane $xz$. The normal components of the fields are in the $y$-direction. The 1-D problem can thus be formulated only in terms of the tangential component of the magnetic or the electric field. The penetration of these fields through the thin lateral surfaces of the shell are neglected, but not their normal components along the width of the thin region. In Section 3.6.4, we will discuss the behavior of the normal components of the fields in the classical TS approach.

**1-D problem in terms of the magnetic field**

The governing equation for a 1-D problem defined in terms of $\bar{\boldsymbol{h}}_t$ in the time-harmonic regime (using the phasor notation introduced in Section 2.2.2) is obtained from the strong form of the Faraday and Ampère's laws (2.6) and (2.5), respectively, and reads

$$\partial_y^2 \bar{\boldsymbol{h}}_t + \jmath\omega\sigma\mu\bar{\boldsymbol{h}}_t = 0. \tag{3.11}$$

Moreover, two BCs associated with $y = \pm d/2$ are defined as

$$\bar{\boldsymbol{h}}_t\Big|_{d/2} = \bar{\boldsymbol{h}}_t^+, \tag{3.12}$$

$$\bar{\boldsymbol{h}}_t\Big|_{-d/2} = \bar{\boldsymbol{h}}_t^-, \tag{3.13}$$

where $\bar{\boldsymbol{h}}_t^{\pm}$ are known local values of $\bar{\boldsymbol{h}}_t$ on $\Gamma_s^{\pm}$.

The distribution of $\boldsymbol{h}_t$ across $d$ is obtained analytically from (3.11), (3.12) and (3.13), and reads [46]

$$\bar{\boldsymbol{h}}_t = \frac{1}{\sinh(\vec{a}d)}\left[\bar{\boldsymbol{h}}_t^+ \sinh\left(\frac{\vec{a}d}{2} + \vec{a}y\right) + \bar{\boldsymbol{h}}_t^- \sinh\left(\frac{\vec{a}d}{2} - \vec{a}y\right)\right], \tag{3.14}$$

where $\vec{a} = (1+\jmath)/\delta$ and

$$\delta = \sqrt{\frac{2}{\mu\sigma\omega}}, \tag{3.15}$$

is the *penetration depth*. From (3.14), we compute the local magnetic surface current density (3.4) as

$$\begin{aligned}
\bar{\boldsymbol{k}}_h &= \int_{-d/2}^{d/2} -\jmath\omega\mu\bar{\boldsymbol{h}}_t \mathrm{d}y \\
&= \int_{-d/2}^{d/2} -\jmath\omega\mu\frac{1}{\sinh(\vec{a}d)}\left[\bar{\boldsymbol{h}}_t^+ \sinh\left(\frac{\vec{a}d}{2} + \vec{a}y\right) + \bar{\boldsymbol{h}}_t^- \sinh\left(\frac{\vec{a}d}{2} - \vec{a}y\right)\right] \mathrm{d}y \\
&= -\frac{\jmath\omega\mu}{\vec{a}}\tanh\left(\frac{\vec{a}d}{2}\right)\left(\bar{\boldsymbol{h}}_t^+ + \bar{\boldsymbol{h}}_t^-\right).
\end{aligned} \tag{3.16}$$

Then, defining $\vec{\eta}_h = -\frac{\jmath\omega\mu}{\vec{a}}\tanh\left(\frac{\vec{a}d}{2}\right)$, the IC (3.6) can be rewritten as

$$\bar{\boldsymbol{e}}_t^+ - \bar{\boldsymbol{e}}_t^- = \vec{\eta}_h\left(\bar{\boldsymbol{h}}_t^+ + \bar{\boldsymbol{h}}_t^-\right), \tag{3.17}$$

which connects the discontinuities of $\bar{\boldsymbol{e}}_t$ to the mean value of $\bar{\boldsymbol{h}}_t$ with coefficient $\vec{\eta}_h$, representing therefore the surface current density $\bar{\boldsymbol{k}}_h$.

Now, if we consider $\bar{\boldsymbol{j}}_e = \partial_y \bar{\boldsymbol{h}}_t$, from (3.14), we have

$$\bar{\boldsymbol{j}}_e = \frac{\vec{a}}{\sinh(\vec{a}d)} \left[ \bar{\boldsymbol{h}}_t^+ \cosh\left(\frac{\vec{a}d}{2} + \vec{a}y\right) - \bar{\boldsymbol{h}}_t^- \cosh\left(\frac{\vec{a}d}{2} - \vec{a}y\right) \right], \tag{3.18}$$

and, from (3.3), the electric surface current density is

$$\begin{aligned} \bar{\boldsymbol{k}}_e &= \int_{-d/2}^{d/2} \bar{\boldsymbol{j}}_e \mathrm{d}y \\ &= \int_{-d/2}^{d/2} \frac{\vec{a}}{\sinh(\vec{a}d)} \left[ \bar{\boldsymbol{h}}_t^+ \cosh\left(\frac{\vec{a}d}{2} + \vec{a}y\right) - \bar{\boldsymbol{h}}_t^- \cosh\left(\frac{\vec{a}d}{2} - \vec{a}y\right) \right] \mathrm{d}y \\ &= \bar{\boldsymbol{h}}_t^+ - \bar{\boldsymbol{h}}_t^-, \end{aligned} \tag{3.19}$$

which satisfies (3.5).

Expression (3.17) is the first ICs that we were looking for. The coefficient $\vec{\eta}_h$ depends essentially on the permeability of the thin region and can certainly describe the interior behavior of the field quantities in cases involving ferromagnetic materials. We shall next find an equivalent expression for (3.5).

### 1-D problem in terms of the electric field

The governing equation for a 1-D problem defined in terms of $\bar{\boldsymbol{e}}_t$ in the time-harmonic regime is obtained from the strong form of the Faraday and Ampère's laws (2.6) and (2.5), respectively, and is written as

$$\partial_y^2 \bar{\boldsymbol{e}}_t + \jmath\omega\sigma\mu\bar{\boldsymbol{e}}_t = 0. \tag{3.20}$$

Moreover, two BCs associated with $y = \pm d/2$ are defined as

$$\bar{\boldsymbol{e}}_t\Big|_{d/2} = \bar{\boldsymbol{e}}_t^+, \tag{3.21}$$

$$\bar{\boldsymbol{e}}_t\Big|_{-d/2} = \bar{\boldsymbol{e}}_t^-, \tag{3.22}$$

where $\bar{\boldsymbol{e}}_t^{\pm}$ are known local values of $\bar{\boldsymbol{e}}_t$ on $\Gamma_s^{\pm}$.

The distribution of $\bar{\boldsymbol{e}}_t$ across $d$ is obtained analytically from (3.20), with (3.21) and (3.22), and reads

$$\bar{\boldsymbol{e}}_t = \frac{1}{\sinh(\vec{a}d)} \left[ \bar{\boldsymbol{e}}_t^+ \sinh\left(\frac{\vec{a}d}{2} + \vec{a}y\right) + \bar{\boldsymbol{e}}_t^- \sinh\left(\frac{\vec{a}d}{2} - \vec{a}y\right) \right]. \tag{3.23}$$

From (3.23), we can compute the local electric surface current density (3.3) as

$$\begin{aligned}\bar{\boldsymbol{k}}_e &= \int_{-d/2}^{d/2} \sigma \bar{\boldsymbol{e}}_t \mathrm{d}y \\ &= \int_{-d/2}^{d/2} \sigma \frac{1}{\sinh(\vec{a}d)} \left[\bar{\boldsymbol{e}}_t^+ \sinh\left(\frac{\vec{a}d}{2} + \vec{a}y\right) + \bar{\boldsymbol{e}}_t^- \sinh\left(\frac{\vec{a}d}{2} - \vec{a}y\right)\right] \mathrm{d}y \\ &= \frac{\sigma}{\vec{a}} \tanh\left(\frac{\vec{a}d}{2}\right)\left(\bar{\boldsymbol{e}}_t^+ + \bar{\boldsymbol{e}}_t^-\right).\end{aligned} \tag{3.24}$$

Then, defining $\vec{\eta}_e = \frac{\sigma}{\vec{a}} \tanh\left(\frac{\vec{a}d}{2}\right)$, the IC (3.5) can be rewritten as

$$\bar{\boldsymbol{h}}_t^+ - \bar{\boldsymbol{h}}_t^- = \vec{\eta}_e \left(\bar{\boldsymbol{e}}_t^+ + \bar{\boldsymbol{e}}_t^-\right), \tag{3.25}$$

which connects the discontinuities of $\bar{\boldsymbol{h}}_t$ to the mean value of $\bar{\boldsymbol{e}}_t$ with coefficient $\vec{\eta}_e$ representing the surface current density $\bar{\boldsymbol{k}}_e$.

With $\bar{\boldsymbol{j}}_h = \partial_y \bar{\boldsymbol{e}}_t$, from (3.23), we have

$$\bar{\boldsymbol{j}}_h = \frac{\vec{a}}{\sinh(\vec{a}d)} \left[\bar{\boldsymbol{e}}_t^+ \cosh\left(\frac{\vec{a}d}{2} + \vec{a}y\right) - \bar{\boldsymbol{e}}_t^- \cosh\left(\frac{\vec{a}d}{2} - \vec{a}y\right)\right], \tag{3.26}$$

and, from (3.4), the magnetic surface current density is

$$\begin{aligned}\bar{\boldsymbol{k}}_h &= \int_{-d/2}^{d/2} \bar{\boldsymbol{j}}_h \mathrm{d}y \\ &= \int_{-d/2}^{d/2} \frac{\vec{a}}{\sinh(\vec{a}d)} \left[\bar{\boldsymbol{e}}_t^+ \cosh\left(\frac{\vec{a}d}{2} + \vec{a}y\right) - \bar{\boldsymbol{e}}_t^- \cosh\left(\frac{\vec{a}d}{2} - \vec{a}y\right)\right] \mathrm{d}y \\ &= \bar{\boldsymbol{e}}_t^+ - \bar{\boldsymbol{e}}_t^-,\end{aligned} \tag{3.27}$$

which satisfies (3.6).

Finally, expressions (3.17) and (3.25) are the ICs of the classical TS approach [95]. The coefficient $\vec{\eta}_e$ in (3.25) depends essentially on the conductivity of the thin region and can describe the interior behavior of the field quantities in cases involving thin conducting materials.

The effects of the ICs in the TS approach are more or less pronounced depending on the materials parameters in the thin region. For example, considering a purely conductive shell at low frequency, by satisfying the ICs (3.25) and (3.6) with $\boldsymbol{k}_h = 0$, we obtain an accurate solution to problems involving thin conductive subdomains (and equivalent to the strip approximation if $\delta \gg d$). Dually, with the ICs (3.17) and (3.5) with $\boldsymbol{k}_e = 0$, we obtain

an accurate approximation for the EM behavior of ferromagnetic shells. Applying these combinations of ICs in the TS approach gives expressions for the fields equal to those found with the special elements without potential jumps as defined in [33]. However, satisfying simultaneously the ICs (3.25) and (3.17) allows the TS model to be applied to a wider range of problems (problems with and without potential or tangential fields jumps). The coupling of these ICs in the weak form of the $H$- and $A$- formulations is detailed next.

### 3.6.2 Thin-shell approach in the $H$-formulation

The weak form of the $H$-formulation, including additional integral terms over $\Gamma_s^{\pm}$, is obtained by multiplying (2.48) by a test function $\boldsymbol{g}$, integrating it over the domain $\Omega$ (described in Section 3.2), and applying Green's second identity (2.47). The weak form of the $H$-formulation in the time-harmonic regime is

Find $\boldsymbol{h} \in \boldsymbol{H}_h(\mathbf{curl}, \Omega)$ such that

$$\begin{aligned}\left(\rho\nabla\times\bar{\boldsymbol{h}}, \nabla\times\boldsymbol{g}\right)_{\Omega} + \jmath\omega\left(\mu\bar{\boldsymbol{h}}, \boldsymbol{g}\right)_{\Omega} + \left\langle \boldsymbol{n}\times\bar{\boldsymbol{e}}, \boldsymbol{g}\right\rangle_{\Gamma_e} \\ + \left\langle \boldsymbol{n}_s\times\bar{\boldsymbol{e}}, \boldsymbol{g}\right\rangle_{\Gamma_s^+} - \left\langle \boldsymbol{n}_s\times\bar{\boldsymbol{e}}, \boldsymbol{g}\right\rangle_{\Gamma_s^-} = 0\end{aligned} \tag{3.28}$$

$\forall\ \boldsymbol{g} \in \boldsymbol{H}_h^0(\mathbf{curl}, \Omega)$.

The two last terms in (3.28) represent discontinuities of the electric field across $\Gamma_s$. Without discontinuities of $\boldsymbol{h}_t$ and $\boldsymbol{e}_t$, (3.28) becomes equal to (2.49), i.e. it becomes equivalent to the standard $H$-formulation, and the thin interfaces are disregarded.

From (3.17) and (3.25), we obtain

$$\bar{\boldsymbol{e}}_t^+ = \frac{1}{2}\left[\bar{\boldsymbol{h}}_t^+\left(\frac{1}{\vec{\eta}_e} + \vec{\eta}_h\right) - \bar{\boldsymbol{h}}_t^-\left(\frac{1}{\vec{\eta}_e} - \vec{\eta}_h\right)\right], \tag{3.29}$$

$$\bar{\boldsymbol{e}}_t^- = \frac{1}{2}\left[\bar{\boldsymbol{h}}_t^+\left(\frac{1}{\vec{\eta}_e} - \vec{\eta}_h\right) - \bar{\boldsymbol{h}}_t^-\left(\frac{1}{\vec{\eta}_e} + \vec{\eta}_h\right)\right]. \tag{3.30}$$

To include the thin region physics, the interface terms in (3.28) are then written

$$\begin{aligned}\left\langle \boldsymbol{n}_s\times\bar{\boldsymbol{e}}, \boldsymbol{g}\right\rangle_{\Gamma_s^+} - \left\langle \boldsymbol{n}_s\times\bar{\boldsymbol{e}}, \boldsymbol{g}\right\rangle_{\Gamma_s^-} &= \left\langle \frac{1}{2}\left[\bar{\boldsymbol{h}}_t^+\left(\frac{1}{\vec{\eta}_e} + \vec{\eta}_h\right) - \bar{\boldsymbol{h}}_t^-\left(\frac{1}{\vec{\eta}_e} - \vec{\eta}_h\right)\right], \boldsymbol{g}\right\rangle_{\Gamma_s} \\ &\quad - \left\langle \frac{1}{2}\left[\bar{\boldsymbol{h}}_t^+\left(\frac{1}{\vec{\eta}_e} - \vec{\eta}_h\right) - \bar{\boldsymbol{h}}_t^-\left(\frac{1}{\vec{\eta}_e} + \vec{\eta}_h\right)\right], \boldsymbol{g}\right\rangle_{\Gamma_s}.\end{aligned} \tag{3.31}$$

The standard $H$-formulation permits discontinuities of $\bar{\boldsymbol{e}}_t$, but not discontinuities of $\bar{\boldsymbol{h}}_t$, since

the continuity of $\bar{\boldsymbol{h}}_t$ is implicit imposed (e.g. by the use of the Whitney 1-form (2.8.8)). Therefore, the implementation of a TS model that includes (3.31) requires the duplication of the DoFs on the surface $\Gamma_s$. It can be done by geometrically duplicating the interface $\Gamma_s$, thereby creating a cracked region $\Gamma_s = \Gamma_s^+ \cup \Gamma_s^-$, or by decomposing $\boldsymbol{h}_t$ into its continuous and discontinuous components across $\Gamma_s$ ( denoted by $\bar{\boldsymbol{h}}_{tc}$ and $\bar{\boldsymbol{h}}_{td}$, respectively), i.e. $\bar{\boldsymbol{h}}_t = \bar{\boldsymbol{h}}_{tc} + \bar{\boldsymbol{h}}_{td}$ [95]. Both approaches result in the same number of variables and exactly the same solution. The advantage of decomposing the $\boldsymbol{h}_t$ is that the surface $\Gamma_s$ does not need to be geometrically duplicated and the domain remains simply connected. The discontinuous component of $\bar{\boldsymbol{h}}_t$ ($\bar{\boldsymbol{h}}_{td}$) has support limited to a layer of finite elements (a *transition layer*) related to one side of $\Gamma_s$ [95]. However, the duplication of the interface $\Gamma_s$ and the introduction of cuts in a $H$-$\phi$-formulation, for example, may allow imposing a current in the shell, as we will see later in this thesis.

Considering the ICs (3.17) and (3.5) with $\boldsymbol{k}_e = 0$ in the $H$-formulation allows simulating ferromagnetic thin structures without a discontinuity of $\boldsymbol{h}_t$, and for a prescribed $\boldsymbol{k}_h$ in the shell. In this case, the weak form of the $H$-formulation is simplified to

Find $\boldsymbol{h} \in \boldsymbol{H}_h(\mathbf{curl}, \Omega)$ such that

$$\begin{aligned}\Big(\rho\nabla\times\bar{\boldsymbol{h}}, \nabla\times\boldsymbol{g}\Big)_\Omega + \jmath\omega\Big(\mu\bar{\boldsymbol{h}}, \boldsymbol{g}\Big)_\Omega + \Big\langle \boldsymbol{n}\times\bar{\boldsymbol{e}}, \boldsymbol{g}\Big\rangle_{\Gamma_e} \\ + \Big\langle \boldsymbol{n}_s \times \left(\bar{\boldsymbol{e}}_t^+ - \bar{\boldsymbol{e}}_t^-\right), \boldsymbol{g}\Big\rangle_{\Gamma_s} = 0\end{aligned} \tag{3.32}$$

$\forall\ \boldsymbol{g} \in \boldsymbol{H}_h^0(\mathbf{curl}, \Omega)$. In this configuration, the TS approach is equivalent to the strip approximation for ferromagnetic thin regions (in the time-harmonic regime and with $\delta \gg d$) and to the degenerate element approach (also with $\delta \gg d$). Note that the discontinuity of $\bar{\boldsymbol{e}}_t$ that appears in the last term of (3.32) can be used to directly impose a prescribed $\bar{\boldsymbol{k}}_h$, according to (3.6).

### 3.6.3 Thin-shell approach in the $A$-formulation

As with the $H$-formulation, the weak form of the $A$-formulation, including additional integral terms over $\Gamma_s^\pm$, is obtained by multiplying (2.64) by a test function $\boldsymbol{g}$, integrating it over the domain $\Omega$ (described in Section 3.2), and applying Green's second identity (2.47). The weak form of the $A$-formulation in the time-harmonic regime is

Find $\bar{\boldsymbol{a}} \in \boldsymbol{H}_e(\mathbf{curl}, \Omega)$ such that

$$\begin{aligned}\left(1/\mu \nabla \times \bar{\boldsymbol{a}}, \nabla \times \boldsymbol{g}\right)_{\Omega} + \left(\sigma \jmath \omega \bar{\boldsymbol{a}}, \boldsymbol{g}\right)_{\Omega} + \left\langle \boldsymbol{n} \times \bar{\boldsymbol{h}}, \boldsymbol{g} \right\rangle_{\Gamma_h} \\ + \left\langle \boldsymbol{n}_s \times \bar{\boldsymbol{h}}, \boldsymbol{g} \right\rangle_{\Gamma_s^+} - \left\langle \boldsymbol{n}_s \times \bar{\boldsymbol{h}}, \boldsymbol{g} \right\rangle_{\Gamma_s^-} = 0,\end{aligned} \tag{3.33}$$

$\forall\ \boldsymbol{g} \in \boldsymbol{H}_e^0(\mathbf{curl}, \Omega)$.

The two last terms in (3.33) represent the discontinuity of the magnetic field across $d$. Without discontinuities of $\boldsymbol{h}_t$ and $\boldsymbol{e}_t$, (3.33) becomes equal to (2.65), i.e. the standard $A$-formulation. Note that the presented implementation can also be extended to the $A$-$V$-formulation.

From (3.17) and (3.25), we obtain

$$\bar{\boldsymbol{h}}_t^+ = \frac{1}{2}\left[\bar{\boldsymbol{e}}_t^+ \left(\frac{1}{\vec{\eta}_h} + \vec{\eta}_e\right) - \bar{\boldsymbol{e}}_t^- \left(\frac{1}{\vec{\eta}_h} - \vec{\eta}_e\right)\right], \tag{3.34}$$

$$\bar{\boldsymbol{h}}_t^- = \frac{1}{2}\left[\bar{\boldsymbol{e}}_t^+ \left(\frac{1}{\vec{\eta}_h} - \vec{\eta}_e\right) - \bar{\boldsymbol{e}}_t^- \left(\frac{1}{\vec{\eta}_h} + \vec{\eta}_e\right)\right]. \tag{3.35}$$

To include the thin region physics, the interface terms in (3.33) are then written

$$\begin{aligned}\left\langle \boldsymbol{n}_s \times \bar{\boldsymbol{h}}, \boldsymbol{g} \right\rangle_{\Gamma_s^+} - \left\langle \boldsymbol{n}_s \times \bar{\boldsymbol{h}}, \boldsymbol{g} \right\rangle_{\Gamma_s^-} = \left\langle \frac{1}{2}\left[\bar{\boldsymbol{e}}_t^+ \left(\frac{1}{\vec{\eta}_h} + \vec{\eta}_e\right) - \bar{\boldsymbol{e}}_t^- \left(\frac{1}{\vec{\eta}_h} - \vec{\eta}_e\right)\right], \boldsymbol{g} \right\rangle_{\Gamma_s} \\ - \left\langle \frac{1}{2}\left[\bar{\boldsymbol{e}}_t^+ \left(\frac{1}{\vec{\eta}_h} - \vec{\eta}_e\right) - \bar{\boldsymbol{e}}_t^- \left(\frac{1}{\vec{\eta}_h} + \vec{\eta}_e\right)\right], \boldsymbol{g} \right\rangle_{\Gamma_s},\end{aligned} \tag{3.36}$$

which is dual to the interface terms of the $H$-formulation given by (3.31). As with the $H$-formulation, the magnetic vector potential can also be decomposed into its continuous and discontinuous components across $\Gamma_s$ to avoid a multiply connected domain. Moreover, since $\bar{\boldsymbol{a}}$ is the primitive in time of $\bar{\boldsymbol{e}}$, the interface terms can be expressed purely in terms of the tangential components of $\bar{\boldsymbol{a}}$ ($\bar{\boldsymbol{a}}_t^{\pm}$).

Considering the ICs (3.25) and (3.6) with $\boldsymbol{k}_h = 0$ in the $A$-formulation, we can model thin regions without a discontinuity of $\bar{\boldsymbol{e}}_t$ but with a prescribed $\bar{\boldsymbol{k}}_e$ in the shell. The weak form of the $A$-formulation is simplified to

Find $\bar{\boldsymbol{a}} \in \boldsymbol{H}_e(\mathbf{curl}, \Omega)$ such that

$$\begin{aligned}\left(\nu \nabla \times \bar{\boldsymbol{a}}, \nabla \times \boldsymbol{g}\right)_{\Omega} + \left(\sigma \jmath \omega \bar{\boldsymbol{a}}, \boldsymbol{g}\right)_{\Omega} + \left\langle \boldsymbol{n} \times \bar{\boldsymbol{h}}, \boldsymbol{g} \right\rangle_{\Gamma_h} \\ + \left\langle \boldsymbol{n}_s \times \left(\bar{\boldsymbol{h}}_t^{+} - \bar{\boldsymbol{h}}_t^{-}\right), \boldsymbol{g} \right\rangle_{\Gamma_s} = 0,\end{aligned} \tag{3.37}$$

$\forall\ \boldsymbol{g} \in \boldsymbol{H}_e^0(\mathbf{curl}, \Omega)$. Again, the TS approach becomes equivalent to the strip approximation in the $A$-formulation under in the time-harmonic regime and assuming $\delta \gg d$.

### 3.6.4 Normal components for the fields

So far, we presented the shell elements and the classical TS approach essentially in terms of the tangential components of both the magnetic and electric fields, as well as its implementation in the $H$- and $A$- formulations. In this section, we propose a discussion concerning the normal components of these field quantities in the classical TS approach.

Recalling that the local geometry of the shell in 3-D where the plane $xz$ is parallel to the thin surface and the $y$ axis is in its normal direction (Fig. 3.2), the magnetic field can be expressed in terms of its own components as $\bar{\boldsymbol{h}} = \bar{h_x}\hat{\boldsymbol{\imath}} + \bar{h_y}\hat{\boldsymbol{\jmath}} + \bar{h_z}\hat{\boldsymbol{k}}$. So, its tangential component reads $\bar{\boldsymbol{h}}_t = \bar{h_x}\hat{\boldsymbol{\imath}} + \bar{h_z}\hat{\boldsymbol{k}}$. Similarly, the electric field is expressed in terms of its own components as $\bar{\boldsymbol{e}} = \bar{e}_x\hat{\boldsymbol{\imath}} + \bar{e}_y\hat{\boldsymbol{\jmath}} + \bar{e}_z\hat{\boldsymbol{k}}$, and its tangential component is $\bar{\boldsymbol{e}}_t = \bar{e}_x\hat{\boldsymbol{\imath}} + \bar{e}_z\hat{\boldsymbol{k}}$.

From Faraday's law (2.6), we can write

$$\partial_z \bar{e}_x^{\pm} - \partial_x \bar{e}_z^{\pm} = -\jmath\omega\mu\bar{h}_y^{\pm}. \tag{3.38}$$

Moreover, from (3.17) and (3.25), we have

$$\bar{e}_z^{+} + \bar{e}_z^{-} = \frac{1}{\vec{\eta}_e}\left(\bar{h}_x^{+} - \bar{h}_x^{-}\right), \tag{3.39}$$

$$\bar{e}_x^{+} + \bar{e}_x^{-} = -\frac{1}{\vec{\eta}_e}\left(\bar{h}_z^{+} - \bar{h}_z^{-}\right), \tag{3.40}$$

$$\bar{e}_x^{+} - \bar{e}_x^{-} = \vec{\eta}_h\left(\bar{h}_z^{+} + \bar{h}_z^{-}\right), \tag{3.41}$$

$$\bar{e}_z^{+} - \bar{e}_z^{-} = -\vec{\eta}_h\left(\bar{h}_x^{+} + \bar{h}_x^{-}\right). \tag{3.42}$$

Substituting (3.39) and (3.40) in (3.38) we find

$$\partial_z\left(-\frac{1}{\vec{\eta}_e}\left(\bar{h}_z^{+} - \bar{h}_z^{-}\right)\right) - \partial_x\left(\frac{1}{\vec{\eta}_e}\left(\bar{h}_x^{+} - \bar{h}_x^{-}\right)\right) = -\jmath\omega\mu\left(\bar{h}_y^{+} + \bar{h}_y^{-}\right), \tag{3.43}$$

and with (3.41) and (3.42) in (3.38),

$$\partial_z\left(\vec{\eta}_h\left(\bar{h}_z^+ + \bar{h}_z^-\right)\right) + \partial_x\left(\vec{\eta}_h\left(\bar{h}_x^+ + \bar{h}_x^-\right)\right) = -\jmath\omega\mu\left(\bar{h}_y^+ - \bar{h}_y^-\right). \tag{3.44}$$

Besides, the divergence of a vector field $\boldsymbol{u}$ on a surface $S$, in terms of the coordinates $x$ and $z$, can be defined as

$$\mathrm{div}_s\boldsymbol{u} = \partial_x u_x + \partial_z u_z, \tag{3.45}$$

where $u_x$ and $u_z$ are the corresponding components of $\boldsymbol{u}$ [36]. Therefore, the ICs (3.43) and (3.44) can be respectively represented as

$$-\frac{1}{\vec{\eta}_e}\mathrm{div}_s\left(\bar{\boldsymbol{h}}_t^+ - \bar{\boldsymbol{h}}_t^-\right) = -\jmath\omega\mu\left(\bar{\boldsymbol{h}}_n^+ + \bar{\boldsymbol{h}}_n^-\right), \tag{3.46}$$

$$\vec{\eta}_h\mathrm{div}_s\left(\bar{\boldsymbol{h}}_t^+ + \bar{\boldsymbol{h}}_t^-\right) = -\jmath\omega\mu\left(\bar{\boldsymbol{h}}_n^+ - \bar{\boldsymbol{h}}_n^-\right). \tag{3.47}$$

Expressions (3.46) and (3.47) connect the normal and tangential components of the magnetic field on both sides of the thin region. They are called the *H-representation* of the ICs (3.17) and (3.25) [32]. Since both ICs are taken into account in the classical TS approach, we conclude that the normal components of the magnetic field are implicitly taken into account in this approach.

The ICs in the classical TS approach can also be expressed in terms of only the electric field components. Using Ampere's law as

$$\partial_z\bar{h}_x^\pm - \partial_x\bar{h}_z^\pm = \sigma\bar{e}_y^\pm, \tag{3.48}$$

and substituting (3.39) and (3.40) into it, we obtain

$$\partial_z\left(\vec{\eta}_e\left(\bar{e}_z^+ + \bar{e}_z^-\right)\right) + \partial_x\left(\vec{\eta}_e\left(\bar{e}_x^+ + \bar{e}_x^-\right)\right) = \sigma\left(\bar{e}_y^+ - \bar{e}_y^-\right). \tag{3.49}$$

Moreover, with (3.41) and (3.42) in (3.38) we have

$$\partial_z\left(-\frac{1}{\vec{\eta}_h}\left(\bar{e}_z^+ - \bar{e}_z^-\right)\right) - \partial_x\left(\frac{1}{\vec{\eta}_h}\left(\bar{e}_x^+ - \bar{e}_x^-\right)\right) = \sigma\left(\bar{e}_y^+ + \bar{e}_y^-\right). \tag{3.50}$$

The ICs in terms of $\bar{\boldsymbol{e}}_t$ and $\bar{\boldsymbol{e}}_n$ are

$$\vec{\eta}_e\mathrm{div}_s\left(\bar{\boldsymbol{e}}_t^+ - \bar{\boldsymbol{e}}_t^-\right) = \sigma\left(\bar{\boldsymbol{e}}_n^+ + \bar{\boldsymbol{e}}_n^-\right), \tag{3.51}$$

$$-\frac{1}{\vec{\eta}_h}\mathrm{div}_s\left(\bar{\boldsymbol{e}}_t^+ + \bar{\boldsymbol{e}}_t^-\right) = \sigma\left(\bar{\boldsymbol{e}}_n^+ - \bar{\boldsymbol{e}}_n^-\right), \tag{3.52}$$

which are called the *E-representation* of the ICs (3.17) and (3.25). Expressions (3.51) and (3.52) connect the normal and tangential components of the electric field. Note that we can extend this definition and find an *A-representation* of the ICs (3.17) and (3.25). We conclude that the normal components of $\bar{\boldsymbol{e}}$ (or $\bar{\boldsymbol{a}}$) are also implicitly taken into account in the classical TS approach.

### 3.6.5 Thin regions with strong penetration depth

When the skin depth (3.15) is much larger than the thickness of the thin region ($\delta \gg d$), the coefficients in the ICs (3.17) and (3.25) with the form $1/a \tanh(ad/2)$ can be approximated by $d/2$. Therefore, these ICs become

$$\frac{\bar{\boldsymbol{e}}_t^+ - \bar{\boldsymbol{e}}_t^-}{d} = -\jmath\omega\mu \frac{\left(\bar{\boldsymbol{h}}_t^+ + \bar{\boldsymbol{h}}_t^-\right)}{2}, \tag{3.53}$$

$$\frac{\bar{\boldsymbol{h}}_t^+ - \bar{\boldsymbol{h}}_t^-}{d} = \sigma d \frac{\left(\bar{\boldsymbol{e}}_t^+ + \bar{\boldsymbol{e}}_t^-\right)}{2}, \tag{3.54}$$

respectively. This relationship between $\bar{\boldsymbol{e}}_t^{\pm}$ and $\bar{\boldsymbol{h}}_t^{\pm}$ can also be represented in their matrix form, which is therefore equivalent to (3.10) with $\delta \gg d$. It demonstrates again that the classical TS approach with $\delta \gg d$ and the use of degenerate finite elements (in time-harmonic regime) are equivalent approaches.

It can also be seen at this point that the IC (3.53) connects a jump in $\bar{\boldsymbol{e}}_t$ across $d$ to exactly the mean value of $\bar{\boldsymbol{h}}_t$, which is related to the amount of perpendicular flux absorbed in the thin region, if we recall its representation as in (3.46). The IC (3.53) connects the jump in $\bar{\boldsymbol{h}}_t$ across $d$ to the mean value of $\bar{\boldsymbol{e}}_t$, which is related to the electric current that flows in the thin region [31].

Despite being very general, the classical TS approach as presented here is only valid for time-harmonic simulations. Time-transient extensions of this approach were proposed in the literature and are discussed in the next section. Moreover, since the penetration of the fields on the reduced-dimension geometry is described by an analytical 1-D linear flux diffusion solution across $d$, it is known that edge and corner effects are not well estimated by this approach. An option to fix these inaccuracies is to use the *subproblem technique* [97]. Indeed, this technique has been successfully applied to correct leakage fluxes in small air gaps in [98] and edge and corner effects in conductive and ferromagnetic shells in [99, 100]. However, it still relies on the complete discretization of the thickness of the thin region (at least near the edges and corners) and requires efforts to couple the different subproblems.

### 3.7 Time-transient and nonlinear extension of the classical thin-shell model

A time-transient extension of the classical TS approach in the $A$-formulation was proposed in [101], applied in dual formulations in [11], and to the nonlinear analysis of shielding problems in [12]. In this extension, the electric current density and the magnetic flux density inside the shell are represented by mathematical expansions in terms of $N+1$ Legendre polynomials, denoted by $\alpha_i(y)$ and normalized as $|\alpha_i(\pm d/2)| = 1$, for $i = 0, \ldots, N$. In 2-D, we write

$$j_z(y,t) = \sum_{i=0}^{N} \alpha_i(y) j_i(t), \qquad b_x(y,t) = \sum_{i=0}^{N} \alpha_i(y) b_i(t). \tag{3.55}$$

The increase in $N$ allows improving the accuracy of the model, enabling the representation of the nonlinear behavior of the fields inside the shell. The choice of $N$ depends on the problem to be solved and the desired accuracy. In [12] the TS extension with $N = 5$ provided very satisfactory results for a problem of a nonlinear magnetic plate placed above a pair of conductors carrying sinusoidal currents in opposite directions. To apply the TS extension in the $H$-formulation, we substitute (3.55) in (3.20). Integrating the resulting equation twice over the thickness of the shell, we obtain the solution for a 1-D problem in terms only of the tangential component of the electric field ($\boldsymbol{e}_t = e_z \boldsymbol{k}$), i.e.

$$e_z(y,t) = \frac{e_z^+(t) + e_z^-(t)}{2} + \frac{e_z^+(t) + e_z^-(t)}{d} y + \mu d^2 \sum_{i=0}^{N} \beta_i(y) \partial_t j_i(t), \tag{3.56}$$

with $e^+(t) = e_z(d/2, t)$, $e_z^-(t) = e_z(-d/2, t)$, and $\beta_i(z)$ satisfying $d^2 \partial_y^2 \beta_i(y) = \alpha_i(y)$ and $\beta_i(\pm d/2) = 0$ [12]. In addition, either for the linear or the nonlinear cases, the constitutive law $e_z(y,t) = \rho j_z(y,t)$ is weakly imposed by an integral constraint defined as

$$\int_{-d/2}^{d/2} \alpha(y)(e_z(y,t) - \rho j_z(y,t)) \mathrm{d}y = 0, \tag{3.57}$$

leading to $N+1$ differential equations in terms of $j_0 \cdots j_N, e_z^+$ and $e_z^-$. The relevant global quantities are the average current density $j_0$ and the average flux density $b_0$ given by

$$b_0(t) = \frac{1}{d} \int_{-d/2}^{d/2} b_x(y,t) \mathrm{d}y, \quad \text{and} \quad j_0(t) = \frac{1}{d} \int_{-d/2}^{d/2} j_z(y,t) \mathrm{d}y. \tag{3.58}$$

With (3.56), the first IC (related to (3.25) in the classical TS approach) is defined in terms of $e_z^+$, $e_z^-$ and $j_i$, for $i = 1$ to $N$, depending on the Legendre polynomials expansion. The second IC (related to (3.17) in the classical TS approach) is calculated from the average flux density (3.58), the interface condition $e_z^- - e_z^+ = \boldsymbol{n}_s \times d \partial_t b_0(t)$ and the Faraday law (2.6). Thus, as in the classical TS approach, the two ICs are satisfied in this extension. Moreover, it allows the estimation of the EM behavior of both ferromagnetic and conducting thin structures in

time-transient regime since these ICs are now independent of the frequency of operation. In a nonlinear case, the algebraic system of equations is solved using the Newton-Raphson method, just as in the standard $H$-formulation [12].

In [101], the expansion of the TS approach was developed using the $A$-formulation, and even orthogonal Legendre polynomials functions were applied for the time-transient analysis of laminated iron cores. In the $A$-formulation, the solution of (3.20) with (3.55) is expressed in terms of the magnetic field and the constitutive law $h_x(y,t) = \nu b_x(y,t)$ is weakly imposed leading to a system of equation dual to that of the $H$-formulation presented above. A similar approach was used in [102, 103] to develop a time-domain extension of the homogenization technique for laminated iron cores.

Results obtained with this extension of the classical TS approach have shown good agreement with a standard FE solution obtained with the full representation of the shell volume in [12, 101]. In [11], the $H$-formulation was considered and the application of the extension of the TS approach provided reductions of more than 60% in the total number of DoFs, and approximately 80% in the computational time. This reduction was largely the consequence of using a coarse mesh in the neighborhood of the thin shell and avoiding meshing the high aspect ratio geometry. More recently, the expansion of the magnetic flux density using similar polynomial functions was applied to model nonlinear laminated iron cores in power machines [104].

Another time-transient extension of the classical TS approach was proposed in [9]. In that paper, the authors proposed a recursive form for $\boldsymbol{h}_t$ and $\boldsymbol{e}_t$ to avoid computing these field quantities across the thickness of the thin structure during their time-evolution analysis. The two ICs of the classical TS approach were also taken into account in this extension. In [10], the same authors proposed the use of inverse Fast Fourier Transform (FFT) of the time-harmonic solutions to update the residual at each iteration of the fixed point method. Problems involving nonlinear and hysteretic ferromagnetic shields were also tackled in those papers.

All time-transient extensions presented in [9–12, 101, 103, 104] were restricted to ohmic conductors or nonlinear ferromagnetic sheets analysis under external field excitation, i.e. none of them consider cases of nonlinear conductors carrying a current such as HTS tapes, for example. In [105], the authors proposed a TS approach based of the *London theory*[1] [106] to estimate the shielding efficiency of superconducting layers and multi-layered shields.

[1]This theory assumes that the magnetic flux cannot penetrate the superconductor deeper than a short depth. Despite being able to model the Meissner effect in superconductors, there is no formal proof for the London theory. It assumes a perfect diamagnetism, which is not necessarily a feature of all superconductors.

However, this theory does not represent the physics for practical superconductors correctly. So far, no TS model has been used to model nonlinear conductive sheets, such as type-II superconducting layers, other than considering the strip approximation discussed in Section 3.4.

### 3.8 The $T$-$A$-formulation

A model based on a mixed $T$-$A$-formulation was recently proposed to model type-II superconducting tapes [35] and implemented in COMSOL Multiphysics [107]. In this $T$-$A$-formulation, a 1-D problem in terms of a current vector potential $\boldsymbol{t}$ is defined along the width of the tapes. Considering a 2-D problem with the $x$-axis parallel to the width of the tape and the $y$-axis perpendicular to it (Fig. 3.3), the governing 1-D PDE in terms of $\boldsymbol{t}$ is written as

$$\partial_x \rho \partial_x \boldsymbol{t} = -\partial_t \boldsymbol{b}_n, \tag{3.59}$$

where the normal magnetic flux density $\boldsymbol{b}_n$ is a source term defined as

$$\boldsymbol{b}_n = \frac{\boldsymbol{b}_n^+ + \boldsymbol{b}_n^-}{2}, \tag{3.60}$$

with $\boldsymbol{b}_n^\pm$ obtained from the standard $A$-formulation applied to the surroundings of the tapes (according to the COMSOL documentation [107]). Since the tapes are generally surrounded by air space, we have $\boldsymbol{b}_n^\pm = \mu_0 \boldsymbol{h}_n^\pm$.

Boundary conditions of type $\boldsymbol{t} = I/(2d)$ are applied at the extremities of the tapes to impose

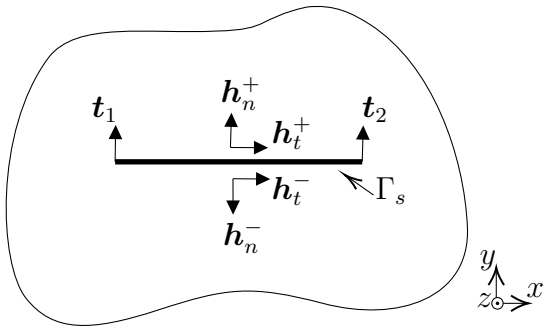


Figure 3.3 Schematic representing the $T$-$A$-formulation for a single tape example: a 1-D problem is defined along the tape width with the current density potential $\boldsymbol{t}$ as state variable. A current density is computed from $\boldsymbol{t}$ and impressed in a pure $A$-formulation through discontinuities of $\boldsymbol{h}_t^\pm$ related to the positive and negative sides of $\Gamma_s$.

a transport current into them. The variation of $\boldsymbol{t}$ along their width gives the current density

$$\boldsymbol{j} = \boldsymbol{n}_s \times (\boldsymbol{n}_s \times \partial_x \boldsymbol{t}) \,. \tag{3.61}$$

Moreover, the equivalent surface current density, assuming a linear variation across the thickness of the tape, is simply $\boldsymbol{k}_e = \boldsymbol{j}_z d$, i.e. the same as in the strip approximation. This surface current density is imposed in the $A$-formulation through discontinuities of the tangential components of the magnetic field that arise naturally in the weak form of this formulation, as shown in (3.33).

Under the previous assumptions, using (3.60) and (3.61) with (3.5) in (3.59), we obtain

$$\partial_x \rho \frac{\left(\boldsymbol{h}_t^+ - \boldsymbol{h}_t^-\right)}{d} = \partial_t \mu \frac{(\boldsymbol{h}_n^+ + \boldsymbol{h}_n^-)}{2}, \tag{3.62}$$

which is the $H$-representation of the IC (3.46) with $a^{-1}\tanh(ad/2)$ approximated by $d/2$ in the classical TS approach. The second IC of the TS approach (equivalent to (3.47) or (3.6)) is fulfilled by the continuity of the tangential component $\boldsymbol{a}_t$ in the $A$-formulation. The $T$-$A$-formulation is consequently only suitable for cases where the permeability of the thin region is equal to the value in its surroundings and the flux diffusion inside the tapes can be neglected, i.e. problems involving ferromagnetic thin regions cannot be addressed using this formulation.

The $T$-$A$-formulation can be seen as a particular realization of the TS approach disregarding the magnetic effects inside the tapes and with a linear approximation of the magnetic field profile across the thickness of the tape. In fact, this formulation is equivalent to the strip approximation in the $A$-formulation, but with the surface current density $\boldsymbol{k}_e$ defined numerically by the 1-D problem in terms of $\boldsymbol{t}$. Note however that the current density is at same time defined as the variation of $\boldsymbol{t}$ (related to $\boldsymbol{h}_n$) along the width of the tape and the variation (or discontinuity) of $\boldsymbol{h}_t$ across its thickness. If the former variation is considered to be linear along the elements on the surface of the shell, the second must also be. From Faraday's law (3.38), we verify that for $\boldsymbol{h}_n$ to be linear, $\boldsymbol{e}_t$ (or $\boldsymbol{a}_t$) must be of second order, otherwise numerical oscillations appear.

In [108], the authors observed the numerical instability when using the $T$-$A$-formulation with first order finite elements for both $\boldsymbol{a}$ and $\boldsymbol{t}$ to estimate the EM behavior of a stack of HTS tapes. When the finite element order for $\boldsymbol{a}$ was increased, the oscillations disappeared. Only 2-D cases were considered in that paper, and the $T$-$A$-formulation performed better than the standard $H$-formulation in terms of computational cost in these cases. However in [109], the

application of the $T$-$A$-formulation to the simulation of a Roebel cable required computational resources comparable to that of the $H$-formulation, since high order elements were used for $\boldsymbol{a}$ to avoid the numerical oscillations. Despite this, the $T$-$A$-formulation has become very popular in recent years to estimate current and fields in HTS devices [108, 110–116]. The stability problem of the $T$-$A$-formulation was studied in greater detail in a very recent article [71].

### 3.9 Chapter summary and remarks

A literature review about the modeling of thin regions with the finite element method was presented in this chapter. Considering the penetration of the tangential components of the fields in the shell, the presented approaches can be categorized into two groups:

- Models that considers a linear tangential field profile across the thickness $d$: strip approximation, degenerate finite elements with first-order Lagrange basis functions, the $T$-$A$-formulation, and the classical TS approach ($\delta \gg d$);
- Models that take into account the nonlinear field profile across $d$: the classical TS approach ($\delta < d$) and its time-transient extensions.

The first group has application limited to cases where the surface current densities can be assumed constant across the thickness. This is the case of problems where the tangential components of the fields fully penetrate the reduced-dimension geometry and where the normal component of the fields dominate the dynamics of the problem. In addition, the strip approximation is only suitable for problems involving thin ferromagnetic or conductive regions at once (in the $H$- and $A$- formulations, respectively) since only the electric or the magnetic surface current density is considered in this approximation. Similarly, the $T$-$A$-formulation is only suitable for modeling thin conducting structures and not ferromagnetic shields, for example. The numerical instability in the $T$-$A$-formulation was also briefly discussed.

The second group takes into account the uneven distribution of the current densities across $d$. However, the classical TS approach is limited to time-harmonic simulations, and the time-transient extensions of this approach rely on complicated analytical solutions for the fields profiles across $d$ such as (3.56). Moreover, edge and corner effects are not well represented by these approaches. We conclude that simpler and more representative models are required for the time-transient analysis of both linear and nonlinear thin regions, especially those encountered in superconducting tapes.

# CHAPTER 4 RESEARCH WORK DEVELOPMENT AND GENERAL ORGANIZATION OF THE DOCUMENT

## 4.1 Research objectives

The main objective of this thesis is to establish a rigorous 3-D FE formulation for domains composed of thin regions that is suitable for time-transient analysis of EM devices while taking into account the nonlinearities of both the conductive and ferromagnetic materials.

This general objective was split into three sub-objectives:

1. Establish a well-posed finite-element approach for modeling thin regions;
2. Demonstrate that the proposed approach gives sufficiently accurate results compared to nonlinear 3-D FEM reference solutions in time-transient analysis;
3. Quantify the benefits of the new approach in terms of mesh simplifications and reduction of the computational cost.

## 4.2 Working assumptions

Given the computational electromagnetic fundamentals and the literature review on modeling thin regions using the FEM presented in chapters 2 and 3, respectively, we identify the following working assumptions:

1. As presented in Section 2.8.6, the edge-based cohomology basis representative (thick cuts) could be useful to impose current constraints in the thin regions with the $H$-$\phi$-formulation, which was already demonstrated to be advantageous to solve problems involving superconductors in [43, 55, 61, 117–120]. When modeling thin structures, the reduced-dimension geometry ($\Gamma_s$) may represent a cavity in the computational domain if it is duplicated as in the degenerate finite elements approach (Section 3.5). This duplication may allow discontinuities of the tangential components of the fields across the shell thickness, which is required to represent the two ICs in the classical TS approach (see discussion in Section 3.6.2). Our assumption is that the computational cost can be reduced by using thick cuts outside from the thin regions while we connect this with a suitable TS model representing its interior physics. These cuts may also allow imposing a transport current or computing eddy-currents in the shell.

2. The currently available approximations for modeling thin structures suffer from four main limitations: (i) they are often restricted to time-harmonic analysis, (ii) they do not consider or neglect the penetration of the tangential components of the magnetic and the electric fields in the shell simultaneously, (iii) they are either suitable only for simulating linear ferromagnetic or conducting thin structures, and (iv) they cannot correctly represent edges and corners effects.

3. Models that assume a linear profile of the tangential fields inside the shell are limited to applications where the penetration depth is much larger than the thickness of the thin region or where the normal components of the fields dominate the dynamic of the problem. To overcome this limitation, a new TS model should consider the nonlinear profile of the fields across the shell thickness.

4. Time-transient extensions of the classical TS approach (Section 3.6) often consider complicated analytical solutions such as (3.56) to be defined at the pre-processing stage, or rely on time-harmonic solutions and post-processing efforts to update the residual at each time step of the simulation. A new TS model should be able to solve the system of equations directly through FEM.

5. All the presented models for superconducting tapes in Chapter 3 neglect the penetration of the field component parallel to the wide faces of the thin structures. A model that takes into account this penetration would be suitable for modeling type-II HTS tapes in any configuration (e.g. closely packed tapes carrying anti-parallel currents [79, 121]).

6. Even models that consider the penetration of the tangential field components cannot accurately represent edges and corners effects [100], since near these regions the tangential components may have a distribution different than the analytical solution for the 1-D linear flux diffusion problem introduced in Section (3.6.1). Indeed, far from the edges and corners the fields may have a profile other than hyperbolic. A more general TS model should consider field profiles of any type inside the shell.

7. Thin-shell approaches in mixed formulation such as the $T$-$A$-formulation may suffer from numerical instability [71, 108, 109]. In this approach, both the tangential and normal components of the magnetic field are coupled to the pure $A$-formulation used in the surroundings of the thin region. A more natural coupling could be achieved using only the tangential components of the fields, as in the classical TS approach, and may resolve the numerical instability observed in the $T$-$A$-formulation.

## 4.3 Methodology

In this thesis, we proceed with two different approaches: (i) by defining dedicated basis functions for the 1-D problem across $d$ that allows the time-transient and nonlinear analysis of thin sheets, and (ii) by considering multiple degenerate finite-elements (or a virtual 1-D mesh) to represent the nonlinear profile of the fields and the uneven distribution of the current density inside the shell. In all cases, the proposed TS models were implemented using the $H$-$\phi$-formulation since it has been considered as the most suitable formulation for modeling HTS devices. However, given the duality of the $H$- and the $A$- formulations discussed in Chapter 2, the proposed methodology can be easily extended to the $A$- or $A$-$V$- formulations.

### 4.3.1 Thin-shell approach with hyperbolic basis functions

From the 1-D solutions in terms of the magnetic and the electric field tangential components, (3.14) and (3.23), respectively, we observe that both of them can be interpreted as a least squares approximation of the tangential components of the field at the boundaries $\Gamma_s^{\pm}$ using hyperbolic functions of type $\frac{\sinh\left(\frac{\vec{a}d}{2}\pm+\vec{a}y\right)}{\sinh(\vec{a}d)}$. Our first approach was then to defined these hyperbolic expressions as basis functions for an auxiliary 1-D problem defined across the thickness of the shell in time-harmonic problems, and to extend it for the time-transient analysis of nonlinear shells by considering a set of basis functions derived from time-harmonic solutions at different frequencies. These hyperbolic basis functions become equivalent to first-order Lagrange basis functions in cases with $\delta \gg d$, but they can represent the profile of the fields inside the shell in cases with $\delta < d$, as in the classical TS approach. The increment of the frequency content used to define the set of basis functions allows the representation of the time-transient behavior of the field quantities in the shell. Moreover, the combination of multiple frequency components allows the non-hyperbolic profile near edges and corners to be represented correctly. The proposed approach is given a detailed presentation in Chapter 5.

### 4.3.2 Thin-shell approach with virtual discretization

In our second approach, we considered multiple degenerate finite elements to represent the thin region. This approach can be seen as a virtual representation of the shell thickness in the computational domain. With a single element across the thickness of the shell, this approach becomes equivalent to the degenerate elements proposed in [86], to the strip approximation (considering both the electric and magnetic phenomena inside the shell), or even to the classical TS approach with $\delta \gg d$ in the time-harmonic regime. Moreover, the ICs can be defined purely in terms of the tangential components of the magnetic field on the

virtual mesh, which can be efficient in computing the EM phenomena in problems involving several HTS tapes. Given that we consider a virtual representation across the thickness of the tape, multiple layers with different materials properties can be simulated as a single lower-dimensional geometry within the domain. The proposed TS approach for 2-D and 3-D cases are formally presented and validated in Chapters 6 and 7, respectively. This approach is more general than the first one since it is independent of the frequency of operation or of the materials physical properties.

All the features of the two proposed approaches were implemented in the open-source code Gmsh [60] and the solver GetDP [122] in order to ensure the availability of these models to the engineering community. Besides, our second approach was also implemented in COMSOL Multiphysics, given that this software has become very popular among the HTS modeling community over the past ten years or so. This implementation was also important for the sake of comparison of our approach with the $T$-$A$-formulation. A full comparison between our model implemented in COMSOL and the $T$-$A$-formulation is presented in Appendix B. Moreover, a shielded induction heater was modeled using the proposed TS approach in order to evaluate the accuracy of the proposed TS model in estimating field and current distributions near the corners and edges of thin conductive and ferromagnetic regions. These results are presented in Appendix C. In all the cases, the solutions obtained with the proposed TS models were compared with reference solutions obtained with standard FE with a $H$-$\phi$-formulation, and with well-established analytical models.

# CHAPTER 5 PAPER 1: HYPERBOLIC BASIS FUNCTIONS FOR TIME-TRANSIENT ANALYSIS OF EDDY CURRENTS IN CONDUCTIVE AND MAGNETIC THIN SHEETS

IEEE TRANSACTION ON MAGNETICS

(Paper submitted on April 6, 2021, and accepted for publication on September 2, 2021)

[1]Bruno de Sousa Alves, [2]Ruth V. Sabariego, [1]Marc Laforest, [1]Frédéric Sirois

[1]Polytechnique Montréal, Montréal, QC H3C 3A7, Canada

[2]Department of Electrical Engineering (ESAT), EnergyVille, KU Leuven, 3001 Leuven, Belgium

**Abstract**

This paper presents a new time-domain finite-element approach for modeling thin sheets with hyperbolic basis functions derived from the well-known steady-state solution of the linear flux diffusion equation. The combination of solutions at different operating frequencies permits the representation of the time-evolution of field quantities in the magnetic field formulation. This approach is here applied to solve a planar shielding problem in harmonic and time-dependent simulations for materials with either linear or nonlinear characteristics. Local and global quantities show good agreement with the reference solutions obtained by the standard finite element method on a complete and representative discretization of the region exposed to a time-varying magnetic field.

## 5.1 Introduction

Thin sheets of high permeability and/or conductivity are often employed to mitigate stray fields produced by electric and electronic devices such as rotating machines, large power transformers, induction heating equipment, welding and forming machines [8, 9, 93, 94, 96]. In the surroundings of these devices, the field intensity needs to be at acceptable value to comply with the exposure limits for humans and for electromagnetic compatibility and interference reasons [9]. However, the shielding efficiency of thin sheets can be directly affected by its material characteristics, shape and position [8]. Consequently, the availability of models able to predict the electromagnetic (EM) behavior in such structures at an affordable computational cost is key to optimizing these devices.

In terms of shape, the high aspect ratio of thin-sheet shields presents a challenge to numerical simulation. Indeed, the direct application of a numerical method, such as the Finite Element Method (FEM), can be computationally expensive or even prohibitive due to the associated meshing difficulties [95]. On the one hand, a coarse mesh inside these sheets is unable to capture the EM phenomena and may lead to elements with high aspect ratio, which affect the FEM solution accuracy and convergence [6]. On the other hand, a high-density mesh can increase inordinately the number of unknowns in the problem and therefore the computational cost. The EM problem is even harder to solve if nonlinear materials characteristics are considered in time-transient analysis.

An efficient way to overcome these difficulties is to use the classical Thin-Shell (TS) model [31–34]. In this model, a reduced-dimension geometry replaces the actual volume of the thin regions, and suitable *impedance boundary conditions* (IBCs) account for the EM behavior within the original volume. These IBCs are defined from the analytical solution of the EM problem throughout the volume of the thin sheet. Thus, since the smallest dimension of the layer is neglected in a geometric sense, errors are avoided that would have been caused by the original anisotropic meshing of the thin structure with poor aspect ratios [93].

The TS model provides a good compromise between accuracy and computational cost [95], but its application is still mostly restricted to linear and harmonic regime analysis since the analytical solution is known *a priori* and the IBCs can be easily established. Currently available time-domain and nonlinear TS-FEM approaches are often derived from classical IBCs, whether using orthogonal polynomial basis functions to express the magnetic flux density through the shell thickness [11,12,101–104], Fast Fourier Transform (FFT) to update the residual from the harmonic solution [8, 9], or simply a linear field variation through its thickness (strip approximations) [35, 77, 108, 110]. However, when considering time-transient analysis of nonlinear thin sheets, more representative models are required.

In [123], low-order *surface impedance boundary conditions* (SIBCs) are defined using basis functions derived from the steady-state analytical solution of semi-infinite slab problems. These SIBCs are applied in time-transient FE simulations to remove large conducting regions from the computational domain. Although the problems involving thin sheets are different, their nature is the same. In SIBCs, field quantities penetrate the surface from one boundary of a bulk domain, whereas in the TS model, the penetration occurs simultaneously from the two extended faces of a thin sheet. Moreover, the IBCs in the TS approach proposed in [31] are derived in a similar way than the SIBCs in [92]. For these reasons, a time-domain extension of the classical TS model with basis functions derived from the steady-state solution of a slab of finite thickness, equivalent to the model proposed in [123] for SIBCs, is a natural

approach to pursue.

This paper presents a novel time-domain extension of the classical TS model to solve 2-D shielding problems. The physics inside the thin region is captured by hyperbolic basis functions derived from the steady-state analytical solution of the linear flux diffusion equation. We demonstrate that the use of two hyperbolic basis functions leads to IBCs equivalent to the classical TS model in harmonic regime. In the time-transient analysis, the use of $n$ pairs of hyperbolic basis functions, each representing different frequencies, coupled to FEM models outside the TS, allows computation of the time evolution of the physical quantities throughout the domain without resolving the TS. The method is here developed for a magnetic field ($H$-)formulation and extended to nonlinear cases. Results show good agreement with the 2-D FE reference solutions, with a greatly reduced number of degrees of freedom (DoFs) and therefore, at a lower computational cost.

## 5.2 1-D Flux Diffusion Problem in a Slab of Finite Thickness

By assuming a thin region with a sufficiently high aspect ratio, the EM problem in a sheet can be formulated as a 1-D flux diffusion problem in a slab of finite thickness. In Fig. 5.1, we consider a thin sheet of thickness $d$ whose normal is parallel to the $y$-axis. The tangential component of the magnetic field ($h_x$) is in the $x$-direction (Fig. 5.1a) and the tangential component of the electric field ($e_z$) is in the $z$-direction (Fig. 5.1b). The slab problem can be then formulated in terms of $h_x$ or $e_z$, i.e.

$$\partial_y(\rho\partial_y h_x(y,t)) + \partial_t \mu h_x(y,t) = 0, \tag{5.1}$$

$$\partial_y(\nu\partial_y e_z(y,t)) + \partial_t \sigma e_z(y,t) = 0, \tag{5.2}$$

where $\rho$ is the electric resistivity ($\sigma = 1/\rho$) and $\mu$ is the magnetic permeability ($\nu = 1/\mu$). These expressions are derived from Faraday's and Ampere's laws, respectively.

We assume that $\rho$ and $\mu$ are constants and that we have harmonic boundary conditions (BCs), i.e.

$$h_x^{\pm}(y = \pm d/2, t) = \hat{h}_x^{\pm}\cos(\omega t + \phi_h^{\pm}), \tag{5.3}$$

$$e_z^{\pm}(y = \pm d/2, t) = \hat{e}_z^{\pm}\cos(\omega t + \phi_e^{\pm}), \tag{5.4}$$

where $\hat{h}_x^{\pm}$ and $\hat{e}_z^{\pm}$ are respectively the magnetic and electric field magnitudes, and $\phi_h^{\pm}$ and $\phi_e^{\pm}$ their related phase shifts. Using a phasor representation (symbols with a bar), i.e.

$\bar{h}_x^{\pm} = \hat{h}_x^{\pm}\exp(\jmath\phi_h^{\pm})$ and $\bar{e}_z^{\pm} = \hat{e}_z^{\pm}\exp(\jmath\phi_e^{\pm})$, we have

$$h_x^{\pm}(y = \pm d/2, t) = \Re\{\bar{h}_x^{\pm}\exp(\jmath\omega t)\}, \tag{5.5}$$

$$e_z^{\pm}(y = \pm d/2, t) = \Re\{\bar{e}_z^{\pm}\exp(\jmath\omega t)\}, \tag{5.6}$$

where $\Re\{.\}$ is the real part of the argument.

The solutions to (5.1)-(5.2) with the boundary conditions (5.5)-(5.6) are given complex notation (symbols with right arrow on top) and can be written as:

$$\bar{h}_x(y) = \bar{h}_x^{+}\vec{\psi}^{+}(y) + \bar{h}_x^{-}\vec{\psi}^{-}(y), \tag{5.7}$$

$$\bar{e}_z(y) = \bar{e}_z^{+}\vec{\psi}^{+}(y) + \bar{e}_z^{-}\vec{\psi}^{-}(y), \tag{5.8}$$

where

$$\vec{\psi}^{\pm}(y) = \frac{\sinh\left(\frac{\vec{a}d}{2} \pm \vec{a}y\right)}{\sinh\left(\vec{a}d\right)}, \tag{5.9}$$

and $\vec{a} = \frac{1+\jmath}{\delta}$, $\jmath = \sqrt{-1}$, $\delta = \sqrt{2/(\mu\sigma\omega)}$, $\omega = 2\pi f$, and $f$ is the operating frequency. Note that the functions $\vec{\psi}^{\pm}(y)$ appear in both (5.7) and (5.8). These functions are used later in this paper to define the basis functions required for the time-transient analysis of thin sheets.

### 5.2.1 Hyperbolic Basis Functions and Classical TS Model

We propose the use of basis functions obtained from steady-state solutions of the 1-D flux diffusion problem governed by (5.1)-(5.4). Taking as example the problem in terms of the magnetic field (5.1), together with the BCs (5.3), the steady-state solution for $h_x$ can be written as

$$\begin{aligned} h_x(y,t) = &\hat{h}_x^{+}\cos(\omega t + \phi_h^{+})\theta_c^{+}(y) \\ &+ \hat{h}_x^{+}\sin(\omega t + \phi_h^{+})\theta_s^{+}(y) \\ &+ \hat{h}_x^{-}\cos(\omega t + \phi_h^{-})\theta_c^{-}(y) \\ &+ \hat{h}_x^{-}\sin(\omega t + \phi_h^{+})\theta_s^{-}(y), \end{aligned} \tag{5.10}$$

where the analytical expressions for $\theta_c^{\pm}$ and $\theta_s^{\pm}$ given in Table 4.2-II of [124]. Here, $\theta_c$ and $\theta_s$ are obtained directly from the real ($\Re$) and imaginary ($\Im$) parts of (5.9), i.e.

$$\theta_c^{\pm}(y) = \Re\{\vec{\psi}^{\pm}(y)\}, \tag{5.11}$$

$$\theta_s^{\pm}(y) = \Im\{\vec{\psi}^{\pm}(y)\}, \tag{5.12}$$


(a) Magnetic field (b) Electric field

Figure 5.1 Thin region $\Omega_s$ of thickness $d$ and its local coordinate system. $\Gamma_s^{\pm}$ denote the top and bottom boundaries of $\Omega_s$ and $\boldsymbol{n}_s^{\pm}$ their respective outward normals.

which means that

$$\vec{\psi}^{\pm}(y) = \theta_c^{\pm}(y) + \jmath\theta_s^{\pm}(y). \tag{5.13}$$

Note that the solution (5.10) can be interpreted as a least squares approximation of $h_x^{\pm}$ in $\Omega_s$ using the hyperbolic functions $\vec{\psi}^{\pm}(y)$. In addition, if we consider the harmonic solution (5.7) with $\delta \gg d$, $\vec{\psi}^{\pm}(y)$ in (5.9) reduces to

$$\vec{\psi}^{\pm}(y)\big|_{(\delta \gg d)} = \frac{d/2 \pm y}{d}, \tag{5.14}$$

which is equivalent to the Lagrange polynomials of first order defined across the thickness $d$ of the sheet. Indeed, with $\delta \gg d$, the field quantities have a linear variation through the sheet thickness, and the functions $\vec{\psi}^{\pm}(y)$ can account for this behavior. To illustrate this, the functions $\theta_c^{\pm}$ and $\theta_s^{\pm}$ for $\delta \gg d$ are plotted in Fig. 5.2.

The equivalent solution in terms of the electric field can be obtained by replacing $\hat{h}_x^{\pm}$ and $\phi_h^{\pm}$ by $\hat{e}_z^{\pm}$ and $\phi_e^{\pm}$ in (5.10). However, in this paper, we are solely interested in magnetic field quantities and the $H$-formulation. The solution depending on the electric field would be useful, say, to implement the proposed approach in the magnetic vector potential ($A$-)formulation.

Besides, it can be demonstrated that the application of the $\vec{\psi}^{\pm}(y)$ functions as basis functions in the variational form of a 1-D finite element problem in the harmonic regime leads to the same IBCs used in the classical TS model [31], which are, using a vector representation (bold symbols),

$$\boldsymbol{n}_s \times (\boldsymbol{h}_x^+ - \boldsymbol{h}_x^-) = \vec{\eta}_e \left(\boldsymbol{n}_s \times \left(\boldsymbol{e}_z^+ + \boldsymbol{e}_z^-\right)\right) \times \boldsymbol{n}_s, \tag{5.15}$$

$$\boldsymbol{n}_s \times (\boldsymbol{e}_z^+ - \boldsymbol{e}_z^-) = \vec{\eta}_h \left(\boldsymbol{n}_s \times \left(\boldsymbol{h}_x^+ + \boldsymbol{h}_x^-\right)\right) \times \boldsymbol{n}_s, \tag{5.16}$$

with $\vec{\eta}_h = -\frac{\jmath\omega\mu}{\vec{a}} \tanh\left(\frac{\vec{a}d}{2}\right)$ and $\vec{\eta}_e = \frac{\sigma}{\vec{a}} \tanh\left(\frac{\vec{a}d}{2}\right)$.

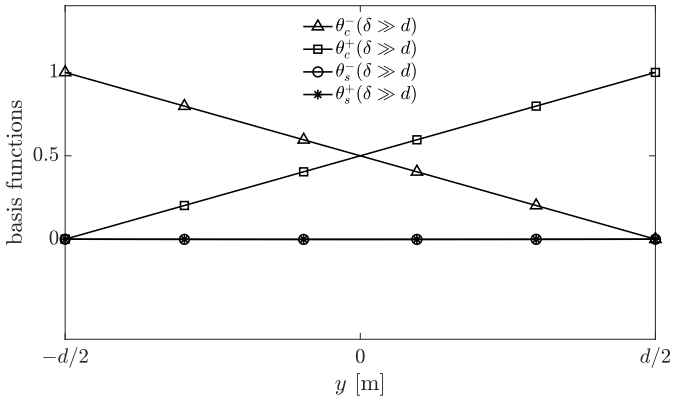


Figure 5.2 Hyperbolic basis functions when $\delta \gg d$.

Expression (5.15) connects the discontinuity of the tangential components of the magnetic field to the mean value of the tangential electric field. This discontinuity is related to the total net current flowing in the sheet [32]. Moreover, equation (5.16) connects the discontinuity of the tangential electric field to the mean value of the tangential magnetic field, which is related to the amount of perpendicular flux absorbed in the plane of the sheet. When $\delta \gg d$, the coefficients $\frac{1}{\vec{a}} \tanh\left(\frac{\vec{a}d}{2}\right)$ in $\vec{\eta}_h$ and $\vec{\eta}_e$ can be approximated by $d/2$ [95].

The classical TS model in the form of IBCs has been used extensively to tackle problems involving thin regions in harmonic regime simulations [8, 31–33, 95, 96]. These IBCs were originally defined from the analytical solution for the field distribution, and the integration of the analytical expressions of the electric and magnetic current densities over the thickness of the thin sheet, which gives equivalent surface currents representatives [31]. However, to the best of our knowledge, no definition of the TS model in the form of the hyperbolic basis functions has been proposed in the literature before. These functions appear naturally in the solution (5.10). Therefore, the proposed approach can be easily extended to time-transient analysis, as described next.

### 5.2.2 Hyperbolic Basis Functions in Time-Transient Analysis

In time-transient analysis, we define $n$ pairs of $\vec{\psi}_k^{\pm}(y)$, where $k$ is the harmonic rank relative to a fundamental frequency $f_1$ chosen in accordance with the problem to model, and $1 \leq k \leq n$. The number of basis functions $n$ is defined according to the frequency content of $h_x$ and the desired accuracy. Therefore, $\vec{\psi}_k^{\pm}(y)$ is still defined by (5.9), with $\omega = 2\pi f_k$ (which affects the values of $\delta$ and $\vec{a}$). Then, according to (5.13), each $\vec{\psi}_k^{\pm}(y)$ generates the even $\theta_{ck}^{\pm}(y)$ and

odd $\theta^{\pm}_{sk}(y)$ functions, which we write as

$$\theta^{\pm}_{c1}(y) = \Re\{\vec{\psi}^{\pm}_1(y)\}, \tag{5.17}$$

$$\theta^{\pm}_{ck}(y) = \Re\{\vec{\psi}^{\pm}_k(y)\} - \theta^{\pm}_{c1}(y), \qquad 2 \leq k \leq n, \tag{5.18}$$

$$\theta^{\pm}_{sk}(y) = \Im\{\vec{\psi}^{\pm}_k(y)\}, \qquad 1 \leq k \leq n. \tag{5.19}$$

The first two cosines satisfy $\theta^{\pm}_{c1}(y = \pm d/2) = 1$ while the remaining functions $\theta^{\pm}_{ck}(y)$ and $\theta^{\pm}_{sk}(y)$ in (5.18-5.19) vanish at the boundaries of the thin region ($\Gamma^{\pm}$). This allows us to connect the 1-D equations to the exterior FE global system of equations; see Section 5.3. Examples of the proposed basis functions with $n = 3$ are presented in Fig. 5.3 for $\delta \leq d$. For cases with $\delta \gg d$, the first two cosines functions are enough to represent the profile of $h_x$ in $\Omega_s$, since it has a linear variation throughout the thickness of the sheet (Fig. 5.2). Furthermore, the sine basis vanish everywhere.

The expansion of $h_x(y,t)$ in terms of (5.17)-(5.19) can be written in matrix form as

$$h_x(y,t) = [h(t)]^T [\theta(y)], \tag{5.20}$$

with the $4n \times 1$ matrices $[h(t)]$ and $[\theta(y)]$ given by

$$\begin{aligned}[h(t)] = [&h^+_{c1}(t) \dots h^+_{cn}(t), h^+_{s1}(t) \dots h^+_{sn}(t),\\ &h^-_{c1}(t) \dots h^-_{cn}(t), h^-_{s1}(t) \dots h^-_{sn}(t)],\end{aligned} \tag{5.21}$$

$$\begin{aligned}[\theta(y)] = [&\theta^+_{c1}(y) \dots \theta^+_{cn}(y), \theta^+_{s1}(y) \dots \theta^+_{sn}(y),\\ &\theta^-_{c1}(y) \dots \theta^-_{cn}(y), \theta^-_{s1}(y) \dots \theta^-_{sn}(y)],\end{aligned} \tag{5.22}$$

where $h^{\pm}_{ck}(t)$ and $h^{\pm}_{sk}(t)$ are unknowns of the problem to model.

Additionally, the 1-D variational form of the partial differential equation (5.1), disregarding homogeneous BCs, is

$$\Big(\rho\, \partial_y h_x, \partial_y h'_x\Big)_{\Omega_s} + \partial_t \Big(\mu\, h_x, h'_x\Big)_{\Omega_s} = 0, \tag{5.23}$$

where $h'_x$ is the test function assumed to vanish at $\Gamma^{\pm}_s$.

The FE discretization of (5.23) by means of $N = 4n$ basis functions $\theta_p(y)$ and $\theta_q(y)$, with $p, q \in [1, N]$, for $h_x$ and $h'_x$ respectively, and assuming isotropic linear materials, leads to a system of equations, expressed in matrix form as

$$\rho\, [\mathcal{S}]\, [h(t)] + \mu\, [\mathcal{M}]\, \partial_t [h(t)] = 0, \tag{5.24}$$

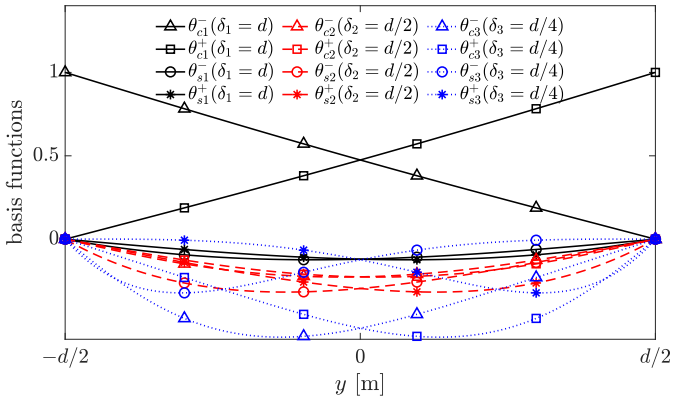


Figure 5.3 Hyperbolic basis functions for time-transient analysis: example with $\delta_1 = d$ (with $f_1$ in accordance), $\delta_2 = d/2$ ($f_2 = 4f_1$) and $\delta_3 = d/4$ ($f_3 = 16f_1$) for $k = 1, 2$ and 3, respectively.

where the elements of $[\mathcal{S}]$ and $[\mathcal{M}]$ are calculated as

$$\mathcal{S}_{pq} = \int_{-d/2}^{d/2} \partial_y \theta_p(y) \partial_y \theta_q(y) dy, \tag{5.25}$$

$$\mathcal{M}_{pq} = \int_{-d/2}^{d/2} \theta_p(y) \theta_q(y) dy, \tag{5.26}$$

which can be evaluated numerically for each pair of basis functions $\theta_p$ and $\theta_q$. Then, considering the implicit Euler scheme for the time-discretization of (5.24), coupled to (5.3), one obtains a system of algebraic equations to be solved at each time-step of the simulation.

The instantaneous loss $\mathcal{L}(t)$ in Joule is calculated as [125]

$$\mathcal{L}(t) = \rho [h(t)]^T [\mathcal{S}] [h(t)], \tag{5.27}$$

where $\mathcal{S}_{pq}$ is given by (5.25).

In the nonlinear case, the still isotropic resistivity $\rho$ (or the magnetic permeability $\mu$) in the variational form (5.23) can depend on the magnetic field intensity $h_x$ or its derivative $\partial_y h_x$. The resulting nonlinear system of equations is solved by the Newton-Raphson (NR) iterative method, as presented in [123], but with integral terms evaluated over the thickness of the thin region, i.e., $-d/2 \leq y \leq d/2$. These integrals are solved numerically using the Legendre-Gauss quadrature at every iteration of the NR method.

### 5.3 FEM Implementation

We study the problem of a thin region $\Omega_s$ embedded in a domain $\Omega = \Omega_c \cup \Omega_c^C$, where $\Omega_c$ and $\Omega_c^C$ denote respectively the conducting and non-conducting parts of $\Omega$. As depicted in Fig. 5.4a, the exterior boundary of $\Omega$ ($\partial\Omega = \Gamma$) is composed of two complementary parts $\Gamma_h$ and $\Gamma_e$ (i.e. $\Gamma = \Gamma_h \cup \Gamma_e$ and $\Gamma_h \cap \Gamma_e = \varnothing$) that may be necessary for symmetry or physical purposes such as connecting different subproblems via their common boundaries [99]. The thin region $\Omega_s$ belongs to the conductive subdomain ($\Omega_s \subset \Omega_c$) and its interior and exterior boundaries are $\Gamma_s^-$ and $\Gamma_s^+$, respectively.

When coupling the TS model with the FEM, $\Omega_s$ is geometrically replaced by a surface located halfway between the original boundaries ($\Omega_s \to \Gamma_s$ in Fig. 5.4b). In the variational form, by assuming distinct BCs on both sides of $\Gamma_s$, we obtain interface integrals to couple with the TS model within $\Omega_s$. Thus, the weak form of the $H$-formulation, obtained from the weak form of Faraday's law, is defined as follows:

Find $\boldsymbol{h} \in \boldsymbol{H}(\mathrm{curl}, \Omega)$ such that

$$\begin{aligned} &\Big(\rho\nabla\times\boldsymbol{h}, \nabla\times\boldsymbol{h}'\Big)_{\Omega_c\setminus\Omega_s} + \partial_t\Big(\mu\boldsymbol{h}, \boldsymbol{h}'\Big)_{\Omega\setminus\Omega_s} \\ &+ \Big\langle \boldsymbol{n}\times\boldsymbol{e}, \boldsymbol{h}'\Big\rangle_{\Gamma_e} - \Big\langle \boldsymbol{n}_s\times\boldsymbol{e}, \boldsymbol{h}'\Big\rangle_{\Gamma_s^+} + \Big\langle \boldsymbol{n}_s\times\boldsymbol{e}, \boldsymbol{h}'\Big\rangle_{\Gamma_s^-} = 0, \end{aligned} \tag{5.28}$$

$\forall\ \boldsymbol{h}' \in \boldsymbol{H}_0(\mathrm{curl}, \Omega)$, where $\boldsymbol{h}'$ are test functions with $\boldsymbol{n}\times\boldsymbol{h}' = 0$ along $\Gamma_h$, $\boldsymbol{n}$ is the outward unit normal vector on $\Gamma$, and $(\cdot,\cdot)_\Omega$ and $\langle\cdot,\cdot\rangle_\Gamma$ denote respectively the volume integral over $\Omega$ and the surface integral over $\Gamma$ of the scalar product of their two arguments. Note that we assume that $\boldsymbol{h} \in \boldsymbol{H}(\mathrm{curl}, \Omega)$ already satisfies the BC on $\boldsymbol{n}\times\boldsymbol{h}$ along $\Gamma_h$.

The two last terms of (5.28) express the discontinuity of the tangential components of the electric field along the surface representing the thin region and we considered that $\boldsymbol{n}_s = -\boldsymbol{n}_{\Gamma_s}^+ = \boldsymbol{n}_{\Gamma_s}^-$ (see Fig. 5.4a). Besides these interface terms, the weak form (5.28) requires the duplication of the DoFs related to the surface of the thin region. In [95], the authors propose the decomposition of the field quantities into its continuous and discontinuous parts in order to avoid nodes and edges duplication. This decomposition is also applied in [11, 12, 101].

Here, nodes and edges of the thin surface are duplicated, but except for the nodes located at its extremities (e.g. points $p_1$ and $p_2$ in Fig. 5.4b). This creates a *crack* in the topological structure, and the non-conducting region becomes non-simply connected. The interfaces $\Gamma_s^+$ and $\Gamma_s^-$ share the nodes at their extremities, such that $\Gamma_s = \Gamma_s^+ \cup \Gamma_s^-$, and the tangential components of the magnetic fields on these surfaces are connected by an 1-D FE problem in

the thin direction of the sheet.

In order to include the 1-D problem in the weak form (5.28), we express the surface integral terms on $\Gamma_s$ in (5.28) by using the variational formulation of Faraday's law over $\Omega_s$, namely

$$\begin{aligned} -\Big\langle \boldsymbol{n}_s \times \boldsymbol{e}, \boldsymbol{h}' \Big\rangle_{\Gamma_s^+} + \Big\langle \boldsymbol{n_s} \times \boldsymbol{e}, \boldsymbol{h}' \Big\rangle_{\Gamma_s^-} = \\ \Big(\rho \nabla \times \boldsymbol{h}, \nabla \times \boldsymbol{h}' \Big)_{\Omega_s} + \partial_t \Big(\mu \boldsymbol{h}, \boldsymbol{h}' \Big)_{\Omega_s}. \end{aligned} \tag{5.29}$$

The volume integrals terms in this expression have opposite signs than those presented in (5.28), since they are on the right side of (5.29). In fact, here we should consider the outward unit normal vector of the boundary of $\Omega_s$, i.e. $\boldsymbol{n}_s^{\pm}$ in Fig. 5.4a, but for the sake of simplicity, we denoted $\boldsymbol{n}_s^+ = -\boldsymbol{n}_s^- = \boldsymbol{n}_s$(Fig. 5.4b).

Inside the sheet, we assume that the local magnetic field is written as $\boldsymbol{h}_x(x,y,z,t) = \boldsymbol{h}_x(x,z,t)\zeta(y)$ and the test function as $\boldsymbol{h}'_x(x,y,z) = \boldsymbol{h}'_x(x,z)\zeta'(y)$, with $\boldsymbol{h}_x(x,z,t)$ and $\boldsymbol{h}'_x(x,z,t)$ tangential to $\Gamma_s$, and $\zeta(y)$ and $\zeta'(y)$ differentiable in the interval $-d/2 \leq y \leq d/2$. The volume integrals terms in (5.29) are then reduced to surface integrals terms as follows

$$\begin{aligned} &\Big(\rho \nabla \times \boldsymbol{h}, \nabla \times \boldsymbol{h}' \Big)_{\Omega_s} = \Big(\rho \nabla \times (\boldsymbol{h}_x \zeta), \nabla \times (\boldsymbol{h}'_x \zeta') \Big)_{\Omega_s} \\ &= \Big(\rho \left(\zeta \nabla \times \boldsymbol{h}_x - \boldsymbol{h}_x \times \nabla \zeta\right), \zeta' \nabla \times \boldsymbol{h}'_x - \boldsymbol{h}'_x \times \nabla \zeta' \Big)_{\Omega_s} \\ &\overset{\text{2-D}}{=} \Big\langle \boldsymbol{h}_x, \boldsymbol{h}'_x \Big\rangle_{\Gamma_s} \cdot \int_{-d/2}^{d/2} \rho \partial_y \zeta \partial_y \zeta' dy, \end{aligned} \tag{5.30}$$

$$\begin{aligned} \partial_t \Big(\mu \boldsymbol{h}, \boldsymbol{h}' \Big)_{\Omega_s} &= \partial_t \Big(\mu \boldsymbol{h}_x \zeta, \boldsymbol{h}'_x \zeta' \Big)_{\Omega_s} \\ &= \partial_t \Big\langle \boldsymbol{h}_x, \boldsymbol{h}'_x \Big\rangle_{\Gamma_s} \cdot \int_{-d/2}^{d/2} \mu \zeta \zeta' dy, \end{aligned} \tag{5.31}$$

where $\Gamma_s = \Gamma_s^+ \cup \Gamma_s^-$. Note that the expansion in (5.30) has been reduced to the 2-D case, so that $\boldsymbol{h}_x$ is independent of $z$, i.e., $\boldsymbol{h}_x(x,t)$, and the terms $\nabla \times \boldsymbol{h}_x$ and $\nabla \times \boldsymbol{h}'_x$ vanish. In 3-D, these terms should be taken into account.

By choosing $\zeta$ and $\zeta'$ as $\theta_p$ and $\theta_q$, respectively, the integral terms in (5.30) and (5.31) are seen to be components of the elementary matrices $[\mathcal{S}]$ and $[\mathcal{M}]$ in (5.25) and (5.26). Finally, taking the weak form of the $H$-formulation (5.28) with the interface terms rewritten (5.29) using (5.30) and (5.31), then estimating for each degree of freedom in $\Gamma_s(x,z)$ the variation in $y$ using (5.20) with a system of the form (5.24), we obtain a coupled system of equations

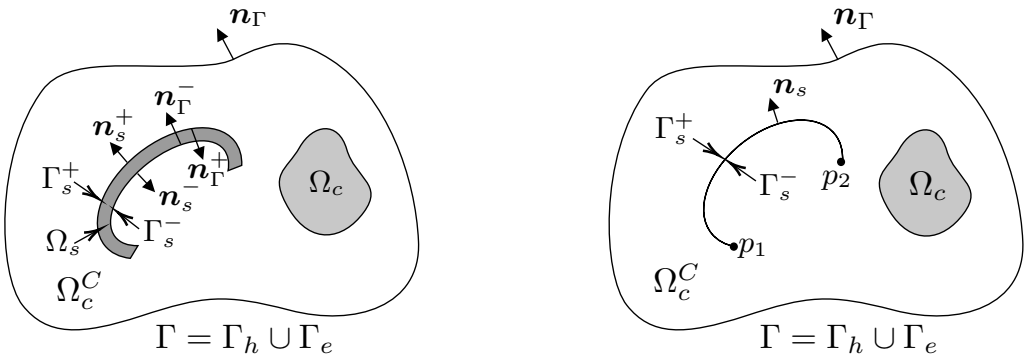


Figure 5.4 Computational domain: (a) full representation of $\Omega_s$ in $\Omega$, and (b) reduced-dimension problem, with $\Omega_s$ replaced by a lower-dimensional region $\Gamma_s$.

for the magnetic field inside and outside the TS. The IBCs in the proposed TS model are obtained from (5.29)-(5.31). Note that, with a single pair of hyperbolic basis functions, these equations become equivalent to the IBCs (5.15) and (5.16) of the classical TS model.

## 5.4 Validation and Application

We consider a 2-D planar shield (width $l = 1\,\text{m}$ and thickness $d = 1\,\text{mm}$) placed over a pair of wires carrying a current $\pm I$ (Fig. 5.5). The conductors are $2\text{x}2\,\text{cm}^2$ separated by a distance of $l_1 = 30\,\text{cm}$, and the distance between the conductors and the shield is $l_2 = 10\,\text{cm}$. The free-space region is $4\text{x}4\,\text{m}^2$. The coordinate system $xyz$ is defined at the center of the shield geometry and we evaluate the magnetic field distribution along the lines $AA'(x = 0,\, y)$, $BB'(x, y = 10\,\text{cm})$ and $CC'(x = l/2 - l/100, y)$, and at points $P_1(x = 0, y = 10\,\text{cm})$, $P_2(x = l/4, 0)$ and $P_3(x = l/2 - l/100, 0)$.

The application of standard FEM using the $H$-formulation with a full 2-D representation of the shield gives the reference solution. The solutions obtained with the application of the TS model are here compared with the reference solution in terms of local field distributions, Joule losses and mesh simplification.

The relative difference ($\mathcal{R}$) between the solutions is calculated as

$$\mathcal{R}\ [\%] = \frac{\|\text{TSS} - \text{FES}\|_2}{\|\text{FES}\|_2} \times 100, \tag{5.32}$$

where TSS and FES are the TS and the reference FE solutions, respectively, and $\|.\|_2$ denote the Euclidean norm of the argument.

In terms of mesh parameters, we defined a structured rectangular mesh in $\Omega_s$ with 12 elements across the shield thickness in the FE model (Fig. 5.6a-left). The shield surface was discretized in 1 mm wide elements, and 100 mm wide elements were considered on the external boundary. Moreover, first-order edge elements were used in $\Omega$.

With the described mesh configuration, the application of the TS model (Fig. 5.6a-right) with $n = 1$ represents a reduction in the total number of DoFs by 14.3% in comparison with the FE model. However, a more significant reduction can be achieved with the TS model since a coarser mesh can be employed while maintaining a sufficiently high mesh quality and solution accuracy.

According to [6], the quality of the triangular mesh can be evaluated by computing the aspect ratio of the inscribed radius to the circumscribed radius of every triangle. For the meshes presented in Fig. 5.6a, the smallest aspect ratios are 0.408 and 0.513 for the 2-D FE and the TS models, respectively. If a coarser mesh is considered, e.g., elements of size 10 mm in the shield surface (Fig. 5.6b), these aspect ratios become 0.085 and 0.621, respectively. In this case, the low quality of the mesh in the standard FE may reduce the solution accuracy and its convergence. Therefore, with elements of 10 mm, the TS approach is preferable. It allows reducing the number of DoFs by 80.9% compared to mesh in the FE reference model while maintaining the initial mesh quality in the 2-D domain. Thus, 10 mm wide elements were used in the TS model.

All the models described in this paper were implemented in the open-source code Gmsh [60] and the solver GetDP [122]. Simulations were conducted on a personal computer with an Intel i7 2400 processor and 16 Gb of memory. Harmonic and time-transient simulations for different types of shields were performed.

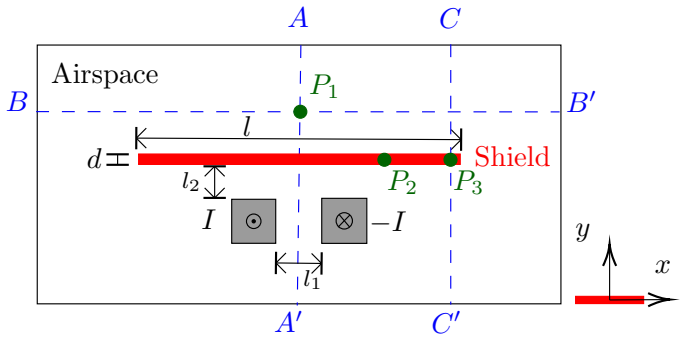


Figure 5.5 Geometry of the planar shield placed over a pair of wires, and lines $AA'$ $BB'$ and $CC'$, and points $P_1$, $P_2$ and $P_3$ where the local distributions of the fields are analyzed.

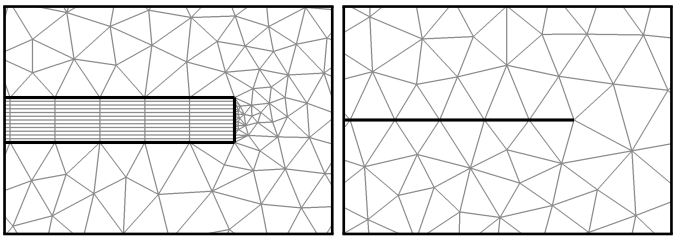

(a) Mesh with 1 mm wide elements: FE (left) and TS (right).

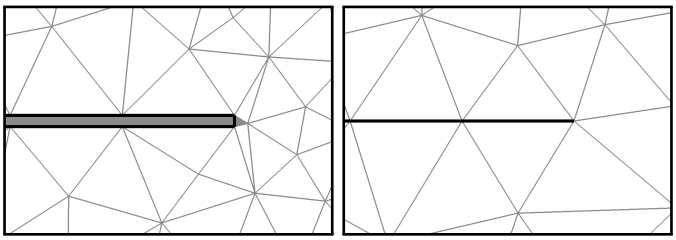

(b) Mesh with 10 mm wide elements: FE (left) and TS (right).

Figure 5.6 Mesh differences near the right edge of the shield with (a) 1 mm and (b) 10 mm wide elements. For better visualization of the elements in the surroundings of the shield, figures in (a) and (b) are not to same scale. Figures in (a) were zoomed-in $\times 4$ compared to figures in (b).

### 5.4.1 Time-Harmonic Regime

Simulations were first performed in the harmonic regime for the sake of validation of the proposed TS model. The current $I$ was set to 6 kA (current density of 15 A/mm$^2$) at an operating frequency of $f = 50$ Hz, and two shield configurations were studied:

**shield 1**: $\mu_r = 1$ and $\sigma = 1$ MS/m $\Rightarrow \delta = 71.2$ mm,

**shield 2**: $\mu_r = 1000$ and $\sigma = 10$ MS/m $\Rightarrow \delta = 0.712$ mm,

where $\mu_r = \mu/\mu_0$ is the relative magnetic permeability with respect to $\mu_0$, the magnetic permeability of air.

The hyperbolic basis functions $\psi^{\pm}$ in (5.9) were defined accordingly. With the first shield configuration, the basis functions are equivalent to those presented in Fig. (5.2), since $\delta \gg d$. With the second configuration, the hyperbolic basis functions were defined with $\delta = 0.712$ mm (or $\delta = 1.40d$, since $d = 1$ mm). For harmonic regime simulations, only one pair of hyperbolic basis functions was considered ($n = 1$).

Real and imaginary components of $h_x$ at points $P_2$ and $P_3$ inside the shields are presented in Fig. 5.7 and in Fig. 5.8, respectively. The field profiles from the TS model were obtained by evaluating the field intensities in the shield with the proposed hyperbolic basis functions.

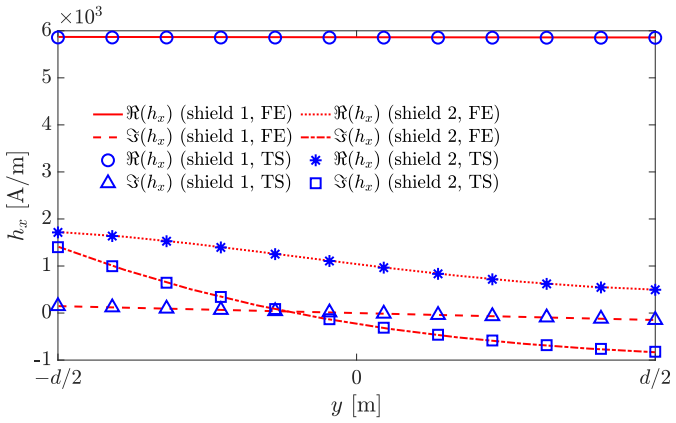


Figure 5.7 Profile of $h_x$ at point $P_2$ inside shield 1 ($\delta \gg d$) and shield 2 ($\delta < d$).

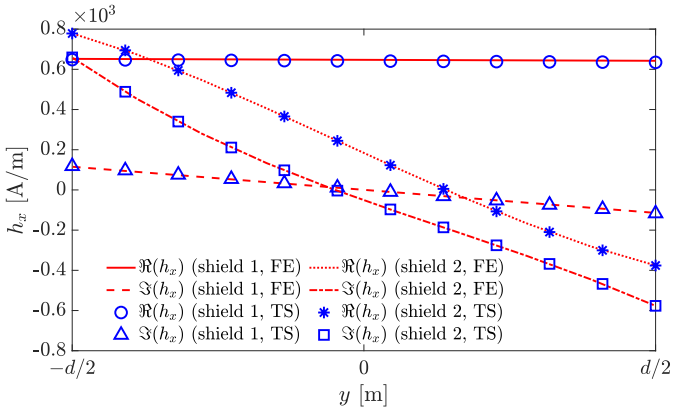


Figure 5.8 Profile of $h_x$ at point $P_3$ inside shield 1 ($\delta \gg d$) and shield 2 ($\delta < d$).

Excellent agreement with reference solutions in terms of real and imaginary components of $h_x$ were observed for both shield configurations. The excellent agreement at point $P_3$ shows that the proposed model can provide accurate solutions also near the extremities of the shield. Therefore, even though no special consideration has been made at its extreme points, edge effects are correctly represented.

In Fig. 5.9, we present a shaded plot of the magnetic flux density. With the first shield configuration (Fig. 5.9a), the replacement of the original 2-D region by a thin sheet has no noticeable impact on the magnetic flux density distribution. Indeed, from Fig. 5.7 and Fig. 5.8, we observe that $h_x$ is almost constant inside shield 1. The tangential components of the field are continuous on the surface representation in the TS model. However, with the second shield configuration (Fig. 5.9b), the physics inside the plate produces a discontinuity of $h_x$ that deforms the flux lines in the air surrounding the edge. Thus, in both shield configurations, the solution from the TS model agrees with the FE solution in terms of field

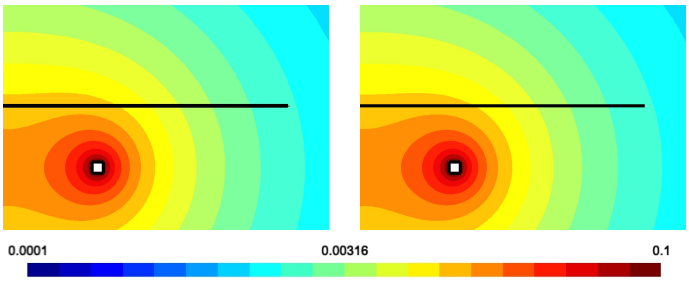


(a) shield 1: FE solution (left) and TS solution (right)

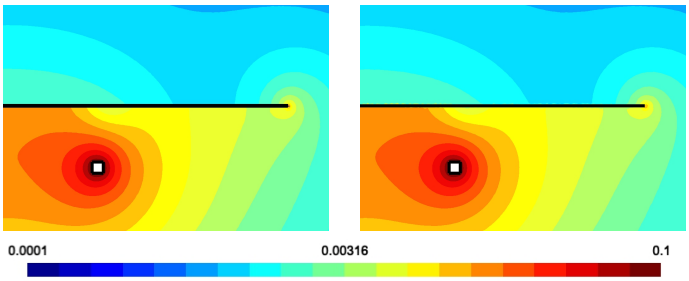


(b) shield 2: FE solution (left) and TS solution (right)

Figure 5.9 Shaded plot of the isovalues of the magnetic flux density ($|\boldsymbol{b}|$) in half of domain (a) shield 1, and (b) shield 2. Note the difference between the solutions depending on the shielding configuration, and the equivalence between the FE (right) and the TS (left) solutions in both cases. The airspace is not to scale.

distributions inside and outside the shield.

The relative differences for the local magnetic field along lines $AA'$, $BB'$ and $CC'$, and at points $P_2$ and $P_3$ were computed with (5.32). The $\mathcal{R}$-values are summarized in Table 5.1. The maximum difference is 2.46% and occurs on line $CC'$ and point $P_3$ with shield 2. This difference may be related to the geometrical difference between the TS and the FE models. Since the thickness of the shield is not represented in the TS model, it is expected to observe at least a slight difference near its extremities.

### 5.4.2 Time-Transient Regime (Linear Case)

Time-transient simulations of the planar shield were also performed. In this study, we applied a pulsed current source in the wires whose waveform produces the magnetic field shown in Fig. 5.10 and 5.11 (black dashed lines) in absence of the shield. The amplitude of the current $I$ is the same as in the harmonic regime cases ($|I| = 6\,\text{kA}$), and the rise time ($t_r$) was set to $20\,\mu\text{s}$. The simulation time was $t_{\text{max}} = 50\,\mu\text{s}$ with a time-step of $t_{\text{max}}/120$. The implicit Euler scheme was used.

Table 5.1 Relative differences for the magnitude of the magnetic field on lines $AA'$, $BB'$, $CC'$, and points $P_2$ and $P_3$ depicted in Fig. 5.5

| | $AA'$ | $BB'$ | $CC'$ | $P_2$ | $P_3$ |
|---|---|---|---|---|---|
| Shield 1 | 0.72% | 1.22% | 1.95% | 0.14% | 0.92% |
| Shield 2 | 0.90% | 1.56% | 2.46% | 1.29% | 2.46% |

In terms of material composition, two new shielding configurations were studied:

**shield 3**: $\mu_r = 1000$ and $\sigma = 1\,\mathrm{MS/m}$,

**shield 4**: $\mu_r = 100$ and $\sigma = 10\,\mathrm{MS/m}$.

Shields 3 and 4 are both ferromagnetic, but shield 4 is more conductive than shield 3. The simulation time was chosen to define the fundamental frequency as $f = 1/(4t_{\max})$, i.e. $f = 5\,\mathrm{kHz}$. Therefore, these shields have same penetration depth $\delta = d/4.44$. Consequently, the same hyperbolic basis functions can be used to tackle these problems. The first set of basis functions was defined with frequency equal to the fundamental ($f_1 = f$). Additional basis functions were then calculated using odd harmonic frequencies of $f_1$, i.e., $f_k/f_1 = 2k - 1$, with $1 \leq k \leq n$.

In Fig. 5.10 and 5.11, the time-evolution of $h_y$ at point $P_1$ was compared with the reference solution for shield 3 and 4, respectively. The number of basis functions in the TS model was varied from 1 to 3, and the solutions approached the reference solution as $n$ increased.

The relative differences of the profiles of $h_y$ in the TS model to the reference solution as a function of the number of basis functions $n$ are presented in Fig. 5.12. The maximum relative difference $\mathcal{R}$ decreases from 245.8% with $n = 1$ to 2.95% with $n = 2$, and to less than 2% for $n \geq 3$. Simulations with $n > 3$ show little improvement in terms of solution accuracy. This is mainly due to the geometrical differences between the FE and the TS models, as discussed in the time-harmonic regime case. Despite this, the application of the TS model shows a good compromise between computational cost and solution accuracy.

The number of DoFs, the computation time and the Joule losses in the reference and TS models are summarized in Table 5.2. Since a coarser mesh was applied in the TS model, simulations are more than five times faster with this approach than with standard FE. The number of DoFs is nearly independent of $n$, and is reduced by more than 70%, even with $n = 5$. Despite this, the relative error in losses estimation is less than 2% with $n \geq 3$ in shields 3 and 4.

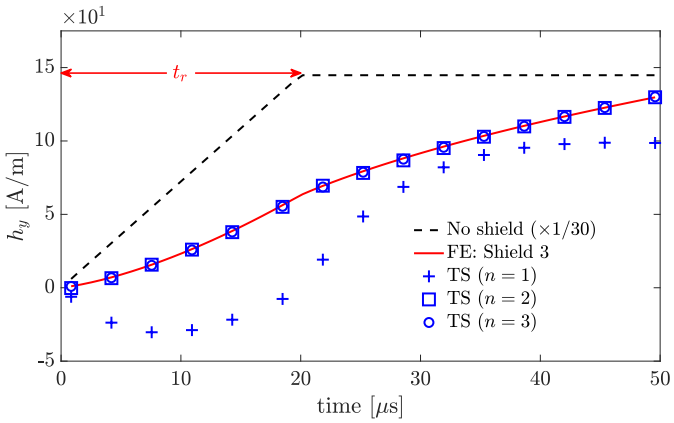


Figure 5.10 Time-evolution of $h_y$ at point $P_1$ with pulsed current imposed to the wires and a ferromagnetic shield configuration (Shield 3). Results obtained with $n$ up to 3 in the TS model compared with the FE solution.

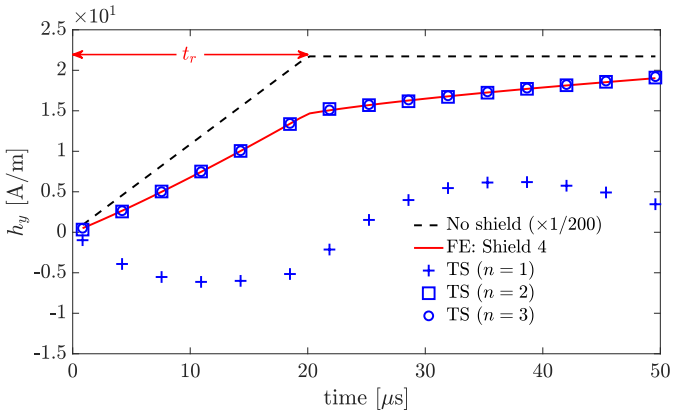


Figure 5.11 Time-evolution of $h_y$ at point $P_1$ with pulsed current imposed to the wires and a conductive shield configuration (Shield 4). Results obtained with $n$ up to 3 in the TS model compared with the FE solution.

### 5.4.3 Time-Transient Regime (Nonlinear Case)

In an attempt to extend the proposed TS model to nonlinear analysis, the shielding problem was also studied for shields with nonlinear magnetic permeability ($\mu = \mu(\boldsymbol{h})$). A sinusoidal supply current of amplitude $|I| = 6\,\text{kA}$ at an operating frequency $f = 1\,\text{kHz}$ was applied to the wires. The effects of the saturation and the influence of the number basis functions in the proposed TS model were analyzed in terms of solution accuracy.

The material properties were modelled with an isotropic saturation law expressing the

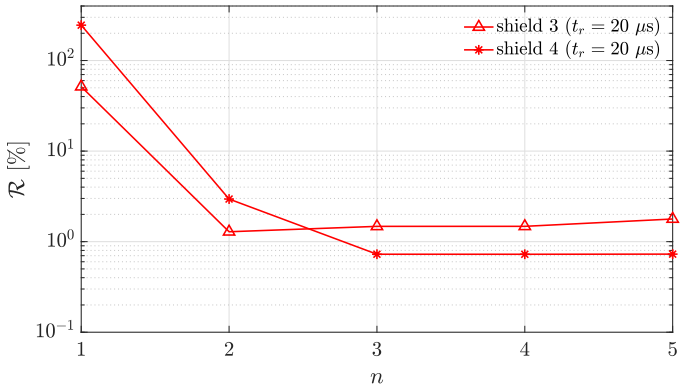


Figure 5.12 Relative difference $\mathcal{R}$ of instantaneous $h_y$ at point $P_1$ as a function of $n$ in the TS approach for $t_r = 20\,\mu$s in the time-transient study. Note the fast convergence towards the FE solution.

Table 5.2 Number of DoFs, CPU time and total Joule losses in shields 3 and 4 in time-transient analysis

| Model | Number of DoFs | CPU time [s] | Joule losses Shield 3 [J/m] | Joule losses Shield 4 [J/m] |
|---|---|---|---|---|
| Standard FE | 176054 | 1040.12 | 2.4915 | 0.7514 |
| TS ($n = 1$) | 33636 | 189.97 | 2.4503 | 0.7676 |
| TS ($n = 2$) | 34036 | 205.19 | 2.5103 | 0.7596 |
| TS ($n = 3$) | 34436 | 221.40 | 2.5099 | 0.7592 |
| TS ($n = 4$) | 34836 | 276.58 | 2.5099 | 0.7592 |
| TS ($n = 5$) | 35236 | 309.15 | 2.5087 | 0.7592 |

magnetic permeability as a function of the magnetic field intensity, i.e.,

$$\mu(\boldsymbol{h}) = \mu_0 \left(1 + \left(\frac{1}{\mu_{r0} - 1} + \frac{||\boldsymbol{h}||}{m_0}\right)^{-1}\right), \tag{5.33}$$

where $\mu_{r0}$ is the relative permeability at origin and $m_0$ the saturation magnetic field in A/m. The differential permeability required for the application of the NR-scheme was defined as in [43]. We carried out simulations with $\mu_0 m_0 = 1.31$ and $\mu_{r0} = 12500$. The $B$-$H$ curve is presented in Fig. 5.13. Furthermore, the electrical conductivity of the shield was fixed at $\sigma = 1\,$MS/m.

One time period was simulated, i.e., $t_{max} = 1/T$, with $T = 1/f$. Moreover, the time-step was set to $\Delta t = T/120$, and the maximum number of iterations for the NR-scheme was set to 12 in both the reference and the proposed TS models. Besides, the number of points used in the Legendre-Gauss quadrature was 20 points. This number of points is considered sufficiently

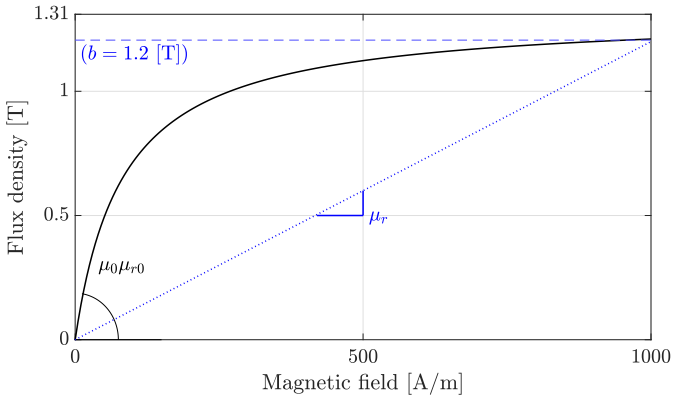


Figure 5.13 $B$-$H$ saturation curve obtained from (5.33) with $\mu_0 m_0 = 1.31$ and $\mu_{r0} = 12500$. The intersection of the $B$-$H$ curve with the horizontal dashed line gives $\mu_r = 1000$, which was used to parametrize the hyperbolic basis functions.

high to avoid errors related to the numerical integration of the hyperbolic functions across whole the thickness of the shield. Depending on the penetration depths of the basis functions, less integration points could be used, but we kept 20 at all times to remains on the safe side.

The first set of hyperbolic basis functions was defined by taking $f_1 = f$ and higher order basis functions that are odd multiples of $f_1$. Furthermore, the magnetic permeability used in the definition of the basis functions was taken from the $B$-$H$ curves corresponding to a flux density $b = 1.2$ T, i.e., $\mu_r = 1000$ for $\mu_{r0} = 12500$. A similar approach was used in [123] to parametrize basis functions for nonlinear SIBCs.

Fig. 5.14 shows the $h_x$ profile throughout the thickness of the shield for three specific simulation times ($T/8$, $T/4$ and $T/2$). Results are presented for $n = 1$ to 3 and compared with the 2-D FE solution. Note that the accuracy of the proposed TS model clearly improves with $n$. Since the penetration depth used to define the hyperbolic basis functions is at the same time inversely proportional to the square root of $f$ and $\mu_r$, the additional frequency components can be interpreted as a way to consider an increase of the magnetic permeability. For this reason, the saturation effects observed at $t = T/8$ and $t = T/2$ are well represented with the proposed TS model when considering higher harmonic components. The relative difference between the solutions at $t = T/8$ is reduced to less than 1% with $n = 3$ (Fig. 5.15).

The time-evolution of $h_y$ at point $P_1$ is shown in Fig. 5.16. The solution of the 2-D FE problem without the shield gives the field at this point, which has the same waveform as the current $I$ applied to the wires. The solution for a linear shield problem with $\mu_r = 12500$ is presented for the sake of comparison with the nonlinear solution. Finally, the solution for the shield modeled with the TS model shows improvement as $n$ increases, while high accuracy is

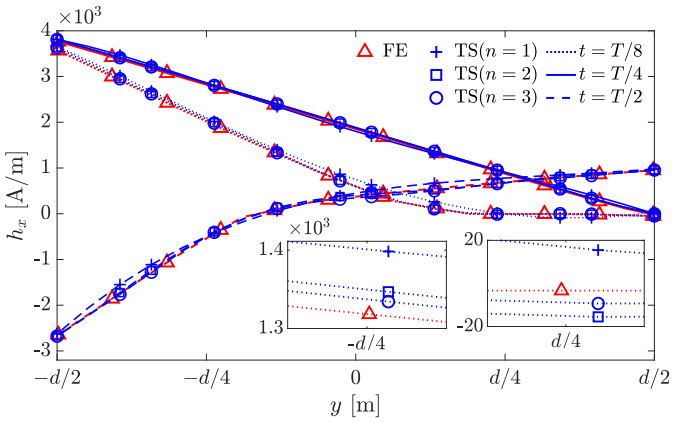


Figure 5.14 Profiles of $h_x$ inside the nonlinear shield at point $P_2$ and at $t = T/8$, $T/4$ and $T/2$ obtained with the 2-D FE solution and with the TS model for $n = 1$ to 3. The insets show the solutions at $T/8$ and $y = \pm d/4$.

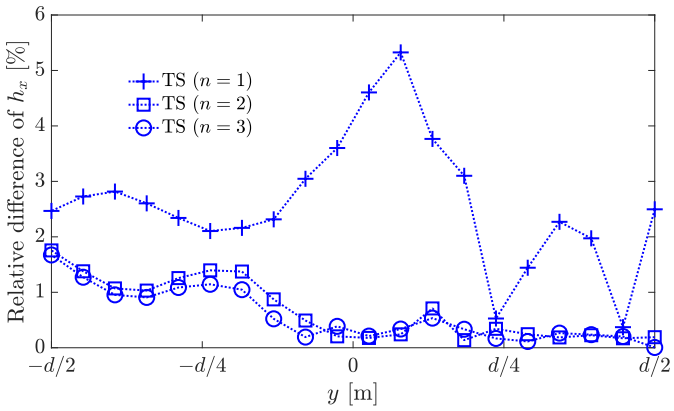


Figure 5.15 Relative difference between the TS and the reference FE solutions for the $h_x$ profile inside the nonlinear shield at $P_2$ and $t = T/8$.

observed when compared to the nonlinear reference solution. The saturation effect is clearly observed.

The relative difference of the TS model to the FE solution at $P_1$ at each time step is presented in Fig. 5.17. It was reduced from more than 5% with $n = 1$ to less than 1% with $n \geqslant 2$. With a suitable choice of the basis functions, the proposed TS model can certainly be an option for simulating nonlinear thin sheets.

## 5.5 Conclusion

In this paper, a time-domain extension of the classical TS model for thin sheets was elaborated and discussed using the $H$-formulation. In our approach, the addition of $n$ sets of basis

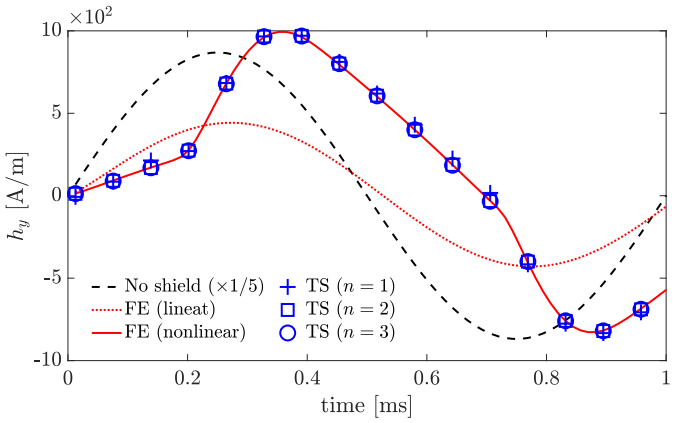


Figure 5.16 Time-evolution of $h_y$ at point $P_1$ for the nonlinear case. The solutions obtained from the TS model with $n = 1$ to 3 are compared with the 2-D FE solution. Solutions without the shield and in linear case ($\mu_r = 12500$) are presented for the sake of comparison.

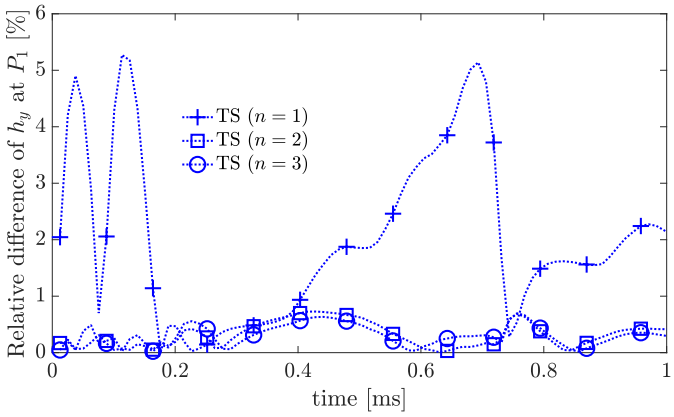


Figure 5.17 Relative difference between the TS and the reference FE solutions for the time-evolution of $h_y$ at point $P_1$ for the nonlinear case.

functions derived from the steady-state solutions for the problem of a slab of finite thickness permits the representation of the time evolution of the field quantities inside the thin region and its surroundings. We did apply this method to analyze the shielding efficiency of conducting and ferromagnetic planar sheets in harmonic and time-transient regimes for linear and nonlinear shield configurations.

In the harmonic regime, the proposed model gives IBCs equivalents to those used in the classical TS model, since both methods are based on the solutions (5.7) and (5.8) and are directly included in the FE formulation. Our model, however, can also be used in time-transient FE analysis. We showed that, by adding a small number of hyperbolic basis functions, high precision can be achieved. In all cases, the relative differences were $< 3\%$

with the reference solutions with $n \geqslant 3$, including the critical region near the extremities of the shield. Furthermore, the proposed model can achieve comparable errors with less degrees of freedom, and hence at a lower computational cost, while also avoiding meshes with poor aspect ratios.

The TS model presented in this paper is still application-dependent since the set of hyperbolic basis functions must be defined according to the frequency content of the magnetic field inside the thin region, as well as the material composition of the sheet. Although we did not yet find a general rule to select the basis functions, the latter are easy to derive since they originate from the analytic solutions of the 1-D linear flux diffusion problem in harmonic regime. Therefore, as long as the set of basis functions is rich enough to represent a diversity of penetration depths (which varies dynamically with local magnetic saturation), nonlinear solutions can be well approximated with this approach. Finally, the presented methodology can be easily extended to other FE formulations, such as the $A$-formulation, as well as 3-D shielding problems.

**Acknowledgment**

The authors would like to thank Prof. Christophe Geuzaine for fruitful discussions and for putting the Gmsh and GetDP codes in the public domain.

This work has been supported in part by the Coordenação de Aperfeiçoamento de Pessoal de Nível Superior – Brazil (CAPES) - Finance code 001, and in part by the Fonds de Recherche du Québec - Nature et Technologies (FRQNT). Also, the collaboration between the authors was greatly facilitated by the MITACS Globalink internship program.

# CHAPTER 6 PAPER 2: THIN-SHELL APPROACH FOR MODELING SUPERCONDUCTING TAPES IN THE $H$-$\phi$ FINITE-ELEMENT FORMULATION

IOP SUPERCONDUCTOR SCIENCE AND TECHNOLOGY

(Paper submitted on August 13, 2021, and accepted for publication on December 2, 2021)

[1]Bruno de Sousa Alves, [2]Valtteri Lahtinen, [1]Marc Laforest, [1]Frédéric Sirois

[1]Polytechnique Montréal, Montréal, QC H3C 3A7, Canada

[2]QCD Labs, Department of Applied Physics, QTF Centre of Excellence, Aalto University, 00076, Aalto, Finland

**Abstract**

This paper presents a novel finite-element approach for the electromagnetic modeling of superconducting coated conductors. We combine a thin-shell (TS) method to the $H$-$\phi$-formulation to avoid the meshing difficulties related to the high aspect ratio of these conductors and reduce the computational burden in simulations. The interface conditions in the TS method are defined using an auxiliary 1-D finite-element (FE) discretization of $N$ elements along the thinnest dimension of the conductor. This procedure permits the approximation of the superconductor's nonlinearities inside the TS in a time-transient analysis. Four application examples of increasing complexity are discussed: (i) single coated conductor, (ii) two closely packed conductors carrying anti-parallel currents, (iii) a stack of twenty superconducting tapes and (iv) a full representation of a HTS tape comprising a stack of thin films. In all these examples, the profiles of both the tangential and normal components of the magnetic field show good agreement with a reference solution obtained with standard 2-D $H$-$\phi$-formulation. Results are also compared with the widely used $T$-$A$-formulation. This formulation is shown to be dual to the TS model with a single FE ($N = 1$) in the auxiliary 1-D systems. The increase of $N$ in the TS model is shown to be advantageous at small inter-tape separation and low transport current since it allows the tangential components of the magnetic field to penetrate the thin region. The reduction in computational cost without compromising accuracy makes the proposed model promising for the simulation of large-scale superconducting applications.

## 6.1 Introduction

High-Temperature Superconducting (HTS) tapes are used in increasingly complicated geometries [24, 27, 28, 126] and the accurate simulation of their current distribution in such geometries is being held back by (i) the high aspect ratio of the meshes required to resolve the interior of the tapes and (ii) the nonlinearity of the $E$-$J$ relationship. Despite the diversity of available formulations of Maxwell's equations, the development of accurate and efficient numerical models is also hampered by the limitations of each formulation [67]. The purpose of this research is to develop a finite-element (FE) model to accurately and efficiently predict current distribution and losses in HTS tapes. The techniques proposed in this research are shown to be valid for time-domain models, treating nonlinear materials (both HTS and ferromagnetic), and complex magnetic field profiles in the tapes.

We assume a 2-D computational domain $\Omega$ comprising $K$ disjoint thin conducting regions $\Omega_{c,1}, \ldots, \Omega_{c,K}$, each of which can be described in its own local coordinate system as a very long tape of length $L$ in the $z$-direction (out-of-plane), of width $l \approx$ 4-12 mm in the $x$-direction, and of thickness $d \approx 1\,\mu$m in the $y$-direction (Fig. 6.1a). The current distribution is assumed constant in $z$. For HTS tapes, where the magnetic field penetration generates sharp current fronts, traditional FE meshes require several elements in the $y$-direction and hence introduce elements with high aspect ratios. These irregular meshes lead to poor accuracy and slow convergence for iterative nonlinear solvers.

In conventional (ohmic) conductors and linear ferromagnetic materials, the meshing of each thin layer can be avoided by using the classical *thin-shell* (TS) model [31–34]. In this case, the volume of the thin region (or its surface in a 2-D case) is collapsed onto a surface (or a line in 2-D) situated halfway in the $y$-direction between its upper and lower faces (Fig. 6.2b) while permitting discontinuities for field quantities across the surface. The TS model averages the magnetic flux density and current profiles in the transverse direction and couples the electric and magnetic effects by means of two interface conditions (ICs) [34]. The dimensionality reduction in this model avoids completely the need for meshing the thin region, resulting in gains in terms of computational cost [8].

The ICs in the classical TS model are obtained from the analytical solutions of the 1-D linear flux diffusion equation across the thickness of the thin structure [34]. Depending on the choice of the primary variables for the EM problem, these ICs can be written in terms of different field quantities [95]. For example, in the weak form of the magnetic field ($H$)-formulation, the interface terms arising from the application of Green's formula depend on the value of the *tangential component of the electric field* [9–12], while in a magnetic vector potential


(a) Reference model (b) TS model

Figure 6.1 Computational domain comprising $K$ disjoint thin conducting regions $\Omega_{c,1}, \ldots \Omega_{c,K}$ and their representation in the TS model. The non-conducting region is denoted by $\Omega_c^C$ such that $\Omega = \Omega_c \cup \Omega_c^C$ and $\Omega_c = \cup_{i=1}^{K} \Omega_{c,i}$.

($A$)-formulation, the equivalent interface terms depend on the *tangential components of the magnetic field* [11, 12, 93, 94, 101, 102].

Time-domain and nonlinear extensions of the TS model are usually derived from the ICs described above. In [102], the authors proposed using mathematical expansions in terms of Legendre polynomials to define ICs in laminated iron cores. The method is extended to nonlinear shielding analysis in [12], and the nonlinear system of equations is solved using the Newton-Raphson (NR) method. Both the $H$- and $A$- formulations are studied in that paper. In [9], the inverse fast Fourier transform of harmonic solutions with classical ICs is used to update the residual in nonlinear time-domain simulations. Shielding problems are also tackled in that paper, but only in the context of nonlinear ferromagnetic materials. So far, no time-domain TS model that considers tangential field penetrations has been proposed or applied to solve problems involving highly nonlinear conductive thin films, such as those found in HTS tapes.

When the current density distribution across the thickness of the thin region is assumed constant, the ICs expressions can be simplified. This approach is called *strip approximation* [76], and it has been originally implemented with integral methods [17]. The strip approximation implies that the tangential components of $H$ have a linear profile inside the tape, which differs from the hyperbolic profiles encountered in the classical TS model [127]. Only the losses related to the normal flux density components (edge losses) are taken into account by this approximation, which means that the so-called top/bottom losses [79] are disregarded. This is valid as long as the *normal component* of $H$ dominates the dynamics of the problem, which is often the case when modeling simple problems involving HTS tapes, but not when these tapes are closely together [25, 128, 129].

In recent years, a TS model based on a $T$-$A$-formulation and fully implemented in FE has been proposed [35]. This model is now widely used to model HTS tapes [108, 110, 113, 114].

It involves solving an auxiliary 1-D FE problem in terms of the current vector potential $T$, related to the normal component of $H$ across the tape width. A surface current density is computed from $T$ and imposed in the standard $A$-formulation. However, combining the 1-D expressions for $T$ in the $A$-formulation, we find ICs similar to a TS model with linear $H$-profile inside the tape (or a constant current density across its thickness). As in the strip approximation, the $T$-$A$-formulation is only suitable for cases where the influence of the tangential components of $H$ can be neglected [108]. Moreover, the coupling between the state variables $T$ and $A$ requires higher-order FE for $A$ in order to avoid oscillations in the numerical solution [108], which mostly limits its application to 2-D simulations [109]. A similar FE approach based on a mixed $A$-$H$-formulation has also been proposed in [72, 73].

In this paper, a new time-domain TS model is presented and applied to a $H$-based formulation for solving the current challenges in modeling HTS tapes. The ICs are here developed for 2-D cases and written in terms of a small number of auxiliary 1-D FE problems across the tape thickness to compute the penetration of the tangential components of $H$. Four examples are presented: (i) single HTS tape, (ii) two closely packed tapes, (iii) a stack of twenty HTS tapes, and (iv) an HTS tape comprising three thin layers. The magnetic scalar potential ($\phi$) is considered in non-conducting parts of the computational domain, and edge-based cohomology basis functions (or thick cuts) are used to impose a net transport current in the tapes. Since the state variables in the 1-D and the global FE systems are naturally connected, shape functions of same order can be used in both the systems, and no numerical oscillations appear. Moreover, the use of a single element in the 1-D FE discretization makes the proposed model equivalent to the $T$-$A$-formulation under specific conditions, while the 1-D mesh refinement enables improvements in the solution accuracy. We show that top/bottom and edge losses are correctly taken into account with our approach. All of these features make the proposed TS model ideal for simulating HTS devices in any context of use.

## 6.2 Mathematical Formulation

Before deriving the TS model, we define the EM problem and review the so-called magnetic field and magnetic scalar potential ($H$-$\phi$)-formulation, since our TS model is later integrated in this formulation. Note that the TS model presented in this paper could have also been rewritten in a pure $H$-formulation since $\phi$ is used mostly to reduce the computational cost in the non-conducting region.

### 6.2.1 Problem Definition

The electrodynamics of superconductors at low frequencies can be formulated as a nonlinear eddy-current problem. The computational domain is defined as $\Omega = \Omega_c \cup \Omega_c^C \subset \mathbb{R}^3$, where $\Omega_c$ and $\Omega_c^C$ denote the conductive and non-conductive parts of $\Omega$, respectively. Moreover, $\Omega$ has a boundary $\partial\Omega$ denoted by $\Gamma$. The superconducting region, denoted by $\Omega_s$, belongs to $\Omega_c$, i.e., $\Omega_s \subset \Omega_c$. Neglecting displacement currents, the Maxwell equations governing this problem are

$$\nabla \times \boldsymbol{h} = \boldsymbol{j}, \tag{6.1}$$

$$\nabla \times \boldsymbol{e} = -\partial_t \boldsymbol{b}, \tag{6.2}$$

$$\nabla \cdot \boldsymbol{b} = 0, \tag{6.3}$$

where bold characters represent vectors, $\boldsymbol{h}$ is the magnetic field, $\boldsymbol{b}$ is the magnetic flux density, $\boldsymbol{e}$ is the electric field and $\boldsymbol{j}$ the current density. The operator $\partial_t$ represents the time derivative. Additionally, two constitutive relations connecting these four fields quantities are required, i.e.

$$\boldsymbol{b} = \mu \boldsymbol{h}, \tag{6.4}$$

$$\boldsymbol{j} = \sigma \boldsymbol{e}, \tag{6.5}$$

where $\mu$ is the magnetic permeability and $\sigma$ is the electrical conductivity.

The boundary conditions impose the tangential components of either $\boldsymbol{h}$ or $\boldsymbol{e}$ in the following manner. We assume that there are known tangential vector fields $\boldsymbol{f}_h$ and $\boldsymbol{f}_e$ such that for all $t$,

$$\boldsymbol{n} \times \boldsymbol{h}(\boldsymbol{x}, t) = \boldsymbol{f}_h(\boldsymbol{x}, t), \qquad \forall \boldsymbol{x} \in \Gamma_h, \tag{6.6}$$

$$\boldsymbol{n} \times \boldsymbol{e}(\boldsymbol{x}, t) = \boldsymbol{f}_e(\boldsymbol{x}, t), \qquad \forall \boldsymbol{x} \in \Gamma_e, \tag{6.7}$$

where $\boldsymbol{x}$ is any point in $\mathbb{R}^3$ and $\Gamma$ is subdivided into two complementary components $\Gamma_h$ and $\Gamma_e$ (i.e. $\Gamma = \Gamma_h \cup \Gamma_e$ and $\Gamma_h \cap \Gamma_e = \varnothing$) where boundary conditions (6.6) and (6.7) may be applied, respectively.

The resulting system (6.1)-(6.3) is nonlinear when $\mu$ and $\sigma$ depend on the fields quantities. For type-II superconductors, the nonlinear $E$-$J$ relation is often expressed by a power-law characteristic [21], i.e.

$$\rho(\boldsymbol{j}) = \frac{e_c}{j_c} \left( \frac{|\boldsymbol{j}|}{j_c} \right)^{n_s - 1}, \tag{6.8}$$

where $\rho$ is the electrical resistivity ($\rho = 1/\sigma$) and the electric field criterion $e_c$ also determines the critical current density $j_c$ [43]. The power index $n_\mathrm{s}$ determines the steepness of the $E$-$J$ curve.

### 6.2.2 $H$-$\phi$-Formulation

The well-known $H$-formulation is obtained from the weak form of Faraday's law (6.2). Let $\boldsymbol{H}(\mathrm{curl}, \Omega) = \{\boldsymbol{u} : \Omega \to \mathbb{R}^3 \,|\, \|\boldsymbol{u}\| < \infty, \|\nabla \times \boldsymbol{u}\| < \infty, \boldsymbol{n} \times \boldsymbol{u} = \boldsymbol{f}_h \text{ over } \Gamma_h\}$ where $\|\boldsymbol{u}\|^2 = \int_\Omega \|\boldsymbol{u}\|^2 d\boldsymbol{x}$ is the $L^2$ norm, while $\boldsymbol{H}_0(\mathrm{curl}, \Omega)$ is the same space except with homogeneous boundary conditions $\boldsymbol{n} \times \boldsymbol{u} = 0$ over $\Gamma_h$. Following the usual process, the weak formulation is :

Find $\boldsymbol{h} \in \boldsymbol{H}(\mathrm{curl}, \Omega)$ such that

$$\Big(\rho \nabla \times \boldsymbol{h}, \nabla \times \boldsymbol{g}\Big)_\Omega + \partial_t \Big(\mu \boldsymbol{h}, \boldsymbol{g}\Big)_\Omega + \Big\langle \boldsymbol{n} \times \boldsymbol{e}, \boldsymbol{g} \Big\rangle_{\Gamma_e} = 0 \tag{6.9}$$

$\forall\, \boldsymbol{g} \in \boldsymbol{H}_0(\mathrm{curl}, \Omega)$, where $\boldsymbol{g}$ are test functions, $\boldsymbol{n}$ is the outward unit normal vector on $\Gamma$, and $(\cdot, \cdot)_\Omega$ and $\langle \cdot, \cdot \rangle_\Gamma$ respectively denote the volume and surface integrals over $\Omega$ and $\Gamma$ of the scalar product of their two arguments. The last term in (6.9) is required to impose Neumann boundary conditions (6.7) on the complementary surface portion $\Gamma_e$ of $\Gamma$, for physical or symmetry purposes [40]. Also, $\boldsymbol{h} \in \boldsymbol{H}(\mathrm{curl}, \Omega)$ already takes into account BC (6.6) along $\Gamma_h$.

In a pure $H$-formulation, $\boldsymbol{h}$ and $\boldsymbol{g}$ are normally described with the help of Whitney edge elements [65]. However, it is known that expressing the magnetic field in terms of the magnetic scalar potential ($\boldsymbol{h} = -\nabla\phi$) in $\Omega_c^C$ reduces the total number of DoFs and avoids errors such as leakage currents in $\Omega_c^C$, which appear in the pure $H$-formulation [61, 118]. In the so-called $H$-$\phi$-formulation, nodal elements are used in $\Omega_c^C$ and edge elements are used in $\Omega_c$. Since $\nabla(S^0) \subset S^1$, where $S^0$ and $S^1$ are respectively the nodal and the edge FE space, $\boldsymbol{h}$ and $\phi$ are naturally connected at the interface between $\Omega_c$ and $\Omega_c^C$ [64].

When $\Omega_c^C$ is multiply connected, the representation of $\boldsymbol{h}$ through $\phi$ is not enough to express Ampère's law in this region, since $\nabla \times \nabla\phi = 0\ \forall\phi$. Uniqueness is resolved by imposing discontinuities in $\phi$ along thin cuts in $\Omega_c^C$, whose values determine the currents in connected components of $\Omega_c$ [49]. However, manually defining these thin cuts can be tiresome for complex geometries comprising multiple conducting subdomains. Alternatively, thick cuts can be uniquely determined by requiring that they be dual to the set of closed loops $C_i$ around each independent conducting subdomain $\Omega_{c,i}$, $i = 1, \ldots, K$, with the loops being

constructed during the meshing process. The computation of these so-called cohomology basis representatives is inexpensive and implemented in Gmsh [55].

The general discrete expression for the magnetic field is

$$\boldsymbol{h} = \sum_{e\in\Omega_c} h_e \boldsymbol{w}_e + \sum_{n\in\Omega_c^C} -\phi_n \nabla w_n + \sum_{C_i\in\Omega_c^C} I_i \boldsymbol{\psi}_i, \tag{6.10}$$

where $\boldsymbol{w}_e$ are the vector basis functions (edge elements) of each edge $e$ in $\Omega_c$, $w_n$ are the nodal basis functions of each node $n$ in $\Omega_c^C$, and $\boldsymbol{\psi}_i$ are the edge-based cohomology basis functions dual to the set of closed loops $C_i$ whose coefficients $I_i$ correspond to the value of the integrals of $\boldsymbol{h}$ over these loops [55]. The discontinuity of $\phi$ is taken into account by the functions $\boldsymbol{\psi}_i$ so the $H$-$\phi$-formulation obeys Ampère's law everywhere in $\Omega$ [62].

The time derivative in (6.9) can be approximated by a finite difference discretization (e.g. implicit Euler, Runge-Kutta, etc). Then, substituting (6.10) into (6.9), and applying the Galerkin weighted residuals method, one obtains a nonlinear system of equations that can be solved, for example, with the NR-method.

In this paper, the $H$-$\phi$-formulation is selected to construct the reference FE solutions and the TS model of the next section. In order to illustrate the geometry of $\Omega$, Fig. 6.2a shows a single HTS tape in an air space region, which is, in this case, a multiply connected region since the tape represents a hole in $\Omega_c^C$. A single thick cut $\boldsymbol{\psi}_1$ is necessary to impose a current constraint in the tape and is presented in blue. The tape and the air space are not to scale. In the example, the mesh is defined with eight elements along the tape width and is merely illustrative. Note that for a fully discretized 2-D solution, elements with high aspect ratios are necessary inside the tape and near its extremities. A suitable discretization will be further considered to obtain reference solutions on a full-thickness geometry.

## 6.3 TS Model in the $H$-$\phi$-Formulation

In the TS model, $\Omega_s$ is collapsed to a surface $\Gamma_s$ located halfway between the original boundaries ($\Omega_s \rightarrow \Gamma_s$ in Fig. 6.2b). Two surface integral terms are then included in the weak form of the $H$-formulation (6.9), which becomes

$$\begin{aligned}\Big(\rho\nabla\times\boldsymbol{h},\nabla\times\boldsymbol{g}\Big)_{\Omega\setminus\Omega_s} + \partial_t\Big(\mu\boldsymbol{h},\boldsymbol{g}\Big)_{\Omega\setminus\Omega_s} \\ + \Big\langle \boldsymbol{n}\times\boldsymbol{e},\boldsymbol{g}\Big\rangle_{\Gamma_e} - \Big\langle \boldsymbol{n}_s\times\boldsymbol{e},\boldsymbol{g}\Big\rangle_{\Gamma_s^+} + \Big\langle \boldsymbol{n}_s\times\boldsymbol{e},\boldsymbol{g}\Big\rangle_{\Gamma_s^-} = 0,\end{aligned} \tag{6.11}$$

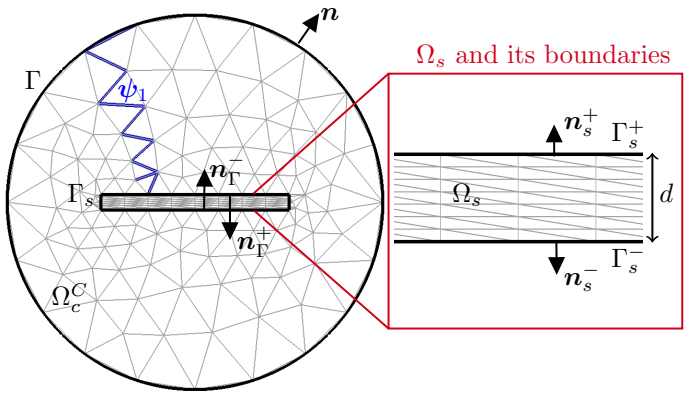


(a) Fully discretized HTS tape for standard FE application

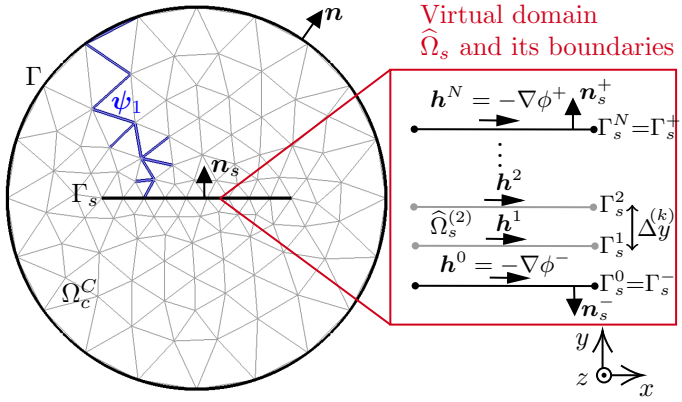


(b) Proposed TS model for a HTS tape

Figure 6.2 (a) Fully discretized domain for standard FEM application and (b) proposed TS model: example of a single HTS tape embedded in a non-conducting domain $\Omega_c^C$ with boundary $\Gamma$. Nodes and edges on the surface representation of the thin structure in the TS model are duplicated, creating a crack in the topological structure. The boundary of the thin region is $\Gamma_s = \Gamma_s^+ \cup \Gamma_s^-$. The thick cut $\boldsymbol{\psi}_1$ used to impose a current constraint in the tape is presented in blue. The 1-D FE system is directly connected to the global FE system of equations via Dirichlet conditions $\boldsymbol{h}_t^- = \boldsymbol{h}^0 = -\nabla\phi^-$ in $\Gamma_s^-$ and $\boldsymbol{h}_t^+ = \boldsymbol{h}^N = -\nabla\phi^+$ in $\Gamma_s^+$. The size of the air space region is not to scale, and the presented meshes are merely illustrative.

where $\Gamma_s^+$ and $\Gamma_s^-$ are two copies of the collapsed boundary, at the same position but allowing independent variables along both boundaries. Note that the last two integral terms depend essentially on the tangential components of the electric field $\boldsymbol{e}_t^+ = \boldsymbol{n}_s \times \boldsymbol{e}|_{\Gamma_s^+}$ and $\boldsymbol{e}_t^- = \boldsymbol{n}_s \times \boldsymbol{e}|_{\Gamma_s^-}$, where $\boldsymbol{n}_s = -\boldsymbol{n}_\Gamma^+ = \boldsymbol{n}_\Gamma^-$. These terms are required to include the ICs in the TS model.

The expression (6.11) requires the duplication of the DoFs on $\Gamma_s$. Therefore, the surface

mesh entities (nodes and edges on $\Gamma_s$) are duplicated, while the nodes at the extremities are not. This allows the tangential components of the magnetic field to be discontinuous across $\Gamma_s$. The thin surface corresponds to a crack in the topological structure of the discretized domain, and the non-conducting region becomes multiply connected. Consequently, a current constraint can be imposed in the thin structure using the shape functions $\boldsymbol{\psi}_i$ exactly as in the standard $H$-$\phi$-formulation.

### 6.3.1 Interface Conditions Derivation

To include the physics of the thin region in the simulations, the local subdomain $\Omega_s$ with boundaries $\Gamma_s^{\pm}$ is analyzed separately (Fig. 6.2a). The local weak form of the $H$-formulation in $\Omega_s$ is written as

$$\begin{aligned} -\Big\langle \boldsymbol{n}_s \times \boldsymbol{e}, \boldsymbol{g} \Big\rangle_{\Gamma_s^+} + \Big\langle \boldsymbol{n_s} \times \boldsymbol{e}, \boldsymbol{g} \Big\rangle_{\Gamma_s^-} \\ = \Big(\rho \nabla \times \boldsymbol{h}, \nabla \times \boldsymbol{g}\Big)_{\Omega_s} + \partial_t \Big(\mu \boldsymbol{h}, \boldsymbol{g}\Big)_{\Omega_s}, \end{aligned} \tag{6.12}$$

where the integrals on $\Gamma_s^{\pm}$ on the left side are identical to the two last terms in (6.11). The lateral surfaces of $\Omega_s$ are neglected. This is valid since the thickness of the tape is much smaller than its width and length, and the field penetration from its wide faces can be assumed stronger than from its lateral faces, i.e., along its thickness.

The domain integrals on the right side of (6.12) can be then reduced to boundary integrals on the collapsed geometry $\Gamma_s^{\pm}$, depending only on the tangential components of $\boldsymbol{h}$ as follows.

First, the profile of $\boldsymbol{h}$ in the $y$-direction across the thickness of the thin region is locally defined as a 1-D FE problem in $\widehat{\Omega}_s$ (Fig. 6.2b), where $\widehat{\Omega}_s$ is the virtual domain representing the original $\Omega_s$. The local coordinate systems $xyz$ is defined at the center of the thin geometry. The normal of the thin region is parallel to the $y$-axis, and $\boldsymbol{h}_t$ is in the $x$-direction. Since the tangential components of the magnetic field on $\Gamma_s^{\pm}$ are the same state variables as in $\Omega_c^C$, the two subdomains $\Omega_c^C$ and $\widehat{\Omega}_s$ are still naturally connected. For example, in Fig. 6.2b, the tangential fields in $\Gamma_s^+$ and $\Gamma_s^-$ are $\boldsymbol{h}^N = \boldsymbol{h}_t^+ = -\nabla\phi^+$ and $\boldsymbol{h}^0 = \boldsymbol{h}_t^- = -\nabla\phi^-$, respectively.

Then, by virtually discretizing $\widehat{\Omega}_s$ into $N$ FE of size $\Delta y^{(k)}$, with $1 \leq k \leq N$, the domain integral terms in (6.12) become

$$\begin{aligned}\Big(\rho\nabla\times\boldsymbol{h},\nabla\times\boldsymbol{g}\Big)_{\Omega_s}&+\partial_t\Big(\mu\boldsymbol{h},\boldsymbol{g}\Big)_{\Omega_s}\\&=\sum_{k=1}^{N}\Big(\rho\nabla\times\boldsymbol{h},\nabla\times\boldsymbol{g}\Big)_{\widehat{\Omega}_s^{(k)}}\\&\qquad+\sum_{k=1}^{N}\partial_t\Big(\mu\boldsymbol{h},\boldsymbol{g}\Big)_{\widehat{\Omega}_s^{(k)}},\end{aligned}\tag{6.13}$$

where $\rho^{(k)}$ and $\mu^{(k)}$ are the electrical resistivity and magnetic permeability in element $k$ and the virtual domain $\widehat{\Omega}_s$ has been subdivided into $N$ slabs $\widehat{\Omega}_s^{(k)}=\Gamma_s\times[y_{k-1},y_k]$ at heights $y_0<y_1<\cdots<y_N$.

Using linear Lagrange polynomials as basis functions for the 1-D problem, i.e.

$$\theta_1(y)=\frac{y_k-y}{\Delta y^{(k)}},\qquad\qquad\theta_2(y)=\frac{y-y_{k-1}}{\Delta y^{(k)}},\tag{6.14}$$

we can write $\boldsymbol{h}$ in each element $\widehat{\Omega}_s^{(k)}$ as

$$\boldsymbol{h}(x,y,t)\big|_{\widehat{\Omega}_s^{(k)}}=\sum_{j=1}^{2}\boldsymbol{h}^m(x,t)\theta_j(y),\tag{6.15}$$

where $m=m(k,j)=k-2+j$ relates $\boldsymbol{h}^m$ to the boundary of $\widehat{\Omega}_s^{(k)}$, i.e. $\boldsymbol{h}^{m(k,1)}=\boldsymbol{h}^{k-1}$ and $\boldsymbol{h}^{m(k,2)}=\boldsymbol{h}^k$. Recall that the vector field $\boldsymbol{h}$ is at all times perpendicular to the $y$-direction.

Next, choosing the test function $\boldsymbol{g}(x,y)=\boldsymbol{g}(x)\theta_i(y)$, with $i=1,2$, to be in the same space as $\boldsymbol{h}$ (Galerkin method), we can use the vector calculus identity $\nabla\times(\boldsymbol{v}u)=\nabla u\times\boldsymbol{v}+u\nabla\times\boldsymbol{v}$, where $u$ and $\boldsymbol{v}$ are any scalar and vector functions, and decompose the domain integrals on $\widehat{\Omega}_s^{(k)}$ in (6.13) into integrals over $\Gamma_s^m$ and $[y_{k-1},y_k]$. In fact, the decomposition below in 2-D uses the observation that $\nabla\times\boldsymbol{h}^m$ and $\nabla\times\boldsymbol{g}^n$ are in the $y$-direction and the inner products of type $(\nabla\theta_j\times\boldsymbol{h}^m)\cdot(\theta_i\nabla\times\boldsymbol{g}^n)$ vanish. Using these facts and setting $n=n(k,i)=k-2+i$, one deduces

$$\begin{aligned}&\Big(\rho^{(k)}\nabla\times\boldsymbol{h},\nabla\times\boldsymbol{g}\Big)_{\widehat{\Omega}_s}\\&\quad=\sum_{j=1}^{2}\Big(\rho^{(k)}(\nabla\theta_j\times\boldsymbol{h}^m+\theta_j\nabla\times\boldsymbol{h}^m),(\nabla\theta_i\times\boldsymbol{g}^n+\theta_i\nabla\times\boldsymbol{g}^n)\Big)_{\widehat{\Omega}_s^{(k)}}\\&\quad\overset{\text{2-D}}{=}\sum_{j=1}^{2}\Big\langle\rho^{(k)}\boldsymbol{h}^m,\boldsymbol{g}^n\Big\rangle_{\Gamma_s}\cdot\mathcal{S}_{ij}^{(k)}\qquad\qquad\forall\,i=1,2,\end{aligned}\tag{6.16}$$

and

$$\begin{aligned}
&\partial_t\Big(\mu\boldsymbol{h},\boldsymbol{g}\Big)_{\widehat{\Omega}_s^{(k)}} \\
&\quad=\sum_{j=1}^{2}\partial_t\Big(\mu^{(k)}\boldsymbol{h}^m\theta_j,\boldsymbol{g}^m\theta_i\Big)_{\widehat{\Omega}_s^{(k)}} \\
&\quad=\sum_{j=1}^{2}\partial_t\Big\langle\mu^{(k)}\boldsymbol{h}^m,\boldsymbol{g}^n\Big\rangle_{\Gamma_s}\cdot\mathcal{M}_{ij}^{(k)} \qquad \forall\, i=1,2,
\end{aligned} \tag{6.17}$$

where

$$\mathcal{S}_{ij}^{(k)}=\int_{\Delta y^{(k)}}\partial_y\theta_i\partial_y\theta_j dy, \qquad \mathcal{M}_{ij}^{(k)}=\int_{\Delta y^{(k)}}\theta_i\theta_j dy. \tag{6.18}$$

Finally, the ICs in the proposed TS model are obtained by inserting (6.16) and (6.17) into (6.13). Substituting (6.13) in (6.12), the interface terms depending on the tangential components of the electric field are written in terms of $\boldsymbol{h}^m$ as

$$\begin{aligned}
&-\Big\langle\boldsymbol{n}_s\times\boldsymbol{e},\boldsymbol{g}\Big\rangle_{\Gamma_s^+}+\Big\langle\boldsymbol{n_s}\times\boldsymbol{e},\boldsymbol{g}\Big\rangle_{\Gamma_s^-} \\
&\quad=\sum_{k=1}^{N}\sum_{j=1}^{2}\Big\langle\rho^{(k)}\boldsymbol{h}^m,\boldsymbol{g}^n\Big\rangle_{\Gamma_s^m}\cdot\mathcal{S}_{ij}^{(k)} \\
&\quad+\sum_{k=1}^{N}\sum_{j=1}^{2}\partial_t\Big\langle\mu^{(k)}\boldsymbol{h}^m,\boldsymbol{g}^{n)}\Big\rangle_{\Gamma_s}\cdot\mathcal{M}_{ij}^{(k)} \quad \forall\, i=1,2.
\end{aligned} \tag{6.19}$$

Given that polynomials of degree one were considered in (6.14), the profile of $\boldsymbol{h}$ in each element of $\widehat{\Omega}_s$ is linear, and the current density $\boldsymbol{j}_z$ is

$$\boldsymbol{j}_z\Big|_{\widehat{\Omega}_s^{(k)}}=\boldsymbol{n}_s\times\partial_y\boldsymbol{h}\Big|_{\widehat{\Omega}_s^{(k)}}=\boldsymbol{n}_s\times\left(\frac{\boldsymbol{h}^k-\boldsymbol{h}^{k-1}}{\Delta y^{(k)}}\right), \tag{6.20}$$

constant in $\widehat{\Omega}_s^{(k)}$. Thus, the elementary 1-D $E$-$J$ power-law (6.8) becomes

$$\rho^{(k)}\overset{\text{2-D}}{=}\frac{e_c}{j_c}\left(\frac{|\boldsymbol{n}_s\times(\boldsymbol{h}^k-\boldsymbol{h}^{k-1})|}{j_c\Delta y^{(k)}}\right)^{n_{\text{HTS}}-1}. \tag{6.21}$$

Moreover, the matrices (6.18) can be evaluated analytically for the polynomials (6.14), giving us

$$\mathcal{S}^{(k)}=\frac{1}{\Delta y^{(k)}}\begin{bmatrix}1 & -1\\ -1 & 1\end{bmatrix}, \quad \mathcal{M}^{(k)}=\frac{\Delta y^{(k)}}{6}\begin{bmatrix}2 & 1\\ 1 & 2\end{bmatrix}. \tag{6.22}$$

The complete weak form for the problem is obtained from (6.11) and (6.19). The time-

derivative can be discretized by implicit Euler method, and the nonlinear system of equations is solved by the NR method.

In terms of post-operation, the instantaneous loss density ($\mathcal{L}(t)$) in Joule inside the thin region is calculated as [12]

$$\mathcal{L}(t) = \sum_{k=1}^{N} \int_{\Gamma_s} \rho^{(k)} H^{(k)T} \mathcal{S}^{(k)} H^{(k)} d\Gamma, \tag{6.23}$$

where $H^{(k)}$ is the $2 \times 1$ vector of unknowns for each element $k$, i.e.

$$H^{(k)} = \begin{bmatrix} h^k \\ h^{k-1} \end{bmatrix}, \tag{6.24}$$

and $h^k$ and $h^{k-1}$ are the magnitude of the tangential field on $\Gamma_s^k$ and $\Gamma_s^{k-1}$, respectively, defined in (6.15).

The ICs in the proposed TS model were here developed using the polynomials of first order (6.14). For higher-order basis functions, (6.15) must be modified accordingly. The approach can also be developed for the $A$-formulation. In this case, the boundary terms will depend uniquely on the tangential components of $A$.

### 6.3.2 Comparison with the Classical TS model

For the sake of validation of the developed equations, we shall compare the ICs in the proposed model with those from the classical TS model for linear cases in harmonic regime [31–34]. Considering a single 1-D element in $\widehat{\Omega}_s$ ($N = 1$), and $\delta \gg d$, where $\delta = \sqrt{2\rho/(\omega\mu)}$ is the skin depth and $\omega$ is the angular frequency, from (6.19), one obtains

$$\rho \frac{\boldsymbol{h}_t^+ - \boldsymbol{h}_t^-}{d} = \frac{\boldsymbol{e}_t^+ + \boldsymbol{e}_t^-}{2}, \tag{6.25}$$

$$\frac{\boldsymbol{e}_t^+ - \boldsymbol{e}_t^-}{d} = -\partial_t \mu \frac{\boldsymbol{h}_t^+ + \boldsymbol{h}_t^-}{2}, \tag{6.26}$$

which are identical to the ICs for $\delta \gg d$ presented in [95].

Expression (6.25) links the variation of $\boldsymbol{h}_t^{\pm}$ through the thickness $d$ of the thin conductor (or the surface current density (6.20)) to the mean value of $\boldsymbol{e}_t$, which is itself related to the mean value of the normal flux density by Faraday's law as

$$\partial_x \boldsymbol{e}_t^{\pm} = -\mu \partial_t \boldsymbol{h}_n^{\pm}, \tag{6.27}$$

where $\boldsymbol{h}_n$ is the normal component of the magnetic field. Furthermore, expression (6.26) links the variation of $\boldsymbol{e}_t$ through $d$ (or the normal flux density) to the mean value of $\boldsymbol{h}_t$ (or the flux divergence on the thin surface). It expresses the conservation of the magnetic flux inside the thin region [32].

Depending on the problem one wishes to solve, the effects of the two ICs (6.25) and (6.26) are more or less predominant. For HTS modeling, with $\mu = \mu_0$ and $\rho$ being highly nonlinear, (6.25) becomes more important than (6.26). Similar to the classical TS approach, the proposed model includes both ICs. However, since these ICs are defined from auxiliary 1-D FE problems, the TS model constructed in this paper permits time-transient and nonlinear analysis while considering the penetration of $\boldsymbol{h}_t$ in the thin region.

### 6.3.3 Comparison with the $T$-$A$-formulation

In the $T$-$A$-formulation, as presented and implemented in Comsol Multiphysics in [35], a 1-D FE problem problem is defined along the width of the thin regions. The state variable is the normal component of the current vector potential ($\boldsymbol{t}_n$), and the differential form for the 1-D problem is

$$\partial_x\big(\rho\partial_x\boldsymbol{t}_n\big) = -\partial_t\boldsymbol{b}_n \tag{6.28}$$

where $\boldsymbol{b}_n$ is the normal magnetic flux density. Moreover, the conventional $A$-formulation is applied to the air space region, and a surface current density $\boldsymbol{j}_z$ is imposed on $\Gamma_s$ by a discontinuity in $\boldsymbol{h}_t$. The total transport current is imposed in the tapes via BCs of the type $\boldsymbol{t}_n = I/d$ at the extremities of $\Gamma_s$.

Since $\boldsymbol{j}_z = \boldsymbol{n}_s \times \partial_x\boldsymbol{t}_n = \boldsymbol{n}_s \times (\boldsymbol{h}_t^+ - \boldsymbol{h}_t^-)/d$, and $\boldsymbol{b}_n = (\boldsymbol{b}_n^+ + \boldsymbol{b}_n^-)/2$, (6.28) with (6.27) corresponds to IC (6.25). Also, in Comsol Multiphysics, the interface condition $\boldsymbol{e}_t^+ - \boldsymbol{e}_t^- = 0$ is automatically fulfilled [107]. So, IC (6.26) is not taken into account in the $T$-$A$-formulation. Since $\mu = \mu_0$ in $\Omega_s$, this approximation is valid for modeling HTS tapes only when the superconducting layer is represented as a thin strip. Problems involving thin regions with $\mu > \mu_0$ cannot be addressed by this formulation since a conservative normal flux density is implicitly imposed by $\boldsymbol{e}_t^+ - \boldsymbol{e}_t^- = 0$.

Given that $T$-$A$ formulation can be defined simply as the IC (6.25) applied in a pure $A$-formulation, it is proven to be dual to the proposed TS model with $N = 1$ in the $H$-formulation and when disregarding the magnetic flux divergence on the thin surface given by (6.26). However, its use should be carefully considered. The current density depends at the same time on both the variation of $\boldsymbol{h}_t$ across the thickness $d$ and the variation of $\boldsymbol{h}_n$ along its width. The former variation is assumed linear, and the second must also be. From (6.27), one verifies that, for $\boldsymbol{h}_t$ to be linear, $\boldsymbol{e}_t$ must be of second-order. Otherwise,

numerical oscillations appear [108, 109]. Consequently, with second order FE for $\boldsymbol{e}_t$ (or $\boldsymbol{a}_t$), the number of DoFs greatly increases in the $T$-$A$-formulation. The computation time with this formulation becomes comparable to a pure $H$-formulation in 3-D cases [109].

In the proposed TS model, the ICs are written only in terms of $\boldsymbol{h}_t$, which are also the state variables in the $H$-formulation used to model the surroundings of the thin region. This represents a more natural coupling and avoids the oscillations that appears in the $T$-$A$-formulation. The application of the equivalent TS model in a pure $A$-formulation would require ICs depending on the tangential components of the electric field. However, this formulation might be preferable to model soft ferromagnetic materials. For superconducting tapes, the use of the $H$-formulation is more advantageous [43].

## 6.4 Validation

The proposed TS model was applied in two benchmark problems: (i) a single HTS tape, (ii) two closely-packed tapes carrying anti-parallel currents. In both examples, width of the tapes was $l = 4$ mm, and their thickness was scaled to $d = 10\,\mu$m in the full-discretized reference model in order to reduce the number of DoFs while ensuring reasonable accuracy. Despite this, the aspect ratio of the tapes remains relatively high. Only the superconducting layer is modeled in these examples. The magnetic permeability is equal to $\mu_0$ in all domains.

In the $E$-$J$ power-law (6.8), and in (6.21), $e_c = 10^{-4}\,\mathrm{V/m}$, $j_c = 5 \times 10^8\,\mathrm{A/m^2}$ and $n = 21$. Moreover, a sinusoidal transport current of $I(t) = I_{\max}\sin(2\pi f t)$ is imposed in the tapes, where $f = 50$ Hz is the operating frequency and $I_{\max} = F_c I_c$, where $I_c = J_c S$ is the critical current density, $S$ is the cross-section area of the tape, and $F_c \in [0, 1]$ is a constant defining the transport current amplitude as a fraction of the critical current.

The results obtained with the proposed TS model are compared with reference solutions obtained with standard FE using the $H$-$\phi$ formulation presented in Section 6.2.2, and with the $T$-$A$-formulation proposed in [35] and briefly described in Section 6.3.3. In output, the local distribution of magnetic field inside and outside the tapes, current density, and total AC losses in the tapes are compared.

In terms of mesh, the HTS tapes in the reference model are fully discretized with a structured rectangular mesh with 11 elements across the tape thickness and 400 elements along its width (Fig. 6.3a). In the proposed TS model and in the $T$-$A$-formulation, the surface representing the thin region also includes 400 elements across its width (Fig. 6.3b). The influence of the number of 1-D elements ($N$) in the TS model is studied independently in each application example. The total number of DoFs is further compared with the reference model.

(a) Full mesh (b) Mesh TS model

Figure 6.3 Zoom of the meshes near the right edge of the tape: (a) full mesh for standard FE application (reference model), and (b) simplified mesh used with the the TS model and the $T$-$A$-formulation. Note the difference in the number of elements surrounding the extremity of the tape and their aspect ratio.

The reference and the TS models were implemented in the open-source code Gmsh [60] and the solver GetDP [122]. The results of the $T$-$A$-formulation were obtained using Comsol Multiphysics 5.5. All the simulations were performed using a personal computer with an Intel i7 2400 processor with 16 Gb of memory. In GetDP, an adaptive time-step procedure was used to improve convergence. This procedure is well explained in [43]. In our simulations, the NR scheme was used to solve the nonlinear system of equations. The convergence criterion requires the relative change between two consecutive NR iterations to be smaller than a given tolerance. The maximum number of iterations was set to 12, the initial time step was set 7.5 $\mu$s, the maximum time step was set 200 $\mu$s. The relative tolerance of the calculation was set to $10^{-5}$, with absolute tolerance set to $10^{-7}$. Moreover, a zeroth-order extrapolation was used, i.e. the initial guess in each NR iteration was taken as the solution of the previous time step.

### 6.4.1 Single HTS Tape

We first considered the example of a single HTS tape embedded in an air space region, as illustrated in Fig. 6.2. The origin of the coordinate system $xy$ was located at the center of the tape. The number of 1-D elements ($N$) was initially set to 1. The current imposed in the tape was $0.9Ic$, i.e. $F_c = 0.9$.

In Fig. 6.4, the distribution of the magnetic flux density in and around the tape is shown for the TS model and for the $H$-$\phi$ reference model at $t = [T/8, T/4, T/2]$, where $T = 1/f$. Due to symmetry, only half of the tape is shown. The figures on left show the flux distribution obtained with the $H$-$\phi$ model, and the figures on right show the results obtained with the TS model with $N = 1$. The distributions computed by the two models show excellent agreement,

validating the proposed TS model in terms of field distribution outside the tape.

For the sake of comparison with the $T$-$A$-formulation and solution validation inside the tape, Fig. 6.5 shows the profile of the normal component of $H$ ($h_n = |\boldsymbol{h}_n|$) along half of the tape width ($0 < x < l/2$), and at $t = T/8$ and $t = T/4$. In the TS model ($H$-$\phi$ TS), the $h_n$ profile was obtained by computing its mean value on surfaces $\Gamma_s^{\pm}$, i.e., $h_n = (h_n^+ + h_n^-)/2$. In the reference model ($H$-$\phi$), $h_n$ was taken at the middle of the tape ($y = 0$). Moreover, in the $T$-$A$-formulation, $h_n = (b_n^+ + b_n^-)/2\mu_0$, with $b_n^{\pm} = |\boldsymbol{b}_n^{\pm}|$ derived from $A$. Note the excellent agreement of the $h_n$ profiles of the TS model with the two other solutions. The slight difference observed at the extremities of the tape may be related to the geometrical differences between the TS and the reference model. The thinner the thin film is, the lower the difference between the TS and the reference solutions will be at these extremities.

The profile of the tangential component of $H$ ($h_t = |\boldsymbol{h}_t|$) across the tape thickness at $x = 0$ is presented in Fig. 6.6. In this case, $N = 11$ to correspond to the number of mesh elements across the thickness in the fully discretized $H$-$\phi$ model. The profile of $h_t$ in the $T$-$A$-formulation was obtained by linear interpolation of the field intensities at the center of the tape. This solution is similar to the TS model solution with $N = 1$. Indeed, with the increase in $N$, the proposed TS model allows the tangential components of the fields to penetrate the tape.

In the modeling of a single HTS tape, the increase in $N$ in the TS model does not have a major impact on the quality of the solution. From Fig. 6.5 and Fig. 6.6, one observes that $h_n$ is larger than $h_t$ ($\sim 3.5$ times). Thus, the assumption of a linear variation of $h_t$ across $d$ is reasonable for a single tape, and $N = 1$ gives sufficiently accurate solutions, similar as the $T$-$A$-formulation.

One advantage of the TS model with the discretization across the tape thickness is that the current density $\boldsymbol{j}_z$ can be locally evaluated. Fig. 6.7 shows the normalized current density relative to $j_c$ ($|\boldsymbol{j}_z|/j_c$) near the extremity of the tape for $N = 11$. The results of the TS model (Fig. 6.7b,d,f) were obtained by a projection of $|\boldsymbol{j}_z|/j_c$ across $d$, and coincides with the reference solution (Fig. 6.7a,c,e).

For the TS model, the AC losses inside the tape were evaluated using (6.23) with $N = 1$. The results are presented in Fig. 6.8 as a function of $I/I_c$. For a single tape, the losses from the three discussed models are similar. The differences in terms of AC loss appears when more than a one tape is studied.

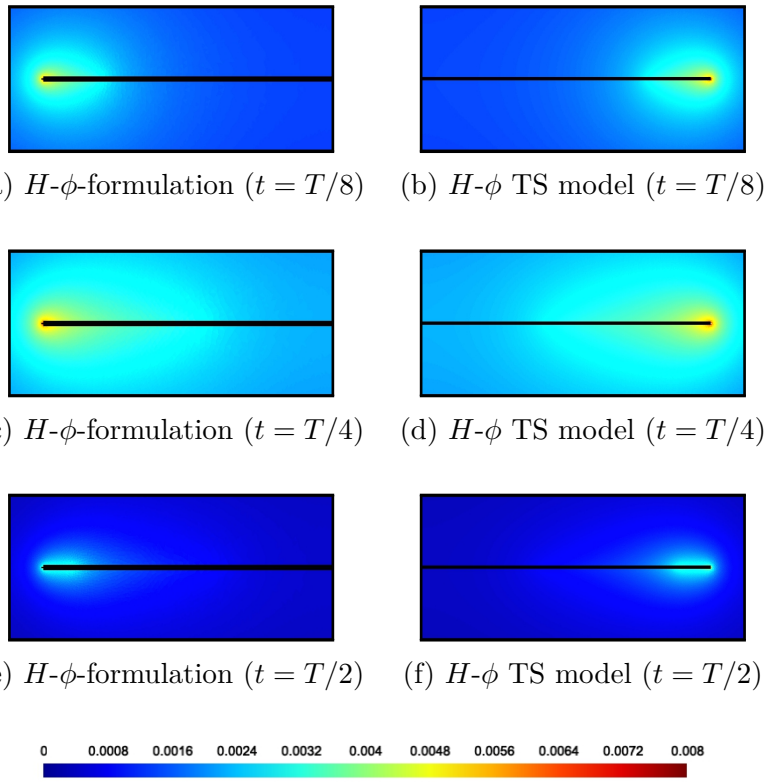


(a) $H$-$\phi$-formulation ($t = T/8$) (b) $H$-$\phi$ TS model ($t = T/8$)

(c) $H$-$\phi$-formulation ($t = T/4$) (d) $H$-$\phi$ TS model ($t = T/4$)

(e) $H$-$\phi$-formulation ($t = T/2$) (f) $H$-$\phi$ TS model ($t = T/2$)

Figure 6.4 Norm of magnetic flux density $|\boldsymbol{b}|$ [T] for the single HTS tape example with $F_c = 0.9$ at three different simulation times ($T/8$, $T/4$ and $T/2$) . Left: fully discretized $H$-$\phi$ reference model. Right: proposed TS approach with $N = 1$.

### 6.4.2 Two Closely Packed HTS Conductors

In large-scale HTS applications, the use of more than one tape is required. When these tapes are closely packed and carry anti-parallel currents, the tangential components of the magnetic field are important and the current density is unevenly distributed across the thickness of the tape. Consequently, the strip approximation and the $T$-$A$-formulation cannot provide an accurate solution, and a pure $H$-formulation requires tremendous computational efforts to discretize the thin region [17].

To demonstrate that the proposed TS model is suitable for simulating HTS problems of any type, an example of two closely-packed tapes carrying anti-parallel currents was considered. The inter-tape separation was $L = 250\,\mu$m. Only half of the geometry was modeled due to symmetry (Fig. 6.9). One tape is located at a distance $L/2$ from the exterior boundary $\Gamma_h$. Since the BC on $\nabla \times \boldsymbol{h}$ along $\Gamma_h$ is naturally satisfied in the $H$-$\phi$-formulation, symmetry condition is automatically fulfilled.

Fig. 6.10 shows the profile of the normal component of $H$ ($h_n = |\boldsymbol{h}_n|$) along half of the tape

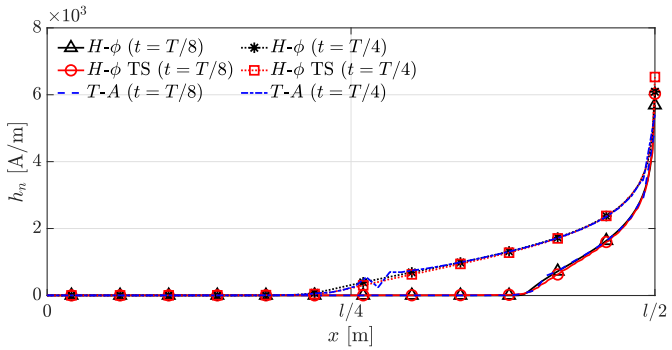


Figure 6.5 Profile of normal component of $H$ ($h_n = |\boldsymbol{h}_n|$) along half of the tape width with $I = 0.9I_c$ and at $t = T/8$ and $t = T/4$. The TS solution with $N = 1$ is compared with the $H$-$\phi$ and $T$-$A$ solutions.

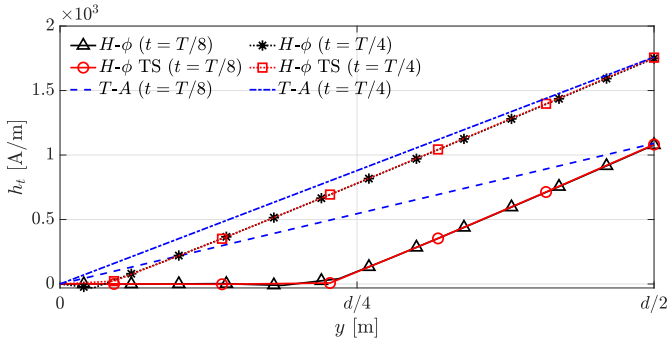


Figure 6.6 Profile of tangential component of $H$ ($h_t = |\boldsymbol{h}_t|$) across half of the tape thickness with $I = 0.9I_c$ and at $t = T/8$ and $t = T/4$. The TS solution with $N = 11$ is compared with the $H$-$\phi$ and $T$-$A$ solutions.

width. The solution of the TS model with $N = 1$ is compared with the solutions of the $H$-$\phi$ and the $T$-$A$ models for $F_c = 0.9$. Once again, the solution of the three models agree. In the $T$-$A$ solution, one observes oscillations at the sharpest points of the $h_n$ profile. No oscillations are noted in the TS solution.

In Fig. 6.11, the profile of $h_t$ for various $N$ values in the TS model are shown. The solution with $N = 1$ gives a linear distribution of $h_t$ across the thickness of the tape, which is similar to the profile obtained with the $T$-$A$-formulation. When $N$ increases, the solution of the TS model approaches the $H$-$\phi$ solution. With $N = 6$, the TS solution is very close to the reference one. Note that in this case the value of $h_t$ in the middle of the tape is comparable to the value of $h_n$ at its extremities (see Fig. 6.10 and 6.11). The tangential components certainly have an determining impact when modeling multiple tapes in configurations similar to this example.

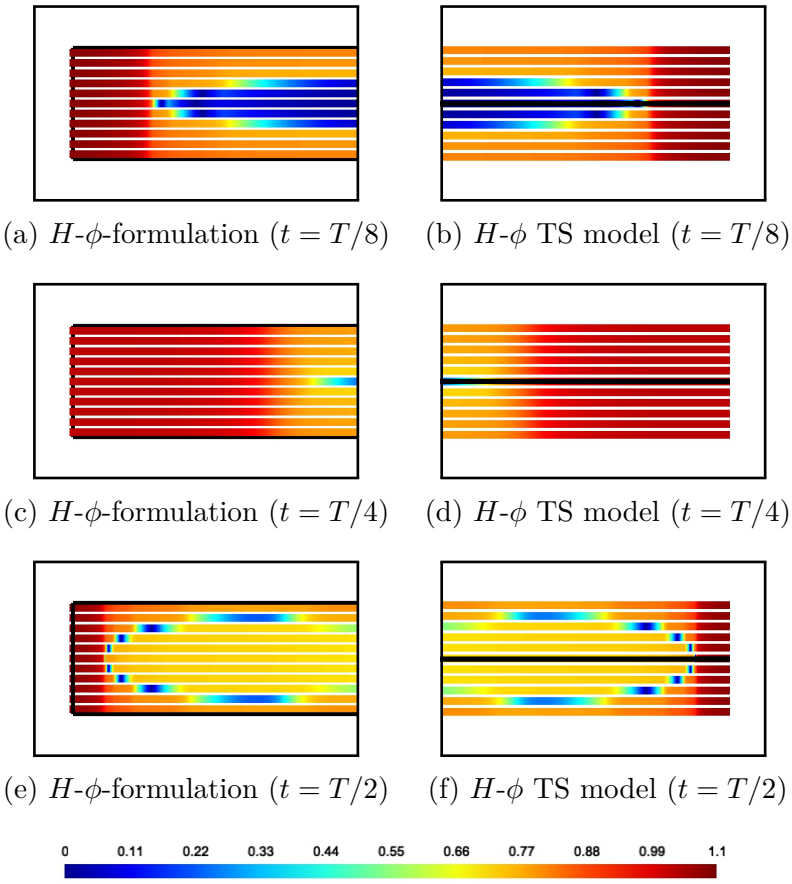


(a) $H$-$\phi$-formulation ($t = T/8$) (b) $H$-$\phi$ TS model ($t = T/8$)

(c) $H$-$\phi$-formulation ($t = T/4$) (d) $H$-$\phi$ TS model ($t = T/4$)

(e) $H$-$\phi$-formulation ($t = T/2$) (f) $H$-$\phi$ TS model ($t = T/2$)

Figure 6.7 Normalized relative current density ($|\boldsymbol{j}_z|/J_c$) near the extremity of the tape at $t = T/8$, $t = T/4$ and $t = T/2$: (a,c,e) $H$-$\phi$-formulation, and (b,d,f) $H$-$\phi$ TS model with $N = 11$. The TS solution is obtained by a projection of the $|\boldsymbol{j}_z|/J_c$ on the virtual position of the 1-D elements. The black lines in the middle of (b,d,f) represent the tape in the TS model (lines in 2-D).

The AC losses as a function of $I/I_c$ obtained with the three models are also presented in Fig. 6.8. In the TS model, $N = 11$ was considered for the sake of comparison with the reference solution and with the single tape example presented in Section 6.4.1. The TS solution perfectly agrees with the $H$-$\phi$ solution. The $T$-$A$-formulation underestimates the AC losses at low transport current. Indeed, with a linear variation of the fields inside the tape, so-called top/bottom losses are not taken into account by the $T$-$A$-formulation.

In order to define a minimum number of 1-D elements necessary to obtain an accurate solution in terms of AC loss in the TS model, simulations were performed using different $N$ and $F_c$ values. The AC losses as a function of $F_c = I/I_c$ for $N = 1$, 2, 4 and 6 are presented in Fig. 6.12. With $N = 1$, $h_t$ does not fully penetrates the tape, and the TS model also underestimates the AC losses at low transport current. With the increase in $N$, one observes

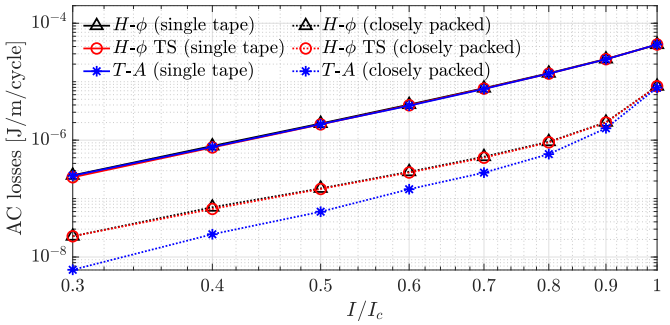


Figure 6.8 Total AC losses as a function of the normalized transport current in the single tape and in the two closely packed tapes examples. For a single tape $N = 1$, and, for two closely packed tapes, $N = 11$ in the TS model.

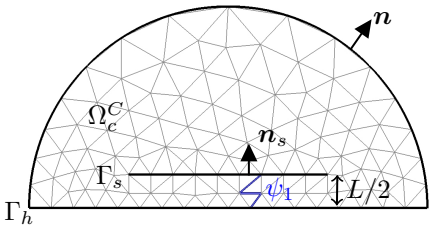


Figure 6.9 Calculus domain for the example of two closely packed HTS tapes. Due to the symmetry, only half of the geometry is presented. The distance between the conductors is $L$. The air space region, the mesh and the distance $L$ are not to scale.

the convergence of the TS solution towards the $H$-$\phi$ solution.

The number of DoFs, the CPU time and the total number of time iterations (NoIs) for the two closely-packed tapes example are summarized in Table 6.1. The proposed TS model with $N = 1$ represented a reduction of more than 40% in the total number of DoFs and was more than seven times faster than the reference $H$-$\phi$ model. The three parameters in Table 6.1 increased with $N$. Even with $N = 11$, the reduction in the number of DoFs in the TS model is still about 30%, and simulations are 1.3 faster than the $H$-$\phi$ model with complete discretization of the tape. The application of the TS model with $N = 4$ shows a good compromise between solution accuracy and computational cost even for the case of closely packed HTS tapes with anti-parallel transport current.

With the $T$-$A$ model, the number of DoFs in this example was 33282 and the solution was obtained after 141 s and 481 iterations. This number of DoFs is comparable to the $H$-$\phi$ model since second-order finite elements are used for $A$. Despite this, the CPU time was shorter with the $T$-$A$ than the proposed TS model with $N = 1$. This difference may be related to the solvers: the $T$-$A$-formulation is implemented in Comsol, and the two other models are in Gmsh/GetDP. A fair comparison in terms of computational costs would require these models

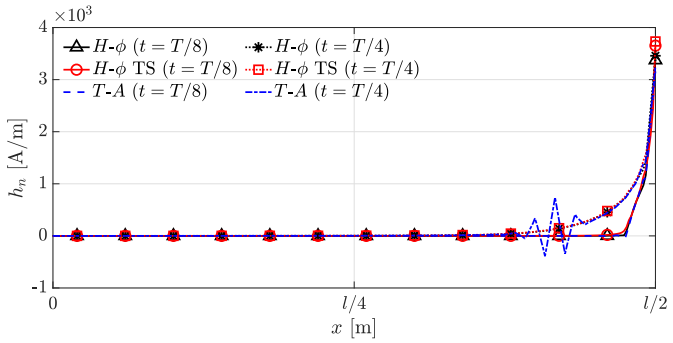


Figure 6.10 Profile of normal component of $H$ ($h_n = |\boldsymbol{h}_n|$) along half of the tape width for $I = 0.9I_c$ and at $t = T/8$ and $t = T/4$ for the case of two closely packed tapes. The TS solution with $N = 1$ is compared with the $H$-$\phi$ and $T$-$A$ solutions.

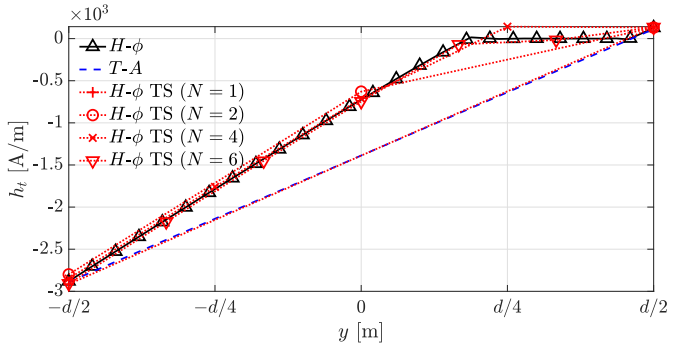


Figure 6.11 Profile of tangential component of $H$ ($h_t = |\boldsymbol{h}_t|$) across half of the tape thickness with $I = 0.9I_c$, and at $t = T/8$ and $t = T/4$. The TS solution with $N = 1$, 2, 4 and 6 is compared with the $H$-$\phi$ and $T$-$A$ solutions.

to be implemented in the same software environment.

## 6.5 Realistic Examples

### 6.5.1 Racetrack Coil

To demonstrate the applicability of the proposed model for modeling large-scale HTS devices, we considered a stack of twenty HTS tapes in a 2-D infinitely long representation of a racetrack coil. The tapes have the same physical and geometrical characteristics as in the two previous examples and an inter-tape separation of $L = 250\,\mu$m. A transport current of $0.9I_c$ at a frequency of $f = 50\,$Hz was imposed in each tape in two configurations: (i) all the tapes carrying the same transport current and (ii) each subsequent pair of tapes carrying anti-parallel currents of equal magnitude.

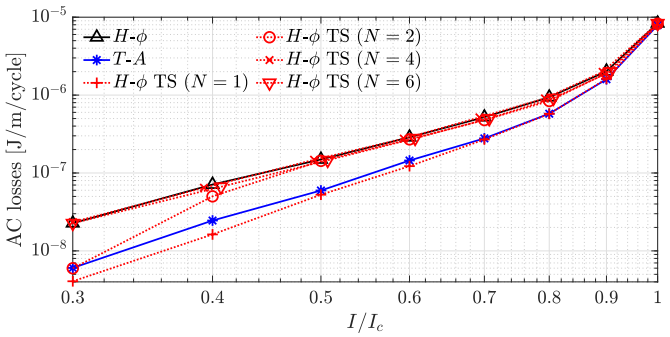


Figure 6.12 Total AC losses as a function of the normalized transport current for the closely-packed tapes example. The solution of the TS model with different $N$ values is compared with the $H$-$\phi$ and $T$-$A$ solutions. Note the convergence of the TS solution to the $H$-$\phi$ at low current transport. The increase in $N$ permits the TS to take top/bottom losses into account.

Table 6.1 Number of DoFs, CPU time, and total number of iterations (NoIs) in the $H$-$\phi$ and in the TS models for different $N$ values

| | $H$-$\phi$ | TS ($N = 1$) | TS ($N = 2$) | TS ($N = 4$) | TS ($N = 6$) | TS ($N = 11$) |
|---|---|---|---|---|---|---|
| DoFs | 33188 | 18727 | 19127 | 19927 | 20727 | 22727 |
| Time | 4015.65s | 553.57s | 563.34s | 806.30s | 1252.21s | 3079.08s |
| NoIs | 488 | 114 | 114 | 125 | 188 | 383 |

According to the results presented in the last example, $N = 4$ in the TS model is enough to provide a good estimation of the AC losses in the tapes. Therefore, the results obtained with the TS model with $N = 4$ for the racetrack coil problem were compared to the results from the $H$-$\phi$-formulation in terms of local field distribution and AC losses. Each tape was represented as as a reduced-dimension geometry and modeled using the proposed TS model.

Fig. 6.13 shows the norm of the flux density at $t = T/4$ in the case where the same transport current is imposed in each tape. Fig. 6.14 shows the equivalent distribution for the case with anti-parallel currents imposed in each pair of tapes. In both figures, the reference solution is presented on the left and the TS model solution is presented on the right. Excellent agreement is observed in all cases.

In Fig. 6.15, we present the AC losses per cycle as a function of the position of the tapes, with 1 corresponding to the bottom tape and 20 to the top tape. Note that the AC losses computed with the TS model fit perfectly the losses obtained with the $H$-$\phi$ reference model. This demonstrates that the TS model with the appropriate number of 1-D elements in the thin film representation of the tape is suitable for modeling HTS systems involving multiple tapes.

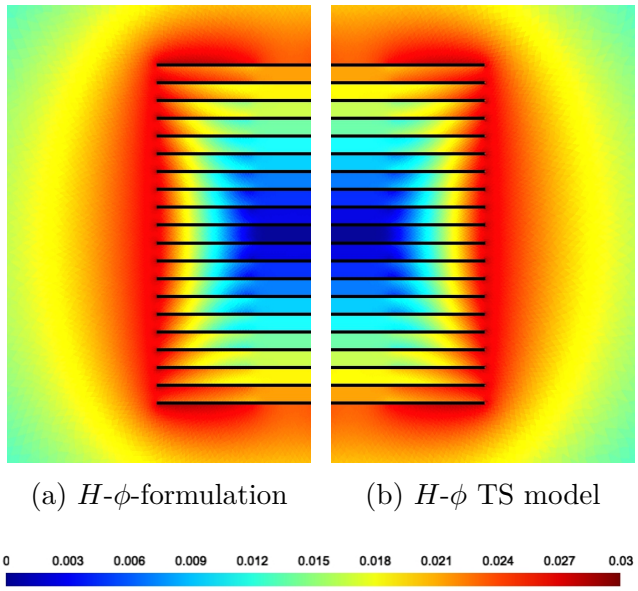


(a) $H$-$\phi$-formulation (b) $H$-$\phi$ TS model

Figure 6.13 Norm of magnetic flux density $|\boldsymbol{b}|$ [T] for the racetrack coil example with twenty HTS tapes in a infinitely long 2-D representation at $t = T/4$. A transport current of $I = 0.9I_c$ is imposed in each tape. Half of the domain is presented due to the symmetry. (a) Reference solution from the $H$-$\phi$ formulation, and (b) solution from the TS model with $N = 4$.

### 6.5.2 HTS Tape with ferromagnetic substrate

In our last example, we considered one HTS tape comprising a stack of three thin layers: (i) the bottom layer is a ferromagnetic substrate ($\sigma_{\text{subs}} = 10\,\text{kS/m}$, $\mu_{r,\text{subs}} = 100$, $d_{\text{subs}} = 50\,\mu\text{m}$), (ii) the middle layer was the HTS ($\mu_{r,\text{HTS}} = 1$, $d_{\text{HTS}} = 10\,\mu\text{m}$), and (iii) the top layer was a silver stabilizer ($\sigma_{\text{Silver}} = 63\,\text{MS/m}$, $\mu_{r,\text{Silver}} = 1$, $d_{\text{Silver}} = 20\,\mu\text{m}$). As in the previous examples, the thicknesses of the HTS and silver layers, $d_{\text{HTS}}$ and $d_{\text{Silver}}$, respectively, were scaled up to ensure reasonable accuracy of the reference solution. In the TS model, the three layers were collapsed on a single surface. Fig. 6.16 shows the geometry and mesh simplifications in the TS model (Fig. 6.16b) compared with the reference geometry (Fig. 6.16a).

We initially considered the TS model with one virtual element in the substrate and the silver layers, and four virtual elements in the HTS layer (i.e., $N = 6$ in total). A high dense mesh inside the tape was considered in the reference model (Fig. 6.16a). Fig. 6.17 shows the magnetic flux density magnitude in the surroundings of the tape with $I/I_c = 0.9$ and $f = 50\,\text{Hz}$ at $t = T/2$. Due to the high permeability of the substrate, the magnetic flux density is absorbed by this layer and magnified near the top face of the tape. The TS model well represents this behavior, and the solution visually agrees with the reference one.

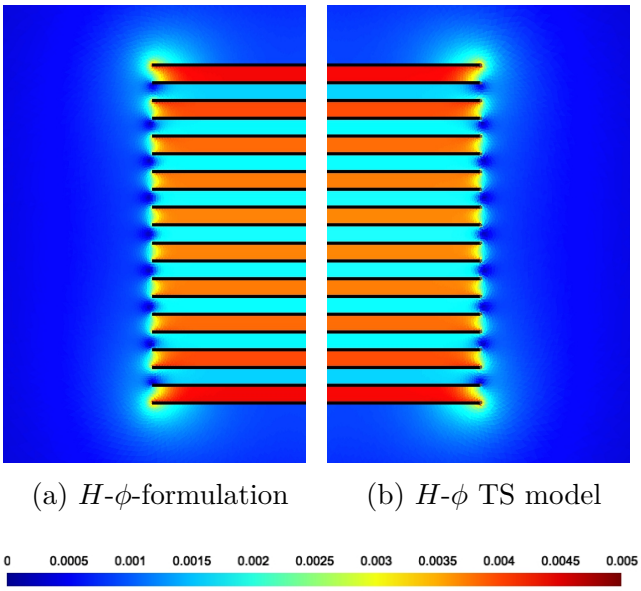


(a) $H$-$\phi$-formulation (b) $H$-$\phi$ TS model

Figure 6.14 Norm of magnetic flux density $|\boldsymbol{b}|$ [T] for the racetrack coil example with twenty HTS tapes in a infinitely long 2-D representation at $t = T/4$. An anti-parallel transport current of $I = 0.9I_c$ is imposed in each subsequent pair of tapes. Half of the domain is presented due to the symmetry. (a) Reference solution from the $H$-$\phi$ formulation, and (b) solution from the TS model with $N = 4$.

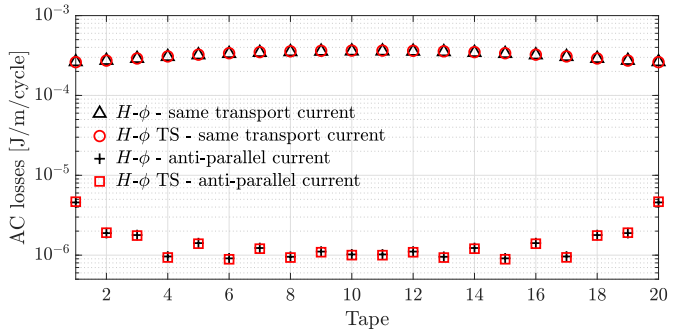


Figure 6.15 Total AC losses in each tape of the racetrack coil. Results are presented for the two studied cases: same transport current in each tape and anti-parallel currents in each pair of tapes.

Next, we increased the number of virtual elements used to represent the HTS layer in order obverse the uneven distribution of the current density in the HTS layer. We considered nine elements across the thickness of the HTS layer, and one element in the substrate and the silver layers ($N = 11$). Fig. 6.18 shows the normalized current density $|\boldsymbol{j}_z|/j_c$. Note the differences between this distribution and the one when only the HTS layer was modeled (Fig. 6.7). Under this configuration, the current is concentrated near the silver layer, i.e. far from the substrate.

(a) Full mesh (b) TS model mesh

Figure 6.16 Zoom of the meshes near the right edge of the tape: (a) full mesh for standard FE application (reference model), and (b) simplified mesh used with the TS model. Although all layers of the HTS tape are represented as a single line in the TS model, the stacking order is still respected in the virtual discretization.

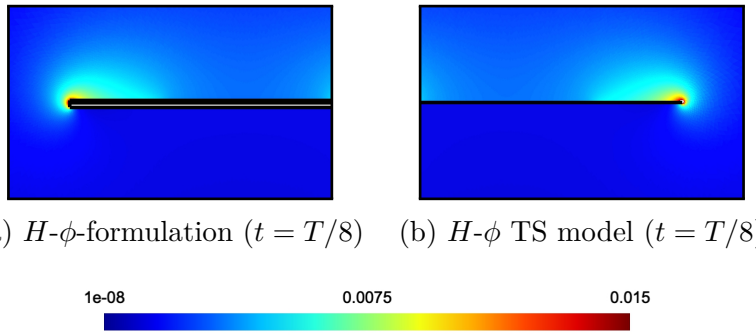


(a) $H$-$\phi$-formulation ($t = T/8$) (b) $H$-$\phi$ TS model ($t = T/8$)

Figure 6.17 Norm of magnetic flux density $|\boldsymbol{b}|$ [T] for a single HTS tape comprising three thin layers with $I/I_c = 0.9$ at $T/2$. (a) Fully discretized $H$-$\phi$ reference model, and (b) proposed TS approach with $N = 6$.

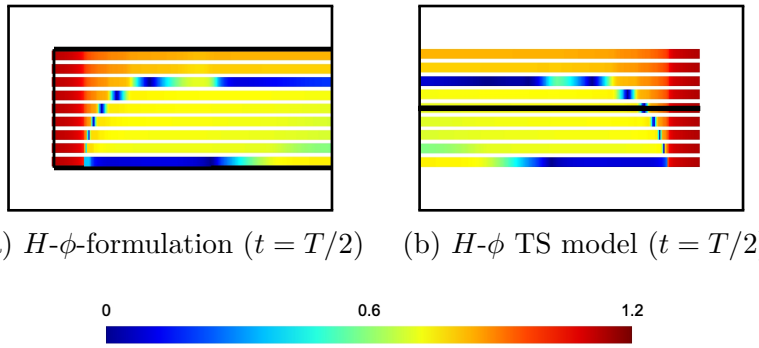


(a) $H$-$\phi$-formulation ($t = T/2$) (b) $H$-$\phi$ TS model ($t = T/2$)

Figure 6.18 Normalized relative current density ($|\boldsymbol{j}_z|/j_c$) near the extremity of the HTS tape with three layers at $t = T/2$: (a) $H$-$\phi$ reference solution, and (b) $H$-$\phi$ TS solution with $N = 11$. The TS solution was obtained by a projection of the $|\boldsymbol{j}_z|/j_c$ on the virtual position of the 1-D elements. The black line in the middle of (b) represents the tape in the TS model (a line in 2-D).

Simulations with the TS model were twice as fast as the simulations using the reference model with same size mesh elements on the surfaces of the tapes. The number of DoFs was reduced by around 30% in this case. However, as discussed in this paper, a coarser mesh could have been used in the TS model. The considered high-density mesh served to validate the TS model in terms of accuracy.

The AC losses per cycle of time as a function of the transport current in each layer of the tape are presented in Fig. 6.19. Given the low resistivity value of HTSs, the current flows mainly in this layer. Therefore, AC losses in the HTS layer are more important than in the other two layers. This example demonstrates that the TS model various HTS devices architectures including HTS tapes comprising multiple layers made of different materials.

## 6.6 Conclusion

In this paper, a new thin shell (TS) model for modeling thin HTS tapes in 2-D was developed and validated through examples. The model is based on the $H$-$\phi$-formulation and the addition of auxiliary 1-D FE equations for the variation of the tangential components of the magnetic field inside the tapes. This procedure allows representing the nonlinearities associated with the HTS material in time-transient FE simulations. Compared to a reference solution based on standard FE with the $H$-$\phi$-formulation, the TS model provided good results for all the studied cases while also reducing the number of DoFs by more than 40% and speeding up simulations by seven times in some cases.

The TS model was also compared with the widely used $T$-$A$-formulation in terms of local accuracy and AC losses. For problems where the magnetic field normal components are more intense than the tangential components, the TS model with $N = 1$ is comparable to the $T$-$A$-formulation since both models consider a linear field distribution across the thickness of the tape. However, when the tapes are closely-packed together, the $T$-$A$-formulation does not provide good solutions. The TS model application with $N > 1$ has shown to give a correct solution in these cases. We demonstrated that the virtual discretization can be especially interesting to tackle problems involving multiple thin layers, such as those in real HTS tapes.

In future work, the presented TS model will be extended for 3-D simulation of HTS devices. However, its use goes beyond modeling HTS systems. The presented model represents a generalization of the classical TS model with interface conditions (ICs) defined as 1-D auxiliary problems across the thickness of the thin region. This allows tackling problems involving multilayers of different materials and the use of special basis functions in the 1-D problem. In addition, the presented methodology can easily be extended to a pure $H$- or

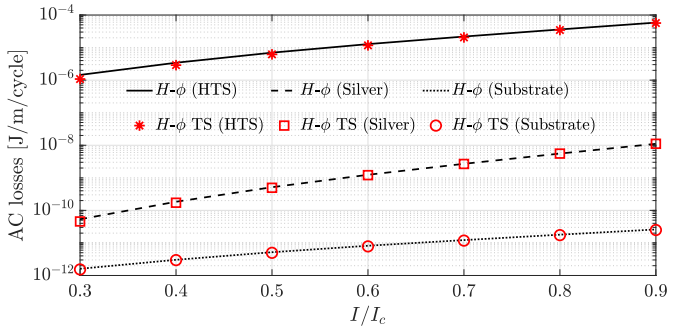


Figure 6.19 Total AC losses in each layer of an HTS tape as a function of the relative transport current $I/I_c$. Note the good agreement between the solutions in each layer of the HTS tape.

$A$-formulation with the ICs properly defined. Its application in a $A$-formulation would be relevant for modeling nonlinear ferromagnetic thin regions in time-transient analysis, such as nonlinear shielding problems, for example.

**Acknowledgments**

The authors would like to acknowledge Frédéric Trillaud for sharing his codes on this matter, Ruth V. Sabariego and Christophe Geuzaine for their insights concerning this work and the help with the FE implementation using Gmsh and GetDP, and Alexandre Arsenault for all the discussions concerning the $H$-$\phi$-formulation.

This work has been supported by the Coordination for the Improvement of Higher Education Personnel (CAPES) - Brazil - Finance Code 001, and the Fonds de Recherche du Québec - Nature et Technologies (FRQNT).

# CHAPTER 7 PAPER 3: 3-D FINITE-ELEMENT THIN-SHELL MODEL FOR HIGH-TEMPERATURE SUPERCONDUCTING TAPES

IEEE TRANSACTIONS ON APPLIED SUPERCONDUCTIVITY

(paper submitted on October 29, 2021)

[1]Bruno de Sousa Alves, [1]Marc Laforest, [1]Frédéric Sirois

[1]Polytechnique Montréal, Montréal, QC H3C 3A7, Canada

**Abstract**

This paper presents a new three-dimensional time-domain finite-element thin-shell model for the electromagnetic modeling of high-temperature superconducting (HTS) tapes, as well as its validation on benchmark problems and its application to an HTS Roebel cable with 14 strands. The thin-shell model is based on the magnetic field formulation that considers the diffusion of the parallel components of the magnetic field into the tapes. The nonlinear behavior of the superconducting tapes is described with an $E$-$J$ power-law model in a virtual discretization across their thickness. This approach allows the calculation of the non-uniform current distribution through the thickness and in the place of the tapes, so the losses in multiple HTS tape assemblies are determined accurately. The results of the proposed approach are compared with those obtained with a full 3-D representation of the thin regions and show excellent agreement while reducing substantially the computational burden of the simulations.

## 7.1 Introduction

Recent advances in large-scale high-temperature superconductor (HTS) devices have driven the evolution of numerical methods to accurately and efficiently estimate their electromagnetic (EM) behavior through simulations. Indeed, the 3-D modeling of large-scale devices involving many HTS tapes is of high interest to the industry and to the academia. Many superconductor applications require cables with higher current capacity than that of a single tape, as well as lower AC losses [126]. Therefore, cable architectures such as TSTC (twisted stack tape conductor [23]), CORC (conductor on round core [24]) and Roebel cables [27] all use symmetrically transposed HTS tapes to reduce losses by reducing eddy currents and sharing the transport current equally between each tape. This transposition

creates a truly three-dimensional (3-D) geometry that does not allow any simplification by symmetry and thus requires a 3-D model [26].

Among the available numerical methods, the finite element (FE) method has proved to be efficient in tackling nonlinear problems with complex 3-D geometries [22]. Despite this, modeling HTS devices involving REBCO tapes with FE is still time-consuming, mainly due to their high aspect ratio and associated discretization issues [110]. Moreover, the electrical resistivity of HTS materials, usually described by an $E$-$J$ power-law model [21], is highly nonlinear and makes it hard to achieve convergence [110].

Two primary and dual classes of FE formulations are often applied to model HTS devices: the magnetic field ($H$-)based formulations [68–70] and the magnetic scalar potential ($A$)-based formulations [130]. In [43], the $H$-formulation with the Newton-Raphson method has proved to be more efficient in tackling problems involving HTS than the $A$-formulation, which would be preferable for modeling nonlinear ferromagnetic materials. Therefore, solutions obtained with the standard $H$-formulation are often considered as a reference for developing new numerical approaches to model HTS devices [68]. In cases involving both HTS and ferromagnets, the use of mixed formulations could be advantageous [72, 73, 131], but their coupling must be done carefully [71].

In [35], the authors proposed a mixed formulation that uses $T$ (current vector potential) and $A$ to solve problems involving HTS tapes. In this so-called $T$-$A$-formulation, a 1-D problem depending on $T$ describes the physical behavior along the width of the tapes, which is represented as a line in a 2-D calculus domain. A current density is obtained from $T$, which is used as a source term in an $A$-formulation that models the surroundings of the superconducting tapes. This procedure avoids meshing the thin regions and provides significant reductions in the computational cost [110].

The $T$-$A$-formulation is currently considered as the most computationally efficient model to simulate HTS tapes, and it has been widely used recently by the HTS modeling community [114–116]. However, two major problems impede its application to model 3-D large-scale HTS devices. Firstly, the coupling between $T$ and $A$ requires higher-order shape functions for $A$ than for $T$ in order to ensure the numerical stability of the model [108]. This increases the total number of degrees of freedom (DoFs) in the non-conducting regions, which essentially limits the application of the $T$-$A$-formulation to 2-D simulations. Indeed, in 3-D, the number of DoFs in the $T$-$A$-formulation is comparable to that in a pure $H$-formulation, providing little computational advantage [109]. Secondly, this formulation assumes a constant current density across the thickness of the tape, which is not a valid approximation when modeling closely-packed tapes carrying anti-parallel currents [78]. Similarly as in the strip

approximation [17], the $T$-$A$-formulation underestimates the AC losses in such cases [79].

In addition to the $T$-$A$-formulation, some effort has also been made to reduce the overall computational cost of modeling HTS tapes with the $H$-formulation. In [61, 118], the authors proposed to use the magnetic scalar potential ($\phi$) in the non-conducting regions to avoid leakage currents in such regions and reduce the total number of DoFs. Compared to a pure $H$-formulation, this so-called $H$-$\phi$-formulation can reduce the DoFs and CPU time by more than 75% in some cases [119]. This formulation overcomes the problem of mixed formulations since the coupling between $H$ and $\phi$ is implicit [64]. Discontinuities along cuts in the computational domain allow imposing net currents in the conductors [49]. These cuts can be manually defined, as in [50, 132], or generated automatically at low cost during the pre-processing phase [55].

In [133], we proposed a 2-D thin-shell (TS) model based on the $H$-$\phi$-formulation. The HTS tapes were represented as reduced-dimension geometries (lines) in the domain, and the duplication of nodes and edges in their discretization allowed discontinuities in the tangential components of the magnetic field across the tapes. The transport current was imposed in the tapes through discontinuities of the magnetic scalar potential along cuts, as in the standard $H$-$\phi$-formulation. Moreover, a virtual discretization across the thickness of the tapes allowed taking into account their EM response in the calculations. We demonstrated that a single virtual element makes this approach equivalent to the classical TS approach for ohmic conductors [127] and dual to the $T$-$A$-formulation under specific conditions. The virtual mesh refinement in the proposed TS model overcomes the limitations of the $T$-$A$-formulation when simulating a large number of HTS tapes in any configuration and comprising multiple thin layers, such as a superconducting and a ferromagnetic layer in some type of HTS tapes (e.g. RABiTS [27]).

In this paper, we extend the TS model proposed in [133] to 3-D cases. The interface conditions (ICs) in the TS model are derived from 1-D auxiliary problems defined across to the thickness of the tapes. These auxiliary problems are written in terms of the parallel components of the magnetic field, which can thus penetrate the reduced-dimension geometries (surfaces) representing the HTS tapes in the 3-D model. We demonstrate that this approach can provide accurate solutions for HTS tapes under transport current and external field excitations. The model is also applied to simulate a Roebel cable with 14 strands. The local field, current distributions and AC losses show good agreement with the reference solutions obtained with standard FE solutions in 3-D. The use of the TS model can significantly speed up the simulations compared to a full 3-D $H$-$\phi$-formulation, which is already very advantageous compared to a pure $H$-formulation [119, 120, 132].

## 7.2 Mathematical Formulation of the Model

### 7.2.1 Computational domain definition

Although the 2-D TS model proposed in [133] can account for any number of layers in the thin region, to keep the equations readable, we assume in this paper that the thin region is solely composed of a superconducting layer. The regions surrounding the tapes are assumed to contain only air. This assumption is usually valid (and frequently used) since the substrate and the coating layers of HTS tapes have resistivities several orders of magnitude higher than the superconducting material. Our computational domain is thus denoted as $\Omega = \Omega_s \cup \Omega_s^C \in \mathbb{R}^3$ (see Fig. 7.1a), with boundary $\partial\Omega$ decomposed as $\partial\Omega = \Gamma_h \cup \Gamma_e$, where $\Omega_s$ and $\Omega_s^C$ are respectively the superconducting and the non-superconducting subdomains of $\Omega$, and $\Gamma_h$ and $\Gamma_e$ are respectively the portions of $\partial\Omega$ along which Dirichlet and Neumann boundary conditions are applied.

It is also assumed that $\Omega_s$ comprises $K$ disjoint thin regions $\Omega_{s,1}, \dots \Omega_{s,K}$. Each region can be described in its own $xyz$ local coordinate system in which the thickness $d \approx 1\,\mu$m is along the $z$-direction, the width $w \approx$ 4-12 mm is along the $x$-direction, and the length $l$ (typically $\gg w$) is along the $y$-direction. Given the high aspect ratio of the $\Omega_{s,i}$ subdomains ($w/d$ is typically $> 1000$), these regions are approximated by reduced-dimension geometries in $\Omega$ ($d \to 0$), denoted by $\Gamma_{s,i}$, i.e. the volumetric subdomains $\Omega_{s,i}$ are collapsed onto surfaces situated halfway between their wide faces $\Gamma_{s,i}^{\pm}$ (see Fig. 7.1b). For convenience, the developments presented below consider a single thin HTS surface denoted by $\Gamma_s$, as in the example shown in Fig. 7.2(a). The approach can obviously be generalized to consider as many tapes as required to model a HTS device.

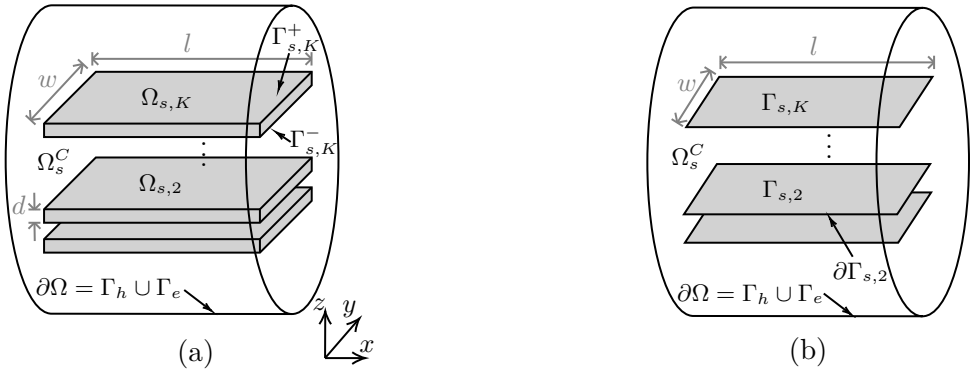


Figure 7.1 (a) Standard and (b) thin-shell domains with their respective subdomains, boundaries, and geometrical parameters identified.

### 7.2.2 FE model in the surrounding of the HTS tapes

To include the physics of the thin superconducting region in the calculations, the first step is to duplicate the mesh nodes, edges and faces on $\Gamma_s$, except nodes and edges on its lateral boundaries $\partial\Gamma_s$ (e.g., $\partial\Gamma_{s,2}$ in Fig. 7.1b). This creates a crack in the topological structure of $\Omega_s^C$, which becomes multiply-connected. Thereby, the boundary of the superconducting region is described by two complementary faces, namely $\Gamma_s = \Gamma_s^+ \cup \Gamma_s^-$, with $\Gamma_s^+$ and $\Gamma_s^-$ corresponding to the top and bottom sides of $\Gamma_s$, respectively (see Fig. 7.2b and 7.2c). This duplication also allows the tangential components of the magnetic field (parallel to the thin surfaces) to be discontinuous across $\Gamma_s$.

Let $\boldsymbol{H}(\mathrm{curl}, \Omega_s^C) = \{\boldsymbol{u} : \Omega \to \mathbb{R}^3 \,|\, \|\boldsymbol{u}\| < \infty, \|\nabla\times\boldsymbol{u}\| < \infty, \boldsymbol{n}\times\boldsymbol{u} = \boldsymbol{f}_h \text{ over } \Gamma_h\}$ where $\|\boldsymbol{u}\|^2 = \int_\Omega \|\boldsymbol{u}\|^2 d\boldsymbol{x}$ is the $L^2$ norm and $\boldsymbol{f}_h$ is a known tangential vector field, while $\boldsymbol{H}_0(\mathrm{curl}, \Omega_s^C)$ is the same space as $\boldsymbol{H}(\mathrm{curl}, \Omega_s^C)$ except with homogeneous boundary conditions $\boldsymbol{n} \times \boldsymbol{u} = 0$ over $\Gamma_h$. Assuming a low-frequency regime and homogeneous Neumann boundary conditions in $\Gamma_e$, and disregarding the displacement current, the variational form of the $H$-formulation for the aforedescribed problem in $\Omega_s^C$ is defined from Ampere's and Faraday's laws as follows:

Find $\boldsymbol{h} \in \boldsymbol{H}(\mathrm{curl}, \Omega_{\mathrm{s}}^{\mathrm{C}})$ such that

$$\Big(\partial_t \mu \boldsymbol{h}, \boldsymbol{g}\Big)_{\Omega_s^C} - \Big\langle \boldsymbol{n}_s \times \boldsymbol{e}, \boldsymbol{g}\Big\rangle_{\Gamma_s^+} + \Big\langle \boldsymbol{n}_s \times \boldsymbol{e}, \boldsymbol{g}\Big\rangle_{\Gamma_s^-} = 0, \tag{7.1}$$

$\forall\ \boldsymbol{g} \in \boldsymbol{H}_0(\mathrm{curl}, \Omega_{\mathrm{s}}^{\mathrm{C}})$, where bold characters represent vectors, $\boldsymbol{h}$ is the magnetic field, $\boldsymbol{e}$ is the electric field, $\mu$ is the magnetic permeability, and $(\cdot,\cdot)_{\Omega_s^C}$ and $\langle\cdot,\cdot\rangle_{\Gamma_s^\pm}$ respectively denote the volume integral over $\Omega_s^C$ and the surface integral over $\Gamma_s^\pm$ of the scalar product of their two arguments. For simplicity, we consider $\boldsymbol{n}_s = \boldsymbol{n}_s^+ = -\boldsymbol{n}_s^-$, where $\boldsymbol{n}_s^\pm$ are the outward unit normal vectors on $\Gamma_s^\pm$ (see Fig. 7.2c). The two last terms in (7.1) represent the interface conditions required to include the physics of the thin region in the TS model. Note that $\boldsymbol{h} \in \boldsymbol{H}(\mathrm{curl}, \Omega_{\mathrm{s}}^{\mathrm{C}})$ includes the boundary condition for $\boldsymbol{n} \times \boldsymbol{h}$ (i.e. the tangential magnetic field) along $\Gamma_h$ (Dirichlet boundary condition).

In $\Omega_s^C$, the magnetic field is defined in terms of the magnetic scalar potential ($\boldsymbol{h} = -\nabla\phi$). This allows reducing the total number of DoFs and avoids errors such as leakage currents in $\Omega_s^C$, which appear in a pure $H$-formulation [61]. Despite this, the $\boldsymbol{h}$-representation through $\phi$ in $\Omega_s^C$ is not enough to satisfy Ampere's law in this region when the HTS tape carries a net transport current, since $\forall\phi$, $\nabla \times \nabla\phi = 0$. Cuts are introduced to make $\Omega_s^C$ simply connected and to impose discontinuities on $\phi$, whose values determine the net current in each connected components of $\Omega_s$ (i.e. in each conductor).

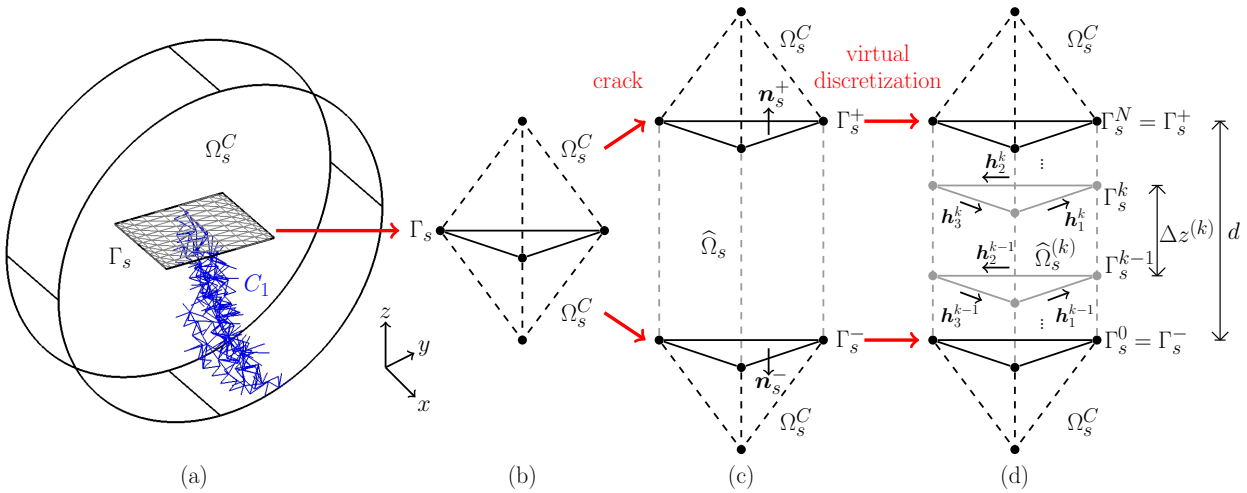


Figure 7.2 Proposed TS approach: (a) domain with a single thin HTS tape represented as an embedded surface ($\Gamma_s$) in $\Omega_s^C$, (b) example of two tetrahedral elements sharing a common face in $\Gamma_s$, (c) duplication of the mesh entities in $\Gamma_s$, creating a crack in $\Omega_s^C$, and resulting in a virtual prismatic domain $\widehat{\Omega}_s$, and (d) virtual discretization throughout the thickness of the tape into $N$ elements of thickness $\Delta z^{(k)} = d/N$ denoted by $\widehat{\Omega}_s^{(k)}$. The thick cut $C_1$ depicted in blue in (a) is generated automatically in our modeling environment (Gmsh) and is used to impose a current constraint in the virtual domain $\widehat{\Omega}_s$

In this paper, we use thick cuts such as in [55]. Therefore, the magnetic field in $\Omega_s^C$ is discretized as follows

$$\boldsymbol{h} = \sum_{n \in \Omega_s^C} -\phi_n \nabla w_n + \sum_{C_i \in \Omega_s^C} I_i \boldsymbol{\psi}_i, \tag{7.2}$$

where $w_n$ are the nodal basis functions associated to each node $n$ in $\Omega_s^C$, and $\boldsymbol{\psi}_i$ are edge-based cohomology basis functions (thick cuts) dual to the cycles $C_i$ around each superconducting subdomain $\Omega_{s,i}$. The integration of $\boldsymbol{h}$ over these cycles gives the related net current $I_i$ to be imposed in each thin conductor $\Omega_{s,i}$. An example of a thick cut in $\Omega_s^C$ is depicted in Fig. 7.2(a). Tetrahedral FE with first-order Nédélec basis functions are used in $\Omega_s^C$.

### 7.2.3 FE model inside the HTS tapes

The next step is to describe the physics inside the tape by means of the surface integral terms over $\Gamma_s^{\pm}$ that appear in (C.1). To this end, we analyze the original volume $\Omega_s$ separately as a virtual FE problem. Each pair of tetrahedral elements sharing a common triangular face on $\Gamma_s$ (Fig. 7.2b) gives rise to a local problem in a virtual domain denoted $\widehat{\Omega}_s$ (Fig. 7.2c). The lateral faces of $\widehat{\Omega}_s$ can be ignored because of the high aspect ratio of the HTS tapes and their representation as a zero-thickness geometry in the calculus domain. Note that it does

not mean that the normal components of the fields are neglected, as discussed in [133].

Taking $\boldsymbol{h}$ as a working variable, the weak form for the local problem in $\widehat{\Omega}_s$ is

$$\begin{aligned} -\Big\langle \boldsymbol{n}_s \times \boldsymbol{e}, \boldsymbol{g} \Big\rangle_{\Gamma_s^+} + \Big\langle \boldsymbol{n_s} \times \boldsymbol{e}, \boldsymbol{g} \Big\rangle_{\Gamma_s^-} \\ = \Big(\rho \nabla \times \boldsymbol{h}, \nabla \times \boldsymbol{g}\Big)_{\widehat{\Omega}_s} + \Big(\partial_t \mu \boldsymbol{h}, \boldsymbol{g}\Big)_{\widehat{\Omega}_s}, \end{aligned} \tag{7.3}$$

where $\rho$ is the electrical resistivity.

We then consider the virtual discretization of $\widehat{\Omega}_s$ into $N$ prismatic FEs $\widehat{\Omega}_s^{(k)}$, $1 \leq k \leq N$, with thickness $\Delta z = d/N$ and lower and upper boundaries $\Gamma_s^{k-1}$ and $\Gamma_s^k$ (Fig. 7.2d). The volume integrals in (7.3) become

$$\Big(\rho \nabla \times \boldsymbol{h}, \nabla \times \boldsymbol{g}\Big)_{\Omega_s} + \partial_t \Big(\mu \boldsymbol{h}, \boldsymbol{g}\Big)_{\Omega_s} = \sum_{k=1}^{N} \Big(\rho^{(k)} \nabla \times \boldsymbol{h}, \nabla \times \boldsymbol{g}\Big)_{\widehat{\Omega}_s^{(k)}} + \Big(\partial_t \mu^{(k)} \boldsymbol{h}, \boldsymbol{g}\Big)_{\widehat{\Omega}_s^{(k)}}, \tag{7.4}$$

where $\rho^{(k)}$ and $\mu^{(k)}$ are the electrical resistivity and the magnetic permeability, respectively, in $\widehat{\Omega}_s^{(k)}$. A local coordinate system $xyz$ is located at the center of the virtual volume. Therefore, the outward normal on $\Gamma_s$ is parallel to the $z$-axis, and the tangential components of $\boldsymbol{h}$, denoted by $\boldsymbol{h}^{k-1}$ and $\boldsymbol{h}^k$ in $\Gamma_s^{k-1}$ and $\Gamma_s^k$, respectively, are in the $xy$-plane. Note that in what follows, the space and time dependence of $\boldsymbol{h}^k$ is omitted in the notation, excepted when needed for clarity.

Next, we use first degree Lagrange basis functions to describe the profile of $\boldsymbol{h}$ in the $z$-direction (across $\Delta z^{(k)}$), i.e.

$$\theta_1(z) = \frac{z_k - z}{\Delta z^{(k)}}, \qquad \theta_2(z) = \frac{z - z_{k-1}}{\Delta z^{(k)}}, \tag{7.5}$$

where $z_{k-1}$ and $z_k$ are the virtual positions of faces $\Gamma_s^{k-1}$ and $\Gamma_s^k$, respectively. The magnetic field in each virtual volumetric element $\widehat{\Omega}_s^{(k)}$ thus reads

$$\begin{aligned} \boldsymbol{h}(x,y,z,t)|_{\widehat{\Omega}_s^{(k)}} &= \sum_{i=1}^{2} \boldsymbol{h}^{\gamma}(x,y,t)\theta_i(z) \\ &= \sum_{m=1}^{3} \sum_{i=1}^{2} h_m^{\gamma}(t) \boldsymbol{w}_m(x,y)\theta_i(z), \end{aligned} \tag{7.6}$$

where $\gamma = \gamma(k,i) = k-2+i$ relates the tangential component of the magnetic field $\boldsymbol{h}^{\gamma}$ in each intermediate surface $\Gamma_s^{\gamma}$ of $\widehat{\Omega}_s$ to the boundaries of $\widehat{\Omega}_s^{(k)}$ (see Fig. 7.2d), $h_m^{\gamma}$ is the magnitude of $\boldsymbol{h}^{\gamma}$ along the edges $m = 1, 2$ and 3 of the triangular element in $\Gamma_s^{\gamma}$, and $\boldsymbol{w}_m$ is the edge basis function related to edge $m$.

Then, using the vector calculus identity $\nabla \times (\boldsymbol{v}u) = \nabla u \times \boldsymbol{v} + u\nabla \times \boldsymbol{v}$, where $u$ and $\boldsymbol{v}$ are scalar and vector functions, respectively, we have that

$$\nabla \times \boldsymbol{h}|_{\widehat{\Omega}_s^{(k)}} = \sum_{m=1}^{3}\sum_{i=1}^{2} h_m^{\gamma}\left(\nabla\theta_i \times \boldsymbol{w}_m + \theta_i \nabla \times \boldsymbol{w}_m\right). \tag{7.7}$$

The test functions $\boldsymbol{g}$ in (7.4) are chosen from the same space as $\boldsymbol{h}$ (Galerkin method), except for homogeneous boundary conditions (i.e., $\boldsymbol{g} \in \boldsymbol{H}_0(\mathrm{curl}, \Omega)$). We define $\boldsymbol{g}(x,y,z)|_{\widehat{\Omega}_s^{(k)}} = \boldsymbol{w}_n(x,y)\theta_j(z)$, for $n = 1, 2$ and 3 and $j = 1$ and 2, corresponding respectively to the $n^{\text{th}}$-edge and $j^{\text{th}}$-surface in $\widehat{\Omega}_s$ (a boundary of $\widehat{\Omega}_s^{(k)}$).

Inserting (7.6) and (7.7) into (7.4), the inner product $(\nabla \times \boldsymbol{h}) \cdot (\nabla \times \boldsymbol{g})$ gives rise to terms of the form $(\theta_i \nabla \times \boldsymbol{w}_m) \cdot (\nabla\theta_j \times \boldsymbol{w}_n)$, which are identically zero since $\theta_i \nabla \times \boldsymbol{w}_m$ is in the $z$-direction and $\nabla\theta_j \times \boldsymbol{w}_n$ is in the $xy$-plane. The remaining terms are of the form $\nabla\theta_i \cdot \nabla\theta_j(\boldsymbol{w}_m \cdot \boldsymbol{w}_n)$, $\theta_i\theta_j(\nabla \times \boldsymbol{w}_m) \cdot (\nabla \times \boldsymbol{w}_n)$ and $\theta_i\theta_j(\boldsymbol{w}_m \cdot \boldsymbol{w}_n)$. They represent the variation of the fields in $\Gamma_s$ given by the functions $\boldsymbol{w}_m$ and $\boldsymbol{w}_n$ (and their curl) multiplied by the field variation along $\Delta z^{(k)}$ given by the functions $\theta_i$ and $\theta_j$ (and their gradient). Consequently, the volume integrals over $\widehat{\Omega}_s$ in (7.4) can be represented as the product of the surface integrals over $\Gamma_s^{\gamma}$ and line integrals over $\Delta z^{(k)}$. The complete development of these terms, which is the core of the method, is presented in Appendix A.

Given that $\Gamma_s^{k-1}$ and $\Gamma_s^{k}$ are copies of $\Gamma_s$, we can define the 2-D stiffness ($\mathcal{A}^{(k)}$) and mass ($\mathcal{B}^{(k)}$) matrices in $\Gamma_s$ as

$$\mathcal{A}_{mn}^{(k)} = \left\langle \nabla \times \boldsymbol{w}_m, \nabla \times \boldsymbol{w}_n \right\rangle_{\Gamma_s}, \tag{7.8}$$

$$\mathcal{B}_{mn}^{(k)} = \left\langle \boldsymbol{w}_m, \boldsymbol{w}_n \right\rangle_{\Gamma_s}. \tag{7.9}$$

The 1-D elementary matrices over $\Delta z^{(k)}$ as

$$\mathcal{C}_{ij}^{(k)} = \int_{\Delta z^{(k)}} \partial_z\theta_i \, \partial_z\theta_j \, \mathrm{d}z, \tag{7.10}$$

$$\mathcal{D}_{ij}^{(k)} = \int_{\Delta z^{(k)}} \theta_i\theta_j \, \mathrm{d}z, \tag{7.11}$$

which can be evaluated analytically as in [133]. The resulting stiffness and mass matrices for the 3-D virtual element are

$$\mathcal{S}^{(k)} = \left(\mathcal{A}^{(k)} \otimes \mathcal{D}^{(k)}\right) + \left(\mathcal{B}^{(k)} \otimes \mathcal{C}^{(k)}\right), \tag{7.12}$$

and

$$\mathcal{M}^{(k)} = \mathcal{B}^{(k)} \otimes \mathcal{D}^{(k)}, \tag{7.13}$$

respectively, where $\otimes$ is the Kronecker product [134] of the matrices in the argument, which results in block matrices of dimension $6 \times 6$. Since (7.8)-(7.11) are symmetric, so are (7.12) and (7.13). The detailed definitions of the matrices $\mathcal{S}^{(k)}$ and $\mathcal{M}^{(k)}$ are given in Appendix B. Finally, the volume integrals in (7.4) become

$$\left(\rho^{(k)}\nabla \times \boldsymbol{h}, \nabla \times \boldsymbol{g}\right)_{\widehat{\Omega}_s^{(k)}} = \rho^{(k)}\mathcal{S}^{(k)}H^{(k)}, \tag{7.14}$$

$$\left(\partial_t \mu^{(k)}\boldsymbol{h}, \boldsymbol{g}\right)_{\widehat{\Omega}_s^{(k)}} = \partial_t \mu^{(k)}\mathcal{M}^{(k)}H^{(k)}, \tag{7.15}$$

where the vector of unknowns $H^{(k)}$ in $\widehat{\Omega}_s^{(k)}$ is

$$H^{(k)} = \left[h_1^{k-1}, h_1^k, h_2^{k-1}, h_2^k, h_3^{k-1}, h_3^k\right]^T. \tag{7.16}$$

The current density $\boldsymbol{j}$ in each virtual element $\widehat{\Omega}_s^{(k)}$ is constant across $\Delta z^k$ and is defined as

$$\boldsymbol{j}|_{\widehat{\Omega}_s^{(k)}} = \boldsymbol{n}_s \times \partial_z \boldsymbol{h}|_{\widehat{\Omega}_s^{(k)}} = \boldsymbol{n}_s \times \left(\frac{\boldsymbol{h}^k - \boldsymbol{h}^{k-1}}{\Delta z^{(k)}}\right), \tag{7.17}$$

Therefore, the nonlinear resistivity in $\widehat{\Omega}_s^{(k)}$, which depends on $\boldsymbol{j}$ in the power-law model for superconductors, can be written as

$$\rho^{(k)} = \frac{E_c}{J_c}\left(\frac{|\boldsymbol{h}^k - \boldsymbol{h}^{k-1}|}{J_c \Delta z^{(k)}}\right)^{n_s - 1} \tag{7.18}$$

where $J_c$ is the critical current density, $n_s$ is the power-law exponent, and $E_c = 1\,\mu\text{V/cm}$ is the electric field criterion. The magnetic permeability $\mu^{(k)}$ is assumed constant in superconductors, i.e. $\mu^{(k)} = \mu_0$ in $\Omega_s^{(k)}$, but this is not a limitation of the proposed model. In [133], ferromagnetic thin layers were modeled with the 2-D version of the presented TS model and can also be done in 3-D.

### 7.2.4 Coupling of the finite-element models

We can use (7.3), (7.4), (7.14) and (7.15) to find an equivalent expression for the interface terms in (7.1), i.e.

$$\begin{aligned} -\left\langle \boldsymbol{n}_s \times \boldsymbol{e}, \boldsymbol{g}\right\rangle_{\Gamma_s^+} + \left\langle \boldsymbol{n_s} \times \boldsymbol{e}, \boldsymbol{g}\right\rangle_{\Gamma_s^-} \\ = \sum_{k=1}^{N} \rho^{(k)}\mathcal{S}^{(k)}H^{(k)} + \partial_t \mu^{(k)}\mathcal{M}^{(k)}H^{(k)}. \end{aligned} \tag{7.19}$$

This expression represents the interface conditions (ICs) used in our approach, i.e. it provides a well-defined relationship between the tangential components of the electric and magnetic fields on each side of the thin layer.

The complete weak form for the model is obtained by inserting (7.19) into (7.1). The tangential fields in $\Gamma_s^0$ and $\Gamma_s^N$ are $\boldsymbol{h}^0 = -\nabla\phi^-$ and $\boldsymbol{h}^N = -\nabla\phi^+$, respectively, which provides a natural connection between the thin layer model and the global system of equations in $\Omega_s^C$. The cuts necessary to impose the current in the tapes can be generated automatically by finding the edge-based cohomology basis representative of $\Omega_s^C$ after the introduction of the crack at $\Gamma_s$ has made $\Omega_s^C$ multiply-connected. The time derivative can be estimated by a numerical scheme such as implicit Euler, and the nonlinear system of equations can be solved by the Newton-Raphson (NR) method, as is often done [43].

In terms of post-processing, the instantaneous AC losses inside the superconducting thin layer is calculated from this compact expression:

$$\mathcal{L}(t) = \sum_{k=1}^{N} \int_{\Gamma_s} \rho^{(k)} (H^{(k)})^T \mathcal{S}^{(k)} H^{(k)} d\Gamma. \tag{7.20}$$

The 3-D TS approach described in this paper was implemented in Gmsh and GetDP. All the simulations were performed using a personal computer with an Intel i7 2400 processor and 16 Gb of memory. In GetDP, an adaptive time-stepping procedure was used in order to improve convergence, as explained in [14]. In our simulations, the maximum number of iterations of the nonlinear solver was set to 12, the initial time step was set to 7.5 $\mu$s, the maximum time step was set to 200 $\mu$s, the relative tolerance of the calculation was set to $10^{-5}$, and the absolute tolerance was set to $10^{-7}$. Finally, the NR scheme was used to solve the nonlinear system of equations with the initial guess at each new NR iteration equals to the solution at the previous time step.

## 7.3 Model Validation

Two 3-D benchmark problems were used to validate the proposed TS model: (i) a single HTS tape carrying a current, and (ii) a thin HTS disc immersed in a perpendicular magnetic field.

### 7.3.1 Single HTS Tape

We first considered the example of a single HTS tape embedded in air, similar to the geometry presented in Fig. 7.2a. The superconducting layer was 1 $\mu$m thick and 12 mm wide. The total length modeled was 4 mm. A current $I = I_0 \sin(2\pi f t)$ at an operating frequency $f = 50$ Hz

was imposed in the tape using a cut in $\Omega_s^C$, as discussed in Section 7.2. The solution obtained with the 3-D TS model was compared with (i) the standard FE solution of an equivalent 2-D problem and its complete discretization (2-D FE), and (ii) the solution obtained with the 2-D TS model proposed in [133].

In terms of mesh, the thin surface was discretized into 60 FEs across the width of the tapes using a bump of 0.1, meaning that elements near the tape extremities were ten times smaller than those at the center of the tape. In the 2-D reference FE model, a structured rectangular mesh with 10 elements across the thickness of the tape was considered. Moreover, we assumed $N = 1$ in the 2-D and 3-D TS models. Since here the normal components of the magnetic field dominate the dynamics of the problem, one virtual FE was enough to represent the physics of a single tape, as discussed in [133]. Also, Lagrange polynomials of first order were considered as basis functions in both the non-conducting region and in the virtual 1-D FE auxiliary systems of the proposed TS approach.

The normalized current density ($|\boldsymbol{j}/J_c|$) distributions along the tape width at $t = T/8$, $t = T/4$ and $t = T/2$, with $T = 1/f$, $I_0 = 0.9I_c$ and $n_s = 101$ are presented in Fig. 7.3. Note the good agreement between the 3-D and the 2-D solution at every time step. This validates the approach presented in Section 7.2 in terms of local current distribution inside a single HTS tape.

We further compared the models in terms of AC losses at different transport currents. The total losses per cycle were calculated analytically using the Norris formula [135]

$$\mathcal{Q} = \frac{\mu_0 I_c^2}{\pi} \left[ \begin{matrix} (1 - f_c)\ln(1 - f_c) \\ + (1 + f_c)\ln(1 + f_c) - f_c^2 \end{matrix} \right], \tag{7.21}$$

where $f_c = I_0/I_c$. The total losses with the TS models were obtained by integrating (7.20) over one cycle, i.e. $0 \leq t \leq T$. The simulations were performed with two exponent values in the power-law model (7.18): $n_s = 25$, and $n_s = 101$. The results were compared with the analytical solution (7.21) and are presented in Fig. 7.4. The higher the exponent $n_s$, the better is the agreement between the numerically computed losses and the Norris model (formally exact only when $n_s \to \infty$). The proposed TS model with $N = 1$ perfectly suits the problem of a single 3-D HTS tape.

To evaluate the computational speed of the proposed TS model, we performed simulations with a full discretization of the tape in 3-D while scaling the thickness of the HTS layer to 10 $\mu$m. This enabled a sufficiently fine discretization of the tape and consequently ensured that the solution was accurate. Two mesh elements across the thickness of the tape were

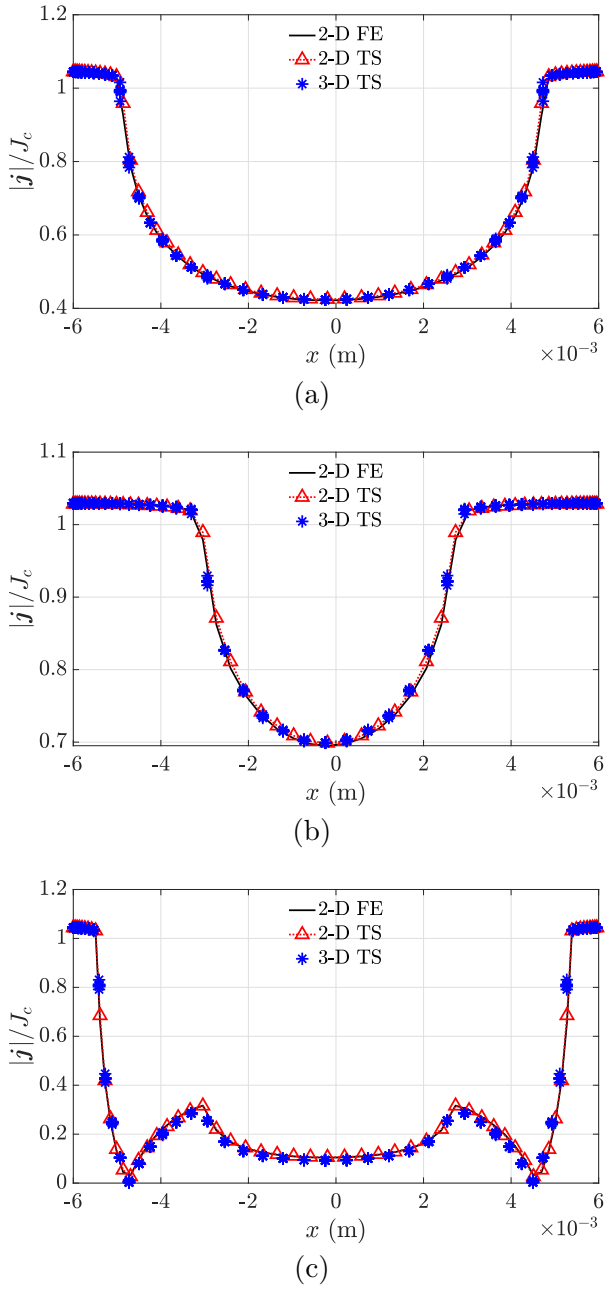


Figure 7.3 Normalized current density ($|\boldsymbol{j}|/J_c$) at (a) $t = T/8$, (b) $t = T/4$ and (c) $t = T/2$, with $T = 1/f$, $f = 50\,\text{Hz}$, $I_0 = 0.9I_c$ and $n_\text{s} = 101$.

considered and a standard $H$-$\phi$-formulation was used.

The number of DoFs, the CPU time, and the number of linear problems solved (LPS) before convergence with $I = 0.9I_c$ are summarized in Table 7.1. The use of the TS model in 2-D represented a reduction of 47% and 26% in DoFs and CPU time, respectively, compared to the reference 2-D model. No significant difference in the number of LPS was observed in this

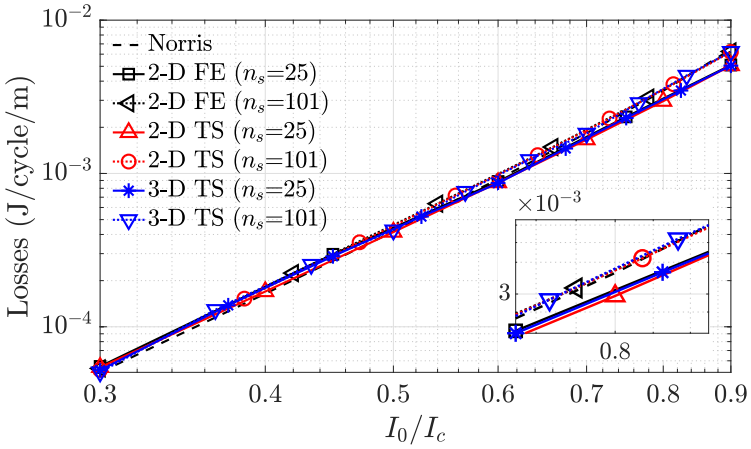


Figure 7.4 Transport AC losses of a single tape with $f = 50\,\text{Hz}$, including the results of the Norris analytical model, the 2-D FE model (infinitely long tape), the 2-D TS approach, and the proposed 3-D TS model. Two values of power-law exponent $n_s$ were considered: 25 and 101. The inset shows the AC losses close to $I_0/Ic = 0.8$. Note the excellent agreement between the solutions.

case. In 3-D, however, the reductions in DoFs and CPU time obtained with the TS model were 76% and 90%, respectively, while the number of LPS was about half of the LPS of the reference 3-D model. This proves that the proposed TS model can provide accurate solutions while speeding up 3-D simulations.

Mesh elements with poor aspect ratios in the reference 3-D model certainly hindered its convergence. In addition to reducing the number of DoFs related to the discretization of the thin layer itself, the TS model enhanced the mesh quality by avoiding poor quality elements near the extremities of the tape, both in the air and in the HTS tape. In the 3-D reference model, the worst aspect ratio of the FEs was ten times larger than that in the TS model. Consequently, more NR-iterations were necessary, increasing the number of LPS and the CPU time.

Although finite elements of first order were considered everywhere, no spurious oscillations such as those observed in the $T$-$A$-formulation [35] occurred with the proposed TS model. Indeed, the natural coupling between the TS model and the global FE system, done through the tangential components of the magnetic field, ensures the stability of the solution. The number of DoFs can be further reduced in the TS model since a coarser mesh can be considered on the surface representing the tape without worsening the quality of the 3-D mesh. Moreover, the use of the magnetic scalar potential in the non-conducting region provides an additional reduction of DoFs in comparison with a pure $H$ or $A$-formulation. All these features make the proposed model scale efficiently when simulating large-scale 3-D

Table 7.1 Number of DoFs, CPU time and number of linear problems solved (LPS) before convergence in 2-D and 3-D with complete discretization of the HTS tape and using the TS model with $I_0 = 0.9I_c$ and $N = 1$ in all cases

| | 2-D H-$\phi$ | 2-D TS H-$\phi$ | 3-D H-$\phi$ | 3-D TS H-$\phi$ |
|---|---|---|---|---|
| Number DoFs | 5927 | 3109 | 72121 | 16831 |
| CPU time [s] | 197.6 | 145.8 | 10052.4 | 957.4 |
| Number of LPS | 681 | 657 | 867 | 441 |

HTS devices.

### 7.3.2 Thin HTS disc in perpendicular magnetic field

To validate the proposed TS model under an external field excitation, we considered the example of the magnetization of a thin HTS disc, similar to the problem in [35]. The radius of the disc was $R = 10\,\text{mm}$ and its thickness was $d = 1\,\mu\text{m}$. No cuts in $\Omega_c^C$ were necessary in this example since the geometry is already simply connected and no current constraint needs to be imposed in the disk.

An external magnetic field $H(t) = H_0 \sin(2\pi f t)$ at an operating frequency $f = 50\,\text{Hz}$ was applied perpendicular to the disc surface. The chosen peak value was $H_0 = H_c$, where $H_c = J_c d/2$ is the full penetration field for a slab of thickness $d$ with critical state model, and $J_c = 5 \times 10^8\,\text{A/m}^2$. The power-law exponent was $n_s = 101$ in this example.

The current density distribution obtained using the TS model with $N = 1$ (single layer of elements in the virtual discretization) at different time steps is presented in Fig. 7.5. Note the continuous increase of the penetration depth before the external magnetic field reaches the first peak value (Fig. 7.5a-c). Also note the presence of persistent currents when the applied field returns to zero at $t = T/2$ (Fig. 7.5d).

The numerical results were validated with analytical solutions obtained with the Biot-Savart law and the critical state model, following the developments presented in [136]. The relative current density as a function of the radial position ($r$) inside the disc is

$$\frac{|\boldsymbol{j}(r)|}{J_c} = \begin{cases} \frac{2}{\pi} \tan^{-1}\left(\frac{r}{R}\left(\frac{R^2-a^2}{a^2-r^2}\right)^{1/2}\right), & \text{if } r < a, \\ 1, & \text{if } r \geq a, \end{cases} \tag{7.22}$$

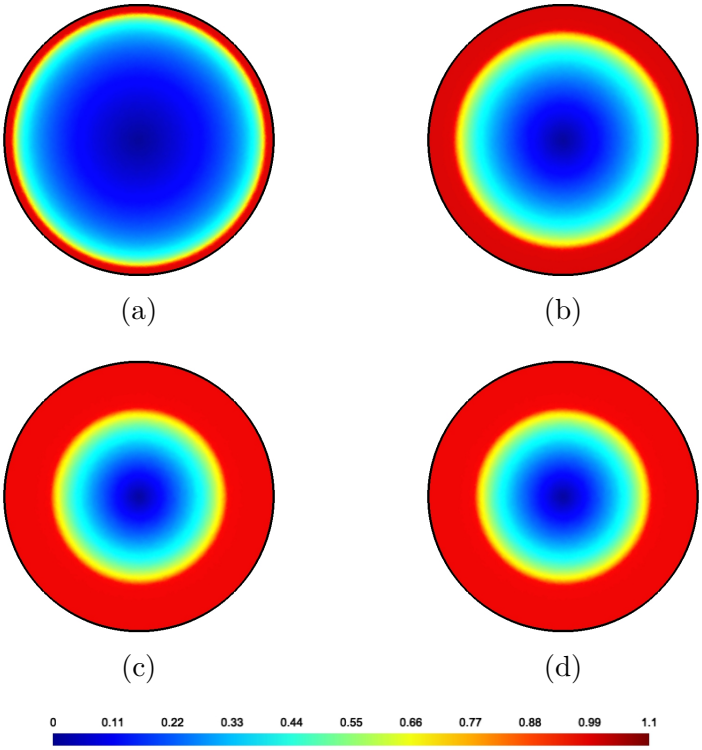


Figure 7.5 Normalized current density distribution ($|\boldsymbol{j}|/J_c$) in an HTS disc submitted to a 50 Hz external sinusoidal field: (a) $t = T/16$, (b) $t = T/8$, (c) $t = T/4$ (peak), and (d) $t = T/2$ (zero external field).

where $a$ is the penetration depth defined as

$$a = R\left(\frac{1}{\cosh(H/H_c)}\right). \tag{7.23}$$

Moreover, the normal component of the magnetic field ($\boldsymbol{h}_n$) on the disc surface relative to the critical field is

$$\frac{|\boldsymbol{h}_n(r)|}{H_c} = \cos^{-1}\left(\frac{R}{a}\right) - \cos^{-1}\left(\frac{R}{r}\right) + q(r), \tag{7.24}$$

where

$$q(r) = \frac{2}{\pi}\int_{\sin^{-1}(a/r)}^{\pi/2}\left(\frac{(1-\beta\cot\beta)}{(1-r/R^2\sin\beta)^{1/2}}\right)\mathrm{d}\beta. \tag{7.25}$$

The relative current density and magnetic field distributions against the radius are presented in Fig. 7.6a and 7.6b, respectively. The numerical solutions were taken at the peak field value at $t = T/4$. The normal component of the magnetic field in the numerical solution was taken as the mean value of the field on the top and bottom sides of the thin disc. Again, the excellent agreement between these solutions validates the proposed TS model for a 3-D

problem with an external field excitation.

In the TS model developed in Section 7.2, only the tangential components of the magnetic field were explicitly taken into account to describe the physics in the thin region. Despite that, our results show that the TS model provides accurate solutions also in terms of normal components of the magnetic field in the surroundings of the thin region. This is because by (7.19) the time variation of the mean value of the tangential components of the magnetic field is related to the discontinuity in the tangential components of the electric field on the thin surface. This discontinuity can therefore be related to the discontinuity of the normal magnetic flux density using Faraday's law, as explained in [32]. Therefore, the presented TS model obeys the magnetic flux conservation across the thin surface. The TS model is very general and can be used in simulations involving field components that are both normal and tangential to the thin region.

## 7.4 Application Example: the Roebel Cable

We applied our 3-D TS model to simulate the EM behavior of a Roebel cable with 14 strands and compared our results with those obtained with the fully 3-D $H$-formulation reference model proposed in [26]. The cable layout is shown in Fig. 7.7a, and the geometrical and electrical parameters are given in Table 7.2. For a more complete description of the cable geometry, we refer the reader to [28].

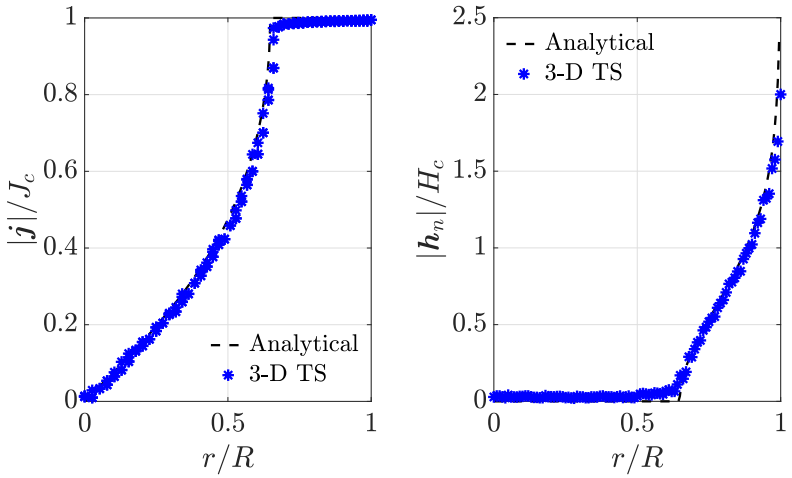


Figure 7.6 Normalized current density ($|\boldsymbol{j}|/J_c$) and magnetic field ($|\boldsymbol{h}_n|/H_c$) against the disc radius submitted to a 50 Hz external sinusoidal field at $t = T/4$, i.e. at the peak applied field.

The surroundings of the Roebel cable were assumed to be air, and only the superconducting layers of the HTS tapes were represented as thin surfaces in the TS model. Besides, in the reference model, the thickness of the superconducting layers were scaled to 10 $\mu$m in order to reduce the total number of DoFs in the air space and inside the tapes.

The transposition length and the number of strands defines a periodicity in the cable. For the given geometry, the EM analysis of 1/14th of its total transposition length (Fig. 7.7b) was sufficient to compute the current and field distributions, and the total AC losses per unit length. In [26], the authors used a periodic boundary condition (PBC) to map the magnetic field from one end of the model to the other end (lines $AA'$ and $BB'$ in Fig. 7.7). However, since the gap between the strands is very small compare to the simulated length, the current flows mostly in the length direction, and the magnetic field is consequently tangential to the boundary $\Gamma$, so PBC are not really necessary here. Therefore, in our 3-D TS model, only boundary conditions of type $\boldsymbol{n} \times \boldsymbol{h} = 0$ were considered in $\Gamma_h$.

In terms of mesh, two elements were considered across the thicknesses of the strands in the reference model. In the TS model, we also considered two layers of virtual elements ($N = 2$) in order to agree with the number of elements in the reference model and to observe the different current distributions on the top and bottom faces of the strands.

In our TS model, FE faces, edges and nodes on the lower-dimensional representation of the strands were duplicated by creating 14 cracked regions equivalent to holes in $\Omega_s^C$. The cohomology basis representatives (thick cuts) were then computed using the Gmsh code and comprise 14 thick cuts that were not necessarily associated with each individual strand of the Roebel cable. Indeed, some of them could be linear combinations of the individual cuts [132]. This issue was solved by using the automated method proposed in [55]: we obtained the desired cohomology basis representatives by taking the boundary of the relative homology basis $H_2(\Omega, \Omega_s)$ and by computing the cohomology basis dual to the resulting homology basis.

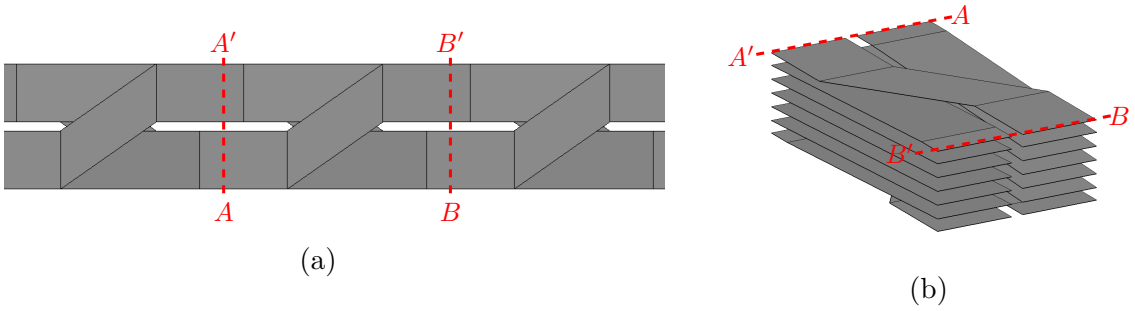


Figure 7.7 Geometry of the Roebel cable with 14 strands: (a) top view and (b) 3-D geometry.

Table 7.2 Geometrical and electrical parameters of the simulated Roebel cable

| Parameter | Value | Unit |
|---|---|---|
| Number of strands ($n_s$) | 14 | - |
| Transposition length ($l_t$) | 109 | mm |
| Cable width ($w_c$) | 4.3 | mm |
| Gap between strands ($g$) | 0.3 | mm |
| Strands width ($w_s$) | 2 | mm |
| Tape's thickness ($d$) | 10 | $\mu$m |
| Operating frequency ($f$) | 50 | Hz |
| Critical current ($I_c$) | 465 | A |
| Critical electric field ($E_c$) | $10^{-4}$ | V/m |
| Power-law exponent ($n$) | 21 | - |

This ensured that each generated cut was associated with only one strand of the cable, and a current constraint could be imposed on each one of them individually.

A current $I = I_0 \sin(2\pi f t)$ at an operating frequency $f = 50$ Hz and $I_0 = 400$ A was imposed in the cable strands. The resulting magnetic field distributions at $t = T/8$, $t = T/4$ and $t = T/2$ are presented in Fig. 7.8. Note the increase in the magnetic field penetration between Fig. 7.8a and 7.8b, and the remanent magnetic field at $t = T/2$, i.e. when the total net current is zero. In Fig. 7.8c, one also observes a field concentration in the outer rim of the straight section of the strand below the crossover section. This is the region where higher AC losses are found, as explained in [26]. Indeed, at the crossover region, the upper strand in the stack is exposed to a higher field, while the middle strands experience lower fields due to the magnetic screening provided by the upper and lower strands.

Fig. 7.9 shows the normalized current density vector distributions in the crossover region at $t = T/4$ (peak current value). Note that the outer face carries a larger current than the inner face. The current tends to flow mostly in the external portion of the strand, as pointed out in [26]. Moreover, the inner face of the crossover is exposed to the field variation from the lower strands, which generate screening currents that affect the overall current vector intensity and orientation across the thickness of the upper strand. The use of the proposed TS model with $N = 2$ allows the tangential components of the magnetic field to penetrate the wide faces of the strands and properly takes into account the interaction of multiple tapes. Observe for instance the irregular distribution of the current vectors in Fig. 7.9b, which is similar to the results presented in [26].

The total AC losses per unit length in the Roebel cable was calculated over one cycle with the integral in (7.20). The result was compared with the AC losses obtained with the reference

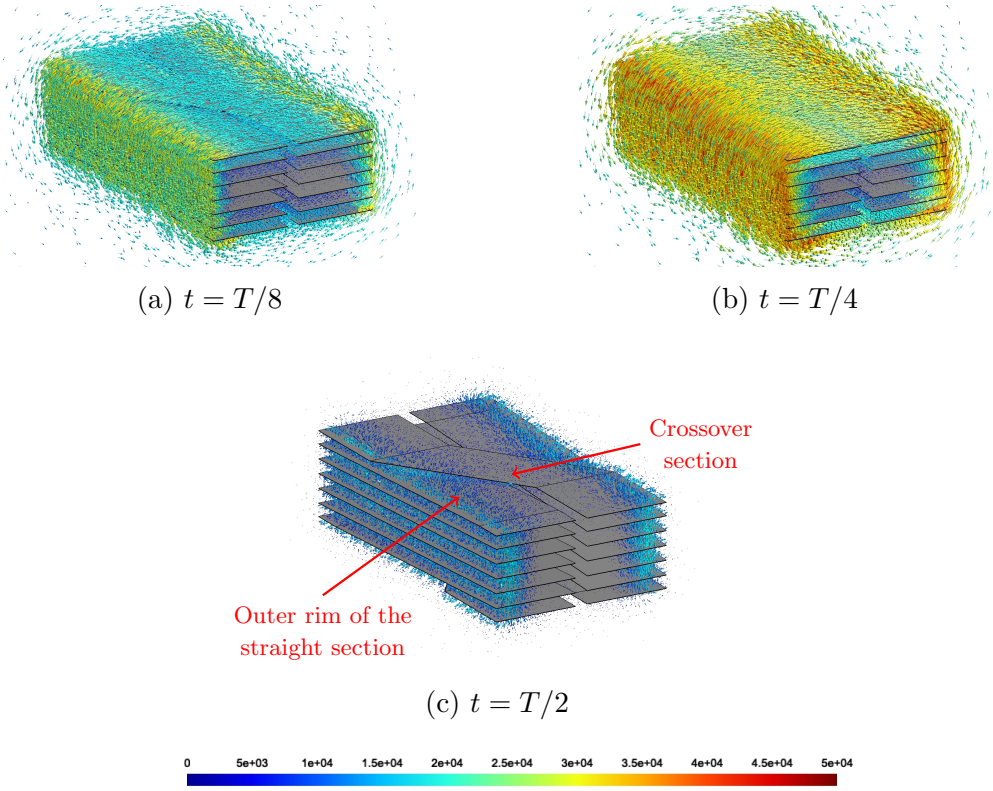


(a) $t = T/8$ (b) $t = T/4$

(c) $t = T/2$

Figure 7.8 Magnetic field distribution in a Roebel cable for a 50 Hz sinusoidal transport current of $I_0 = 400\,\mathrm{A}$ peak at (a) $t = T/8$, (b) $t = T/4$, and (c) $t = T/2$.

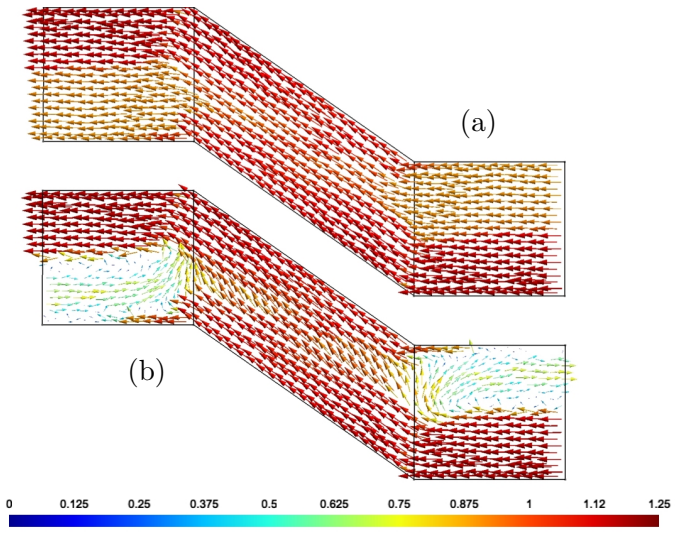


Figure 7.9 Normalized current density distribution in the crossover segment of one strand of the Roebel cable for $I_0 = 400\,\mathrm{A}$ at $t = T/4$ (peak current value): (a) outer face, and (b) inner face. Note the difference in the current density profiles on both faces of the strand.

model for $I_0 = 400\,\mathrm{A}$ (see Table 7.3). The relative difference between the solutions was 1.76%, while the number of DoFs was reduced by more than 75% when using the TS model. In terms of CPU time, simulations using the reference model took 127,971 s to complete vs. 44,609 s for the 3-D TS model, i.e. simulations with the TS model were about three times faster than the reference model.

We further computed the total AC losses at several transport current values, and the results are shown in Fig. 7.10. In general, the AC losses of the TS model are consistent with those of the reference model. However, at low transport currents, the TS model provided higher AC losses than the reference model. This difference is probably related to the poor mesh quality in the reference model, which certainly reduce its accuracy at low transport currents. In the TS model, FE with high aspect ratio are avoided, thus, the results of the TS model are likely to be the most accurate ones.

## 7.5 Conclusion

This paper proposed a 3-D thin-shell model based on the $H$-$\phi$-formulation to simulate HTS tapes. The superconducting layers in such tapes were represented as zero-thickness geometries (surfaces) in the 3-D calculus domain to avoid creating finite elements with high aspect ratio. The electromagnetic behavior in the tapes was taken into account by a virtual discretization of their thickness. This representation allowed the tangential components of the magnetic field to be discontinuous and the current density to be non-uniformly distributed across the thickness of the tapes. Moreover, the magnetic scalar potential was the working variable in the non-conducting region surrounding the tapes, which provided additional reductions in the total number of degrees of freedom (DoFs) in our model when compared to a standard $H$-formulation.

The proposed model was validated with well-established analytical solutions on two benchmark problems: (i) a single HTS tape carrying a transport current, and (ii) a thin HTS disc in a perpendicular external field excitation. In both cases, the 3-D TS solution showed excellent agreement with the analytical solutions in terms of normal and tangential field components, as well as current density distribution and total AC losses. The 3-D TS model was also compared with standard FE solutions obtained with a 3-D discretization of the HTS tapes, and by using a standard $H$-$\phi$-formulation (reference model). We demonstrated that the proposed model can speed up 3-D FE simulations by up to a factor of ten compared to the $H$-$\phi$ reference model, which is known to be already advantageous when compared to the standard $H$-formulation.

Table 7.3 AC losses and total number of degrees of freedom (DoFs) in the Roebel cable with $I_0 = 400\,\text{A}$ and $N = 2$

| Model | AC Losses (mJ/cycle/m) | Relative difference | Number of DoFs | DoFs Reduction |
|---|---|---|---|---|
| 3-D FEM (reference) | 9.64 | - | 483,520 | - |
| 3-D TS-FEM ($N = 2$) | 9.81 | 1.76% | 120,097 | 75% |

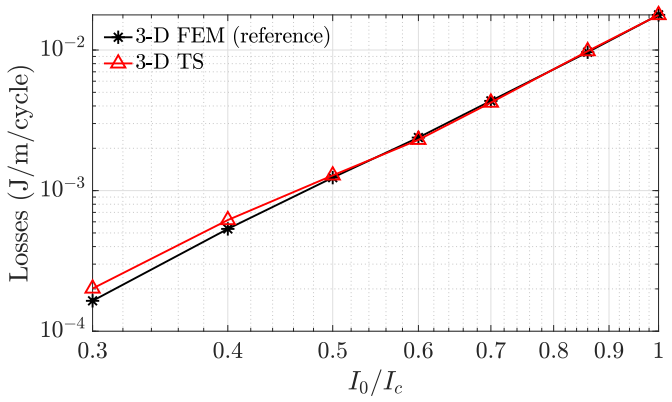


Figure 7.10 Total AC losses per length unit of the Roebel cable with 14 strands as a functions of the peak transport current. Results obtained with the proposed TS model are compared with the results of the reference model proposed in [26].

We also applied the 3-D TS model to estimate the current and field distributions and total AC losses in an HTS Roebel cable with 14 strands. Our solutions were consistent with those obtained using the model proposed in [26]. The relative difference in the AC losses between these two models was less than 2%, while the total number of DoFs in the TS model was less than 30% that of the other model. Moreover, the increase in the number of virtual elements in the TS model was demonstrated to be efficient in the study of the current distribution in the crossover region of the Roebel cable. These results confirm the efficiency of the 3-D TS model to simulate HTS devices comprising multiple thin HTS tapes, such as coils and magnets (to be tested in future work).

## Appendices

### A. Development of the terms in equation (7.4)

Given the definition of $\boldsymbol{h}$ and $\nabla \times \boldsymbol{h}$ in the virtual element $\widehat{\Omega}_s$ in (7.6) and (7.7), respectively, and choosing $\boldsymbol{g}$ in the same function space as $\boldsymbol{h}$, we have

$$
\begin{aligned}
&\nabla \times \boldsymbol{h} \cdot \nabla \times \boldsymbol{g} \\
&\quad = \sum_{m=1}^{3} \sum_{i=1}^{2} h_m^{\gamma} \left( \nabla \theta_i \times \boldsymbol{w}_m + \theta_i \nabla \times \boldsymbol{w}_m \right) \\
&\qquad\qquad \cdot \left( \nabla \theta_j \times \boldsymbol{w}_n + \theta_j \nabla \times \boldsymbol{w}_n \right) \\
&\quad = \sum_{m=1}^{3} \sum_{i=1}^{2} h_m^{\gamma} \left[ \left( \nabla \theta_i \times \boldsymbol{w}_m \right) \cdot \left( \nabla \theta_j \times \boldsymbol{w}_n \right) \right. \\
&\qquad\qquad + \left( \nabla \theta_i \times \boldsymbol{w}_m \right) \cdot \left( \theta_j \nabla \times \boldsymbol{w}_n \right) \\
&\qquad\qquad + \left( \theta_i \nabla \times \boldsymbol{w}_m \right) \cdot \left( \nabla \theta_j \times \boldsymbol{w}_n \right) \\
&\qquad\qquad \left. + \left( \theta_i \nabla \times \boldsymbol{w}_m \right) \cdot \left( \theta_j \nabla \times \boldsymbol{w}_n \right) \right] \\
&\quad = \sum_{m=1}^{3} \sum_{i=1}^{2} h_m^{\gamma} \left[ \left( \nabla \theta_i \times \boldsymbol{w}_m \right) \cdot \left( \nabla \theta_j \times \boldsymbol{w}_n \right) \right. \\
&\qquad\qquad \left. + \left( \theta_i \nabla \times \boldsymbol{w}_m \right) \cdot \left( \theta_j \nabla \times \boldsymbol{w}_n \right) \right] \\
&\quad = \sum_{m=1}^{3} \sum_{i=1}^{2} h_m^{\gamma} \left[ \nabla \theta_i \cdot \nabla \theta_j (\boldsymbol{w}_m \cdot \boldsymbol{w}_n) \right. \\
&\qquad\qquad \left. + \theta_i \theta_j (\nabla \times \boldsymbol{w}_m) \cdot (\nabla \times \boldsymbol{w}_n) \right],
\end{aligned}
\tag{7.26}
$$

and

$$
\begin{aligned}
\boldsymbol{h} \cdot \boldsymbol{g} &= \sum_{m=1}^{3} \sum_{i=1}^{2} h_m^{\gamma} \boldsymbol{w}_m \theta_i \cdot \boldsymbol{w}_n \theta_j \\
&= \sum_{m=1}^{3} \sum_{i=1}^{2} h_m^{\gamma} \theta_i \theta_j \left( \boldsymbol{w}_m \cdot \boldsymbol{w}_n \right),
\end{aligned}
\tag{7.27}
$$

$\forall\, j = 1, 2$, $\forall\, n = 1, 2, 3$.

### B. Kronecker product definition

The Kronecker product (or matrix direct product) is defined as the product of two matrices resulting in a block matrix [134]. For instance, the first term in (7.12) is

$$\mathcal{A}^{(k)} \otimes \mathcal{D}^{(k)} = \begin{bmatrix} \mathcal{A}_{11}^{(k)}[\mathcal{D}^{(k)}] & \mathcal{A}_{12}^{(k)}[\mathcal{D}^{(k)}] & \mathcal{A}_{13}^{(k)}[\mathcal{D}^{(k)}] \\ \mathcal{A}_{21}^{(k)}[\mathcal{D}^{(k)}] & \mathcal{A}_{22}^{(k)}[\mathcal{D}^{(k)}] & \mathcal{A}_{23}^{(k)}[\mathcal{D}^{(k)}] \\ \mathcal{A}_{31}^{(k)}[\mathcal{D}^{(k)}] & \mathcal{A}_{32}^{(k)}[\mathcal{D}^{(k)}] & \mathcal{A}_{33}^{(k)}[\mathcal{D}^{(k)}] \end{bmatrix}, \tag{7.28}$$

where $\mathcal{A}^{(k)} \otimes \mathcal{D}^{(k)}$ is a $6 \times 6$ matrix. The treatment of the second term in (7.12) and the matrix product in (7.13) is done the same way.

**Acknowledgment**

This work has been supported by the Coordination for the Improvement of Higher Education Personnel (CAPES) - Brazil - Finance Code 001, the Fonds de Recherche du Québec - Nature et Technologies (FRQNT), and the Natural Sciences and Engineering Research Council (NSERC) of Canada.

# CHAPTER 8 GENERAL DISCUSSION

Two new TS models were presented, validated and applied in this thesis. The first proposed approach considered hyperbolic basis functions for the time-transient analysis of thin conductive and ferromagnetic shields. This approach provided accurate results with a small number of additional high-frequency basis functions and consistent with the results obtained with standard FEM. It was also extended to the time-transient analysis of nonlinear ferromagnetic shields. In the time-harmonic regime, the model showed a relative difference of less than 3% in terms of local field distribution in all points evaluated. In time-transient analysis, the relative differences were also reduced to less than 3% when using at least 3 sets of hyperbolic basis functions, including in the critical region near the extremities of the shield. Compared to the reference model obtained with a standard FEM, the total number of degrees of freedom was reduced by more than 80% and simulations were at least ten times faster with the TS model. The computational efficiency and accuracy of this model satisfy the specific objectives we established for this thesis and presented in Chapter 4. A paper introducing the approach and presenting the main results was published in IEEE Transaction on Magnetics [127], and was included as Chapter 5 of this thesis.

The second approach proposed a TS model with a virtual discretization across the thickness of the thin regions, which could handle the nonlinearities of both ferromagnetic and superconducting materials. In Chapter 6, this approach was applied to simulate 2-D problems involving HTS tapes. We started with the example of a single tape and progressively increased the problem complexity by augmenting the number of tapes and the number of thin layers in these tapes. In all cases, the solution from the TS model was in good agreement with that of the reference models in terms of the local fields and the current distributions and AC losses. Among the current available TS models, the proposed TS model is the only one that allows taking into account the uneven distribution of the current density across the thickness of HTS tapes, models multiple thin layers as a single reduced-dimension geometry in the computational domain, and is accurate in evaluating AC losses in HTS tapes of any configuration. Our approach and results were presented in a paper [133] recently submitted to the IOP Superconductor Science and Technology and was included as Chapter 6 of this thesis.

In Chapter 7, we extended the approach with virtual discretization across the thickness of HTS tapes to 3-D cases. The interface conditions were defined in this chapter as the Kronecker product between the 2-D elementary matrices defined on the surface representing

the thin region and the 1-D FE matrices defined across their virtual thickness thereby simplifying its discretization and coupling its physics to the fields outside the conducting regions. The model was validated on benchmark problems for transport currents and external field excitation, and applied for simulating the electromagnetic behavior of a Roebel cable comprising 14 transposed strands. It was shown that the proposed TS model can speed up 3-D simulations without compromising the solution accuracy. All the features of the 3-D model and its validation were presented in a paper [133] submitted to IEEE Transactions on Applied Superconductivity. In further work, this approach can be applied to simulate HTS cables containing several HTS tapes, such as CORC and TSTC cables.

For a fair comparison with the $T$-$A$-formulation (Section 3.8), we also implemented our TS model with virtual discretization in COMSOL Multiphysics. The model implementation and a complete comparison with the $T$-$A$-formulation were presented in an additional paper that is included in Appendix B. In this paper, we demonstrated that the computational time when simulating a few HTS tapes using one virtual element across their thickness is comparable to that of the $T$-$A$-formulation. We also studied the problem of a stack of twenty tapes. In this case, the proposed approach provided the solution ten times faster than the models with the standard $H$-$\phi$-formulation and the $T$-$A$-formulation. Also, in the case of two closely packed tapes carrying anti-parallel currents, the $T$-$A$-formulation underestimated the AC losses as expected, while our TS approach with a virtual mesh refinement provided results closer to those obtained with the pure $H$-formulation, but around hundred times faster than that. This significant reduction in the computational time was mainly due to the use of a coarser mesh in the TS model, thanks to the reduced-dimension representation of the tapes. The main differences between the paper presented in Appendix B and that in Chapter 5 rely on the implementation of the TS model in COMSOL Multiphysics and the use of thin cuts [132] to impose current constraints in the tapes instead of the edge-basis cohomology basis functions [55].

As presented in Chapter 3, the classical TS approach normally considers a hyperbolic profile for the fields inside the shell. This is a valid approximation in regions far from edges and corners but not close to them. Since in our approach with virtual discretization the interface conditions are independent of the field profile, it was demonstrated in Appendix C that, with a sufficiently high number of virtual elements, the approach can provide a good estimation for the fields and the current distributions near edges and corners of thin regions. It is worth mentioning that the virtual mesh refinement could be performed locally near the edges and corners. Far from them, the use of a few elements should be enough to represent the physics in the shell, mainly depending on the penetration depth. The approach overcomes the limitations of the classical TS approach to model edge and corner effects in harmonic

regimes and avoids the use of techniques such as the subproblem technique to correct the related inaccuracies locally. All these features make the second proposed TS model very promising for simulating large-scale devices involving HTS tapes and other thin structures in electromagnetic devices.

# CHAPTER 9 CONCLUSIONS AND RECOMMENDATIONS

In this thesis, we had the main objective to establish a rigorous 3-D FE formulation for the time-transient analysis of domains composed of thin regions made of nonlinear conductive and/or magnetic materials. We proposed two different thin-shell (TS) models and demonstrated their efficiency and accuracy in 2-D and 3-D FEM simulations. Both respond to our objectives and overcome the main limitations of other models found in the literature.

The first proposed TS model considered hyperbolic basis functions derived from harmonic solutions of the linear flux diffusion equation inside the shell. These basis functions perfectly suit problems in the time-harmonic regime and time-transient problems in which the fields can be approximated by the superposition of a set of harmonic solutions. In an attempt to extend this approach to nonlinear cases, we also simulated the saturation effects in a nonlinear planar shield. Indeed, since the penetration depth depends simultaneously on the operating frequency and the material properties, the increase in the frequency components to define our basis functions was a good approximation for this analysis.

Only 2-D simulations were performed using the hyperbolic basis functions in this thesis. In future work, this approach could be extended to 3-D simulations, and different fields profiles across the thickness of the shell could be used to define new dedicated basis functions. Ideally, these new basis functions should be defined independently of the operating frequency and materials properties, so the model applications would be wider. Despite this, the presented approach overcomes the limitations of the classical TS model by permitting time-transient analysis of nonlinear thin regions.

The second proposed TS model considered a virtual discretization across the thickness of HTS tapes to estimate their electromagnetic behavior. This approach is more general than the first one. It was validated in several benchmark problems and applied to simulate HTS tapes with different configurations in 2-D and 3-D simulations for transport current and external field excitation. In future work, it could be applied to simulate new HTS cables architectures comprising many HTS tapes. It may also allow future parametric studies and the simulation of large-scale HTS devices and their optimization, providing substantial advancement in this research field. Moreover, applications of the proposed TS approach are not limited to simulations involving HTS tapes. The approach was already demonstrated to be efficient in solving problems involving thin ferromagnetic regions and estimating edge and corner effects. Another extension of this approach may include the thermal effects in HTS tapes for

quenching analysis.

Given the presented literature review and the two introduced approaches, the proposed methodology seems very general. By applying the hyperbolic basis functions in a single virtual element across the thickness of the thin region in the harmonic regime results in interface conditions equivalent to the classical TS approach; using first-order Lagrange basis functions it becomes equivalent to the degenerate finite-elements approach, and finally, it is dual to the $T$-$A$-formulation if we consider that $\mu_r = 1$ inside the tapes. Finally, the two proposed approaches could easily be extended to the $A$- or $A$-$v$-formulation. We hope the reported findings can help future research involving HTS tapes and contribute significantly to the development of the next generation of electromagnetic devices.

# REFERENCES


[1] M. Kaltenbacher, *The Finite Element (FE) Method.* Springer Berlin Heidelberg, 2015.

[2] P. Silvester and M. V. K. Chari, "Finite element solution of saturable magnetic field problems," *IEEE Transactions on Power Apparatus and Systems*, vol. PAS-89, no. 7, pp. 1642–1651, Sept 1970.

[3] G. Paoli, O. Bíró, and G. Buchgraber, "Complex representation in nonlinear time harmonic eddy current problems," *IEEE Transactions on Magnetics*, vol. 34, no. 5, pp. 2625–2628, Sept 1998.

[4] O. Bíró, G. Koczka, and K. Preis, "Finite element solution of nonlinear eddy current problems with periodic excitation and its industrial applications," *Applied Numerical Mathematics*, vol. 79, pp. 3 – 17, May 2014.

[5] R. Plasser, G. Koczka, and O. Bíró, "Improvement of the finite-element analysis of 3-D, nonlinear, periodic eddy current problems involving voltage-driven coils under DC bias," *IEEE Transactions on Magnetics*, vol. 54, no. 3, pp. 1–4, Mar 2018.

[6] E. Marchandise, J.-F. Remacle, and C. Geuzaine, "Optimal parametrizations for surface remeshing," *Engineering with Computers*, vol. 30, no. 3, pp. 383–402, 2014.

[7] L. Quéval, V. M. R. Zermeño, and F. Grilli, "Numerical models for ac loss calculation in large-scale applications of HTS coated conductors," *Superconductor Science and Technology*, vol. 29, no. 2, p. 024007, jan 2016.

[8] O. Bottauscio, M. Chiampi, and A. Manzin, "Numerical analysis of magnetic shielding efficiency of multilayered screens," *IEEE Transactions on Magnetics*, vol. 40, no. 2, pp. 726–729, mar 2004.

[9] O. Bottauscio, M. Chiampi, and A. Manzin, "Transient analysis of thin layers for the magnetic field shielding," *IEEE Transactions on Magnetics*, vol. 42, no. 4, pp. 871–874, 2006.

[10] O. Bottauscio, M. Chiampi, and A. Manzin, "Nonlinear ferromagnetic shield modeling by the thin-shell approximation," *IEEE Transactions on Magnetics*, vol. 42, no. 10, pp. 3144–3146, 2006.

[11] R. Sabariego, C. Geuzaine, P. Dular, and J. Gyselinck, "$h$- and $a$-formulations for the time-domain modelling of thin electromagnetic shells," *IET Science, Measurement and Technology*, vol. 2, pp. 402–408, Nov 2008.

[12] R. V. Sabariego, C. Geuzaine, P. Dular, and J. Gyselinck, "Nonlinear time-domain finite-element modeling of thin electromagnetic shells," *IEEE transactions on magnetics*, vol. 45, no. 3, pp. 976–979, 2009.

[13] J. G. Bednorz and K. A. Müller, "Possible high Tc superconductivity in the Ba-La-Cu-O system," *Zeitschrift für Physik B Condensed Matter*, vol. 64, no. 2, pp. 189–193, 1986.

[14] A. Goyal, D. P. Norton, J. D. Budai, M. Paranthaman, E. D. Specht, D. M. Kroeger, D. K. Christen, Q. He, B. Saffian, F. A. List, D. F. Lee, P. M. Martin, C. E. Klabunde, E. Hartfield, and V. K. Sikka, "High critical current density superconducting tapes by epitaxial deposition of yba2cu3ox thick films on biaxially textured metals," *Applied Physics Letters*, vol. 69, no. 12, pp. 1795–1797, 1996.

[15] M. W. Rupich, D. T. Verebelyi, W. Zhang, T. Kodenkandath, and X. Li, "Metalorganic Deposition of YBCO Films for Second-Generation High-Temperature Superconductor Wires," *MRS Bulletin*, vol. 29, no. 8, pp. 572–578, 2004.

[16] Y. Zhao, J.-M. Zhu, G.-Y. Jiang, C.-S. Chen, W. Wu, Z.-W. Zhang, S. K. Chen, Y. M. Hong, Z.-Y. Hong, Z.-J. Jin, and Y. Yamada, "Progress in fabrication of second generation high temperature superconducting tape at shanghai superconductor technology," *Superconductor Science and Technology*, vol. 32, no. 4, p. 044004, Feb 2019.

[17] F. Grilli, R. Brambilla, L. F. Martini, F. Sirois, D. N. Nguyen, and S. P. Ashworth, "Current density distribution in multiple ybco coated conductors by coupled integral equations," *IEEE Transactions on Applied Superconductivity*, vol. 19, no. 3, pp. 2859–2862, 2009.

[18] F. Grilli and A. Kario, "How filaments can reduce AC losses in HTS coated conductors: a review," *Superconductor Science and Technology*, vol. 29, no. 8, p. 083002, Jul 2016.

[19] S. Elschner, A. Kudymow, J. Brand, S. Fink, W. Goldacker, F. Grilli, M. Noe, M. Vojenciak, A. Hobl, M. Bludau, C. Jänke, S. Krämer, and J. Bock, "Ensystrob – design, manufacturing and test of a 3-phase resistive fault current limiter based on

coated conductors for medium voltage application," *Physica C: Superconductivity and its Applications*, vol. 482, pp. 98–104, 2012.

[20] B. Shen, J. Li, J. Geng, L. Fu, X. Zhang, C. Li, H. Zhang, Q. Dong, J. Ma, and T. Coombs, "Investigation and comparison of ac losses on stabilizer-free and copper stabilizer hts tapes," *Physica C: Superconductivity and its Applications*, vol. 541, pp. 40–44, 2017.

[21] J. Rhyner, "Magnetic properties and ac-losses of superconductors with power law current—voltage characteristics," *Physica C: Superconductivity*, vol. 212, no. 3, pp. 292–300, 1993.

[22] F. Sirois and F. Grilli, "Potential and limits of numerical modelling for supporting the development of hts devices," *Superconductor Science and Technology*, vol. 28, no. 4, p. 043002, 2015.

[23] M. Takayasu, L. Chiesa, L. Bromberg, and J. V. Minervini, "Cabling method for high current conductors made of hts tapes," *IEEE Transactions on Applied Superconductivity*, vol. 21, no. 3, pp. 2340–2344, 2011.

[24] Y. Wang, M. Zhang, F. Grilli, Z. Zhu, and W. Yuan, "Study of the magnetization loss of CORC®cables using a 3D TA formulation," *Superconductor Science and Technology*, vol. 32, no. 2, p. 25003, 2019.

[25] F. Grilli and E. Pardo, "Simulation of AC loss in Roebel coated conductor cables," *Superconductor Science and Technology*, vol. 23, no. 11, p. 115018, oct 2010.

[26] V. M. Zermeno, F. Grilli, and F. Sirois, "A full 3D time-dependent electromagnetic model for Roebel cables," *Superconductor Science and Technology*, vol. 26, no. 5, 2013.

[27] W. Goldacker, F. Grilli, E. Pardo, A. Kario, S. I. Schlachter, and M. Vojenčiak, "Roebel cables from REBCO coated conductors: a one-century-old concept for the superconductivity of the future," *Superconductor Science and Technology*, vol. 27, no. 9, p. 093001, aug 2014.

[28] S. Terzieva, M. Vojenčiak, E. Pardo, F. Grilli, A. Drechsler, A. Kling, A. Kudymow, F. Gömöry, and W. Goldacker, "Transport and magnetization ac losses of ROEBEL assembled coated conductor cables: measurements and calculations," *Superconductor Science and Technology*, vol. 23, no. 1, p. 014023, 2010.

[29] D. Proctor. (2021) Groups announce successful test to advance fusion energy. Accessed September 09, 2021. [Online]. Available: https://www.powermag.com/groups-announce-successful-test-to-advance-fusion-energy/

[30] T. Reuters. (2021) China builds world's fastest train, capable of 600 km/h. Accessed September 09, 2021. [Online]. Available: https://www.cbc.ca/news/science/china-fastest-train-1.6110819

[31] I. D. Mayergoyz and G. Bedrosian, "On calculation of 3-d eddy currents in conducting and magnetic shells," *IEEE Transactions on Magnetics*, vol. 31, no. 3, pp. 1319–1324, 1995.

[32] L. Krahenbuhl and D. Muller, "Thin layers in electrical engineering-example of shell models in analysing eddy-currents by boundary and finite element methods," *IEEE Transactions on Magnetics*, vol. 29, no. 2, pp. 1450–1455, 1993.

[33] C. Guerin, G. Tanneau, G. Meunier, X. Brunotte, and J. . Albertini, "Three dimensional magnetostatic finite elements for gaps and iron shells using magnetic scalar potentials," *IEEE Transactions on Magnetics*, vol. 30, no. 5, pp. 2885–2888, 1994.

[34] O. Bíró, K. Preis, W. Renhart, and K. R. Richter, "A Finite Element Formulation for Eddy Current Carrying Ferromagnetic Thin Sheets," *Transactions on magnetics*, vol. 33, no. 2, 1997.

[35] H. Zhang, M. Zhang, and W. Yuan, "An efficient 3d finite element method model based on the t–a formulation for superconducting coated conductors," *Superconductor Science and Technology*, vol. 30, no. 2, p. 024005, 2016.

[36] P. Monk, *Finite Element Methods for Maxwell's Equations*. Clarendon Press Oxford, 2003.

[37] R. Hiptmair, "Finite elements in computational electromagnetism," *Acta Numerica*, vol. 11, pp. 237–339, 2002.

[38] J. R. Munkres, *Elements of algebraic topology*. CRC press, 2018.

[39] J. D. Jackson, *Classical electrodynamics*. Wiley, 1999.

[40] G. Meunier, *The finite element method for electromagnetic modeling*. John Wiley & Sons, 2010.

[41] J. C. Butcher, *Numerical methods for ordinary differential equations.* John Wiley & Sons, 2016.

[42] A. T. de Hoop, *Handbook of radiation and scattering of waves: Acoustic waves in fluids, elastic waves in solids, electromagnetic waves.* Acoustical Society of America, 2001.

[43] J. Dular, C. Geuzaine, and B. Vanderheyden, "Finite-Element Formulations for Systems with High-Temperature Superconductors," *IEEE Transactions on Applied Superconductivity*, vol. 30, no. 3, 2020.

[44] W. Meissner and R. Ochsenfeld, "Ein neuer effekt bei eintritt der supraleitfähigkeit," *Naturwissenschaften*, vol. 21, no. 44, pp. 787–788, 1933.

[45] C. P. Bean, "Magnetization of hard superconductors," *Physical review letters*, vol. 8, no. 6, p. 250, 1962.

[46] C. Geuzaine, "High order hybrid finite element schemes for Maxwell's equations taking thin structures and global quantities into account," Ph.D. dissertation, Université de Liège, 2001.

[47] P. Dular, "Modélisation du champ magnétique et des courants induits dans des systèmes tridimensionnels non linéaires," Ph.D. dissertation, Université de Liège, 1996.

[48] R. A. Adams and J. F. F. Fournier, *Sobolev Spaces*, ser. Pure and Applied Mathematics. Netherlands: Academic Press, 2003, vol. 140.

[49] P. Kotiuga, "On making cuts for magnetic scalar potentials in multiply connected regions," *Journal of Applied Physics*, vol. 61, no. 8, pp. 3916–3918, Apr 1987.

[50] D. Rodger and J. Eastham, "Multiply connected regions in the a—$\psi$ three-dimensional eddy-current formualtion," *IEE Proceedings A (Physical Science, Measurement and Instrumentation, Management and Education, Reviews)*, vol. 134, no. 1, pp. 58–66, 1987.

[51] P. Dłotko, R. Specogna, and F. Trevisan, "Automatic generation of cuts on large-sized meshes for the t–$\omega$ geometric eddy-current formulation," *Computer Methods in Applied Mechanics and Engineering*, vol. 198, no. 47, pp. 3765 – 3781, Aug 2009.

[52] L. Kettunen, K. Forsman, and A. Bossavit, "Gauging in whitney spaces," *IEEE Transactions on Magnetics*, vol. 35, no. 3, pp. 1466–1469, 1999.

[53] A. Bossavit, *Computational electromagnetism: variational formulations, complementarity, edge elements*. Academic Press, 1998.

[54] M. Spivak, *Calculus on manifolds: a modern approach to classical theorems of advanced calculus*. CRC press, 2018.

[55] M. Pellikka, S. Suuriniemi, L. Kettunen, and C. Geuzaine, "Homology and cohomology computation in finite element modeling," *SIAM Journal on Scientific Computing*, vol. 35, no. 5, pp. B1195–B1214, Jan 2013.

[56] M. Desbrun, E. Kanso, and Y. Tong, "Discrete differential forms for computational modeling," in *Discrete differential geometry*. Springer, 2008, pp. 287–324.

[57] A. Hatcher, *Algebraic topology*. Cambridge: Cambridge Univ. Press, 2000.

[58] P. Nadathur, "An introduction to homology," *University of Chicago*, 2007.

[59] H. Suess, "Simplicial complexes and simplicial homology," *University of Manchester*, 2018.

[60] C. Geuzaine and J.-F. Remacle, "Gmsh: A 3-D finite element mesh generator with built-in pre-and post-processing facilities," *International journal for numerical methods in engineering*, vol. 79, no. 11, pp. 1309–1331, 2009.

[61] V. Lahtinen, A. Stenvall, F. Sirois, and M. Pellikka, "A finite element simulation tool for predicting hysteresis losses in superconductors using an h-oriented formulation with cohomology basis functions," *Journal of Superconductivity and Novel Magnetism*, vol. 28, no. 8, pp. 2345–2354, Aug 2015.

[62] P. Dular, C. Geuzaine, and W. Legros, "A natural method for coupling magnetodynamic h-formulations and circuit equations," *IEEE Transactions on Magnetics*, vol. 35, no. 3, pp. 1626–1629, 1999.

[63] P. Dular, F. Henrotte, and W. Legros, "A general and natural method to define circuit relations associated with magnetic vector potential formulations," *IEEE Transactions on Magnetics*, vol. 35, no. 3, pp. 1630–1633, 1999.

[64] P. Dular, F. Henrotte, F. Robert, A. Genon, and W. Legros, "A generalized source magnetic field calculation method for inductors of any shape," *IEEE Transactions on Magnetics*, vol. 33, no. 2, pp. 1398–1401, 1997.

[65] A. Bossavit, "Whitney forms: a class of finite elements for three-dimensional computations in electromagnetism," *IEE Proceedings A (Physical Science, Measurement and Instrumentation, Management and Education, Reviews)*, vol. 135, pp. 493–500(7), Nov 1988.

[66] J. Webb, "Edge elements and what they can do for you," *IEEE Transactions on Magnetics*, vol. 29, no. 2, pp. 1460–1465, 1993.

[67] O. Bíró, "Edge element formulations of eddy current problems," *Computer methods in applied mechanics and engineering*, vol. 169, no. 3-4, pp. 391–405, 1999.

[68] B. Shen, F. Grilli, and T. Coombs, "Overview of h-formulation: A versatile tool for modeling electromagnetics in high-temperature superconductor applications," *IEEE access*, vol. 8, pp. 100 403–100 414, 2020.

[69] R. Brambilla, F. Grilli, and L. Martini, "Development of an edge-element model for ac loss computation of high-temperature superconductors," *Superconductor Science and Technology*, vol. 20, no. 1, p. 16, 2006.

[70] Z. Hong, A. Campbell, and T. Coombs, "Numerical solution of critical state in superconductivity by finite element software," *Superconductor Science and Technology*, vol. 19, no. 12, p. 1246, 2006.

[71] J. Dular, M. Harutyunyan, L. Bortot, S. Schöps, B. Vanderheyden, and C. Geuzaine, "On the stability of mixed finite-element formulations for high-temperature superconductors," *IEEE Transactions on Applied Superconductivity*, vol. 31, no. 6, pp. 1–12, 2021.

[72] L. Bortot, B. Auchmann, I. C. Garcia, H. D. Gersem, M. Maciejewski, M. Mentink, S. Schöps, J. V. Nugteren, and A. P. Verweij, "A coupled a–h formulation for magneto-thermal transients in high-temperature superconducting magnets," *IEEE Transactions on Applied Superconductivity*, vol. 30, no. 5, pp. 1–11, 2020.

[73] L. Bortot, M. Mentink, C. Petrone, J. V. Nugteren, G. Kirby, M. Pentella, A. Verweij, and S. Schöps, "Numerical analysis of the screening current-induced magnetic field in the HTS insert dipole magnet feather-m2.1-2," *Superconductor Science and Technology*, vol. 33, no. 12, p. 125008, 2020.

[74] O. Bíró, K. Preis, W. Renhart, K. Richter, and G. Vrisk, "Performance of different vector potential formulations in solving multiply connected 3-d eddy current problems," *IEEE Transactions on Magnetics*, vol. 26, no. 2, pp. 438–441, 1990.

[75] E. H. Brandt, M. V. Indenbom, and A. Forkl, "Type-II superconducting strip in perpendicular magnetic field," *Europhysics Letters (EPL)*, vol. 22, no. 9, pp. 735–740, jun 1993.

[76] E. H. Brandt, "Thin superconductors in a perpendicular magnetic ac field: General formulation and strip geometry," *Phys. Rev. B*, vol. 49, pp. 9024–9040, Apr 1994.

[77] E. H. Brandt, "Superconductors of finite thickness in a perpendicular magnetic field: Strips and slabs," *Physical review B*, vol. 54, no. 6, p. 4246, 1996.

[78] R. Brambilla, F. Grilli, L. Martini, and F. Sirois, "Integral equations for the current density in thin conductors and their solution by the finite-element method," *Superconductor Science and Technology*, vol. 21, no. 10, p. 105008, jul 2008.

[79] F. Grilli, F. Sirois, S. Brault, R. Brambilla, L. Martini, D. N. Nguyen, and W. Goldacker, "Edge and top/bottom losses in non-inductive coated conductor coils with small separation between tapes," *Superconductor Science and Technology*, vol. 23, no. 3, p. 034017, Feb 2010.

[80] K. Takeuchi, N. Amemiya, T. Nakamura, O. Maruyama, and T. Ohkuma, "Model for electromagnetic field analysis of superconducting power transmission cable comprising spiraled coated conductors," *Superconductor Science and Technology*, vol. 24, no. 8, p. 085014, jul 2011.

[81] W. K. Chan, P. J. Masson, C. Luongo, and J. Schwartz, "Three-dimensional micrometer-scale modeling of quenching in high-aspect-ratio $YBa_2Cu_3O_{7-\delta}$ coated conductor tapes—part I: Model development and validation," *IEEE Transactions on Applied Superconductivity*, vol. 20, no. 6, pp. 2370–2380, 2010.

[82] T. Nakata, N. Takahashi, K. Fujiwara, and Y. Shiraki, "3d magnetic field analysis using special elements," *IEEE Transactions on Magnetics*, vol. 26, no. 5, pp. 2379–2381, 1990.

[83] D. Rodger, P. Leonard, and H. Lai, "Surface elements for modelling 3d fields around thin iron sheets," *IEEE Transactions on Magnetics*, vol. 29, no. 2, pp. 1483–1486, 1993.

[84] X. Brunotte and G. Meunier, "Line element for efficient computation of the magnetic field created by thin iron plates," *IEEE Transactions on Magnetics*, vol. 26, no. 5, pp. 2196–2198, 1990.

[85] O. Biro, K. Preis, K. Richter, R. Heller, P. Komarek, and W. Maurer, "FEM calculation of eddy current losses and forces in thin conducting sheets of test facilities for fusion

reactor components," *IEEE Transactions on Magnetics*, vol. 28, no. 2, pp. 1509–1512, 1992.

[86] Z. Ren, "Degenerated whitney prism elements-general nodal and edge shell elements for field computation in thin structures," *IEEE Transactions on Magnetics*, vol. 34, no. 5, pp. 2547–2550, 1998.

[87] B. Ramdane, D. Trichet, M. Belkadi, T. Saidi, and J. Fouladgar, "Electromagnetic and thermal modeling of composite materials using multilayer shell elements," *IEEE Transactions on Magnetics*, vol. 47, no. 5, pp. 1134–1137, 2011.

[88] S. Koch, J. Trommler, H. De Gersem, and T. Weiland, "Modeling thin conductive sheets using shell elements in magnetoquasistatic field simulations," *IEEE Transactions on Magnetics*, vol. 45, no. 3, pp. 1292–1295, 2009.

[89] E. Abenius and F. Edelvik, "Thin sheet modeling using shell elements in the finite-element time-domain method," *IEEE Transactions on Antennas and Propagation*, vol. 54, no. 1, pp. 28–34, 2006.

[90] Y. Zhang, D. Nie, and Q. Sun, "Layer-oriented integration vector element of multilayer ram," in *2008 8th International Symposium on Antennas, Propagation and EM Theory*, 2008, pp. 774–776.

[91] C. Guérin, G. Tanneau, G. Meunier, P. Labie, T. Ngnegueu, and M. Sacotte, "A shell element for computing 3d eddy currents-application to transformers," *IEEE Transactions on Magnetics*, vol. 31, no. 3, pp. 1360–1363, 1995.

[92] I. Mayergoyz and G. Bedrosian, "On finite element implementation of impedance boundary conditions," *Journal of Applied Physics*, vol. 75, no. 10, pp. 6027–6029, 1994.

[93] H. Igarashi, A. Kost, and T. Honma, "A three dimensional analysis of magnetic fields around a thin magnetic conductive layer using vector potential," *IEEE Transactions on Magnetics*, vol. 34, no. 5, pp. 2539–2542, 1998.

[94] H. Igarashi, A. Kost, and T. Honma, "Impedance boundary condition for vector potentials on thin layers and its application to integral equations," *EPJ Applied Physics*, vol. 1, no. 1, pp. 103–109, 1998.

[95] C. Geuzaine, P. Dular, and W. Legros, "Dual formulations for the modeling of thin electromagnetic shells using edge elements," *IEEE Transactions on Magnetics*, vol. 36, no. 4, pp. 799–803, Jul 2000.

[96] P. Rasilo, J. Vesa, and J. Gyselinck, "Electromagnetic modeling of ferrites using shell elements and random grain structures," *IEEE Transactions on Magnetics*, vol. 56, no. 2, pp. 1–4, 2020.

[97] P. Dular, R. V. Sabariego, C. Geuzaine, M. V. F. Da Luz, P. Kuo-Peng, and L. Krahenbuhl, "Finite element magnetic models via a coupling of subproblems of lower dimensions," *IEEE Transactions on Magnetics*, vol. 46, no. 8, pp. 2827–2830, 2010.

[98] "Perturbation finite element method for magnetic model refinement of air gaps and leakage fluxes," *IEEE Transactions on Magnetics*, vol. 45, no. 3, pp. 1400–1403, 2009.

[99] P. Dular, V. Q. Dang, R. V. Sabariego, L. Krähenbühl, and C. Geuzaine, "Correction of thin shell finite element magnetic models via a subproblem method," *IEEE Transactions on Magnetics*, vol. 47, no. 5, pp. 1158–1161, 2011.

[100] V. Q. Dang, P. Dular, R. V. Sabariego, L. Krahenbuhl, and C. Geuzaine, "Subproblem Approach for Thin Shell Dual Finite Element Formulations," *IEEE Transactions on Magnetics*, vol. 48, no. 2, pp. 407–410, 2012.

[101] J. Gyselinck, R. V. Sabariego, P. Dular, and C. Geuzaine, "Time-domain finite-element modeling of thin electromagnetic shells," *IEEE Transactions on Magnetics*, vol. 44, no. 6, pp. 742–745, June 2008.

[102] J. Gyselinck and P. Dular, "A time-domain homogenization technique for laminated iron cores in 3-D finite-element models," *IEEE Transactions on Magnetics*, vol. 40, no. 2, pp. 856–859, Mar 2004.

[103] J. Gyselinck, R. V. Sabariego, and P. Dular, "A nonlinear time-domain homogenization technique for laminated iron cores in three-dimensional finite-element models," *IEEE Transactions on Magnetics*, vol. 42, no. 4, pp. 763–766, Apr 2006.

[104] J. Gyselinck, P. Dular, L. Krähenbühl, and R. V. Sabariego, "Finite-element homogenization of laminated iron cores with inclusion of net circulating currents due to imperfect insulation," *IEEE Transactions on Magnetics*, vol. 52, no. 3, pp. 1–4, 2016.

[105] M. Chiampi, L. Gozzelino, A. Manzin, and L. Zilberti, "Thin-shell formulation applied to superconducting shields for magnetic field mitigation," *IEEE Transactions on Magnetics*, vol. 47, no. 10, pp. 4266–4269, 2011.

[106] F. London and H. London, "The electromagnetic equations of the supraconductor," *Proceedings of the Royal Society of London. Series A-Mathematical and Physical Sciences*, vol. 149, no. 866, pp. 71–88, 1935.

[107] C. Multiphysics, "Introduction to comsol multiphysics®," *COMSOL Multiphysics, Burlington, MA*, vol. 9, p. 815, 1998.

[108] E. Berrospe-Juarez, V. M. Zermeño, F. Trillaud, and F. Grilli, "Real-time simulation of large-scale hts systems: multi-scale and homogeneous models using the t–a formulation," *Superconductor Science and Technology*, vol. 32, no. 6, p. 065003, 2019.

[109] Y. Yan, T. Qu, and F. Grilli, "Numerical modeling of ac loss in hts coated conductors and roebel cable using t-a formulation and comparison with h formulation," *IEEE Access*, vol. 9, pp. 49 649–49 659, 2021.

[110] F. Liang, S. Venuturumilli, H. Zhang, M. Zhang, J. Kvitkovic, S. Pamidi, Y. Wang, and W. Yuan, "A finite element model for simulating second generation high temperature superconducting coils/stacks with large number of turns," *Journal of Applied Physics*, vol. 122, no. 4, p. 043903, 2017.

[111] X. Huang, Z. Huang, X. Xu, L. Wang, W. Li, and Z. Jin, "A fully coupled numerical method for coated conductor hts coils in hts generators," *IEEE Transactions on Applied Superconductivity*, vol. 30, no. 4, pp. 1–6, 2020.

[112] S. Mu, R. Yang, T. Zhang, J. Wang, L. Wang, and R. Zhang, "Hts magnet modeling using t-a formulation with a simplified method," *IEEE Transactions on Applied Superconductivity*, vol. 31, no. 8, pp. 1–3, 2021.

[113] Y. Gao, W. Wang, X. Wang, H. Ye, Y. Zhang, Y. Zeng, Z. Huang, Q. Zhou, X. Liu, Y. Zhu, and Y. Lei, "Design, fabrication, and testing of a YBCO racetrack coil for an hts synchronous motor with HTS flux pump," *IEEE Transactions on Applied Superconductivity*, vol. 30, no. 4, pp. 1–5, 2020.

[114] T. Benkel, M. Lao, Y. Liu, E. Pardo, S. Wolfstädter, T. Reis, and F. Grilli, "T–A-formulation to model electrical machines with HTS coated conductor coils," *IEEE Transactions on Applied Superconductivity*, vol. 30, no. 6, pp. 1–7, 2020.

[115] C. R. Vargas-Llanos, S. Lengsfeld, and F. Grilli, "T-A formulation for the design and AC loss calculation of a superconducting generator for a 10 MW wind turbine," *IEEE Access*, vol. 8, pp. 208 767–208 778, 2020.

[116] X. Li, L. Ren, Y. Xu, J. Shi, X. Chen, G. Chen, Y. Tang, and J. Li, "Calculation of corc cable loss using a coupled electromagnetic-thermal t-a formulation model," *IEEE Transactions on Applied Superconductivity*, vol. 31, no. 4, pp. 1–7, 2021.

[117] V. Lahtinen, M. Lyly, A. Stenvall, and T. Tarhasaari, "Comparison of three eddy current formulations for superconductor hysteresis loss modelling," *Superconductor Science and Technology*, vol. 25, no. 11, p. 115001, Sept 2012.

[118] A. Stenvall, V. Lahtinen, and M. Lyly, "An H-formulation-based three-dimensional hysteresis loss modelling tool in a simulation including time varying applied field and transport current: the fundamental problem and its solution," *Superconductor Science and Technology*, vol. 27, no. 10, p. 104004, 2014.

[119] A. Arsenault, F. Sirois, and F. Grilli, "Implementation of the h-$\phi$ formulation in comsol multiphysics for simulating the magnetization of bulk superconductors and comparison with the h-formulation," *IEEE Transactions on Applied Superconductivity*, vol. 31, no. 2, pp. 1–11, 2021.

[120] A. Arsenault, F. Sirois, and F. Grilli, "Efficient modeling of high-temperature superconductors surrounded by magnetic components using a reduced H–$\phi$ formulation," *IEEE Transactions on Applied Superconductivity*, vol. 31, no. 4, pp. 1–9, 2021.

[121] D. N. Nguyen, F. Grilli, S. P. Ashworth, and J. O. Willis, "AC loss study of antiparallel connected YBCO coated conductors," *Superconductor Science and Technology*, vol. 22, no. 5, p. 055014, apr 2009.

[122] P. Dular and C. Geuzaine, "GetDP reference manual: the documentation for GetDP, a general environment for the treatment of discrete problems," *University of Liège*, 2013.

[123] R. V. Sabariego, P. Dular, C. Geuzaine, and J. Gyselinck, "Surface-impedance boundary conditions in dual time-domain finite-element formulations," *IEEE Transactions on Magnetics*, vol. 46, no. 8, pp. 3524–3531, 2010.

[124] H. E. Knoepfel, *Magnetic fields: a comprehensive theoretical treatise for practical use*. John Wiley & Sons, 2008.

[125] J. Gyselinck, P. Dular, C. Geuzaine, and R. V. Sabariego, "Surface-impedance boundary conditions in time-domain finite-element calculations using the magnetic-vector-potential formulation," *IEEE Transactions on Magnetics*, vol. 45, no. 3, pp. 1280–1283, 2009.

[126] Z. S. Hartwig, R. F. Vieira, B. N. Sorbom, R. A. Badcock, M. Bajko, W. K. Beck, B. Castaldo, C. L. Craighill, M. Davies, J. Estrada, V. Fry, T. Golfinopoulos, A. E. Hubbard, J. H. Irby, S. Kuznetsov, C. J. Lammi, P. C. Michael, T. Mouratidis, R. A. Murray, A. T. Pfeiffer, S. Z. Pierson, A. Radovinsky, M. D. Rowell, E. E. Salazar, M. Segal, P. W. Stahle, M. Takayasu, T. L. Toland, and L. Zhou, "VIPER: an industrially scalable high-current high-temperature superconductor cable," *Superconductor Science and Technology*, vol. 33, no. 11, p. 11LT01, oct 2020.

[127] B. D. S. Alves, R. V. Sabariego, M. Laforest, and F. Sirois, "Hyperbolic basis functions for time-transient analysis of eddy currents in conductive and magnetic thin sheets," *IEEE Transactions on Magnetics*, vol. 57, no. 11, pp. 1–10, 2021.

[128] C. Schacherer, A. Bauer, S. Elschner, W. Goldacker, H. Kraemer, A. Kudymow, O. Naeckel, S. Strauss, and V. M. R. Zermeno, "Smartcoil - concept of a full-scale demonstrator of a shielded core type superconducting fault current limiter," *IEEE Transactions on Applied Superconductivity*, vol. 27, no. 4, pp. 1–5, 2017.

[129] J. R. Clem, "Field and current distributions and ac losses in a bifilar stack of superconducting strips," *Physical Review B*, vol. 77, no. 13, p. 134506, 2008.

[130] D. Ruiz-Alonso, T. Coombs, and A. Campbell, "Computer modelling of high-temperature superconductors using an A-V formulation," *Superconductor Science and Technology*, vol. 17, no. 5, p. S305, 2004.

[131] R. Brambilla, F. Grilli, L. Martini, M. Bocchi, and G. Angeli, "A finite-element method framework for modeling rotating machines with superconducting windings," *IEEE Transactions on Applied Superconductivity*, vol. 28, no. 5, pp. 1–11, 2018.

[132] A. Arsenault, B. D. S. Alves, and F. Sirois, "Comsol implementation of the h-$\phi$-formulation with thin cuts for modeling superconductors with transport currents," *IEEE Transactions on Applied Superconductivity*, vol. 31, no. 6, pp. 1–9, 2021.

[133] B. D. S. Alves, V. Lahtinen, F. Sirois, and M. Laforest, "*h*-$\phi$ finite element thin-shell approach for modelling thin superconducting layers," *Superconductor Science and Technology*, 2021.

[134] K. B. Petersen, M. S. Pedersen *et al.*, "The matrix cookbook," *Technical University of Denmark*, vol. 7, no. 15, p. 510, 2008.

[135] W. T. Norris, "Calculation of hysteresis losses in hard superconductors carrying ac: isolated conductors and edges of thin sheets," *Journal of Physics D: Applied Physics*, vol. 3, no. 4, pp. 489–507, apr 1970.

[136] J. R. Clem and A. Sanchez, "Hysteretic ac losses and susceptibility of thin superconducting disks," *Phys. Rev. B*, vol. 50, pp. 9355–9362, Oct 1994.

[137] B. D. S. Alves, V. Lahtinen, F. Sirois, and M. Laforest, "3-d finite-element thin-shell model for high-temperature superconducting tapes," *IEEE Transactions on Applied Superconductivity*, 2021.

[138] "HTS modelling website," http://www.htsmodelling.com, accessed August 05, 2021.

# APPENDIX A SELECTING THE COHOMOLOGY BASIS REPRESENTATIVES TO IMPOSE CURRENT CONSTRAINTS

Electric and electronic devices often comprise more than a single conductor embedded in non-conducting spaces. When the $H$-$\phi$-formulation (Section 2.8.9) is applied to estimate the electromagnetic behavior of such devices, the magnetic scalar potential is considered in non-conducting subdomain $\Omega_c^C$, and the magnetic field strength is the working variable in the conducting subdomains. Then, to completely obey Ampère's law in $\Omega_c^C$, cuts $C_i$ must be introduced in this subdomain. Scalar potential discontinuities along these cuts give a current representative in each independent conducting subdomain $\Omega_{c,i}$ related to $C_i$. It is easy to define the cuts in $\Omega_c^C$ when the model geometry is relatively simple (e.g. only a few conductors in 2-D). Still, it can be an arduous task when the calculus domain comprises multiple transposed conductors in 3-D, such as in a Roebel cable geometry [26], for example.

There exist basically two types of cuts with which we can associate a magnetic scalar discontinuity: (i) thin cuts and (ii) thick cuts. They can be manually defined [132] or generated automatically through specific algorithms [55]. Thin cuts consider potential discontinuities on interfaces (cutting surfaces), making $\Omega_c^C$ simply connected. In contrast, thick cuts impose potential discontinuities along edges in a transition layer of finite elements in $\Omega_c^C$. The application of both types of cuts yields exactly the same solution obtained by using the pure $H$-formulation, i.e. when the magnetic field is defined everywhere in the computational domain. However, the use of the scalar potential instead of a pure $H$-formulation reduces the number of variables in the problem to be solved and avoids errors such as leakage currents in $\Omega_c^C$.

In Gmsh [60], a plugin called *CohomologyComputation* allows one to find thick cuts automatically and uniquely from the triangulation of the domain $\Omega$. They are equivalent to cohomology basis representatives of the topological structure of $\Omega_c^C$, precisely as the example discussed in Section 2.8.6. Only the incidence information is required for the calculation of these cuts.

For a single conductor embedded in air, the Gmsh plugin gives a single 1-cocycle representing the cohomology basis. This 1-cocycle comprises a set of edges in the discretized domain with unitary coefficient and specific orientation, which is therefore related to the orientation of the cycles (closed 1-chains) encompassing the conductor exactly once. The integration of the magnetic field over these cycles dual to the cohomology basis (called homology class) gives the enclosed net current in conducting subdomains. Defining precisely the current in the conductors is essential in most simulations. Therefore, the orientation of the cycles must be constrained accordingly.

In [55], the authors described a helpful approach to select the suitable cohomology basis representatives to impose the desired current in the conductors. Here, we progressively illustrate this approach in 2-D and 3-D cases, and discuss modifications in the Gmsh plugin for periodic domains. We start by presenting the example of a single conductor in 2-D, passing through examples of multiple conductors in 2-D and 3-D, and finally presenting 3-D examples with periodic boundary conditions (PBCs).

Let us start with the example of a single circular conductor of radius 1 cm embedded in air as depicted in Fig. A.1a. We denote by $\mathcal{K}$ the abstract simplicial complex constructed from the triangulation of $\Omega$, with $\mathcal{K}_c$ and $\mathcal{K}_c^C$ the abstract simplicial complex related to the subdomains $\Omega_c$ and $\Omega_c^C$ of $\Omega$, respectively. The direct application of the plugin *CohomologyComputation* in $\mathcal{K}_c^C$ gives a thick cut represented by the group of edges depicted in blue (formally, a 1-cocycle), which is clockwise oriented in this example. Moreover, the use of the $H$-$\phi$-formulation to solve the problem results in the current density and field distributions presented in Fig. A.1b and Fig. A.1c, respectively. The imposed net current in the conductor was 1 A. Note that the orientation of the fields is inverse to the orientation of the 1-cocycle since $\boldsymbol{h} = -\nabla\phi$. The current in the conductor flows out-of-plane according to the right-hand rule.

Suppose now that we want to impose the magnetic scalar potential discontinuity with a specific orientation. In that case, we can either compute the cohomology basis and visually determine the potential scalar discontinuity, or follow the approach described in [55]. This approach consists in choosing a homology basis of the representative 1-chains $\mathcal{H}_1(\mathcal{K}_c^C)$ and then adjust the cohomology basis accordingly. Thanks to $\mathcal{H}_2(\mathcal{K}) = \mathcal{H}_1(\mathcal{K}) = 0$, the 1-chains in $\mathcal{H}_1(\mathcal{K}_c^C)$ can be automatically defined. The following *exact relative homology sequence* [38]

$$0 = \mathcal{H}_2(M) \xrightarrow{j} \mathcal{H}_2(\mathcal{K}, \mathcal{K}_c^C) \xrightarrow{\partial_2} \mathcal{H}_1(\mathcal{K}_c^C) \xrightarrow{i} \mathcal{H}_1(M) = 0, \tag{A.1}$$

shows that $\mathcal{H}_2(\mathcal{K}, \mathcal{K}_c^C)$ and $\mathcal{H}_1(\mathcal{K})$ are isomorphic, and $\mathcal{H}_2(\mathcal{K}, \mathcal{K}_c^C) \cong \mathcal{H}_2(\mathcal{K}_c, \partial\mathcal{K}_c \cap \partial\mathcal{K}_c^C)$ holds by the *excision theorem* [38], where the notation $\mathcal{H}_k(.,.)$ expresses the relative $k$-homology of the first argument with respect to the second. Therefore, a basis for the space $\mathcal{H}_1(\mathcal{K}_c^C)$ can be automatically obtained by applying the boundary operator to the computed 2-chains basis of the space $\mathcal{H}_2(\mathcal{K}_c, \partial\mathcal{K}_c \cap \partial\mathcal{K}_c^C)$. The 2-chains representing the space $\mathcal{H}_2(\mathcal{K}_c, \partial\mathcal{K}_c \cap \partial\mathcal{K}_c^C)$ and the 1-chain representing $\mathcal{H}_1(\mathcal{K}_c^C)$ in our example of a single conductor are presented Fig. A.2a and Fig. A.2b, respectively. Intuitively speaking, a closed 2-chain in $\mathcal{H}_2(\mathcal{K}_c, \partial\mathcal{K}_c \cap \partial\mathcal{K}_c^C)$ is a collection of 2-simpices (triangles) covering $\mathcal{K}_c$ but where boundary falls in $\partial\mathcal{K}_c \cap \partial\mathcal{K}_c^C$.

The orientation of the 1-chain representing $\mathcal{H}_1(\mathcal{K}_c^C)$ is defined from the orientation of the 2-chains in the space $\mathcal{H}_2(\mathcal{K}_c^C, \partial\mathcal{K}_c \cap \partial\mathcal{K}_c^C)$, which are therefore oriented by the geometry definition in Gmsh. The outward normal of these 2-chains always points to the direction

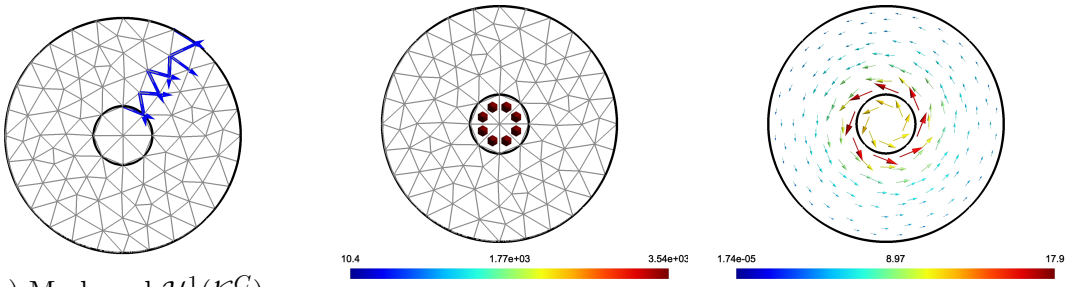


(a) Mesh and $\mathcal{H}^1(\mathcal{K}_c^C)$ (b) Current density (c) Magnetic field

Figure A.1 Single conductor example. (a) Mesh and the cohomology basis representative $\mathcal{H}^1(\mathcal{K}_c^C)$ depicted in blue, (b) current density distribution and (c) local magnetic field.

(a) $\mathcal{H}_2(\mathcal{K}_c^C, \partial\mathcal{K}_c \cap \partial\mathcal{K}_c^C)$ (b) $\mathcal{H}_1(\mathcal{K}_c^C) \cong \partial_2\mathcal{H}_2(\mathcal{K}_c^C, \partial_2\mathcal{K}_c \cap \partial_2\mathcal{K}_c^C)$

Figure A.2 Example of a single conductor: (a) 2-chains (surfaces) representing $\mathcal{H}_2(\mathcal{K}_c^c, \partial\mathcal{K}_c \cap \partial\mathcal{K}_c^C)$, and (b) 1-chains obtained as $\mathcal{H}_1 = \partial_2\mathcal{H}_2(\mathcal{K}_c^C, \partial_2\mathcal{K}_c \cap \partial_2\mathcal{K}_c^C)$.

out-of-plane in a 2-D case. The desired cohomology basis is then obtained by multiplying the previous basis $\mathcal{H}^1(\mathcal{K}_c^C)$ by a unimodular matrix $\mathbf{U}$ satisfying

$$\mathbf{I} = \mathrm{H}_1^T \mathrm{H}^1 \mathbf{U} \tag{A.2}$$

where $\mathbf{I}$ is an identity matrix with dimension equivalent to the dimension of (co)homology basis (equal to 1 here), $\mathrm{H}_1$ is a matrix representing the basis for the space $\mathcal{H}_1(\mathcal{K}_c^C)$, and $\mathrm{H}^1$ a matrix representing the previously computed basis for the space $\mathcal{H}^1(\mathcal{K}_c^C)$. If $z_1, \ldots, z_n$ is the basis of $\mathcal{H}_1(\mathcal{K}_c^C)$, then this allows the identification of the dual basis $\mathcal{H}^1(\mathcal{K}_c^C)$, that is the basis $z^1, \ldots, z^n$ satisfying $z^i(z_j) = \delta_{ij}$.

In our example, with a single conductor, we obtain $\mathbf{U} = -1$. Therefore, the new 1-cochain basis for the space $\mathcal{H}^1(\mathcal{K}_c^C)$ is $\mathrm{H}^1\mathbf{U} = -\mathrm{H}^1$. This cohomology basis is depicted in Fig. A.3a and the current density and magnetic field distributions obtained with the $H$-$\phi$-formulation are presented in Fig. A.3b and Fig. A.3c, respectively. Note that the current density and magnetic field distributions in Fig. A.3b and Fig. A.3c have opposite orientation to those in Fig. A.1b and Fig. A.1c. This orientation can be chosen from the definition of the geometry which defined the 2-chains orientation in $\mathcal{H}_2(\mathcal{K}_c^C, \partial_2\mathcal{K}_c \cap \partial_2\mathcal{K}_c^C)$. This allows the Gmsh user to choose the desired orientation in the conductor.

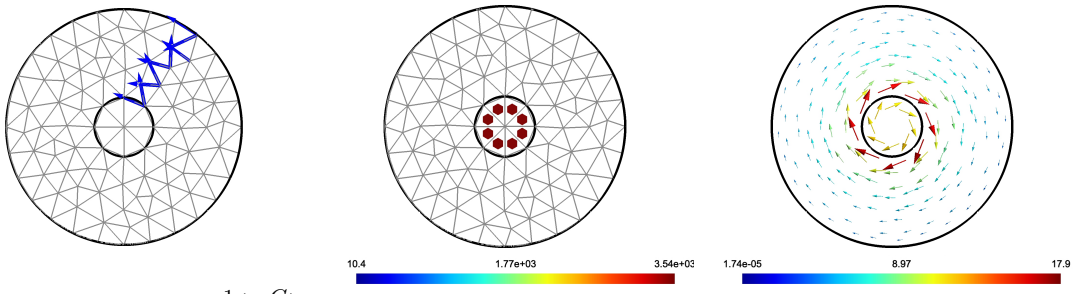


(a) Mesh and new $\mathcal{H}^1(\mathcal{K}_c^C)$ (b) Current density (c) Magnetic field

Figure A.3 Single conductor example with desired cohomology basis representative. (a) Mesh and the cohomology basis representative $\mathcal{H}^1(\mathcal{K}_c^C)$, (b) current density distribution and (c) local magnetic field.

In 2-D cases involving multiple conductors, the 1-cocycles representing a basis for $\mathcal{H}^1(\mathcal{K}_c^C)$ given by Gmsh may not be directly related to each conducting subdomain of $\Omega$. They can be a formal combination of the 1-cocycles dual to the cycles encompassing each individual conducting subdomain and with an arbitrary orientation. For example, Fig. A.4 shows the 1-cochains (in blue) representing the basis of $\mathcal{H}^1(\mathcal{K}_c^C)$ in a domain with seven conductors (small circles).

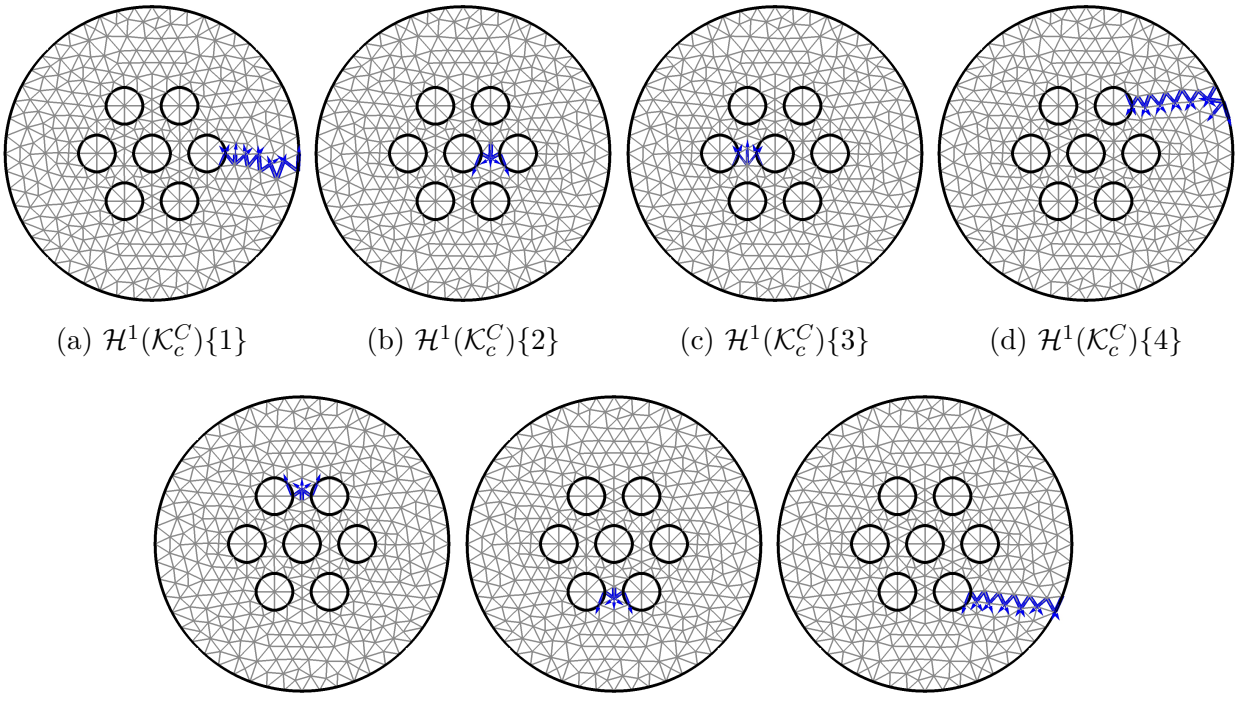

(a) $\mathcal{H}^1(\mathcal{K}_c^C)\{1\}$ (b) $\mathcal{H}^1(\mathcal{K}_c^C)\{2\}$ (c) $\mathcal{H}^1(\mathcal{K}_c^C)\{3\}$ (d) $\mathcal{H}^1(\mathcal{K}_c^C)\{4\}$

(e) $\mathcal{H}^1(\mathcal{K}_c^C)\{5\}$ (f) $\mathcal{H}^1(\mathcal{K}_c^C)\{6\}$ (g) $\mathcal{H}^1(\mathcal{K}_c^C)\{7\}$

Figure A.4 1-cochain cohomology basis ($\mathcal{H}^1(\mathcal{K}_c^C)$) representatives $\{1-7\}$ computed using standard *CohomologComputation* plugin in Gmsh.

Visually identifying the cocycles associated with each conductor in the example given in Fig. A.4 can be tiresome. However, the procedure presented for a single conductor can be extended to cases with multiple conductors. We can compute the bases for the space $\mathcal{H}_2(\mathcal{K}_c^C, \partial\mathcal{K}_c \cap \partial\mathcal{K}_c^C)$ (see Fig. A.5a), and its boundary (see Fig. A.5b) can be used to define $\mathcal{H}_1(\mathcal{K}_c^C)$. The $7 \times 7$ unimodular matrix $\mathbf{U}$ satisfying (A.2) is automatically obtained

$$U = \begin{bmatrix} 1 & -1 & 0 & 0 & 0 & 0 & 0 \\ 0 & 0 & 0 & -1 & 0 & 0 & 0 \\ 0 & 0 & 0 & -1 & 1 & 0 & 0 \\ 1 & -1 & 1 & 0 & 0 & 0 & 0 \\ 0 & 0 & 0 & 0 & 0 & -1 & -1 \\ 0 & 0 & 0 & 0 & 0 & 0 & -1 \\ 1 & 0 & 0 & 0 & 0 & 0 & 0 \end{bmatrix}, \tag{A.3}$$

and is used to define the new cohomology basis $\mathrm{H}^1\mathbf{U}$ represented by the 1-cochains in Fig. A.6 that are dual to the basis of $\mathcal{H}_1(\mathcal{K}_c^C)$. Note that each one of these seven 1-cochains in $\mathcal{H}^1(\mathcal{K}_c^C)$ corresponds uniquely to the individual conductors in our domain. Moreover, these 1-cochains have the same orientation as the 1-chains dual to them, which are shown in Fig. A.5b. Suppose, for this example, we want to impose exactly the same net current (1 A) in each conductor. In that case, we can assign to the new cohomology basis exactly the same magnetic scalar potential discontinuity. The resulting current density and the magnetic field distributions obtained by applying the $H$-$\phi$-formulation are presented in Fig. A.7a and Fig. A.7b, respectively. Note that the conductors carry the same total current, but the current density has a nonuniform distribution along the conductors radius, mainly due to the proximity effects between these conductors. The conductor's radius is 1 cm, and the six outer conductors are separated 1 cm from the inner conductor.

(a) $\mathcal{H}_2(\mathcal{K}_c^C, \partial\mathcal{K}_c \cap \partial\mathcal{K}_c^C)$ (b) $\mathcal{H}_1(\mathcal{K}_c^C) \cong \partial_2\mathcal{H}_2(\mathcal{K}_c^C, \partial\mathcal{K}_c \cap \partial\mathcal{K}_c^C)$

Figure A.5 (a) 2-chains (surfaces) representing $\mathcal{H}_2(\mathcal{K}_c^C, \partial\mathcal{K}_c \cap \partial\mathcal{K}_c^C)$, and (b) 1-chains obtained as $\mathcal{H}_1 \cong \partial_2\mathcal{H}_2(\mathcal{K}_c^C, \partial\mathcal{K}_c \cap \partial\mathcal{K}_c^C)$.

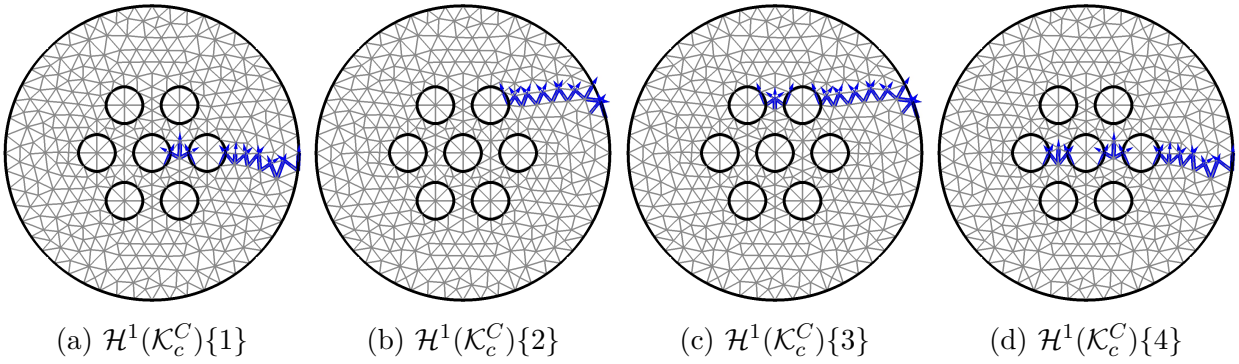

(a) $\mathcal{H}^1(\mathcal{K}_c^C)\{1\}$ (b) $\mathcal{H}^1(\mathcal{K}_c^C)\{2\}$ (c) $\mathcal{H}^1(\mathcal{K}_c^C)\{3\}$ (d) $\mathcal{H}^1(\mathcal{K}_c^C)\{4\}$

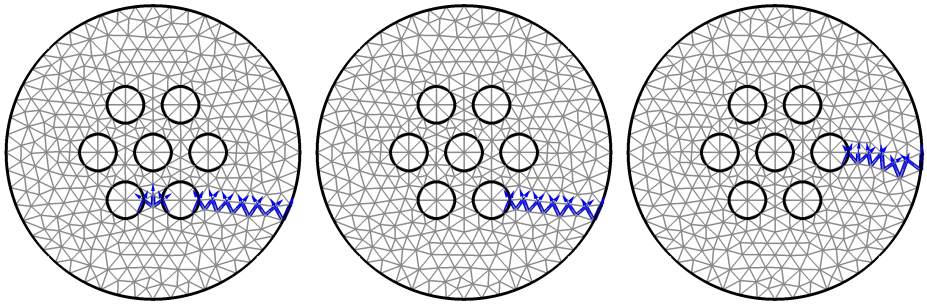

(e) $\mathcal{H}^1(\mathcal{K}_c^C)\{5\}$ (f) $\mathcal{H}^1(\mathcal{K}_c^C)\{6\}$ (g) $\mathcal{H}^1(\mathcal{K}_c^C)\{7\}$

Figure A.6 1-cochain cohomology basis $(\mathcal{H}^1(\mathcal{K}_c^C))$ representatives $\{1-7\}$ dual to $\partial_2\mathcal{H}_2(\mathcal{K}_c^C, \partial\mathcal{K}_c \cap \partial\mathcal{K}_c^C)$.

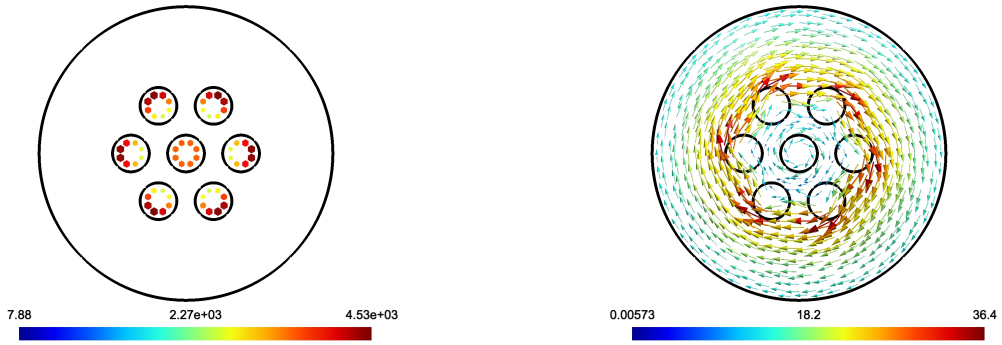


(a) current density (b) Magnetic field

Figure A.7 Example of a 2-D cable comprising seven conductors: (a) current density in the conductors and (b) magnetic field local distribution.

In 3-D cases, the procedure of visually identifying the cohomology basis representatives related to each conductor can be even more complicated. Let us consider an example with seven conductors in 3-D obtained with the extrusion of the 2-D geometry of the previous example onto the third dimension (see Fig. A.8a). The application of the *CohomologComputation* plugin gives 1-cochains similar to the one presented in Fig. A.8b.

Note that it is almost impossible to identify which conductors are related to this 1-cochain visually.

To replicate the approach used in 2-D cases, we can compute the 1-cycles encompassing each one of the conductors that pass through the boundaries of our domain. These 1-cycles are obtained by computing the boundary of 2-chains (Fig. A.9a) in the space $\mathcal{H}_2(\mathcal{K}_c^C, \partial\mathcal{K}_c \cap \partial\mathcal{K}_c^C)$, where $\mathcal{K}_c$ and $\mathcal{K}_c^C$ are the intersection between the non-conducting and conducting subdomains with the exterior boundary $\Gamma$, respectively. The 1-cycles are presented in Fig. (A.9b). They have orientation defined by the subdomain geometries. Then, the 1-cochains forming a basis dual to the basis of 1-chains automatically satisfies (A.2). For illustration, the 1-cochains related to each conductor are presented in Fig. A.10.

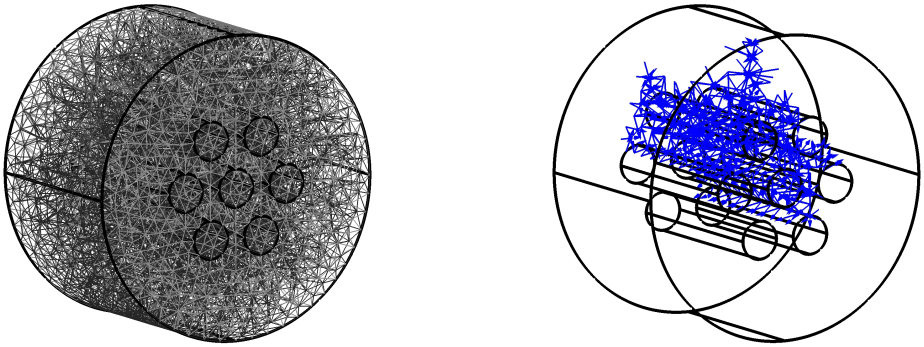

(a) 3-D geometry and mesh (b) $\mathcal{H}^1(\mathcal{K}_c^C)\{1\}$

Figure A.8 3-D geometry example comprising seven conductors: (a) geometry and mesh, and (b) example of one 1-cochain in $\mathcal{H}^1(\mathcal{K}_c^C)$.

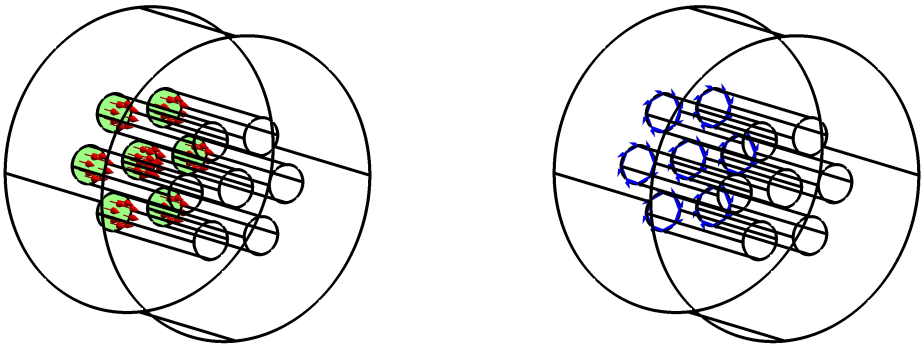

(a) $\mathcal{H}_2(\mathcal{K}_c^C, \partial\mathcal{K}_c \cap \partial\mathcal{K}_c^C)$ (b) $\mathcal{H}_1(\mathcal{K}_c^C) \cong \partial_2\mathcal{H}_2(\mathcal{K}_c^C, \partial\mathcal{K}_c \cap \partial\mathcal{K}_c^C)$

Figure A.9 (a) 2-chains (surfaces) representing $\mathcal{H}_2(\mathcal{K}_c^C, \partial\mathcal{K}_c \cap \partial\mathcal{K}_c^C)$, and (b) 1-chains obtained as $\mathcal{H}_1 \cong \partial_2\mathcal{H}_2(\mathcal{K}_c^C, \partial\mathcal{K}_c \cap \partial\mathcal{K}_c^C)$.

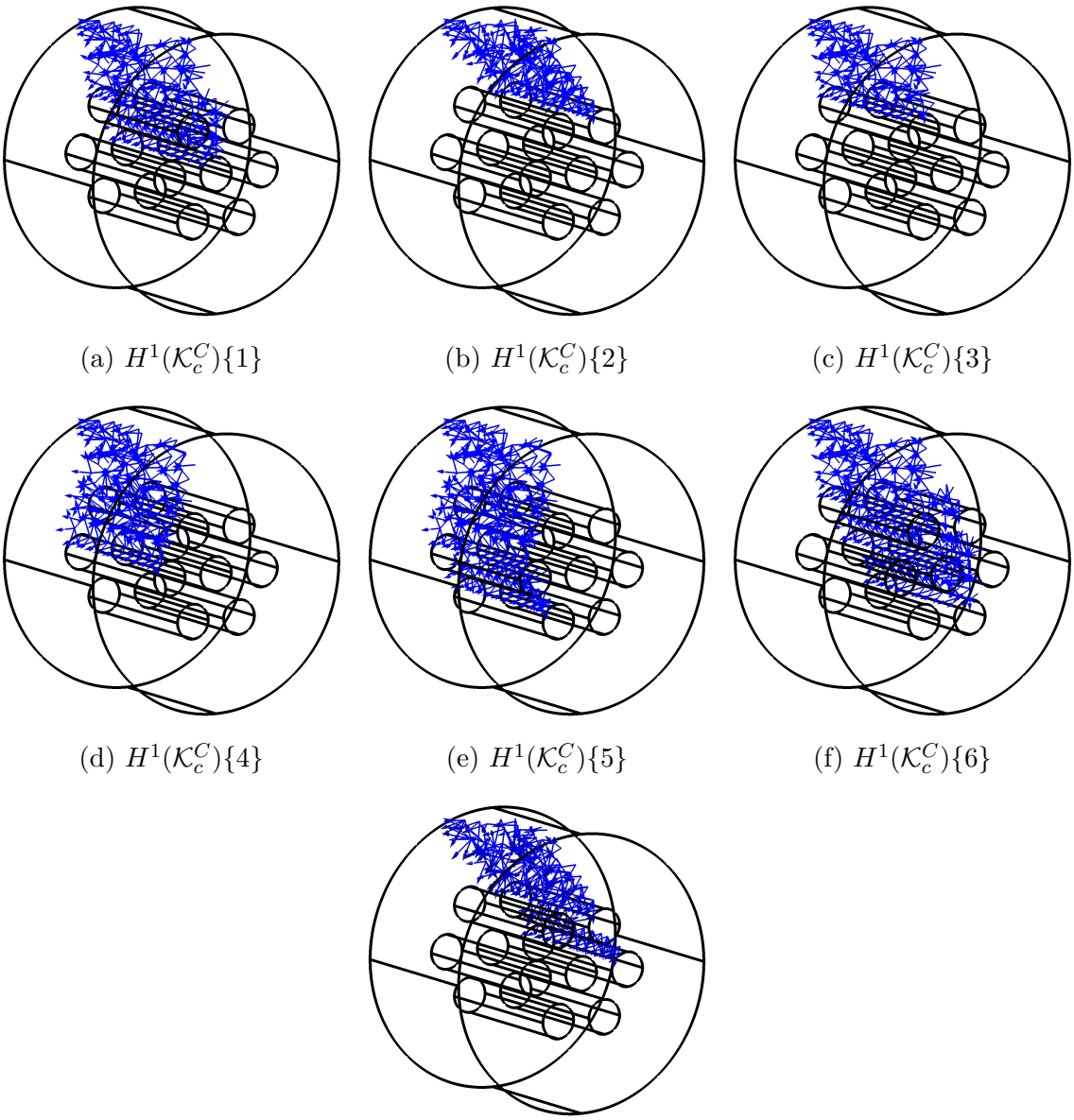

(a) $H^1(\mathcal{K}_c^C)\{1\}$ (b) $H^1(\mathcal{K}_c^C)\{2\}$ (c) $H^1(\mathcal{K}_c^C)\{3\}$

(d) $H^1(\mathcal{K}_c^C)\{4\}$ (e) $H^1(\mathcal{K}_c^C)\{5\}$ (f) $H^1(\mathcal{K}_c^C)\{6\}$

(g) $H^1(\mathcal{K}_c^C)\{7\}$

Figure A.10 1-cochains cohomology basis ($\mathcal{H}^1(\mathcal{K}_c^C)$) representatives $1-7$ in 3-D dual to $\partial_2\mathcal{H}_2(\mathcal{K}_c^C, \partial\mathcal{K}_c \cap \partial\mathcal{K}_c^C)$.

The same net current was imposed in each conductor in 3-D using the new cohomology basis representatives. The current density and the magnetic field distributions are presented in Fig. A.11a and Fig. A.11b, respectively. Note that this solution is equivalent to those obtained for the 2-D cases. Indeed, the 3-D geometry in this example can be approximated by its infinitely-long representation, identical to our 2-D previous model.

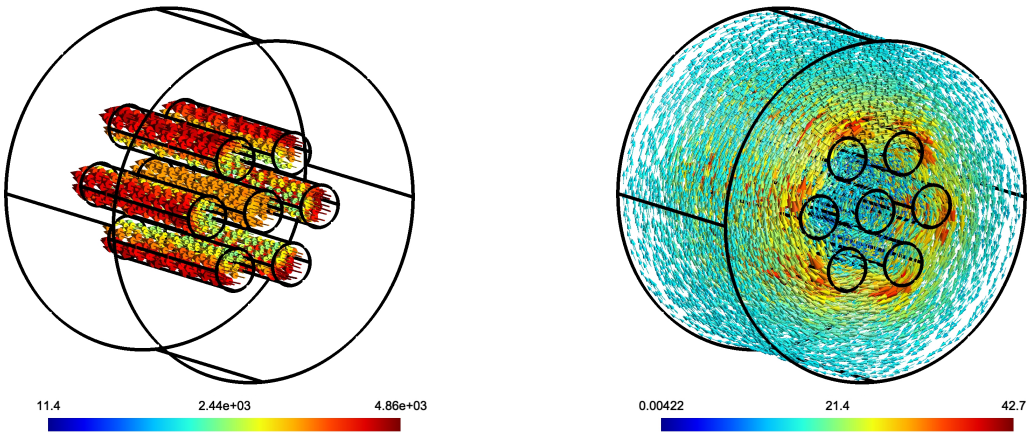


(a) Current density (b) Magnetic field

Figure A.11 Example of a 3-D cable comprising seven conductors: (a) current density in the conductors and (b) magnetic field local distribution.

Modeling device portions can represent a substantial reduction of the number of variables and of the cost of computation. This requires the device geometry to have some symmetry. One example is the 2-D infinitely-long representation of the 3-D cable presented before. Another example is modeling cables with longitudinal symmetry, such as ACSR, TSTC, CORC, and Roebel cables. The application of periodic boundary conditions (PBCs) in FEM allows us to represent small portions of the transposition length or the twist pitch of these cables. These PBCs link variables in one domain boundary to their counterpart in another boundary of the same domain (called periodic surfaces).

When the $H$-$\phi$-formulation is applied in periodic domains, the magnetic scalar potential discontinuities in the cuts must be precisely at the same position on the periodic surfaces. This requires the cohomology basis representatives also to be periodic on these surfaces. However, the actual code of the plugin *HomologyComputation* does not consider the domain periodicity when computing the 1-cohains. To solve this issue, we proposed modifications in this plugin.

The basic idea behind the proposed modifications is that the $k$-chains and $k$-cochains, for $0 \leq k \leq 3$ must be combined to their counterparts on the surfaces identified by the periodicity before creating the abstract simplicial complex representing the actual mesh. With this simple combination, the abstract simplicial complex becomes periodic, and the original algorithm of Gmsh used to find the (co)homology basis can be applied without any further modifications.

For illustration, let us consider the 3-D representation of the cable with seven conductors,

similar to our previous examples, but with a horizontal displacement during the extrusion of the 2-D geometry (Fig. A.12). Without getting into the implementation details of the proposed modifications of Gmsh, the example of a 1-cochain in $\mathcal{H}^1(\mathcal{K}_c^C)$ dual to the cycles around the inner conductor of this cable is presented in Fig. A.13. Note that this 1-cochain is exactly at the same position on the front and back boundaries of our domain.

For the sake of comparison, the solutions with and without the PBCs for current density and field distributions are presented in Fig. A.14. We observe that without PBCs (Fig. A.14a and A.14b ), the finite element model cannot represent fields and currents correctly near the

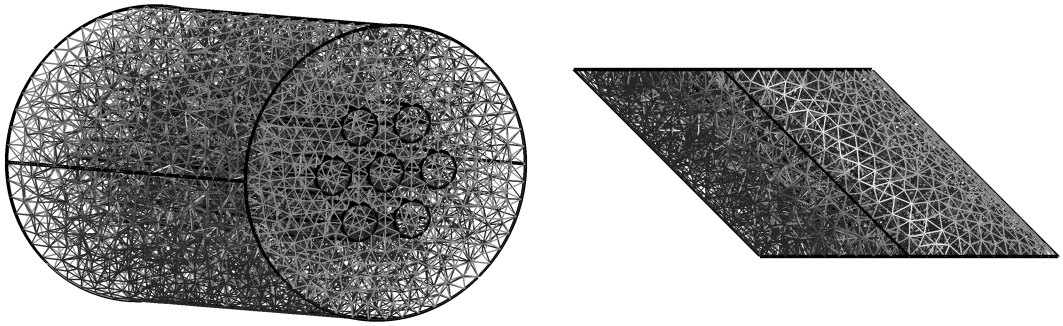

(a) 3-D geometry and mesh (b) Top view

Figure A.12 Example of a 3-D cable comprising seven conductors with horizontal displacement and its discretization.

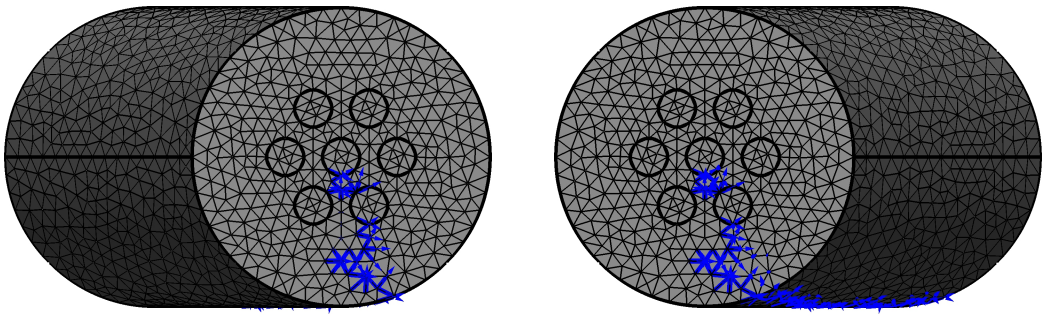

(a) $H^1(\mathcal{K}_c^C)\{1\}$ (front) (b) $H^1(\mathcal{K}_c^C)\{1\}$ (back with horizontal flip)

Figure A.13 $H^1(\mathcal{K}_c^C)\{1\}$ for the example of a 3-D cable comprising seven conductors with horizontal displacement: (a) front view and (b) back view with a horizontal flip. Note that the thick cut is exactly at same position on the front and back boundaries of the calculus domain.

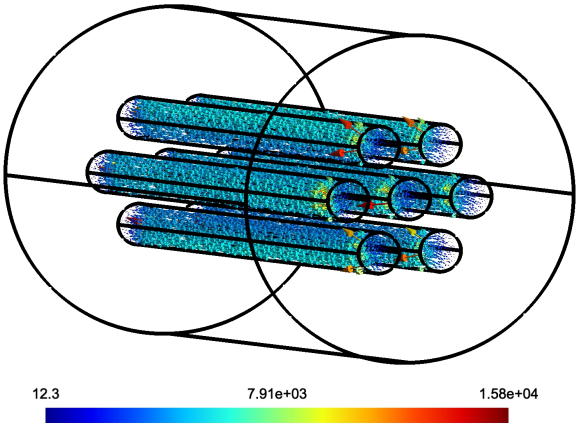


(a) Current density without PBCs

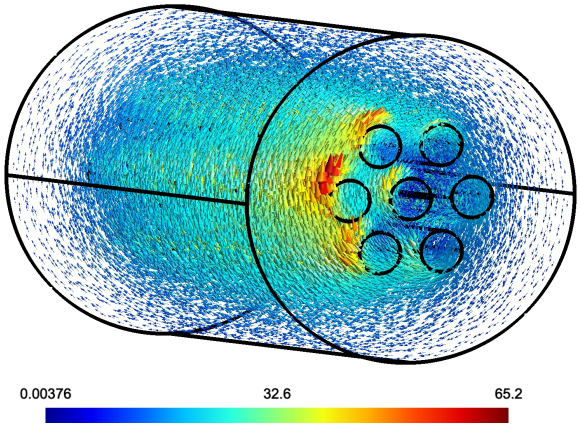


(b) Magnetic field without PBCs

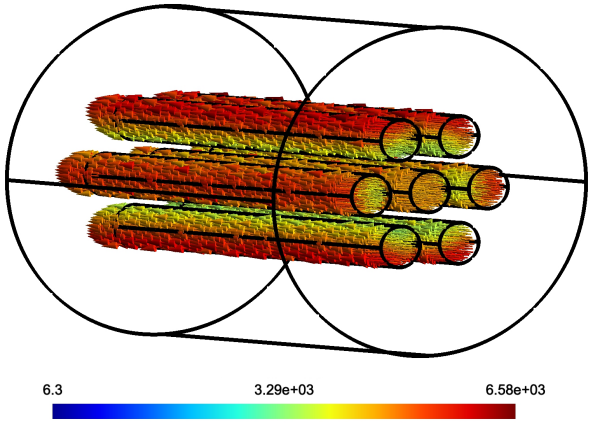


(c) Current density with PBCs

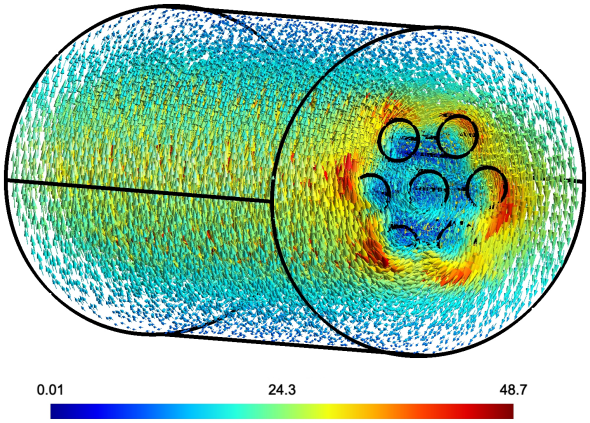


(d) Magnetic field with PBCs

Figure A.14 Example of a 3-D cable comprising seven conductors with horizontal displacement with and without periodic boundary conditions applied: (a) and (c) current density distribution in the conductors, and (b) and (d) magnetic field local distribution.

boundary surfaces. However, when PBCs are applied using the modifications proposed in the Gmsh plugin, a solution equivalent to the previous 2-D infinitely-long representation of the conductors is obtained (Fig. A.14c and A.14d).

As a final example, we considered a cable comprising four counter-clockwise twisted inner conductors with twist pitch of 8 cm and six clockwise twisted outer conductors with twist pitch of 12 cm, i.e. 10 conductors in total. All the conductors were $4\times4$ mm$^2$, the inner radius was 10 mm and the outer radius was 15 mm. The complete 3-D geometry of the cable is presented in Fig. A.15a. Given the periodicity of the twist pitches, the cable can be represented by the periodic geometry depicted in Fig. A.15b. Note that all the four inner

conductors (with frontal boundary faces colored in blue) and the six outer conductors (with frontal boundary faces colored in green) are connected by the periodicity.

The 1-chain basis representative of $H^1(\mathcal{K}_c^C)$ were computed using the plugin *HomologyComputation* with the proposed modifications. The result are two 1-chains with coefficients from 1 to 4 related to the four inner conductors and with coefficients from 1 to 6 related to the six outer conductors in our calculus domain (see Fig. A.16). Note that only these two 1-chains are enough to impose the current in the ten conductors. Since both the inner and outer conductors are connected by the symmetry, it makes sense that these basis representatives have values along the edges coefficients) higher than 1 and equivalent to the number of conductors. Note also the the basis representatives in the front and back boundary faces of our domain are identical.

Finally, we imposed currents of amplitude 6.4 kA in opposite directions in the inner and outer conductors using the computed basis of $H^1(\mathcal{K}_c^C)$. The current density and magnetic field distributions are presented in Fig. A.17a and Fig. A.17b, respectively. The current is perfectly distributed within the conductors and the magnetic field is mostly concentrated in between the inner and outer conductors, as expected.

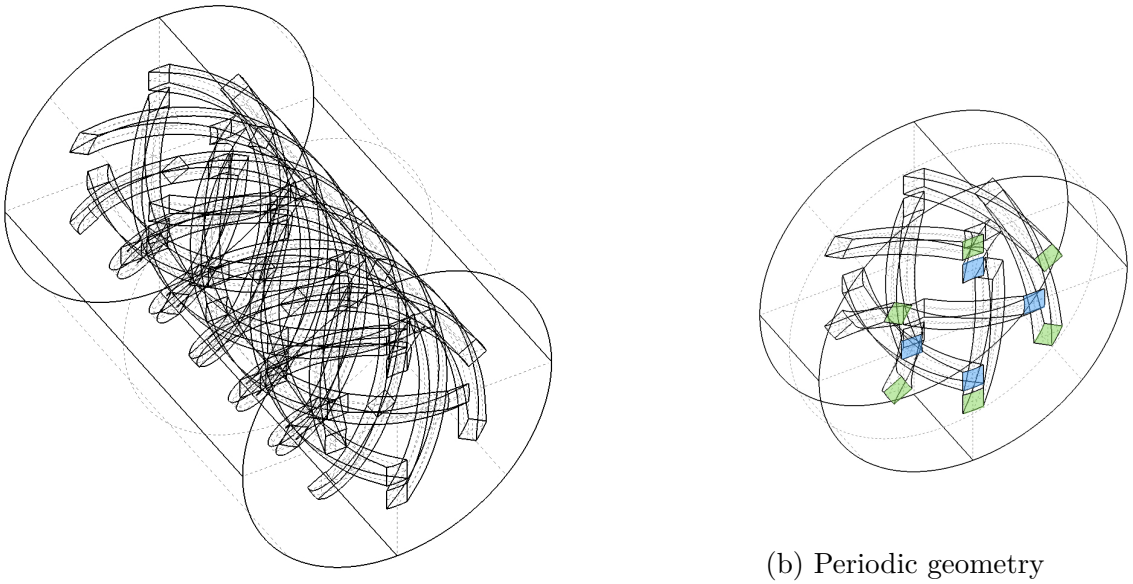

(a) Full 3-D geometry

(b) Periodic geometry

Figure A.15 Example of a 3-D twisted cable comprising ten conductors. The four inner conductors have twist pitch of 8 cm and the six outer conductors have a twist pitch of 12 cm. The complete geometry of this cable is presented in (a) and can be represented by a 2 cm length representation due to its periodicity as in (b).

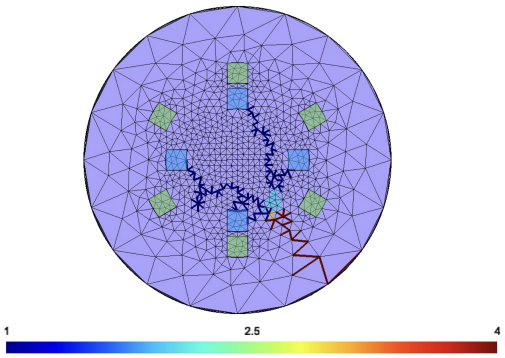


(a) $H^1(\mathcal{K}_c^C)\{1\}$ (front)

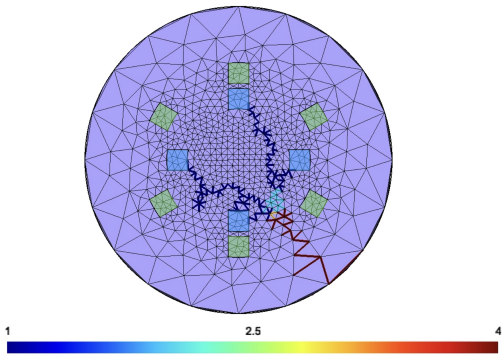


(b) $H^1(\mathcal{K}_c^C)\{1\}$ (back - horizontal flip)

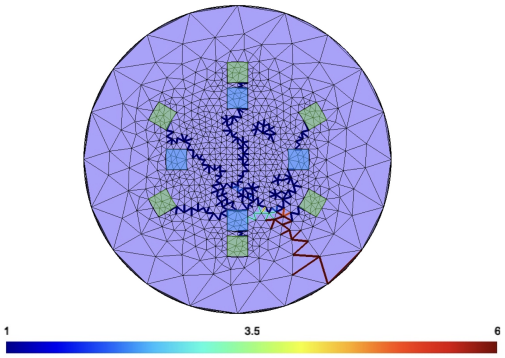


(c) $H^1(\mathcal{K}_c^C)\{2\}$ (front)

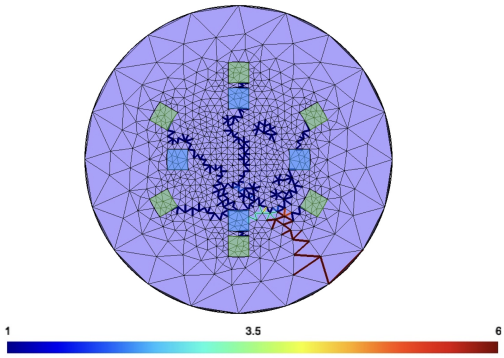


(d) $H^1(\mathcal{K}_c^C)\{2\}$ (back - horizontal flip)

Figure A.16 $H^1(\mathcal{K}_c^C)\{1\}$ and $H^1(\mathcal{K}_c^C)\{2\}$ for the example of a 3-D twisted cable: (a) front view and (b) back view with a horizontal flip. Note that the thick cut is exactly at same position on the front and back boundaries of the calculus domain.

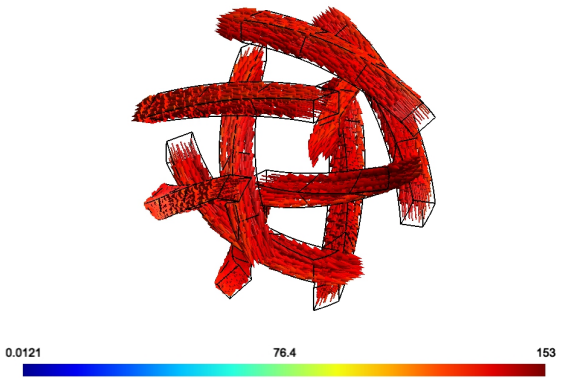


(a) Current density with PBCs

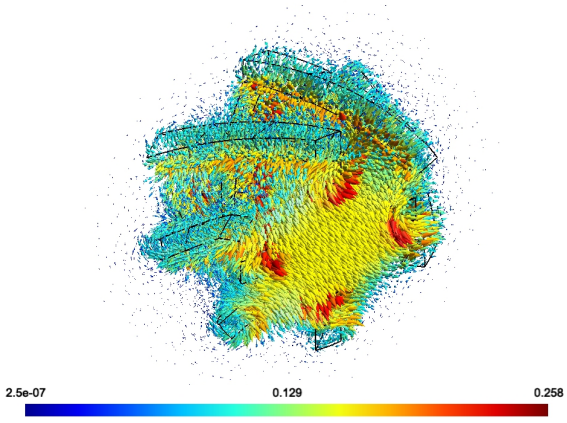


(b) Magnetic field with PBCs

Figure A.17 Current and magnetic field distributions in a twisted cable comprising ten conductors. The six outer conductors carry same current as the four inner conductors but in opposite direction.

# APPENDIX B COMSOL IMPLEMENTATION OF A THIN-SHELL MODEL BASED ON THE $H$-$\phi$-FORMULATION FOR HTS TAPES

[1]Bruno de Sousa Alves, [1]Alexandre Arsenault, [1]Frédéric Sirois

[1]Polytechnique Montréal, Montréal, QC H3C 3A7, Canada

## Abstract

This paper presents the implementation in COMSOL multiphysics of a finite-element thin-shell model and its application for estimating the solution of 2-D problems involving superconducting tapes. The magnetic scalar potential ($\phi$) is the state variable in the surroundings of the tapes, which are represented as reduced-dimension geometries in the calculus domain. Inside the tapes, a 1-D virtual problem depending on the tangential components of the magnetic field ($H$) takes into account the physics across their thickness. The two finite-element matrix systems are generated simultaneously, coupled during the assembly process, and solved jointly. Moreover, the use of the so-called thin cuts allows imposing transport current in the tapes. This procedure permits simulating problems with superconducting tapes in any configuration. We demonstrate that both normal and tangential fields agree well with reference solutions obtained with the widely used $T$-$A$-formulation and with the standard $H$- and $H$-$\phi$-formulations with a full discretization of the thin region. The proposed $H$-$\phi$ thin-shell model estimates AC losses accurately while speeding up simulations. This makes this model ideal for simulating large-scale superconducting devices.

## Introduction

Efficient and accurate estimation of the electromagnetic (EM) behavior of large-scale high-temperature superconducting (HTS) systems is crucial for their optimization and economical operation, but modeling HTSs is still a challenge. These systems typically combine many HTS tapes to reduce the overall AC losses and maximize current capacity [26, 126]. Each of these tape comprises a stack of thin films that hinders the domain meshing with automatic mesh generators for finite element (FE) method application purposes [6, 7]. Moreover, the high nonlinear resistivity of such materials severely impedes the convergence of the numerical model [22].

Finite-element thin-shell (TS) models are often applied to overcome mesh difficulties

associated with the high aspect ratio of thin regions [31, 32, 34]. In these models, a surface representative replaces the actual volume of the shell and interface conditions (ICs) account for their interior EM phenomena. These ICs are generally defined by analytical solutions in terms of tangential components of the field quantities across the thickness of the thin region [127]. Although these solutions are easily calculated in the time-harmonic regime for ohmic conductors, problems involving HTSs are harder to handle due to their nonlinearity.

As a first approximation, one can consider linear field profiles across the thickness of the thin region [76] (the so-called strip approximation). The current density is assumed constant across the thickness and can be defined analytically along the wide dimensions of the thin region using the Biot-Savart law. In [78], the authors proposed a strip approximation based purely on FEM. They assumed that the properties of the conductors do not vary significantly along the thickness of superconducting tapes. The integral expressions for the current density inside the strip proposed in [76] were jointly solved with FEM system of equations. Due to its easy implementation, the this approximation became a popular approach to model HTS tapes [110]. However, since the nonlinear profile of the tangential field is not completely represented by this approximation, the AC losses are underestimated in problems involving multiple interacting tapes [79, 121]. Consequently, its application is limited to cases where the normal components of the fields dominate the dynamic of the problem, since the so-called top/bottom losses are neglected.

Recently, a COMSOL model based on the mixed $T$-$A$-formulation for modeling HTS tapes was formulated [35]. In this model, a 1-D FE problem in terms of $T$ defined over the thin regions gives the surface current density that is used as a source term in a standard $A$-formulation. However, two things impede its application for modeling large-scale HTS systems. Firstly, higher-order FEs are required for $A$ than for $T$, in order to ensure numerical stability [108], which increases the number of degrees of freedom (DOFs) and the computational burden [109]. Secondly, it has the same disadvantages of a strip approximation: (i) constant current density across the thickness and (ii) AC losses are underestimated in cases of closely packed HTS tapes.

In [133], we proposed a TS model based purely on the magnetic field and scalar potential ($H$-$\phi$-)formulation with ICs defined as virtual one dimensional (1-D) FE problems across the thickness of the tape. The procedure allows the tangential components of the field to penetrate the reduced-dimension geometry and accurately estimate the AC losses in HTS tapes. Moreover, the use of $H$ and $\phi$ represents a more natural coupling than the $T$-$A$-formulation, which improves the stability of the numerical scheme. With a suitable virtual discretization of the 1-D FE model, the proposed model was shown to be efficient in tackling

problems involving HTS tapes in any configuration. We also showed that this TS model can be used to address problems involving multilayered tapes with a fraction of the computation time of a reference FE model using the standard $H$-$\phi$-formulation. In [137], the TS model was extended to 3-D simulation cases.

In this paper, we present the implementation of the 2-D TS model based on the $H$-$\phi$-formulation in COMSOL multiphysics. Indeed, this software became very popular in the HTS modeling community due to the easy implementation of finite-element models and its user-friendly interface. For implementing the TS model, the extra-dimension feature of COMSOL is used and the transport current in the tapes is imposed using thin cuts [132]. The results of the TS model are here compared with the standard $H$- and $H$-$\phi$- formulations with full representation of the tapes, and with the $T$-$A$-formulation in terms of solution accuracy and computational time for three 2-D benchmark problems. We demonstrate that the TS model is comparable to the $T$-$A$-formulation when a single FE is considered in the virtual 1-D domain. With the 1-D mesh refinement, the TS model can tackle problems involving many HTS tapes in any configuration.

**Model Definition**

The $H$-$\phi$-formulation solves the standard $H$-formulation in conducting subdomains ($\Omega_c$) and considers the magnetic scalar potential ($\phi$) as the state variable in non-conducting subdomains ($\Omega_c^C$). The coupling between $H$ and $\phi$ at boundary $\Gamma_c = \partial\Omega_c \cap \partial\Omega_c^C$ is imposed naturally by $H = -\nabla\phi$ [64]. Moreover, Ampère's law is applied to Faraday's law and solved jointly in the whole domain $\Omega = \Omega_c \cup \Omega_c^C$ as

$$\nabla \times (\rho \nabla \times H) + \mu \frac{\partial H}{\partial t} = 0, \tag{B.1}$$

where $\rho$ is the electrical resistivity and $\mu$ the magnetic permeability. Note that by applying $H = -\nabla\phi$ in (B.1), its first term vanishes since $\nabla \times (\nabla\phi) = 0 \,\forall\, \phi$. Consequently, disregarding Neumann boundary conditions, holds

$$\mu \frac{\partial \nabla \phi}{\partial t} = 0, \tag{B.2}$$

in $\Omega_c^C$. Additionally, cuts ($C_i$) are introduced in $\Omega_c^C$ to make it simply connected and avoid $\phi$ to be multi-valued. Discontinuities of $\phi$ along these cuts allow imposing net currents in connected parts of the conducting subdomains $\Omega_i \subset \Omega_c$. This approach is well described in [49], and the implementation of the $H$-$\phi$-formulation in COMSOL multiphysics using the

so-called thin cuts is well detailed in [132].

In this paper, we propose a TS model based on the $H$-$\phi$-formulation for modeling HTS tapes. The tapes are represented as reduced-dimension geometries on the calculus domain (lines in 2-D or surfaces in 3-D) and denoted by $\Gamma_s$ (Fig. B.1a). Nodes, edges and surfaces along the tapes' representatives are duplicated creating cracks in $\Omega_c^C$, which becomes multiply connected. It can then be treated exactly as in the standard $H$-$\phi$-formulation, i.e. the introduction of cuts in $\Omega_c^C$ allows imposing a transport current in the tapes.

The physics inside the tapes is taken into account by a virtual representation of their actual thickness denoted by $d$ (Fig. B.1b). A local coordinate system $xyz$ is defined at the center of the tape. Its surface is on the $xz$ plane and its normal is in the $y$-direction. To distinguish the $y$ coordinate in the virtual 1-D domain to the 2-D domain (refereed to here as the original domain), we denote the $y$-coordinate of the 1-D domain as $y_1$. Therefore, the standard form of the $H$-formulation (B.1) is solved for a 1-D problem defined over the virtual domain in $y_1$ and in terms of only the tangential components of $H$ ( denoted by $H_t$) on the $xz$ plane, i.e.

$$\frac{\partial}{\partial y_1}\left(\rho\frac{\partial H_t}{\partial y_1}\right)+\mu\frac{\partial H_t}{\partial t}=0, \tag{B.3}$$

and the nonlinear resistivity of type-II superconductors is expressed by a 1-D power-law characteristic as

$$\rho \overset{\text{2-D}}{=} \frac{E_c}{J_c}\left(\frac{|(\partial H_t/\partial y_1)|}{J_c}\right)^{n-1}, \tag{B.4}$$

where $E_c$ is the electric field criterion used to define the critical current density ($J_c$), and the

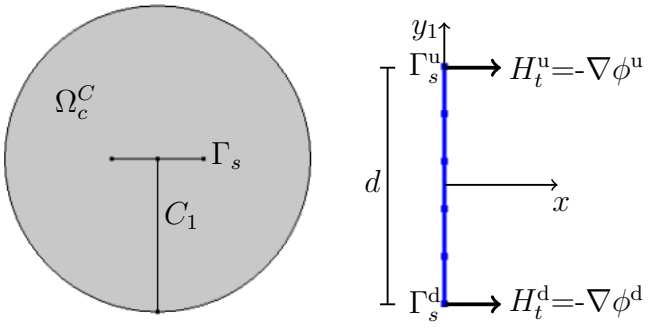


(a) Original 2-D domain (b) Virtual 1-D domain

Figure B.1 (a) Single tape geometry showing the nonconducting subdomain $\Omega_c^C$, the cut $C_1$ associated to the tape, and the tape represented as a reduced-dimension geometry (a line $\Gamma_s$). (b) Virtual 1-D domain across the thickness of the tape $-d/2 \leq y_1 \leq d/2$.

power index $n$ determines the steepness of the $E$-$J$ curve [43].

The coupling between $H_t$ and $\phi$ is imposed by $H_t^{\mathrm{u}} = -\nabla\phi^{\mathrm{u}}$ and $H_t^{\mathrm{d}} = -\nabla\phi^{\mathrm{d}}$ at the boundaries of the 1-D domain $\Gamma_s^{\mathrm{u}}$ and $\Gamma_s^{\mathrm{d}}$, respectively, where the superscripts u and d indicate the upper and the lower sides of $\Gamma_s$, i.e. $y_1|_{\mathrm{u}} = d/2$ and $y_1|_{\mathrm{d}} = -d/2$ (Fig. B.1b). For simplicity, only the superconducting layer of HTS tapes is considered in this paper. This is a valid approximation given the low resistivity of HTSs compared to other conducting layers of these tapes. Moreover, since (B.3) is solved only in the superconductor, $\mu = \mu_0$ everywhere.

The solution of the proposed TS model is obtained by solving (B.2) coupled to (B.3), and using the power law (B.4). This model is equivalent to the one proposed in [133] and extended to 3-D cases in [137]. The main contribution of this paper relies on the implementation of the described TS approach in COMSOL multiphysics, which is presented next.

**Model Implementation in COMSOL Multiphysics**

The $H$-$\phi$-formulation in COMSOL can be implemented basically in two different ways: (i) using predefined *Magnetic Field Formulation* (MFH) and *Magnetic Field No Currents* (MFNC) modules, or (ii) defining our own equations in the *Partial Differential Equation* (PDE) interface [120]. For implementing the TS model, special attention is required in the definition of the thin cuts, the low-dimension geometries representing the HTS tapes, and the coupling between the original and virtual domains.

Discontinuities of $\phi$ are required in both the cut and the tape geometry representatives in the original 2-D domain. This can be done using a *Magnetic Scalar Potential Discontinuity* in the MFNC module, but it only allows constant discontinuities of $\phi$. The proposed TS model for HTS tapes requires more flexible features than simple potential discontinuities across interfaces. For this reason, we use the *Stabilized Convection-Diffusion Equation* (*scdeq*) module of the *Classical PDEs* interface, which is the only COMSOL module that allows imposing an *Interior Dirichlet Boundary Condition* [107]. Despite this, the *Convection-Diffusion Equation* in the *scdeq* module does not allow solving (B.2) directly since the time derivative of the scalar potential gradient is not defined in its equation. Therefore, all the coefficients in this equation are set to zero and we add an extra *Weak Contribution* expressing a weak form of (B.2) in the original domain as

```
mu0*d(hx,t)*test(hx)+mu0*d(hy,t)*test(hy)        (B.5)
```

where `mu0` is the vacuum permeability, `hx=-phix` and `hy=-phiy` are the magnetic field componets in the $x$ and $y$ direction, respectively, and defined as *variables* in the original

2-D domain, `phix` and `phiy` represent the partial derivatives of $\phi$ with respect to $x$ and $y$, and `test(phix)` and `test(phiy)` are the test functions using the COMSOL notation.

Two *Interior Dirichlet Boundary Condition*s are defined: one for imposing potential discontinuities (or net current constraints) across the thin cuts (Fig. B.2a), and the other for representing the cracked thin region (Fig. B.2b). The red arrows in Fig. B.2 point from the lower to the upper side of the geometry and are graphically shown in COMSOL. For thin cuts, the constraints in the *Equation View* of the first *Interior Dirichlet Boundary Condition* are modified to

$$\texttt{up(phi)-down(phi)-I = 0}, \tag{B.6}$$

where `phi` represents $\phi$ and `I` $= I_0 \sin(2\pi f t)$ is the transport current with amplitude $I_0$ imposed in the related conducting region. The operators `up` and `down` give the scalar potential related the sides of the cut. For the TS model, the constraints in the *Equation View* of the second *Interior Dirichlet Boundary Condition* are all set to zero. This creates the cracked region required in our TS model, which is further coupled to the 1-D virtual geometry. The *Equation View* is enabled in the *Show more options* dialog in COMSOL.

For representing the phenomena across the tape thickness, we define a 1-D *Extra Dimension* in *Global Definitions* with `y1` representing $y_1$ in the virtual domain. This 1-D geometry is defined in $-d/2 \leq$ `y1` $\leq d/2$ and *Attached* to the *Component* representing the original 2-D domain under the *Definitions* mode. The interface $\Gamma_s$ is selected to be attached to the *Extra Dimension*.

An interface *Weak Contribution* is then included in $\Gamma_s$ combined with the *Extra Dimension*. We define an *Auxiliary Dependent Variable* `Ht` expressing $H_t$, and the *Weak Contribution*

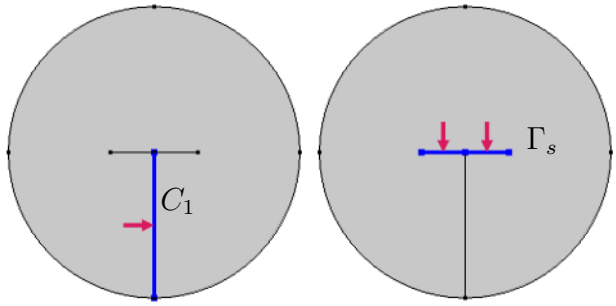


(a) Thin cut (b) Crack

Figure B.2 Example of a single HTS tape geometry in COMSOL: (a) thin cut associated to the potential discontinuity to impose a current constraint to the tape, and (b) a crack representing the HTS tape as a reduced-dimension geometry.

reads

$$\texttt{d(rho*Hty1,y1)+mu*d(Ht,t)=0}, \tag{B.7}$$

in accordance to (B.3). The notation `Hty1` defines the derivative of `Ht` with respect to `y1` also using the COMSOL notation. So far, the physics of the original and virtual domains are still uncoupled.

Two boundary *Pointwise Constraint*s are then applied to couple the original and the virtual domains, one for each side of the thin region ($\Gamma_s^{\mathrm{u}}$ and $\Gamma_s^{\mathrm{d}}$ depicted in Fig. B.1b) as

$$\texttt{up(phix)+Ht=0}, \tag{B.8}$$

$$\texttt{down(phix)+Ht=0}, \tag{B.9}$$

in $\Gamma_s^u$ and $\Gamma_s^d$, respectively.

The electrical nonlinear resistivity can be defined as

$$\texttt{rho = Ec/Jc*(abs(Jz)/Jc)}\wedge\texttt{(n-1)}. \tag{B.10}$$

where `Jz` is taken as the derivative of `Ht` with respect to `y1`, i.e. `Jz = Hty1`.

Finally, the magnetic scalar potential must be gauged to ensure the uniqueness of the solution. In COMSOL, we apply a *Pointwise Constraint* of `phi=0` at any point of the domain. Moreover, Gauss' law is automatically fulfilled by the use of first-order nodal FE elements in the air region.

In terms of post-processing, the total AC losses inside the thin region are obtained by two consecutive integrals: one over the 1-D virtual domain (named `ydintop1`) representing the thickness of the tape, and the other over the line $\Gamma_s$ representing its width in the 2-D original domain. In *Results*, a *derived value* of type *line integration* is defined as

$$\texttt{xdim1.xdintop1(Jz*Ez)}, \tag{B.11}$$

which corresponds to the instantaneous AC losses inside the thin region in W/m, where `Ez = rho*Jz`.

Although some effort is required to implement the $H$-$\phi$-formulation with the proposed TS model in COMSOL, the application of potential discontinuities in problems involving multiple tapes can be made by simply selecting all the geometric entities representing the cuts at once. The same procedure can be adopted for defining the physics inside multiple tapes and using a single *Extra Dimension*. In cases involving multiple tapes with different geometrical or

physical parameters, the procedure needs to be replicated for as many different tapes as the system has. However, in all cases, the thickness, the mesh and the order of the FEs in the virtual domain can easily be modified without changing the original domain and its discretization, which may be especially interesting when performing parametric studies.

The presented TS model was implemented in COMSOL Multiphysics version 5.5. Simulations were performed using a personal computer with an Intel i7 2400 processor with 16 Gb of memory. The relative tolerance of the calculation was set to $10^{-5}$, with absolute tolerance set to $10^{-7}$.

### Simulation Results

To highlight the advantages of the proposed TS model with the $H$-$\phi$-formulation, we simulated three benchmark problems involving HTS tapes in 2-D infinitely-long and axisymmetric representations. In all examples, the critical current density was set to $J_c = 2.5 \times 10^{10}\,\mathrm{A/m^2}$ and the electric field criterion was $E_c = 1 \times 10^4\,\mathrm{V/m}$. The power index in the $E$-$J$ power law was set to $n = 25$. Moreover, the operating frequency was $f = 50\,\mathrm{Hz}$ and the amplitude of transport current imposed in each tape was $I_0 = F_c I_c$, where $I_c = J_c S$ is the critical current, $S$ is the cross sectional area of the tape, and $F_c \in [0, 1]$ is a constant defining the transport current as a fraction of $I_c$.

### Single HTS Tape

Our first example is a 2-D infinitely long representation of a single HTS tape embedded in an air region equivalent to the benchmark problem #1 of the HTS Modelling Workgroup [138]. The tape is 1 $\mu$m thick and 12 mm wide. A circle of radius $R = 10\,\mathrm{cm}$ represents the airspace, and the tape is located at its center. In terms of mesh, we considered 80 finite elements along the tape width and a *normal free triangular* mesh is defined in COMSOL for the air region.

Results obtained with the proposed TS model ($H$-$\phi$ TS) with a single 1-D element in the virtual domain were initially compared with those obtained with the $T$-$A$-formulation proposed in [35] in terms of the local field distribution. In the $T$-$A$-formulation, finite elements of quadratic order were used for $A$, and linear finite elements were used for $T$, as proposed in [108] to avoid numerical oscillations in this model. In the TS model, linear finite elements were used in both the original and virtual domains. The constant $F_c$ was firstly fixed to 0.9 in this example.

Fig. B.3 shows the norm of the magnetic flux density obtained with the $H$-$\phi$ TS and the $T$-$A$ models at peak value ($t = 1/4f$). The two solutions visually agree, validating the

proposed TS model in terms of local field distribution in the original 2-D domain. For further validation, we evaluated the distribution of the magnetic field perpendicular to the tape surface ($y$-component of $H$) along the width of the tape (Fig. B.4). The $H$-$\phi$ TS result was taken as the mean value of $H$ on the sides of the tape, i.e.

$$\texttt{(up(-phiy)+down(-phiy))/2}. \tag{B.12}$$

In the $T$-$A$-formulation, the normal component of $H$ is also taken as the mean value of its components on the sides of the tape according to [107]. The perpendicular field components obtained with the two models along the width of the tape are very close.

The constant $F_c$ was then varied from 0.3 up to 0.9, and we evaluated the total AC losses in the tape using (B.11) for 1, 2 and 3 virtual elements in the virtual domain of the proposed TS model. Our aim with this study was to investigate the influence of the virtual elements when evaluating the AC losses in the tape for different transport current values.

The total AC losses per cycle of time as a function of $F_c$ ($\mathcal{Q}$) obtained with the $T$-$A$ and the $H$-$\phi$ TS models are presented in Fig. B.5. These results are also compared with the Norris analytical model [135], defined as

$$\mathcal{Q} = \frac{\mu_0 I_c^2}{\pi}\left[\begin{array}{r}(1-F_c)\ln(1-F_c) \\ +(1+F_c)\ln(1+F_c)-F_c^2\end{array}\right]. \tag{B.13}$$

We observe that the increase in the number of finite elements in the virtual 1-D domain does not impact the solution in terms of AC losses in this study. The solution with one virtual element is already comparable to the $T$-$A$ solution. As discussed in [133], for problems where the normal component of the magnetic field dominates the dynamics of the problem (such as in this one), a single element in the virtual discretization is enough to provide a sufficiently accurate solution.

The computation times of the two models as a function of $F_c$ are presented in Fig. B.6. We observe that the proposed TS model with one virtual element has a simulation time comparable to the $T$-$A$ model. When the number of elements in the virtual 1-D domain increases ($N > 1$), the simulation time with the TS model increases, especially at high transport current. However, in the example of a single tape, only one virtual element was enough to evaluate the local field distribution and total AC losses accurately, as discussed. The use of more than one virtual element will be required, for example, in cases of closely packed tapes where the magnitude of the tangential field is more important than that in a single tape problem. The case of two closely-packed tapes is presented in Section B.

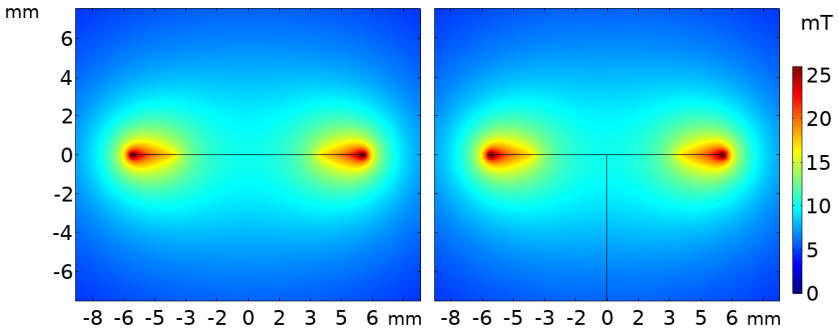


(a) $T$-$A$ (b) $H$-$\phi$ TS

Figure B.3 Magnetic flux density ($|B|$[T]) for the single HTS tape example with $F_c = 0.9$ at peak value ($t = 1/4f$). (a) Result of the $T$-$A$ model and (b) result of the $H$-$\phi$ TS model.

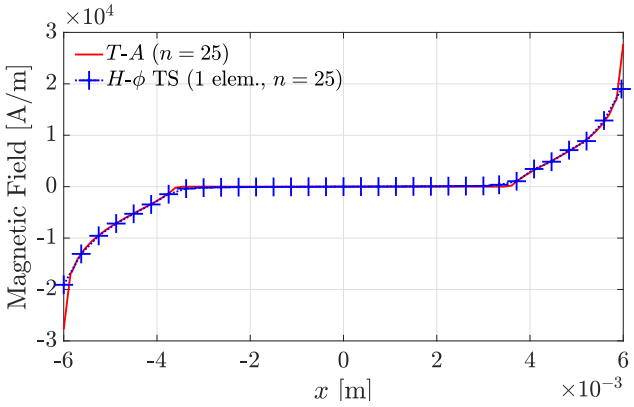


Figure B.4 Normal component of the magnetic field along the tape width at peak value ($t = 1/4f$) evaluated using the $H$-$\phi$ TS and the $T$-$A$ models. A single virtual element was considered in the $H$-$\phi$ TS model.

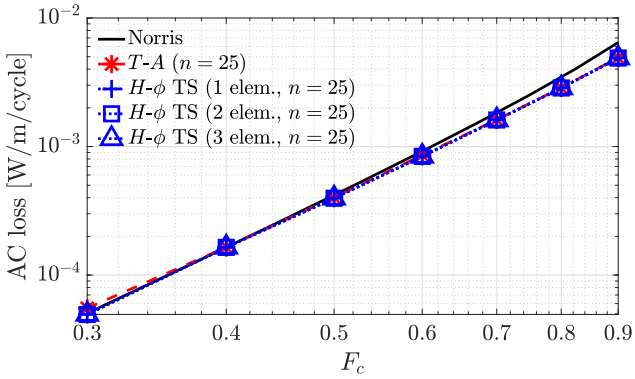


Figure B.5 AC losses in the single tape example as a function of the transport current relative to the critical current. The TS model results with 1, 2 and 3 elements in the virtual domain are compared with the Norris analytical model and with the results of the $T$-$A$-formulation.

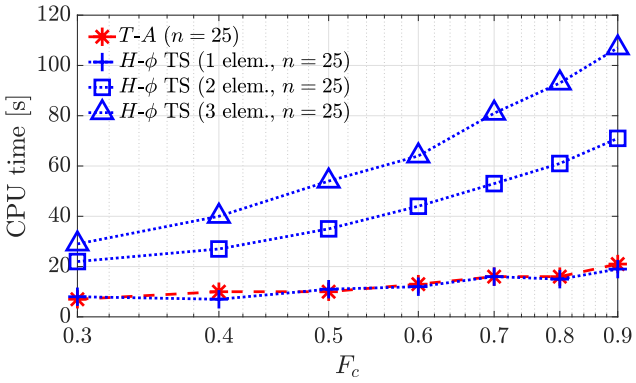


Figure B.6 Simulation times of the single tape example as a function of the transport current relative to the critical current. The TS model simulation times with 1, 2 and 3 elements in the virtual domain are compared with the $T$-$A$ simulation times.

### Axisymmetric Racetrack Coil

We then considered an axisymmetric example of 20 superposed thin HTS tapes representing the cross-section of a racetrack coil (Fig. B.7). The inner tape is located $R_{\text{in}} = 10\,\text{cm}$ away from the symmetry axis ($r = 0$), and the inter-tape distance is $L = 250\,\mu\text{m}$. The mesh and power law parameters are the same as in the first example. This problem is equivalent to the Benchmark problem #3 of the HTS Modelling Workgroup [138].

The implementation of the axisymmetric TS model in COMSOL follows exactly the same steps presented in Section B, except that the variables are defined in a polar coordinate system $(r,z,\theta)$ instead of a Cartesian coordinate system $(x,y,z)$. The transport current is imposed in the tapes using the thin cuts depicted in Fig. B.7. In each cut $C_i$, for $i = 1,\ldots,20$, a scalar potential discontinuity $I_i = iI_0$ was imposed so each tapes carries the same current $I_0$. A more detailed discussion about imposing current constraints using the thin cuts is presented in [119].

The results from the proposed TS model were compared with those of the pure $H$-formulation and of the standard $H$-$\phi$-formulation obtained with a full discretization of the tape, and with

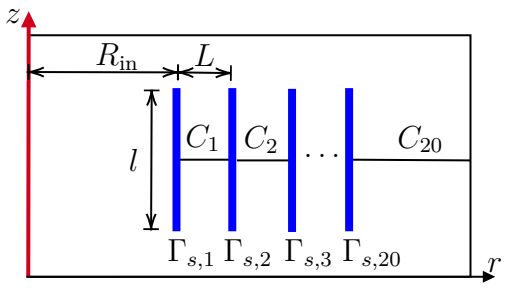


Figure B.7 Racetrack coil axisymmetric domain. The symmetry axis is depicted in red, the 20 HTS tapes ($\Gamma_{s,i}$, for $i = 1,\ldots,20$) in blue, and the thin cuts ($C_i$) in black.

those of the $T$-$A$-formulation. To ensure sufficient accuracy in the $H$ and $H$-$\phi$ models, the thickness of the tapes was scaled up to $10\,\mu$m. Despite this, the aspect ratio of the tapes remains relatively high, and the application of the TS model still makes sense. Therefore, in the $H$-$\phi$ TS and the $T$-$A$ models, each tape was represented as a low-dimension geometry in the original domain. Since all tapes have the same geometrical and material properties, a single *Extra dimension* was defined in COMSOL. Moreover, only one virtual element was considered in the $H$-$\phi$ TS model, and 80 elements were considered for the thin surface discretization. Our objective here was to evaluate the solution accuracy of the proposed model and compare the simulation time with those from the other three models in an example involving multiple tapes.

Fig. B.8 shows the magnetic flux density distribution evaluated using the four models at $t = 1/4f$ and $t = 1/2f$. The solution of the $H$-$\phi$ TS model agrees with the three others in terms of local field distribution. This validates our approach for cases of multiple tapes in terms of local field distribution.

The total AC losses were also evaluated in the TS model with (B.11) and integrated over a cycle of time. The result is compared with those obtained with the other three models at different transport currents in Fig. B.9. We observe again an excellent agreement between the solutions of the four models.

The simulation times as a function of the relative transport current are presented in Fig. B.10. Simulations with the proposed TS model were approximately ten times faster than simulations with the standard $H$-$\phi$-formulation, which were already more than ten times faster than a pure $H$-formulation for this example. When the proposed TS model was compared with the $T$-$A$ model in the previous example, the simulation times of these models were comparable. For the axisymmetric racetrack coil example, the simulation time with the $T$-$A$ model was closer to the simulation time of the standard $H$-$\phi$-formulation. The $H$-$\phi$ TS model performed simulations at least ten times faster than the other three models.

Two facts explain the simulation time differences between the proposed TS and the $T$-$A$ models in this example. First, the quadratic elements used for $A$ in the airspace greatly increases the number of degrees of freedom (DoFs). Indeed, the use of the scalar potential in the airspace and linear finite elements everywhere reduces the total number of DoFs in the $H$-$\phi$ TS model compared to the $T$-$A$ model. Second, the $T$-$A$ model solves a 1-D FE model as a function of $T$ along the width of each tape. Since here the number of tapes was scaled up to 20, the differences in simulation time become more noticeable in this example than in the previous one where the problem of a single HTS tape was studied. The total number of DoFs of the examples presented in this paper are summarized in Table B.1.

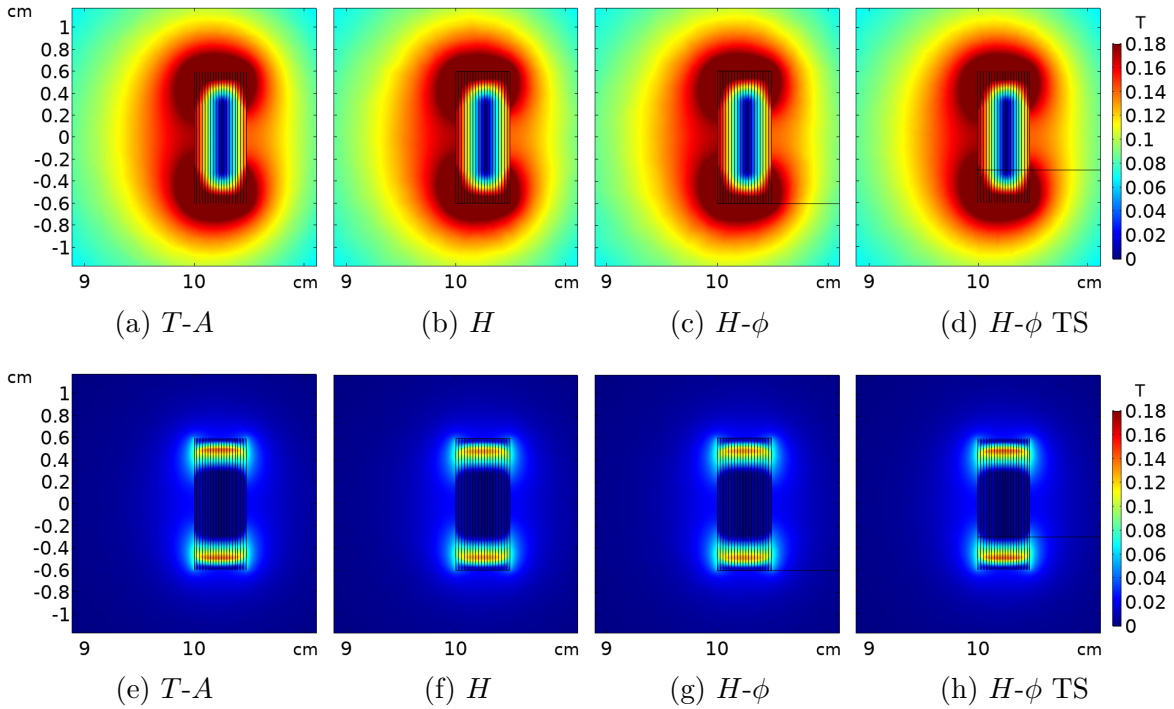


(a) $T$-$A$ (b) $H$ (c) $H$-$\phi$ (d) $H$-$\phi$ TS

(e) $T$-$A$ (f) $H$ (g) $H$-$\phi$ (h) $H$-$\phi$ TS

Figure B.8 Magnetic flux density ($|B|[T]$) distributions for the axisymmetric racetrack coil models at $t = T/4$ (a-d) and $t = T/2$ (e-h). The solution obtained with the proposed TS model in the $H$-$\phi$-formulation is comparable to the solutions of the $H$, $H$-$\phi$ and $T$-$A$ models.

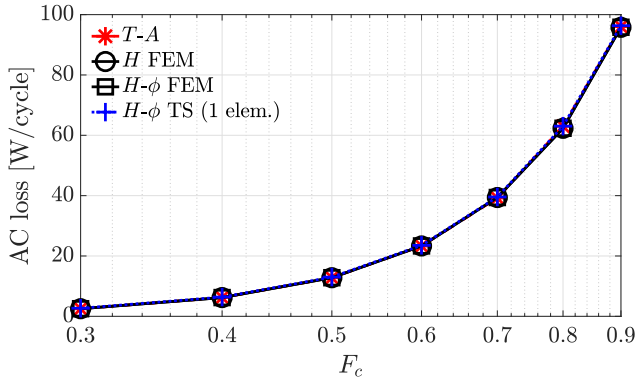


Figure B.9 AC losses in the axisymmetric racetrack coil models. The TS model results with 1 element in the virtual domain is compared with the results of a pure $H$ formulation, $H$-$\phi$-formulation and the $T$-$A$-formulation.

### Two Closely-Packed Tapes

In our third and last example, we considered a 2-D representation of two closely packed tapes embedded in the airspace. The geometry is presented in Fig. B.11. The tapes were 12 mm wide, and their thickness was scaled up to 10 $\mu$m, as justified in the previous example. The

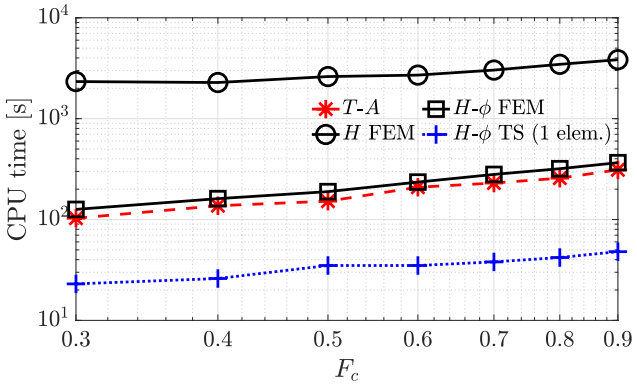


Figure B.10 Simulation times of the axisymmetric racetrack coil models. The TS model time with 1 element in the virtual domain is compared with the times of a pure $H$-formulation, $H$-$\phi$-formulation and the $T$-$A$-formulation at different transport current.

distance between the tapes was $L = 250\,\mu$m and the misalignment $m$ was initially set to zero. An anti-parallel current was imposed into them through a discontinuity of the scalar potential across a single cut $C_1$. This generates a more intense transversal field between the tapes than that in the previous examples.

The total AC losses as a function of the transport current in the tapes is presented in Fig. B.12 for the four models considered: $T$-$A$, $H$, $H$-$\phi$, and $H$-$\phi$ TS. We observe that the $T$-$A$-formulation underestimates the losses at low transport current when compared to a pure $H$ model. This is expected since only the losses related to the normal field component are taken into account by this model [108]. In the proposed TS model, the number of elements in the virtual 1-D domain was varied from 1 to 3. With only one virtual element, our model also underestimates the losses, but the 1-D mesh refinement improves the solution accuracy. With three virtual elements, the estimated AC losses are already very close to those obtained with the pure $H$-formulation and with the $H$-$\phi$-formulation with full discretization of the tapes. Since these two models are able to estimate both the losses related to the normal

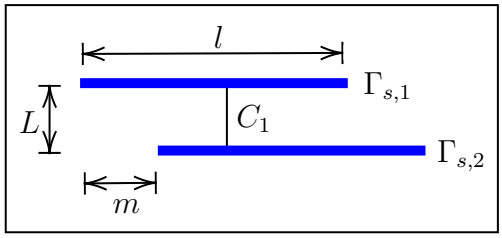


Figure B.11 Example of two closely-packed tapes $\Gamma_{s,1}$ and $\Gamma_{s,2}$. The distance between the tapes is denoted by $L$ and the misalignment by $m$. A single thin cut $C_1$ is required in this case to impose anti-parallel currents in the tapes.

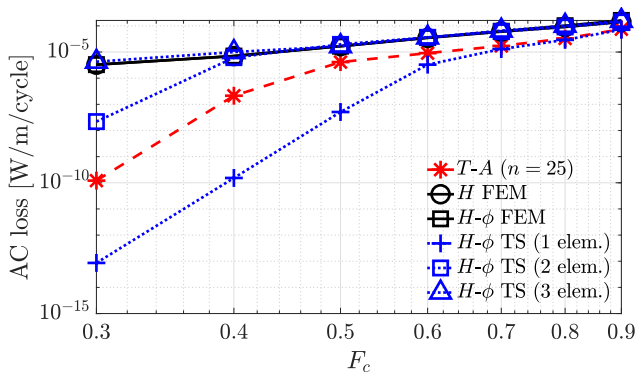


Figure B.12 AC losses in the two closely-packed tapes example. The TS model results with 1, 2 and 3 elements in the virtual domain are compared with the results of the $T$-$A$-formulation and a pure $H$-formulation.

and tangential components of the magnetic field, we conclude that the proposed TS model can be an efficient alternative to estimate losses in problems involving HTS tapes of any configuration.

Fig. B.13 shows the simulation times of the four models as a function of the transport current. They were equivalent for the $T$-$A$ and the $H$-$\phi$ TS models, and were at least a hundred times faster than the pure $H$ model. Simulations with the $H$-$\phi$ model were slower in this example than in the previous one. They were about ten times faster than the $H$ model but much slower than the $H$-$\phi$ TS model at low transport current. At transport currents close to the critical current, the $H$-$\phi$ simulation time was comparable to a pure $H$-formulation. Note that the increment in the number of virtual elements in the $H$-$\phi$ TS model slows down simulations, but it is still much faster than the standard $H$-$\phi$ model and performs better than the $T$-$A$ model in terms of losses estimation.

As a final study, we varied the misalignment between the two tapes and evaluated the AC losses as a function of the relative misalignment to the tapes widths ($m/l$) at $I_0 = 0.5I_c$. Three elements were considered in the virtual 1-D domain of the TS model for this study.

The total AC losses per cycle of time as a function of the misalignment are presented in Fig. B.14. The results are shown for the $H$-$\phi$ and the $H$-$\phi$ TS models. The solution of the two models agrees in any configuration. This further validates the proposed TS model for losses estimation in HTS tapes subjected to both normal and parallel field components.

The total number of DoFs of the three examples studied in this paper are summarized in Table B.1. For the single tape, only simulations with the $T$-$A$ and the $H$-$\phi$ TS models were performed due to the very thin thickness of the tape. Their thickness was then scaled up in the two last examples and results were compared with those from the standard $H$ and $H$-$\phi$

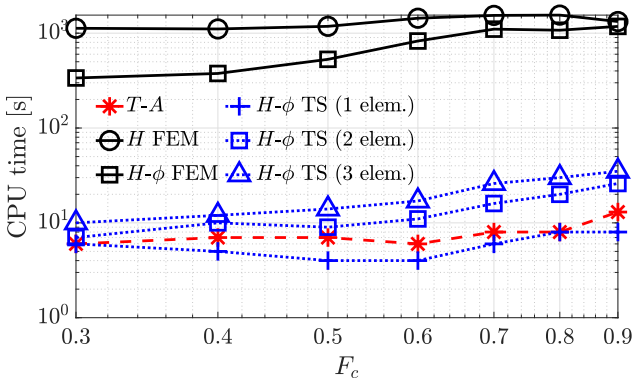


Figure B.13 Simulation times of the two closely-packed tapes example. The TS model time with 1, 2 and 3 elements in the virtual domain are compared with the time of the $T$-$A$-formulation and a pure $H$-formulation at different transport current.

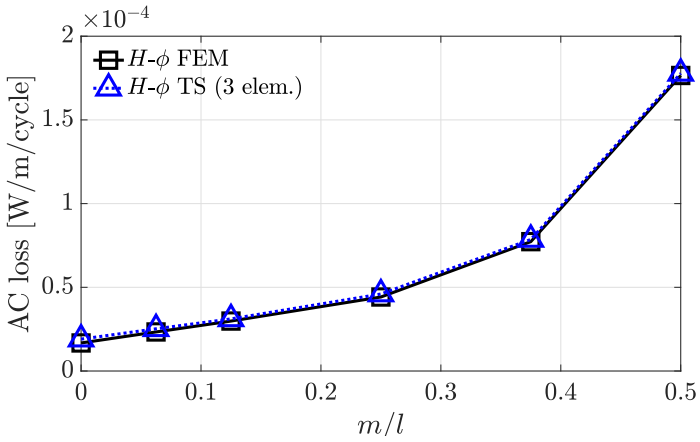


Figure B.14 AC losses as a function of the misalignment between two closely packed tapes carrying anti-parallel currents.

formulations. For the racetrack coil example, the $H$-$\phi$ TS model with one virtual element already provided sufficient accuracy. Note that the $H$-$\phi$ TS model requires less DoFs than all other models for these three examples.

## Conclusion

In this paper, we presented the implementation details of a thin-shell model with a virtual discretization of the shell thickness in COMSOL multiphysics. The virtual domain is directly coupled to the original system of equations and solved jointly.

The TS model was initially compared with the widely used $T$-$A$-formulation for a single HTS tape problem. The tape was 1 $\mu$m thick and 12 mm wide. In both the models, the tapes were

Table B.1 Total number of degrees of freedom (DoFs) in the three benchmark problems analyzed in this paper

| | $T$-$A$ | $H$ | $H$-$\phi$ | $H$-$\phi$ TS | | |
|---|---|---|---|---|---|---|
| | | | | 1 elem. | 2 elem. | 3 elem. |
| Single tape | 6530 | - | - | 1826 | 1906 | 1986 |
| Racetrack coil | 22011 | 621575 | 277280 | 10033 | - | - |
| Two tapes | 14151 | 105336 | 56545 | 2086 | 2246 | 2426 |

represented as a reduced-dimension geometry (a collapsed surface) to speed up calculations. The two models' results were equivalent in terms of local field distributions and total AC losses. Moreover, the simulation time of the proposed TS model with a single virtual element was comparable to that of the $T$-$A$ model, validating the proposed TS model.

We then scaled up the thickness of the tape to 10 $\mu$m and compared the results with the pure $H$-formulation and the standard $H$-$\phi$-formulation with a full representation and discretization of the tapes. Two benchmark problems were studied: an axisymmetric model representative of a racetrack coil, and the example of two closely packed tapes carrying anti-parallel currents. The results of our TS model were again compared in terms of local field distribution, AC losses estimation and simulation time.

For the racetrack coil example, the solutions of the four models were equivalent in terms of local field distribution and AC losses. However, the proposed TS model performed simulation around ten times faster than the standard $H$-$\phi$ and the $T$-$A$ models, which were already ten times faster than a pure $H$-formulation. For the two tapes example, the $H$ and $H$-$\phi$ models provided similar results, while the $T$-$A$ model underestimated the AC losses, especially at low transport current. Similarly, in the proposed TS model, a single finite element in the 1-D virtual domain could not estimate the AC losses correctly. However, the virtual mesh refinement in the TS model was demonstrated to be efficient in computing AC losses. It showed a good compromise between accuracy and efficiency.

In further work, the TS model could be extended for 3-D cases in COMSOL multiphysics (based on [137]) and to different finite-element formulations and applied to model large-scale HTS systems. Moreover, since the thin region is represented in a virtual 1-D domain, its thickness and materials properties can be varied without changing the original computational domain and mesh. Therefore, the proposed TS model can be extremely interesting to perform parametric studies, leading to faster HTS devices optimization.

**Acknowledgments**

This work has been supported by the Coordination for the Improvement of Higher Education Personnel (CAPES) - Brazil - Finance Code 001, the Fonds de Recherche du Québec - Nature et Technologies (FRQNT), the TransMedTech Institute, and the Canada First Research Excellence Fund.

# APPENDIX C AN EFFECTIVE THIN-SHELL APPROACH IN THE MAGNETIC FIELD FORMULATION FOR MODELING EDGES AND CORNERS OF THIN REGIONS

COMPUMAG 2021

(digest submitted June 28, 2021; accepted 27 September, 2021)

[1]Bruno de Sousa Alves, [1]Marc Laforest, [1]Frédéric Sirois

[1]Polytechnique Montréal, Montréal, QC H3C 3A7, Canada

## Abstract

A new thin shell (TS) model based on the magnetic field formulation is presented and applied to approximate a shielded induction heater. All the thin regions (shield, inductors and plate) are modeled as reduced-dimension geometries in the computational domain. The physics of these regions are taken into account by a virtual discretization across their actual thickness. Results show that the proposed TS model with a suitable virtual discretization leads to a very accurate solution near edges and corners of the thin regions, at a fraction of the computation time required by a fully discretized model.

## Introduction

Thin-shell (TS) models are often used to avoid meshing thin structures, to reduce the number of degrees of freedom (DoFs), and it's concomitant computational cost in finite-element (FE) simulations. It is known however that these models poorly represent edge and corner effects [95]. In the classical TS model, thin regions are collapsed on surfaces, and impedance conditions (ICs) are coupled through solutions for the fields defined in terms of hyperbolic trigonometric functions. Yet, near corners and edges, the field quantities may have a profile other than hyperbolic. In [100], the authors proposed a set of subproblems to correct the inaccuracies related to corner and edge effects. This method still relies on a complete discretization of the thin region, and some effort is required to couple the subproblems.

In this paper, we propose a new TS model with IBCs defined as virtual 1-D auxiliary FE systems across the thin region thickness. The 1-D systems are naturally coupled to the global system of equations and jointly solved. This avoids any post-processing and consecutive

resolutions as in the subproblem technique. The proposed model is here applied to tackle a shielded induction heater problem. The shield, the inductors and the heating plate are modeled as zero-thickness structures. The field and current distributions show excellent agreement with a reference solution obtained with standard FE.

### Model Description

The calculus domain is defined as $\Omega = \Omega_c \cup \Omega_c^C \in \mathbb{R}^3$ with boundary $\partial\Omega = \Gamma$, where $\Omega_c$ and $\Omega_c^C$ denote the conductive and non-conductive parts of $\Omega$, respectively. The actual thin region volume ($\Omega_s \subset \Omega_c$) is collapsed to a surface $\Gamma_s$ located halfway between its wide boundaries ($\Gamma_s^{\pm}$), which are still independent ($\Gamma_s = \Gamma_s^+ \cup \Gamma_s^-$). For simplicity, we consider that $\Omega_c = \Omega_s$, i.e., there are no conducting parts in $\Omega$ other than $\Omega_s$.

Assuming the low-frequency regime, disregarding displacement currents and Neumann boundary conditions in $\Gamma$, the variational form of the $\boldsymbol{h}$-formulation reads:

Find $\boldsymbol{h} \in \boldsymbol{H}(\mathrm{curl}, \Omega)$ such that

$$\Big(\mu\partial_t \boldsymbol{h}, \boldsymbol{g}\Big)_{\Omega_c^C} - \Big\langle \boldsymbol{n}_s \times \boldsymbol{e}, \boldsymbol{g}\Big\rangle_{\Gamma_s^+} + \Big\langle \boldsymbol{n}_s \times \boldsymbol{e}, \boldsymbol{g}\Big\rangle_{\Gamma_s^-} = 0, \tag{C.1}$$

$\forall\ \boldsymbol{g} \in \boldsymbol{H}(\mathrm{curl}, \Omega)$, where bold characters represent vectors, $\boldsymbol{h}$ is the magnetic field, $\boldsymbol{e}$ is the electric field, $\mu$ is the magnetic permeability, $\boldsymbol{g}$ are test functions, and $(\cdot,\cdot)_{\Omega_c^C}$ and $\langle\cdot,\cdot\rangle_{\Gamma^{\pm}}$ denote, respectively, the volume integral over $\Omega_c^C$ and the surface integral over $\Gamma_s^{\pm}$ of the scalar product of the arguments.

The magnetic scalar potential ($\phi$) is the working variable in $\Omega_c^C$ ($\boldsymbol{h} = -\nabla\phi$). Since $\Gamma_s$ has two complementary faces, $\Omega_c^C$ is multiply connected, and $\phi$ is not sufficient to express Ampere's law in this region (since $\forall\phi$, $\nabla \times \nabla\phi = 0$). A current representative is thus included in $\Omega_c^C$ through discontinuities in $\phi$ along thick cuts (or cohomology basis representatives of $\Omega_c^C$ [55]). The weight $I$ of the gauge $\phi$ then determines the current constraint on the corresponding conductor.

The ICs are obtained by reducing volume integrals over a virtual domain $\Omega_s'$ (representing $\Omega_s$) to surface integrals over $\Gamma_s^k$ and $\Gamma_s^{k-1}$, boundaries of a virtual 1-D element $\Omega_s^{(k)}$, for $1 \le k \le N$ (Fig. C.1). Note that $\Gamma_s^{\pm}$ share a common node at which $\phi_p$ is defined. Nodes and edges along $\Gamma_s^{\pm}$ are duplicated. Lateral field penetrations are neglected. Therefore, the two last

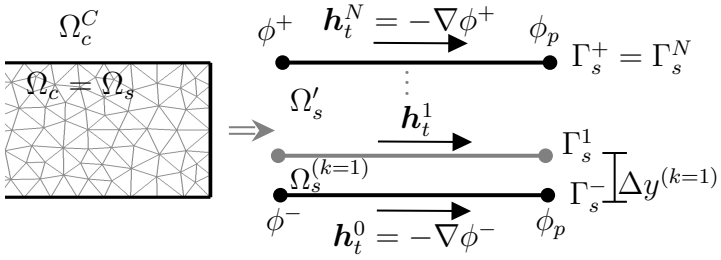


Figure C.1 Reference and proposed TS models.

terms in (C.1) are defined in terms of the tangential components:

$$\begin{aligned} &-\left\langle \boldsymbol{n}_s \times \boldsymbol{e}, \boldsymbol{h}' \right\rangle_{\Gamma_s^+} + \left\langle \boldsymbol{n}_s \times \boldsymbol{e}, \boldsymbol{h}' \right\rangle_{\Gamma_s^-} \\ &\quad = \sum_{k=1}^{N} \sum_{j=1}^{2} \left\langle \rho^{(k)} \boldsymbol{h}_t^m, \boldsymbol{h}' \right\rangle_{\Gamma_s^m} \cdot \mathcal{S}_{ij}^{(k)} \\ &\quad + \sum_{k=1}^{N} \sum_{j=1}^{2} \partial_t \left\langle \mu^{(k)} \boldsymbol{h}_t^m, \boldsymbol{h}' \right\rangle_{\Gamma_s^m} \cdot \mathcal{M}_{ij}^{(k)} \qquad \forall\, i = 1, 2, \end{aligned} \tag{C.2}$$

where $m = k - 2 + j$ relates the $m^{\text{th}}$ tangential component $\boldsymbol{h}_t^m$ to the boundaries $j = 1, 2$ of $k$, i.e., $\boldsymbol{h}_t^{m|_{j=1}} = \boldsymbol{h}_t^{k-1}$ and $\boldsymbol{h}_t^{m|_{j=2}} = \boldsymbol{h}_t^{k}$, for $0 \leq m \leq N$; $\rho^{(k)}$ is the electrical resistivity, and $\mu^{(k)}$ is the magnetic permeability of the element $\Omega^{(k)}$. The 1-D virtual stiffness and mass matrices in (C.2) are

$$\mathcal{S}_{ij}^{(k)} = \int_{\Delta y^{(k)}} \partial_y \theta_i \partial_y \theta_j dy, \qquad \mathcal{M}_{ij}^{(k)} = \int_{\Delta y^{(k)}} \theta_i \theta_j dy, \tag{C.3}$$

where $\theta_i$ are the first order Lagrange polynomials, and $\boldsymbol{h}'$ is chosen in the same function space as $\boldsymbol{h}$ (Galerkin's method).

### Application Example and Discussion

We consider a shielded induction heater comprising two inductors ($\mu_{r,\text{ind}} = 1$, $\sigma_{\text{ind}} = 1\,\text{MS/m}$), a plate in the middle ($\mu_{r,\text{plate}} = 100$, $\sigma_{\text{plate}} = 1\,\text{MS/m}$), and two shields ($\mu_{r,\text{shield}} = 1$, $\sigma_{\text{shield}} = 37.7\,\text{MS/m}$) similar to the example presented in [100]. The geometry is presented in Fig. C.2. Given the high aspect ratio of these regions, all of them were modeled using the proposed TS model. The surroundings were assumed to be filled with air ($\mu = \mu_0$). Simulations were performed in harmonic regime at two operating frequencies: $f = 1\,\text{kHz}$ ($\delta_{\text{ind}} = 0.5\,\text{m}$, $\delta_{\text{plate}} = 1.6\,\text{mm}$, $\delta_{\text{shield}} = 2.6\,\text{mm}$), and $f = 10\,\text{kHz}$ ($\delta_{\text{ind}} = 0.1\,\text{m}$, $\delta_{\text{plate}} = 0.5\,\text{mm}$, $\delta_{\text{shield}} = 0.8\,\text{mm}$). The reference solutions were obtained with elements of size $\gamma_{\text{ref}} = 0.5\,\text{mm}$ at $1\,\text{kHz}$ and $\gamma_{\text{ref}} = 0.25\,\text{mm}$ at $10\,\text{kHz}$. In the TS model, a coarser mesh ($\gamma_{\text{TS}} = 2\,\text{mm}$) was used since it does not hinder the model accuracy as in the reference model. A current $I = 120\,\text{kA}$ was

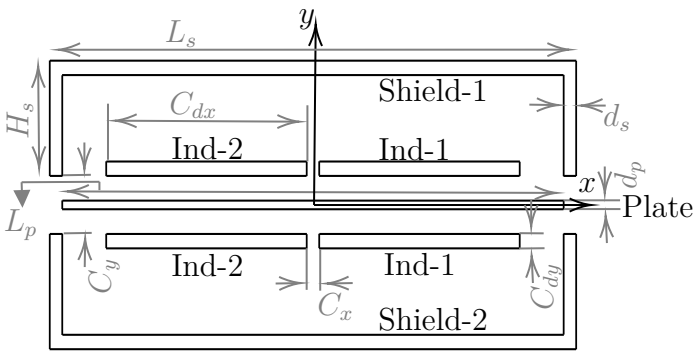


Figure C.2 Induction heater geometry ($L_p = 2\,\text{m}$, $d_p = 6\,\text{mm}$, $C_{dx} = 0.8\,\text{m}$, $C_{dy} = 1\,\text{cm}$, $H_s = 0.4\,\text{m}$, $d_s = 10\,\text{mm}$, and $L_s = L_p + 2d_s$). The thin regions thicknesses are not to scale.

imposed in the thin conductors using thick cuts.

Fig. C.3 shows the magnetic flux density $|\boldsymbol{b}|$ at $f = 1\,\text{kHz}$ obtained with both the reference and the TS models. In the TS model, $N = 9$ was considered. Note the equivalence between these solutions, especially near the edges of the plate, shields and inductors, and at the corners of the shields. The current density vector in each virtual element of the TS model ($\boldsymbol{j}_z^{(k)}$) in the plate was projected onto the $y$-direction. It is compared with the reference solution near the right edge of the plate with $\gamma_{\text{ref}} = \gamma_{\text{TS}} = 1\,\text{mm}$ in Fig. C.4. The uneven distribution of $\boldsymbol{j}_z$ is indeed well represented by the TS model at the plate edge.

The Euclidean (2-)norm of the relative differences on the magnetic flux density with the TS model between the reference solution on the plate surface ($y = d_p/2$) and at $y = C_y/4$ as a function of $N$ are shown in Fig. C.5. The TS solution converges to the reference solution as $N$ increases. The error was reduced from nearly 40% with $N = 1$ to less than 2% with $N = 9$.

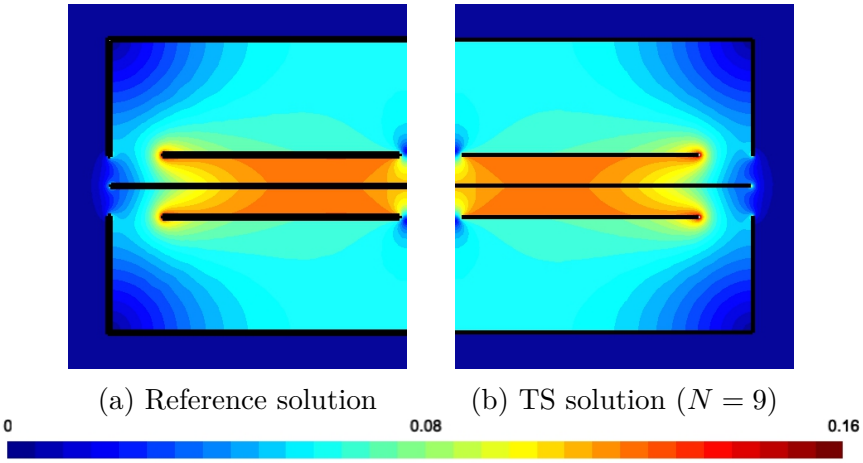


(a) Reference solution (b) TS solution ($N = 9$)

Figure C.3 Shaded plot of the isovalues of the magnetic flux density $|\boldsymbol{b}|$ at $f = 1\,\text{kHz}$ in half of domain with $\gamma_{\text{ref}} = 0.5\,\text{mm}$ and $\gamma_{\text{TS}} = 2\,\text{mm}$.

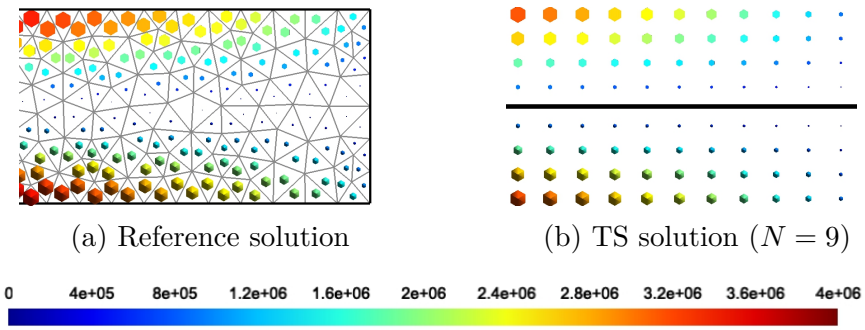


(a) Reference solution (b) TS solution ($N = 9$)

Figure C.4 Current density vector $\boldsymbol{j}_z$ near the right edge of the plate at $f = 1\,\text{kHz}$. The TS solution is obtained by projecting $\boldsymbol{j}_z^{(k)}$ across the thickness of the plate. $\gamma_{\text{ref}} = \gamma_{\text{TS}} = 1\,\text{mm}$ was considered.

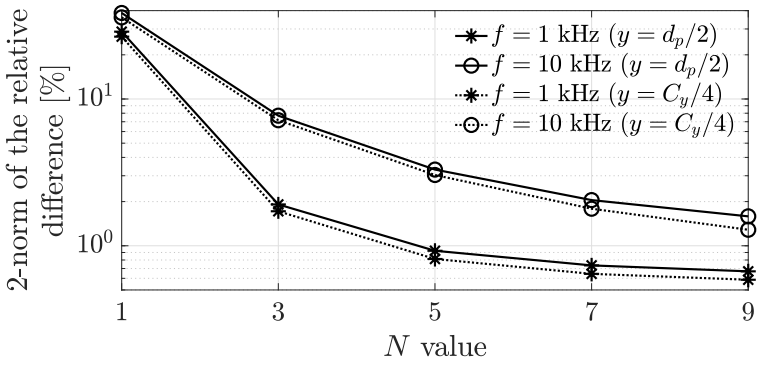


Figure C.5 2-norm of the relative differences of $|\boldsymbol{b}|$ between the TS and the reference solutions as a function of $N$ at $y = d_p/2$ and $y = C_y/4$, and at operating frequency $f = 1\,\text{kHz}$ and $10\,\text{kHz}$.

All models were implemented in Gmsh and GetDP. Simulations were conducted on a personal computer with an Intel i7 2400 processor with 16 Gb of memory. The total number of DoFs and the CPU time are summarized in Table C.1. Even with $N = 9$, the TS model provided a reduction of more than 88% in the number of DoFs and was about six times faster than the reference model. The TS model will be detailed and validated in nonlinear time-transient cases in the extended paper. Our latest progress towards fast 3-D time-transient analysis will also be presented.

Table C.1 Number of DoFs and CPU time in the reference and the TS models depending on $N$ ($f = 1\,\text{kHz}$, $\gamma_{\text{ref}} = 0.5\,\text{mm}$ and $\gamma_{\text{TS}} = 2\,\text{mm}$)

| | Ref. | $N = 1$ | $N = 3$ | $N = 5$ | $N = 7$ | $N = 9$ |
|---|---|---|---|---|---|---|
| DoFs | 2163425 | 202418 | 213222 | 224026 | 234830 | 245634 |
| Time [s] | 483.69 | 48.37 | 55.06 | 60.07 | 67.75 | 71.74 |